INVESTIGATION OF SOME ASPECTS OF HIGH ENERGY EXTRA-TERRESTRIAL RADIATION

A THESIS

submitted by

ROY PETER RAMPLING

for the degree of

DOCTOR OF PHILOSOPHY

in the

UNIVERSITY OF LONDON

October 1971

ABSTRACT

Part 1

An X-ray detector was flown on a high altitude balloon from Cardington, Bedfordshire on June 20th 1970. It comprised a single 3" sodium iodide scintillator crystal and was collimated to a $\pm 20^{o}$ opening angle by a graded metal, passive collimator. The geometrical factor was 5.2 cm^2 ster. The purpose of the experiment was to search for X-radiation in a single energy interval, 30-120 keV, from the known radio pulsar CP0328.

The pulsar fell within the field of view, for approximately $2\frac{3}{4}$ hours but optimisation of the data reduced the fraction of the pulsar traversal which was used to 68 minutes. The time resolution of the recording and analysis system was $\pm$ 2 parts in 10^6 which enabled synchronisation over the period of observation to be maintained to $\lesssim \pm$ 10 ms.

A computer, programmed to function in a multiscalar mode, was used to examine the data for evidence of the pulsar, which was assumed to have a period that could be calculated from published measurements at radio wavelengths. An upper limit of 1.6×10^{-32} W m^{-2} Hz^{-1} is placed for the time averaged spectral power emitted by CP0328 in the observed energy range.

The implications of this result to currently proposed pulsar models are discussed. Results of other workers made at X-ray and optical wavelengths are also discussed in the same context.

Part 2

An examination is made of the inadequacy of the magnetospheric parameters in present use for the description of the arrival patterns of solar flare protons to low altitudes over the polar caps. An alternative ordering system is suggested which results from the use of computed particle

trajectories in a high simulation model of the geomagnetic field. The use of solar protons as probes of the distant magnetotail is suggested.

The new ordering system is applied to the solar flare event of November 18th, 1968, data for which were available from proton telescopes on board the two polar orbiting satellites, ESRO I and II.

The satellites crossed the northern polar cap at almost the same times and in perpendicular directions. Interplanetary particle and magnetic data were also available from Explorers 34 and 35. The results of the analysis suggest that most of the structure in the proton profiles can be explained in terms of the response to interplanetary particle anisotropies of a slowly diverging magnetotail, the field lines in which reconnect to interplanetary field lines across a rotational discontinuity type of magnetopause. The occurrence of a rapid change in particle flux, probably associated with an observed magnetic discontinuity, is also responsible for some structure. Limits to the length, L, of the coherent magnetotail are estimated to be $400\ R_E \lesssim L \lesssim 1000\ R_E$.

CONTENTS

ACKNOWLEDGEMENTS

Firstly I would like to thank Professor H. Elliot for the opportunity to work in the Space Physics Group at Imperial College.

I would also like to thank my supervisor, Dr. R.J. Hynds, for suggesting this work and for his constant encouragement, advice and necessary good humour throughout.

I owe a debt of gratitude to all my colleagues in the Cosmic Ray group for their co-operation during the building and flying of the X-ray detector. In particular I would like to thank Dr. C.P. Hedgecock for his advice and help with the ground equipment, Mrs. A. Evans for her assistance with the analysis programs and Dr. R.K. Sood for his cheerful supervision of the balloon launch.

I am indebted to my colleague Dr. G. Morfill for his invaluable help with the trajectory calculations and for many fruitful discussions.

The interplanetary magnetic field data was generously supplied by Dr. C.P. Sonnet and I am grateful to Mr. A. Bewick for allowing the results of the S-25 experiments to be used prior to publication and to the Director of the Radio and Space Research Station, Slough, for the use of the ESRO I data.

I would like to thank Miss Corri van de Stege for typing this thesis and the Science Research Council for their financial support.

Finally, I would like to thank the members of my family whose constant encouragement and support throughout played such a large part in the production of this thesis.

PART I

A BALLOON BORNE EXPERIMENT TO SEARCH FOR 30-120 keV X-RAYS FROM THE PULSAR CP0328

CHAPTER 1 - X-RAY ASTRONOMY

1.1 General Introduction

X-rays exhibit the same advantages as all electromagnetic radiations in that they traverse space undeflected by magnetic fields and remain coherent in time. X-ray astronomy would, therefore, seem a useful technique for probing the Universe. The absorbing effects of the atmosphere prevent X-ray astronomy from being conducted at ground level and vehicles must be used to transport X-ray telescopes to suitable altitudes. In spite of the restrictions this transportation must impose on the sizes of detectors used, their field of view and the duration of each observation, galactic X-ray astronomy has, in its first ten years, achieved a high level of sophistication. All experiments have so far been conducted using balloons, short duration rocket flights and satellites, but the prospect of a manned orbiting observatory is extremely exciting and will allow the first continuous monitoring of X-ray sources, bringing this branch of astronomy into line, in this respect, with its optical and radio counter parts.

Even when the effect of the atmosphere has been removed, absorption in interstellar space still places a lower limit on those photon energies that can be observed. This limit varies according to the depth in space of the observed object. It is conceivable that, with sufficient resolution, very close objects might become visible at about 0.1 keV but it is more normal for X-ray astronomy to begin at energies > 1 keV when distances of a galactic scale are considered. Observation of extra-galactic objects begins at 2 keV and the complete Hubble sphere is open to photons of energy > 8 keV. The upper limit to this realm of astronomy

is placed, not by absorption, but by the rapid decrease of fluxes with increasing energy. Even so, measurements have been successfully carried out at energies > 50 MeV.

Although the sun had been recognised as a source of soft X-rays since the late 1940's, fourteen years later only an upper limit of 10^{-8} ergs.cm^{-2}sec^{-1}Å^{-1} had been placed on the flux from outside the solar system (Friedman, 1959). In 1962 a rocket flight was made with a detector of much greater sensitivity than had hitherto been used. The purpose was to detect fluorescence X-rays from the moon in the wavelength range 2 - 8 Å. In addition a strongly anisotropic flux was observed to come from the region of the galactic centre (Giacconi et.al., 1962). It was subsequently demonstrated that the cause of this enhancement could only have been a direct observation of a genuine source of soft X-rays lying outside the solar system. Later flights showed the emission to come not from the galactic centre, however, but from the region of Scorpius. The source was finally identified optically by Sandage et.al. (1966) to be a 13th apparent visual magnitude starlike object with an ultraviolet excess. This identification was made possible after the source had been located to 1 sec. of arc in the energy range 1 - 24 keV by Gursky et.al. (1966).

Fifty discrete sources have since been discovered, together with an unresolved, almost isotropic background. Most of the sources lie in the galactic plane with a distribution tending to cluster around the galactic centre. This almost certainly classifies the majority of sources to be galactic objects. A small proportion of the sources have been identified at optical or radio wavelengths, various associations being with supernova remnants, blue stars , radio galaxies, a quasar and a pulsar.

There are many mechanisms which could produce the X-rays detected from cosmic sources, each imposing strict conditions on the nature of the source object. Conclusions as to which mechanisms predominate in a source may be drawn from the spectra, intensity, polarisation and variability of the observed X-rays, particularly when correlated with the position and distribution of the sources themselves. The inferences drawn in this way are compared with those drawn from other forms of astronomy, in the hope of building a consistent picture of the Universe.

The main processes for the production of X-rays that might be applied to cosmic sources are outlined in the following section.

1.2 Production Mechanisms for X-rays

1.2.1 Magnetic Bremsstrahlung

A charged particle in a magnetic field with a velocity vector $\underline{v}$ that is not parallel to the field, performs a helical motion about that field. Implicit in helical motion is a centripetal acceleration which causes the particle to radiate magnetic bremsstrahlung or synchrotron radiation. In most cosmological applications the magnetic fields are weak and ultrarelativistic particles are needed to produce synchrotron X-radiation.

In a vacuum, an ultrarelativistic particle, of energy E, accelerated in a magnetic field, radiates primarily in a cone of half angle mc^2/E, $(= {}^1/_\gamma)$, formed about the direction of instantaneous particle velocity. The radiation is, in general, elliptically polarised and has a power spectral distribution that peaks, for electrons, at an energy

$$h\upsilon_{max} = 5.8 \times 10^{-9} B_\perp \gamma^2 \text{ eV} \qquad (1.2.i)$$

(Morrison, 1967)

where $B_\perp$, the perpendicular component of the magnetic field, is in gauss.

From this it can be seen that to efficiently radiate 10 keV photons in a field of 10 μG, an electron requires an energy $\sim 10^{14}$ eV. The inclusion of the γ^2 term means that demands on proton energies to emit similar radiation are prohibitively large for the effect to be more than negligible.

The spectral density of the total strength of the radiation from a single electron at the maximal frequency is given by

$$p(\upsilon_{max}) = P_{max} = 2.16 \times 10^{-22} B_{\perp} \text{ erg sec}^{-1} \text{ Hz}^{-1} \qquad (1.2.ii)$$

(Ginzburg and Syrovatskii, 1965),

and the total power emitted per electron is

$$P(E, \dot{B}) \simeq 9.9 \times 10^{-4} \gamma^2 |B_{\perp}|^2 \text{ eV sec}^{-1} \qquad (1.2.iii)$$

(Morrison, 1967)

The lifetime of such electrons is given by

$$\tau_{\frac{1}{2}} = \frac{5.1 \times 10^8}{B_{\perp}^2 \gamma} \text{ secs.} \qquad (1.2.iv)$$

which for a 10^{14} eV electron in a 10 μG field yields $\tau_{\frac{1}{2}} \sim 300$ years. As $B_{\perp}$ increases, clearly this value decreases rapidly and whilst such short lifetimes are useful to explain short term cosmological fluctuations in hard X-rays, they also demand a rapid decay of flux or a continuous source injection of very energetic electrons.

The basic laws outlined above for an individual electron have been extrapolated to populations of electrons by Ginzburg and Syrovatskii (1965).

Taking a homogeneous, isotropic distribution of electrons conforming to a power law

$$N(E) = K E^{-\gamma} dE \qquad (1.2.v)$$

they showed that in a field, H, whose direction varied along a line of sight such that the vectorial distribution could be considered random, then the average intensity at a frequency υ was given by

$$I(\upsilon) = 1.35 \times 10^{-22} a(\gamma) LKH^{(\gamma+1)/2} \left(\frac{6.26 \times 10^{18}}{\upsilon} \right)^{\frac{(\gamma-1)}{2}}$$

$$\text{erg. cm}^{-2}\text{sec}^{-1}\text{ster}^{-1}\text{Hz}^{-1} \qquad (1.2.vi)$$

where L is the line of sight dimension of the radiating region and $a(\gamma)$ is an energy dependent, slowly varying parameter of the analysis. Because of the random field direction there would be no polarisation. In cosmological phenomena the fields along a line of sight will not always be randomised and hence much elliptical polarisation is to be expected in the radiation.

From eqn. (1.2.vi) there follows a power law for the frequency spectrum

$$I\upsilon \propto \upsilon^{-(\gamma-1)/2} \qquad (1.2.vii)$$

1.2.2 Thermal Bremsstrahlung

Bremsstrahlung radiation results from acceleration produced in the deflection of charged particles (mainly electrons) in collision with atomic nuclei. This free-free emission can produce photons with a large fraction of the primary energy of the electron and, thus, relatively low energy electrons can produce X-rays in this way.

A most efficient way of producing such radiation is from thermal electrons in a hot plasma. If the electrons have a Maxwellian distribution of velocities, then to a good approximation it can be shown (Allen, 1963)

that the radiation power from a unit volume obtained by integrating the bremsstrahlung formula over the distribution at temperature T is

$$P(\upsilon) = 5.443 \times 10^{-34}\, g \exp\left(-\frac{h\upsilon}{kT}\right) T^{-\frac{1}{2}} \sum_{\substack{\text{all} \\ \text{populations}}} n_e n_i Z^2 \text{ erg.cm}^{-3}\text{sec}^{-1}\text{sr}^{-1} \qquad (1.2.viii)$$

where n_e, n_i are electron and ion densities in cm^{-3} and Ze is the ion charge. The effective Gaunt factor, g, is a function of frequency and temperature. By integrating over all υ it can be shown that the total free-free emission is given by

$$E = 1.435 \times 10^{-27} T^{\frac{1}{2}} g \sum n_e n_i Z^2 \text{ erg. cm}^{-3} \text{ sec}^{-1} \qquad (1.2.ix)$$

These formulae apply only to optically thin plasmas. Above $T = 10^6$ °K both hydrogen and helium are completely ionised. Other abundant cosmic elements, e.g. C, O etc., are also highly ionised. Assuming a population of normal cosmic abundance Tucker and Gould (1966) show that

$$n_e = 1.34\, n_i \quad \text{and} \quad \sum n_e n_i Z^2 = 1.34\, n_e^2$$

In a hot dilute plasma other radiative processes might be acting but Tucker and Gould (1966) show that for energies > 2 keV free-free collision is the dominant production mechanism.

1.2.3 Black-Body Radiation

The total outward flow of radiation from unit surface area of a black-body with surface temperature T is

$$P = \sigma T^4 \text{ erg.cm}^{-2}\text{sec}^{-1} \qquad (1.2.x)$$

where $\sigma = 5.669 \times 10^{-5}$ erg.cm^{-2}sec^{-1}deg^{-4} (Allen, 1963)

The process is so efficient with respect to the source size that it implies sources of small physical area and, for the same reason, the implied life-

times are also very short. In a spherical black-body, the lifetime for the emission of the thermal energy content is given by Morrison (1967) as

$$\tau \sim \left(\frac{R\rho}{T_s^3}\right)\left(\frac{Tav}{Ts}\right) \times 10^{13} \text{ secs} \qquad (1.2.xi)$$

where Ts is the surface temperature, Tav the mean temperature, R the radius and ρ the mean density.

The emittance of photons is governed by the Planck spectrum and can be written as

$$N(\upsilon)d\upsilon = 2\pi\left(\frac{\upsilon^2}{c^2}\right)\left(\exp\left(\frac{h\upsilon}{kT}\right) - 1\right)^{-1} \text{ photons cm}^{-2}\text{sec}^{-1} \text{ in } d\upsilon \qquad (1.2.xii)$$

This radiation is unpolarised and hence the intensity of radiation, linearly polarised in any direction, will be half the total intensity.

Between the optically thin situation discussed for bremsstrahlung production and the true black-body case there are many shades of grey. As the optical depth of the gas surrounding a radiation source becomes thicker, so will the emitted spectrum of the object tend towards a black-body spectrum, because of the degrading of high energy photons and the upgrading of low energy photons in Compton collisions. Optical depth is usually a function of photon energy and hence an object radiating as a black-body in the optical region might show a thermal spectrum at X-ray energies. This is the case with Sco X-1.

1.2.4 Inverse Compton Effect

The production of radiation from the inverse Compton effect requires the interaction of relativistic electrons with an electromagnetic field.

Such an interaction of electrons with an oscillating field might well be expected to show similarities to the interaction of electrons with static magnetic fields (synchrotron radiation). That this is so is well described by Felton and Morrison (1966).

For most astrophysical purposes inverse Compton scattering is considered for electrons with values of γ between 4 and 10^4 in collision with isotropic fields of ambient photons. The upper electron energy limit allows collisions with photons of energy $E > {}^{m_o c^2}/_{\gamma}$ to be neglected and the energy dependent differential scattering cross-section of Klein and Nishina to be approximated to the Thompson limit. The lower limit on electron energy allows the photon beam in the electron rest frame to be considered unidirectional. With these approximations the power from inverse Compton scattering generated per fast electron was shown by Felton and Morrison (1966) to be

$$P_c \simeq 2.66 \times 10^{-14} \gamma^2 \rho \quad \text{eV sec}^{-1} \qquad (1.2.\text{xiii})$$

where ρ is the energy density in the isotropic field in eV cm^{-3}.

The errors incurred by the approximations were investigated by Jones (1965) who also showed that for electrons with a smooth power law distribution of energy, both inverse Compton and synchrotron radiation produced the same spectral shape.

The lifetime of an electron radiating according to eqn. (1.2.xiii) is

$$\tau_{\frac{1}{2}} \sim \frac{2 \times 10^{19}}{\gamma \rho} \text{ secs} \qquad (1.2.\text{xiv})$$

(Felton and Morrison, 1966)

An electron with $\gamma = 10^4$ in the galaxy with $\rho \sim 10^{-1}$ eV cm^{-3} will survive for about 10^9 years. Clearly, on a galactic scale this is a very long-lived process. However, at the surface of a radiating object ρ would increase

drastically and inverse Compton scattering could be responsible for considerable energy loss.

Although relativistic electrons are still needed for this process, inverse Compton scattering requires much lower energy particles to produce X-rays, provided the photon field is sufficiently strong.

If individual sources are proposed to emit via inverse Compton scattering then they must be presumed to be extensive since any magnetic field which contains the electron population must not be so intense as to cause dissipation of substantial energy via synchrotron radiation.

1.2.5 Minor Processes

Line emission - Energy can be lost from a plasma when inelastic electron collisions excite ions to discrete levels which are subsequently depopulated, primarily by radiative transitions. For a Maxwellian electron velocity distribution the energy emitted due to such excitations of the level n' of an ion, charge z, in ground state n is given by

$$\frac{d\,E_{L,\,z,\,n\,n'}}{d\,t\,d\,V} = n_e\, n_i\, 8\pi^2\, e^4\, f_{nn'}\, \langle \bar{g}_{nn'} \rangle\, (6\pi m\, k\, T)^{\frac{1}{2}} \exp\left(-\frac{E_{nn'}}{kT}\right)$$

(Tucker and Gould, 1966)

where $f_{nn'}$ is the dipole oscillator strength for the transition, $\langle \bar{g}_{nn'} \rangle$ is the time averaged effective Gaunt factor and $E_{nn'}$ is the excitation energy. Most of the cosmically abundant elements, however, produce only lines at $<$ 1 keV and hence this cannot be an efficient X-ray production mechanism.

Radiative recombination - An electron of energy E may combine with an ion to form another stable ion of reduced charge, whilst at the same time releasing a photon. If the electron falls into a state n of the ion which

has an ionization potential $I_{z,n}$, then the energy of the photon is $(E + I_{z,n})$. Clearly edges will occur in the continuum spectrum where $h\upsilon = I_{z,n}$.

Dielectronic recombination - In this process the electron is captured, initially without the emission of radiation, but using the excess energy to excite the ion into an upper state. The excitation energy can then be dissipated, either by auto-ionisation, i.e. emission of an Auger electron, or by radiative transitions to the ground state. This process can dominate over radiative recombination at high temperatures.

Nuclear transitions - Nuclear lines are rare for light nuclei, becoming significant only for very high energies. This process can be almost totally neglected in X-ray astronomy.

Knock-on collisions - X-rays may be produced when a fast proton collides with and 'knocks-on' an atomic electron with the release of a photon. This, because of population considerations, is not likely to be an important process.

Line emission, radiative recombination and dielectric recombination are certain to be present in a hot plasma, but at energies where X-rays from cosmic plasmas are seen, i.e. above 1 keV, bremsstrahlung will dominate in the source.

1.3 Absorption of X-rays in Interstellar Space

The processes contributing most to the absorption of X-rays in interstellar space are Compton scattering of free electrons and collisional ionisation, predominantly of neutral hydrogen. Ionised hydrogen has a negligible absorptive effect on X-rays. As the atomic numbers of elements

increase, their cosmic abundance tends to become so reduced as to produce negligible overall absorptive effects. Of course anomalous local enhancements in regions of space might produce conflicting results, but this is always true, as with dust clouds in optical astronomy.

Ionisation absorption becomes significant on a galactic scale for X-rays below $\sim$ 1.5 keV and will have some effect on extragalactic X-rays possibly up to energies of 8 keV, whereafter the effect, even for the maximum plausible mean proton densities ($\sim 10^{-3}$ cm^{-3}) can be neglected. The mean free path for X-rays undergoing Compton scattering in a mean electron density of 2×10^{-4} cm^{-3} is $\sim 10^{10}$ lyears.

1.4 Observational Methods

1.4.1 Rocket borne detectors

Collimated proportional counters have provided most of the present observational knowledge in low energy X-ray astronomy. In spite of their poor energy resolution these counters can determine general spectral shapes even if spectral lines cannot be resolved. The angular resolution of the counters is generally $\sim 1^{\circ}$ but if a source is isolated and sufficiently strong it is possible to locate it to a few arc seconds.

The need for greater resolution has required the development of a focussing imaging system. The grazing incidence telescope makes use of the fact that the refractive index for X-rays is slightly less than unity, so that at sufficiently shallow angles of incidence total external reflection will occur. Although a single paraboloidal mirror has the geometric property of bringing paraxial rays to a point focus, in practical systems at grazing incidence an intolerable amount of comatic aberration is produced. The addition of a second surface, which is an hyperboloid, confocal and coaxial with the first surface, improves the focusing considerably. Use

of such telescopes makes resolution down to several arc seconds possible. The X-ray image thus formed is recorded either directly on film or by converting the X-rays to electrons and subsequently recording the electron image. A good description of these telescopes is given by Giacconi et.al. (1969).

In addition to spatial resolution, high spectral resolution is required. This is best obtained using one of two types of spectrometer. A slitless transmission grating placed in the X-ray path immediately behind a suitable telescope is used to produce an image with various order spectra surrounding it. The grating is normally a layer of very thin plastic, typically 5000 Å thick, with its absorbing lines of gold or platinum. Gratings containing 1440 lines per mm can produce efficiencies up to 9%. (Efficiency here means the fraction of incident power directed into one of the first order spectra.) The second method is to use a suitable crystal in the Bragg condition for X-ray spectroscopy. This is intrinsically capable of achieving higher spectral resolution, but for extended objects a confusion may arise between spatial and spectral distributions unless some collimation is used. The two methods are normally used to complement each other, the latter being particularly suitable when searching for line profiles.

1.4.2 Balloon borne detectors

X-ray detection at balloon altitudes becomes useful at energies upwards of 20 keV, where decreasing flux reduces short duration rocket flight results to a low statistical value. Scintillation in inorganic crystals is the primary method of detection although proportional counters are also used. Collimation is of primary importance for balloon borne detectors but the lower limit to the X-ray background is finally placed by the omnipresent, omnidirectional atmosphere produced component.

1.5 Observational Results

In the section on production mechanisms ideal sources were considered but the actual production of X-rays by a real cosmic body is likely to be complicated by combinations of production processes and by conditions that vary within the source. When sources have been identified at other than X-ray wavelengths it is possible to fit generalised models to the results. It is instructive to look at some well-established objects.

1.5.1 Sco X-1 - A Thermal Source

This was the first X-ray source to be discovered, and is still the brightest. It is the prototype of the thermal objects. The X-ray spectrum is best fitted by an exponential curve for optically thin, thermal bremsstrahlung with a temperature $\sim 10^7\ ^{o}K$, although a non-thermal tail at energies > 40 keV has been reported by Peterson and Jacobson (1966). Optical observations, which also indicate a thermal object, show Sco X-1 to exhibit an essentially unpolarised blue continuum, variable in time and accompanied by emission lines of low and high excitation. These factors suggest a wide range of temperature within the source.

Although the source is optically thin for X-rays it is thick at visual wavelengths and even to some extent at ultra-violet. The thermal nature of Sco X-1 would finally be confirmed if X-ray emission lines could be seen from it. Holt et.al. (1969) reported a "bump" in the spectrum around 6.5 keV, which could correspond to an emission line from iron, but further experiments with high resolution, large area Bragg crystal spectrometers have failed to see the line. Pounds (1971) suggested that this might have been due to a broadening of the line in collisions in the surrounding gas cloud, which still allowed the line to be seen with a coarse resolution proportional counter, but not with a high resolution spectrometer.

No model for Sco X-1 has yet been universally accepted, but it seems likely that it consists of a dense central object, perhaps a neutron star, which is the source of energy and confines, by gravitation, a compact cloud of hot plasma. The energy might come from the infall of an extended surrounding component into the gravitational potential well of the dense central object. This and other theories were comprehensively discussed by Felton (1969).

1.5.2 Tau X-1 (The Crab Nebula) - A non-thermal source

In contrast to Sco X-1, Tau X-1 is an extensive emitting region. Bowyer et.al. (1964) during a rocket flight, observed a lunar occultation of the Crab Nebula, which showed that the angular diameter was $\sim$ 1 minute of arc. It is generally considered to be at a distance of 1.3 kilo-parsecs which makes the dimension of the emitting region to be about 2 light years. The differential energy spectrum in the range 0.1 keV to 1 MeV shows a power law of the form

$$I(E) = 9\,E^{-1.1} \quad \text{keV cm}^{-2}\text{sec}^{-1}\text{keV}^{-1} \quad \text{(see fig. (1.1))}$$

This is consistent with the optical continuum and suggests synchrotron radiation from an electron distribution with a power law index of about -3. The magnetic field in the Nebula is estimated to be approximately 100 μ G. This presents serious problems concerning the lifetime of electrons with energies sufficient to produce X-rays, since electrons producing 100 keV photons would decay in a few days or weeks. Clearly, there must be a source of electrons within the Crab if the X-rays are indeed produced by synchrotron radiation.

Unlike Sco X-1, the radiation flux from Tau X-1 remains remarkably constant on all time scales. Also, in contrast to Sco X-1, there has been no evidence at all for line emission of X-radiation, which also indicates

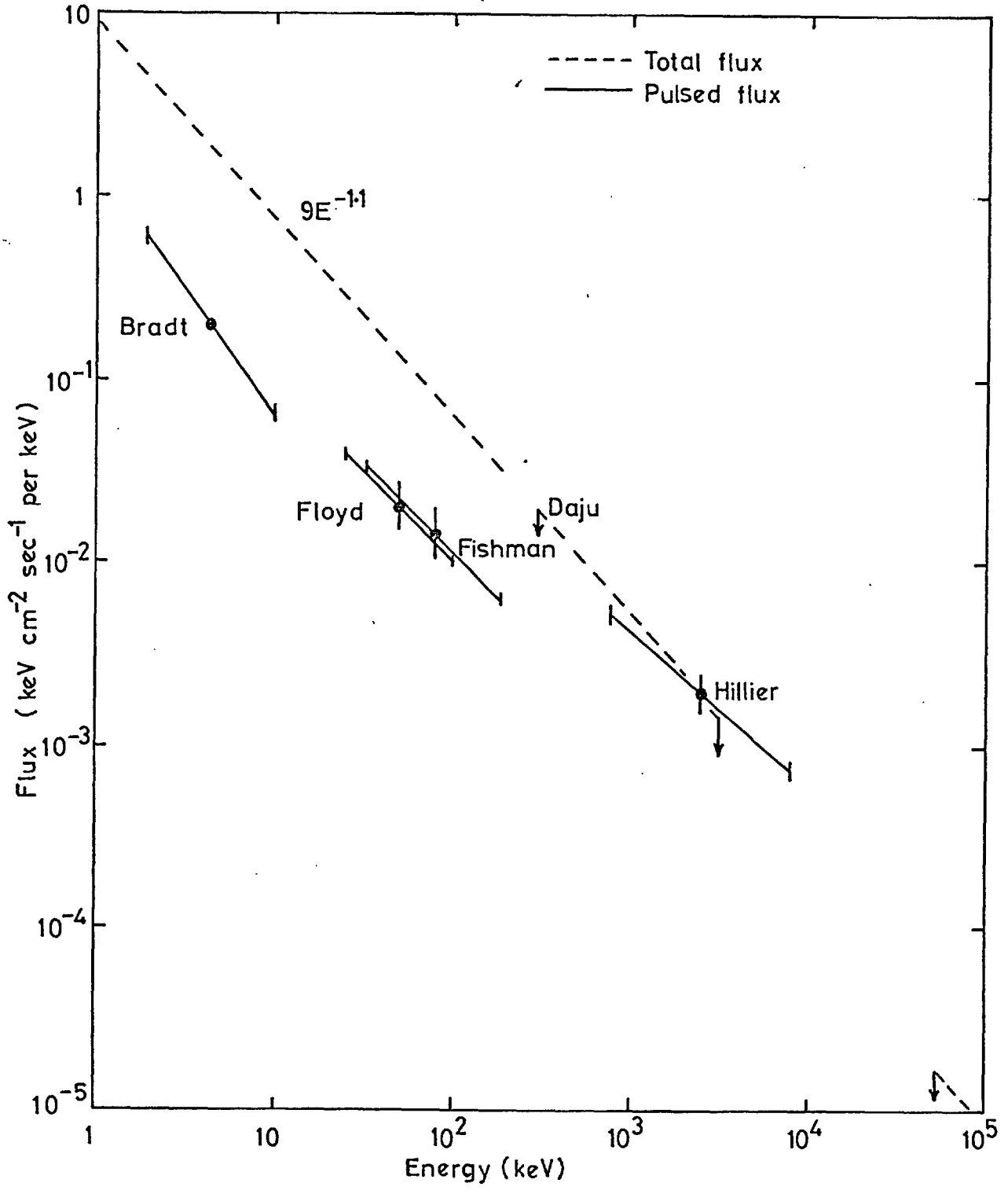

Fig. (1.1) The measured differential X-ray spectra of the pulsed radiation and total radiation from the Crab Nebula (pulsar NP0532). The figure is taken from Hillier et.al. (1970).

that Tau X-1 is a non-thermal source.

The discovery of the pulsar NP0532, situated within the Crab Nebula has alleviated the problem of electron survival, since the pulsar itself is capable of supplying the electrons demanded by the synchrotron emission from the entire Nebula. NP0532 was first discovered by Staelin and Reifenstein (1968) at radio wavelengths and subsequently at optical (Cocke et.al., 1969) and X-ray wavelengths (Fritz et.al., 1969). Assuming a spinning neutron star hypothesis for the pulsar, then the observed rate of increase of period for the star must release rotational energy of about an order of magnitude greater than the energy release due to X-ray emission from the Nebula. The spectra for the X-ray emission from the whole of the Crab Nebula and from the pulsar itself are shown in figure (1.1). It is clear that as the photon energy increases, the pulsar becomes responsible for a progressively larger fraction of the total Crab energy output, possibly reaching 100 per cent at low γ-ray energies $\sim$600 keV (Hillier et.al., 1970).

1.5.3 Extragalactic Sources

Three extragalactic X-ray sources have been observed. The first to be seen was the elliptical galaxy, M87 (Byram et.al., 1966) which is associated with the Virgo A radio source. Recently weak X-ray fluxes have been seen from the strong radio galaxy Cen A and the quasar 3C273 (Bowyer et.al., 1970).

M87 is more than 1,500 pc in total extent and has a bright jet, 400 pc in length, issuing from the central nucleus and containing two bright "knots", each about 70 pc in diameter. The blue continuum in the knots is strongly polarised and certainly indicates synchrotron production here. It is tempting to try to explain the X-ray emission from the galaxy as an

extrapolation of the optical synchrotron radiation, but, as in the case of Tau X-1, serious lifetime problems become evident. Attempts to surmount this dilemma are reviewed by Felten (1969).

Recent observations (e.g. Byram et.al., 1971) show M87 to be variable to such an extent that a small source size is implied. Burbidge (1970) suggests that the energy density of radio photons and the energy content of relativistic electrons pertinent to such a nucleus might allow the right conditions for inverse Compton scattering to produce the observed X-ray flux. This process is without the lifetime problems incurred in the synchrotron process.

1.5.4. X-ray Background

A diffuse primary background of X-rays has been observed which has shown little significant deviation from directional isotropy. This is true for observations in the energy range 0.25 keV to 100 MeV and clearly suggests an extragalactic origin. A study of the power law spectral indices suggests that the electron population responsible for the synchrotron emission of extragalactic radio sources, might also be responsible for the X-rays.

The majority of models thus far proposed involve the integration of the individual X-ray outputs from extragalactic objects, e.g. normal galaxies (Silk, 1968) or radio galaxies (Bergamini et.al., 1967), but these run into a number of difficulties. Firstly, the observed background is very high and it is difficult to make this level of radiation compatible with the known properties of the proposed objects. A more severe criticism is the failure of these models to account for the high degree of isotropy of the background. A break in the spectrum has been observed between 20 - 200 keV (Bleeker and Dereenberg, 1970) which further complicates interpretations of this kind.

Brecher and Morrison (1969) overcame the first two difficulties by suggesting that normal galaxies leak electrons into intergalactic space 100 times faster than previously supposed. Once outside the galaxy, the electrons diffused to isotropy, producing X-rays by inverse Compton collisions with the $3^{o}K$ universal black-body radiation. This predicted a spectrum that fitted the observations very well, but demanded a large cosmic ray electron and proton source strength in normal galaxies

Felten and Rees (1969) considered the X-rays to have been produced at an earlier epoch in remote radio galaxies by an inverse Compton mechanism. By comparing the relative amounts of radio and X-radiation they estimated this epoch to correspond to a red shift of between 3 and 5. It was further suggested that if the injected electrons in a Compton source were subject to a second loss process, then a break in the produced spectrum must occur naturally at that electron energy where the energies lost in each process become comparable. Horstman and Horstman-Moretti (1971), however, claimed that the observed break in the spectrum was due to the improper correction of results obtained at balloon altitudes to thetop of the atmosphere.

CHAPTER 2 - PULSARS

2.1 Introduction

The first evidence of the existence of pulsars came to light towards the end of 1967. The pulsar CP1919 was accidentally included in the field of view of a large, phased radio array set up at Cambridge to study known, compact radio sources. The pulsar manifested itself as a train of equally spaced pulses, variable in strength. These properties of the pulses, together with the high pulse repetition rate argued against a celestial origin and it was not until a considerable amount of evidence had been accumulated that the discovery was revealed in February 1968 (Hewish et.al., 1968).

The discovery of such an unusual new class of object aroused an enormous amount of interest from both an experimental and theoretical point of view. The following two years revealed 50 similar sources which, from their distribution, were able to be classified as galactic phenomena. Also, by this time, much information had been accumulated regarding the character of the pulses themselves. Although such observations limited the number of theories that remained viable, the number of present alternatives is still formidable. In fact the only conclusions that have so far gained general acceptance are that pulsars are neutron stars whose spins determine the pulsar periods.

Most of the experimental work done on pulsars has been in the field of radio astronomy. Inherent in such observations is the problem of dispersion of the wideband emitted pulse during its travel through the interstellar plasma. The resulting swept-frequency nature of the observed

pulse limits the fine structure that can be resolved with a receiver at any particular bandwidth. Also, since dispersion increases in proportion to distance, it limits the depths in space at which pulsars can be observed with a telescope of a fixed collection area.

Only one pulsar, NP0532 in the Crab Nebula, has been observed to have an optical and X-ray counterpart. It is of obvious importance to know which radiations are present in the output of all pulsars and it was for this purpose that the present experiment was conceived.

To gain a perspective on the implications of the results from such an experiment, it seems pertinent to review the present state of knowledge of pulsar properties and also to review the presently viable hypotheses that have been put forward to explain them.

2.2 Observation of Pulsars

2.2.1 Distribution

The distribution of the known pulsars is shown in figure (2.1) using equal-area galactic co-ordinates. The clustering of pulsars towards the galactic plane almost undoubtedly classifies them as galactic objects. As was mentioned earlier, dispersion limits the depth in the galaxy at which a pulsar remains visible to existing telescopes and thus limits the statistics of the distribution.

The clustering of pulsars is particularly noticeable just below the galactic plane. This can be interpreted as being due to enhanced visibility below the plane compared with that above or, as a result of the position of the Sun relative to the plane. Estimates of pulsar distance normally place them at between .1 - 2 kpc.

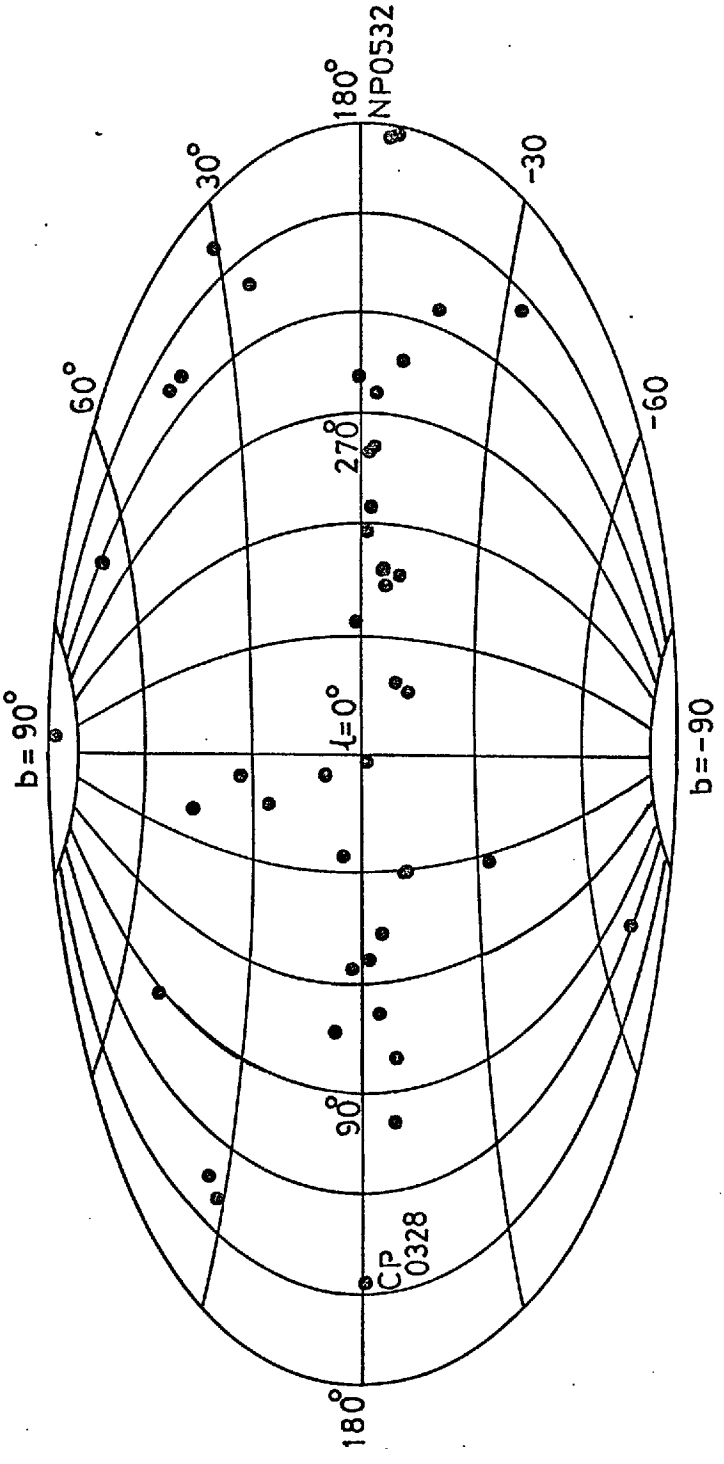

Figure 2(1) The distribution of 43 pulsars in equal-area galactic co-ordinates. This is an updated version of figure 1 in Taylor (1969).

Mills (1969), using suitable approximations about the dispersing medium, has positioned 40 pulsars relative to the galactic centre. His radial plot fails to show spherical symmetry and he suggests that pulsars, like supernova remnants, tend to follow the HI spiral arm pattern along the local and Sagitarius arms.

2.2.2 Pulsar Periods

Every pulsar is characterised by a period, P, that it maintains with great accuracy. Superimposed on this periodicity, however, is a deceleration dP/dt which, again, is very consistent and is of the order 10^{-13} to 10^{-15} secs per sec. A second derivative of the period $\frac{d^2P}{dt^2}$ can even be found for some pulsars and these three parameters completely specify the period, at any time, to the degree of accuracy that is presently obtainable. This accuracy is limited by uncertainties in Doppler corrections to the period and to irregularities in the pulse shape.

A useful quantity is the characteristic time, defined by

$$T = \left(\frac{1}{P}\frac{dP}{dt}\right)^{-1}$$

T shows a proportionate relationship to P for fast pulsars but this breaks down for $T \gtrsim 10^6$ years (Hewish, 1970, figure 5).

The distribution of pulsar periods shows a very marked concentration in the range 0.25 - 2.0 secs with a peak around 0.8 secs. Only four periods are shorter than 0.25 secs and only one greater than 2.0 secs. The paucity of fast pulsars seems to be the result of their deceleration but the reason for the lack of slow pulsars is not so obvious. Pulsars with periods $\gtrsim$ 2 secs appear to have their radiation "switched off" and an explanation of this effect must be included in any satisfactory model of radiation production in pulsars. This will be discussed later.

The two fastest pulsars, PSR0833 and NP0532 have each shown a discontinuous decrease in period accompanied by an increase in $^{dP}/_{dt}$. PSR0833 (Radhakrishnan and Manchester, 1969) decreased its period by 200 ns and increased $^{dP}/_{dt}$ such that it would return to its predicted state in a few years. On the 26th September, 1969, the period of NP0532 showed a similar jump of 2.6×10^{-7} Hz and subsequently assumed a new value 4.3×10^{-8} Hz higher in frequency than the original value after a relaxation time of 4.3 days (Richards et.al., 1969).

2.2.3 Pulse Shape and Variability

Individual Pulses - Emission from pulsars typically shows variations on all time scales from seconds (pulse to pulse) to months. Whilst some of these variations can be attributed to changes in the interstellar medium, most of them, particularly those on the shortest and longest time scales, must originate in the sources themselves. Any individual pulse occurs within a time interval of between one and four per cent of the total period: the pulse window. The width of the pulse window increases in direct proportion to the rotation period of the pulsar so precisely and over such a wide range of periods that a basic connection between the two is indisputable (Hewish, 1970; figure 7).

Individual pulses can show a gross multiple structure which has usually been thought of as multiple-pulsation and it is also common to see a wealth of fine structure that can be resolved down to 0.1 ms. Recogniseable features can appear repeatedly in successive pulses. These often drift through the pulse window at a rate peculiar to an individual pulsar (Drake and Craft, 1968).

It is not unusual for the power in pulses to vary by a factor of 10 but when the power falls from the average by a factor greater than this, Backer (1970) designates the event a pulsar nulling phenomenon. He divides such phenomena into two categories which recur with spacings of about 10 and 50 pulses and such that the nulls persist for 1-2 and 3-10 pulses respectively. Conversely it is not uncommon to see "giant" pulses. This phenomenon applies particularly to NP0532 (Staelin and Reifenstein, 1968).

Mean Pulse Structure - Compared to individual pulses, the mean pulse envelope is a much more stable quantity; repeating faithfully over long periods of time. Correlations between the envelopes of different pulsars are, however, difficult to find. Each pulsar is seemingly as well individualized by its pulse profile as by its period. Most profiles are highly asymmetric and for the longer period pulsars a double pulse structure is a common feature.

Some pulsars exhibit two pulse envelopes, e.g. CP0950, which was the first to be observed (Ricket and Lyne, 1968). NP0532 also shows an interpulse, the role of which increases in significance as the frequency of radiation increases. At radio energies the main pulse is highly structured with a broad precursor followed by a sharp feature, while the interpulse is sharp and contains little power. At optical wavelengths most of the fine structure disappears and the interpulse has grown in significance compared to the main pulse. At low X-ray energies the power contents of the two peaks become comparable (Rappaport et.al., 1971) and at γ-ray energies the interpulse becomes the major feature (Hillier et.al., 1970). Rappaport et.al. (1971) also show that the X-ray and optical pulses are coincident within 0.3 ms. As the radio frequency is reduced from 430 MHz the pulse envelopes tend to broaden until they

coalesce at $\sim$ 110 MHz. This tendency for pulse envelopes to broaden with decreasing frequency is common to a number of pulsars but the correlation is always a weak one and it is by no means certain that it is not entirely due to interstellar dispersion.

It is noteworthy that the pulse-interpulse positions are not usually symmetrically placed with respect to each other within the period. They show a variation in spacing that varies approximately as $\lambda^{\frac{1}{4}}$ (Zeissig and Richards, 1969).

2.2.4 Polarisation

Although some degree of polarisation is a feature common to all pulsars, the extent and type of it are highly variable. Individual pulses tend to show considerably more polarisation than does the mean pulse but repeated averages of pulse polarisation profiles do reveal patterns that are stable. These must be intrinsic to the source (Ekers and Moffet, 1969).

The circularly polarised emission tends to vary within each individual pulse and in successive pulses such that the time average of the pulse polarisation becomes very low. On the other hand, the linearly polarised component has a position angle that usually changes slowly across the pulse in a fashion that repeats from pulse to pulse. It is not uncommon for the position angle to show a discontinuous change somewhere within the pulse structure. Manchester (1970) shows that although the intensity of the polarised component normally will peak at the same position as does the overall intensity of the pulse, the percentage polarisation shows the reverse trend.

Radhakrishnan (1969) demonstrates that the variation of position

angle across the pulse cannot be produced by Faraday rotation and hence it must be a source effect. Also, the fact that these variations are observed to be consistent over a wide frequency range (Ekers and Moffet, 1969) indicates that they are produced at the source since circumstellar and interstellar scattering mechanisms are frequency dependent.

Two exceptional pulsars have been studied. Radhakrishnan et.al. (1969) show PSR0833 to have almost 100% linear polarisation and a position angle that swings through 90^{o} steadily across the pulse and which is almost independent of wavelength. The optical emission from NP0532 shows a similar pattern (Wampler et.al., 1969) but with a considerably lesser degree of polarisation. The radio emission is dissimilar, however, having a precursor pulse that is 100% polarised, followed by a much lower degree of polarisation in the main pulse and an even weaker interpulse polarisation.

2.2.5 Spectra

Pulsar spectra are difficult to measure because the variability of the pulses demands simultaneous observations at several wavelengths. Pulsars have been observed as low as 40 MHz but most are limited at about 100 MHz by interstellar dispersion. Cut-offs are rapid above 1000MHz and only the Crab recovers in the optical and X-ray regions. The spectra in the radio and optical regions do not seem to come from the same source mechanism.

2.3. Pulsar Models.

Since pulsars were first discovered, many hypotheses have been presented speculating on their physical nature. Even so, there has been little success in producing a convincing and comprehensive model to cover

this class of object. If the success has been small, it has certainly not been insignificant and in this short review the more enduring ideas are presented, along with outlines of the most recent models proposed for a complete, periodic, radiating system.

2.3.1 The Period

For any galactic object to maintain such a short duration, regular period it must itself be small in extent and highly condensed. Only two candidate objects seemed reasonable; white dwarves, which were already well established observationally and neutron stars, which had only a theoretical status. Gold (1968) observed that the repeated fine structure in some pulses denied the possibility of pulsars being white dwarves oscillating at higher harmonics of some lower fundamental frequency. Instead he proposed a neutron star model, suggesting that the period was governed by rotation rather than by oscillation, with the pulse being produced from a localised emitting region sweeping into and out of the field of view. Fine structure would then result from changes in production conditions across the emitting region. He also concluded that the emission derived its energy from the rotational energy of the star, being a result of relativistic effects in a corotating magnetosphere. The two predicted consequences of this hypothesis were a general slowing down of pulsar periods and the existence of pulsars with shorter periods, $\sim$ tens of milliseconds, both of which were observed subsequently.

It is a consequence of the theory of neutron stars that supernova explosions might mark the sites of their production. The discovery of pulsars in the remnants of the Vela supernova (Large et.al., 1968) and in the Crab Nebula (Staelin and Reifenstein, 1968) lent weight to this association and prompted Gold to investigate the energetics of pulsars

thus produced (Gold, 1969). Taking the Crab pulsar, NP0532, to be a neutron star of one solar mass rotating at 30 revolutions per second and with a radius of 7 km, then the total contained rotational energy was $\sim 10^{49}$ ergs. From its observed spindown rate of one second in 2,400 years a loss of rotational energy of 2×10^{38} ergs.sec^{-1} could be inferred for the pulsar. This was far more than the total observed radiation flux from the pulsar and it seemed reasonable that it lost the bulk of its energy in the form of relativistic particles spreading into the Nebula itself to become the source of the synchrotron radiation that is observed from the Crab and was discussed in Chapter 1. The observed emission from the Crab is in good agreement with this suggestion.

A description of the physical phenomena following a pulsar producing, supernova explosion, is given by Kardeshev (1970). In the contraction of the centre of the supernova to form a neutron star, conservation of angular momentum and magnetic flux result in it possessing $\sim 10^{53}$ ergs of rotational energy and 10^{41} ergs of magnetic energy due to a dipolar field of surface density 10^{12} gauss. The figure for rotational energy is much higher than can be obtained by extrapolating backwards from observations of all dissipation processes following a supernova explosion, and some additional means of energy loss is necessary during the early stages. The most likely process is gravitational radiation but other suggestions include non-conservation of angular momentum (Kardeshev, 1970) and a sharing of energy between a "family" of pulsars and other non-visible remnants, which undergo rapid separation (Goldreich, 1969). Ostriker and Gunn (1969) claim that only gravitational radiation need be invoked at these early stages to explain all the excess rotational energy dissipation

2.3.2. The Possible Magnetic Field Configuration

It was suggested by Ostriker and Gunn (1969) that pulsars were associated with a young, massive population of stars having moderately sized magnetic fields, perhaps $\sim$ 100 gauss. Such stars were assumed to have highly conducting interiors so that, on collapse, the field evolved in such a manner as to conserve flux. In this way, fields of up to 10^{12} gauss could be expected near the surface of the newly formed neutron star.

Goldreich (1969) outlined the expected properties of a spinning neutron star supporting an intense magnetic field with its axis aligned to the axis of rotation. This model was developed by Goldreich and Julian (1969) who asserted that there must be a co-rotating, magnetospheric plasma close to the stellar surface. This could only occupy a cylindrical region, symmetric about the stellar axis and of radius c/Ω where Ω is the pulsar angular velocity. Outside this region, designated the near region, co-rotation would imply velocities faster than light and hence the field lines must there sweep backwards, much in the manner of the Parker spiral model of the Sun's magnetic field. This region was called the wind zone and all field lines were open there. They closed in the outer or boundary zone, which was arbitrarily defined as the outer 90% of the young super-nova shell. In the near and wind zones the magnetic energy density greatly exceeded the particle kinetic energy density, but in the boundary zone there was equipartition. Goldreich and Julian (1969) also suggested that the magnetic field lines were nearly equipotentials and particles of different sign streamed out along them from separate regions of the star. Modifications of this model are used in the most successful explanations of pulsar radiation and it is useful to refer to figure 2(2) for further illustration.

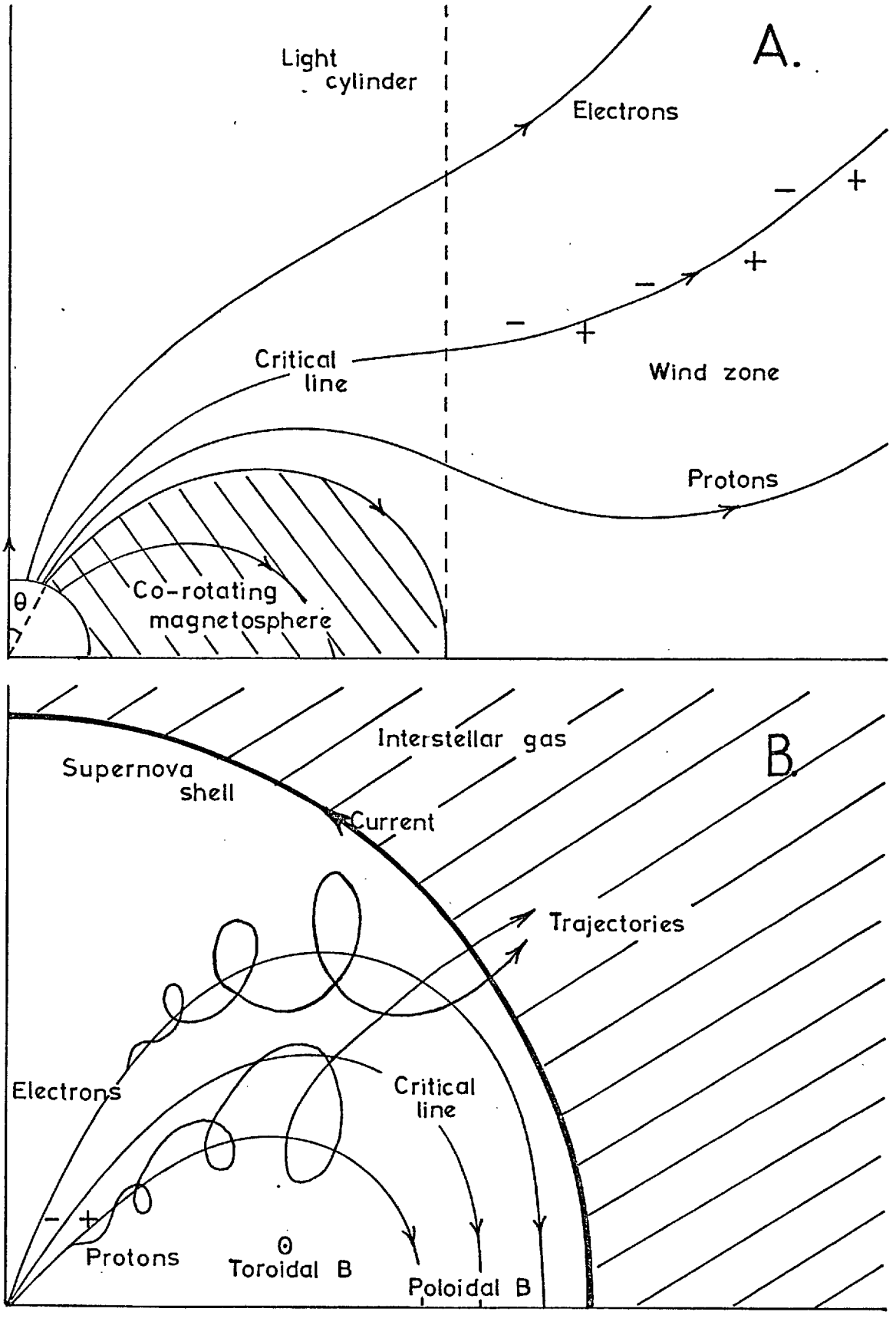

Figure 2(2). Illustrations to the pulsar magnetosphere model of Goldreich and Julian (1969) for inclined rotation and magnetic axes.

A. Figure showing 'near' and 'wind' zones and illustrating particle separation.

B. The same model on a much larger scale showing typical particle trajectories through the boundary zone and supernova shell.

Ostriker and Gunn (1969) based their paper on this model but asserted that pulsars could not be axisymmetric since their appearance from any aspect would be independent of time. Their proposed oblique rotator, similar to that suggested by Paccini (1968), would then result in large quantitites of magnetic dipole and gravitational quadrupole radiation. They simplified their calculations by assuming vacuum conditions. Applying this model to the Crab Nebula they were able to calculate the age of the Crab and predict the second time derivative of the pulsar period.

More recently, Kardeshev (1970) has said that if the force lines in the supernova remnant adhered well to one another, the magnetic field would continue to twist for an unlimited time. The field would decrease with distance less rapidly than a dipole field and thus there must be a current distribution throughout the envelope. He produced a spiral structure for the field pervading the whole Nebula and hence demonstrated that the Crab pulsar could be the ultimate source of both the particles and the magnetic field required for the nebular synchrotron emission.

2.3.3 Radiation Mechanisms and Pulsar Models

The greatest proportion of energy lost by the pulsar is in the form of radiation produced at the frequency of the rotating star, due simply to the corotation of a magnetosphere. Radio wave production plays only a minor role in energy loss and in overall loss terms is parasitic.

The brightness temperature of a star, T_p, is calculated from the measured emission together with the stellar dimensions. Because of the small dimensions of a neutron star this leads to very high values for T_p of between 10^{20} - 10^{25} ^{o}K. Such temperatures demand that a coherent mechanism is producing the radiation, i.e. large numbers of particles are emitting in phase. This

will also produce a large amount of polarisation. For NP0532 the demand is relaxed in the optical and X-ray regions and the radiation may be produced by some familiar mechanism (e.g. synchrotron radiation) that produces incoherent but polarised light.

The majority of acceptable models for pulsar radiation invoke a corotating magnetosphere. A fundamental question is whether the radiation is produced at the velocity of light radius or close to the stellar surface.

Radhakrishnan et.al. (1969) were among the first to propose a useful model of coherent radiation after observing a large rotation of the polarisation angle across the pulse of PSR0833. They suggested a non-axisymmetric pulsar from which relativistic charged particles were carried away along its dipolar field lines. Because of the curvature of the field the particles would radiate in a narrow conical beam about the instantaneous field direction. Any change of polarisation across the pulse would correspond to the rotation of the field lines within the duration of the pulse. Such a large change as was observed for PSR0833 implied that the radiation must have emanated from a region close to the pole of a pulsar whose magnetic axis was inclined at a large angle to the rotational axis. In a later paper, Radhakrishnan and Cook (1969) suggested that the line of sight had to pass within 10^{o} of the pulsar pole.

For Radhakrishnan's model, coherence could be maintained over a line-of-sight depth of about one wavelength. Komesaroff (1970) pointed out that sufficient radio intensities would not be obtained from such a population unless it extended some hundreds of metres in a direction perpendicular to the line of sight. He gave an enlarged, quantitative treatment to the model, assuming that particles were accelerated to relativistic velocities within a very short distance of the stellar surface and possessed negligible

velocity of gyration. Then the radiation would be produced in a hollow beam coaxial with the magnetic axis. One or two pulses would be seen, by virtue of the stars rotation, according as to whether the beam just grazed the line-of-sight or intersected it twice. He showed that the polarisation position angle was a function of the angle between the line-of-sight and the magnetic axis, using these results to explain Radhakrishnan's observations. He was also able to explain the weak dependence of the double pulse envelope spacing on wavelength.

Paccini and Rees (1970) show that X-ray and optical emission could not be produced by the same coherent mechanism that produced radio emission on the grounds that particle densities would be prohibitively high. However, since optical and radio pulses were coincident in time it had to be assumed that they came from the same emitting region. Also the polarisation of the optical pulses in NP0532 suggested that they may be due to normal synchrotron radiation. These authors proceeded by saying that if the emission was being produced close to the star then protons and not electrons must be responsible for the emission if the low frequency optical cut-off from NP0532 was to be explained.

An exotic but comprehensive "near" model was proposed by Sturrock (1971). Considering the pulsar's magnetic field to become twisted outside the velocity of light cylinder, he predicted the currents needed to maintain the field, assuming that each polar cap produced two current streams from separate zones: electron zones and proton zones. These streams became space-charge limited and the flow tended to become oscillatory in nature. The particles, accelerated along curved lines of force, produced a copious flux of γ-rays which, provided the star was rotating sufficiently rapidly, would subsequently produce electron-positron pairs. The positrons

flowed back to the star causing the current to become oscillatory and dividing the electron flow into charge sheets. These charge sheets produced the coherent radiation. From the complex flow patterns around the poles many features in the correspondingly complex pulse structure could be explain The model also gave an upper limit for the pulsar period of about one second since beyond this, pair production could not take place. However it was required that optical and X-radiation emanated from the proton regions only and this did not explain the coincidence with radio pulses.

Acting on initial suggestions by Gold (1969) and Paccini (1968), Bertoti et.al. (1969) were able to give a reasonable, qualitative treatment to the idea of pulsed radiation propagating from the far regions of the velocity of light cylinder. They examined a simple radiative mechanism based on the vectorial acceleration of relativistic electrons with $\gamma \ (= {}^{E}/_{mc^2}) >> 1$. They associated the radio emission with the rotation of the neutron star and the optical and X-ray emission (from NP0532) with the gyrofrequency rotation of particles about the field lines.

Developing Bertoti's ideas, Paccini and Rees (1969) also assumed separate mechanisms for radio and optical emissions and calculated that for the pulses and pulse widths to be coincident, $B < 5 \times 10^4$ gauss if the emission was due to electrons. This estimate agreed with that (separately derived) of Shlovskii (1970) and, of course, implied emission from near the velocity of light radius, since the surface field is much higher, $\sim 10^{12}$ gauss. The radio emission was attributed to particles moving along the field lines in coherent 'bunches' whilst the optical and X-ray emission resulted from small angle synchrotron radiation. The pulsed nature would be a consequence of the electrons being limited, in some way, to a sector of the corotating magnetosphere.

The same paper suggested that the precursor and main feature of the pulse from NP0532 were due to electrons and protons streaming out along different field lines (as in Goldreich and Julian, 1969). This same structur would not be expected in the synchrotron regime of optical emission and this was seen to be the case. Extra strong pulses that are often observed were due simply to extra large bunches of particles being emitted. Paccini and Rees also explained the lack of X-rays from slower pulsars as being due to the lengthening of the velocity of light radius with increasing period which causes a decrease in field strength at the cylinder surface. The synchrotron gyration would then be expected to produce radio emission but not optical or X-rays.

Endean and Allen (1970) analysed the field configuration produced by a co-rotating magnetic field in a plasma of low number density ($< 10^{-13}$ cm^{-3} for the Crab) and whose axis was perpendicular to the axis of rotation. The most rewarding aspect of the analysis was the prediction of two localised emitting regions - as required by Paccini and Rees, above. The regions were located at twice the velocity of light radius from the star and at opposite sides of it. This particular axis orientation, however, implied that what was observed was, in fact, only half the pulsar period, since both emitting regions must be equally visible from any viewpoint for a body rotating in this way. Such an implication is difficult to reconcile with the absence of odd-even pulse effects and, also, it changes disastrously the hitherto reasonable estimates of the age of the Crab Nebula.

Another mechanism of radiation, proposed by Kardeshev (1970), supposed the radio emission spectrum to consist of the higher harmonics of the rotation frequency. The radiation was created within a channel formed between the limiting force lines which close within the luminous cylinder

and the radiation beamed into a conical tube. At each radio frequency we evidently observed the higher harmonics of the rotation frequency; the envelope of the harmonics coinciding with the shape of the pulse thus formed. The optical and X-ray components were once again assumed to be the products of synchrotron radiation.

The problem of the lack of low frequency pulsars seems to resolve itself automatically through the slowing down process. Assuming all pulsars to be created with very short periods, P, relatively rapid rates of slowdown dP/dt, and second time derivatives d^2P/dt^2, then as P increases dP/dt decreases such that pulsar lifetimes, from birth until they are pulsating at about 2 secs, are $\gtrsim$ the decay time of the strong magnetic field. Since the emission depends on a strong magnetic field, the pulsar becomes invisible before it spins down to very slow periods.

An alternative determinant of pulsar lifetimes involves the controversial question of the stability of massive, spherical, magnetic rotators demonstrating axial asymmetry. Whilst Ostriker and Gunn (1969) claim that there is little tendency to axial alignment, Paccini (1968) asserts that an oblique rotator cannot exist indefinitely, since the rotation is not about the principle moment of inertia. If an oblique rotator is required for pulsed radiation then eventual alignment will clearly obliviate the star's performance as a pulsar. The lifetime will then depend on the initial angle of obliqueness and the rate of alignment.

Another interesting problem is the observation of discontinuous decreases in the periods of PSR0833 and NP0532. Michel (1970) attributes the latter decrease to a planet, in a highly eccentric orbit about the pulsar, sweeping in close to it and changing the period. Rees et.al. (1971) make plausible the

survival of the planet during the supernova explosion and suggest that the coincident brightening of the wisp in the Crab Nebula is further evidence of the existence of a planet, as this may be due to evaporation of material from the planet's surface. An alternative cause of the increased frequency is put forward by Ruderman (1969) who proposes that a starquake might have been responsible. In this event the rigid outer layer of the neutron star changes shape discontinuously from oblate towards spheroid as the star slows down and greater stresses appear in the outer crust. This results in a change in moment of inertia and the pulsar period decreases correspondingly. The NP0532 event in September 1969 corresponds to a change in radius of 10^{-6} m.

Although many of the observed properties of pulsars can be represented, in physical terms, it appears very difficult to organise the properties into one comprehensive model. Many models rely on extrapolations to generality made from the particular observations of NP0532. This might be dangerous since NP0532 need not be typical of young pulsars. It might be fruitful to look in optical and X-ray wavelengths for the production of pulsars in the supernova explosions in other galaxies in the hope of extending our knowledge of these younger objects.

CHAPTER III - X-RAY DETECTOR

3.1 Experimental Requirements

The experiment was designed to detect a pulsed X-ray emission in the energy range 30 - 120 keV, from the known radio pulsar CP0328. This had to be done against a background of primary galactic X-rays and secondary X-rays produced in the atmosphere and in the detector itself. The background contribution would be reduced if a collimator was used to define a restricted opening angle.

The pulsar CP0328 had not been identified as an X-ray source and it was to be expected that any pulsed component emitted from it, at these energies, would be very small and almost certainly indistinguishable from the background for a single pulsar period. Detection of the source required the superposition of successive periods and high time resolution was a necessary feature of the experiment. In order that the time analysis of the data be kept as simple as possible, no energy analysis was attempted in the experiment.

Primary X-rays are absorbed rapidly as they descend to greater atmospheric depths, see figure 3(1.a). Secondary X-ray production, however, increases with increasing atmospheric depth until a maximum is reached at about 70 $gm.cm^{-2}$, see figure 3(1.b). This maximum occurs at altitudes well below those normal for balloon experiments and it is desirable to attain as great a floating altitude as possible in order both to increase the primary flux and to decrease that due to secondary X-rays.

When this experiment was conceived, pulsars were a recent discovery with few known properties. With this in mind, the aim was to produce quickly a reliable, inexpensive detector of X-rays in the required energy

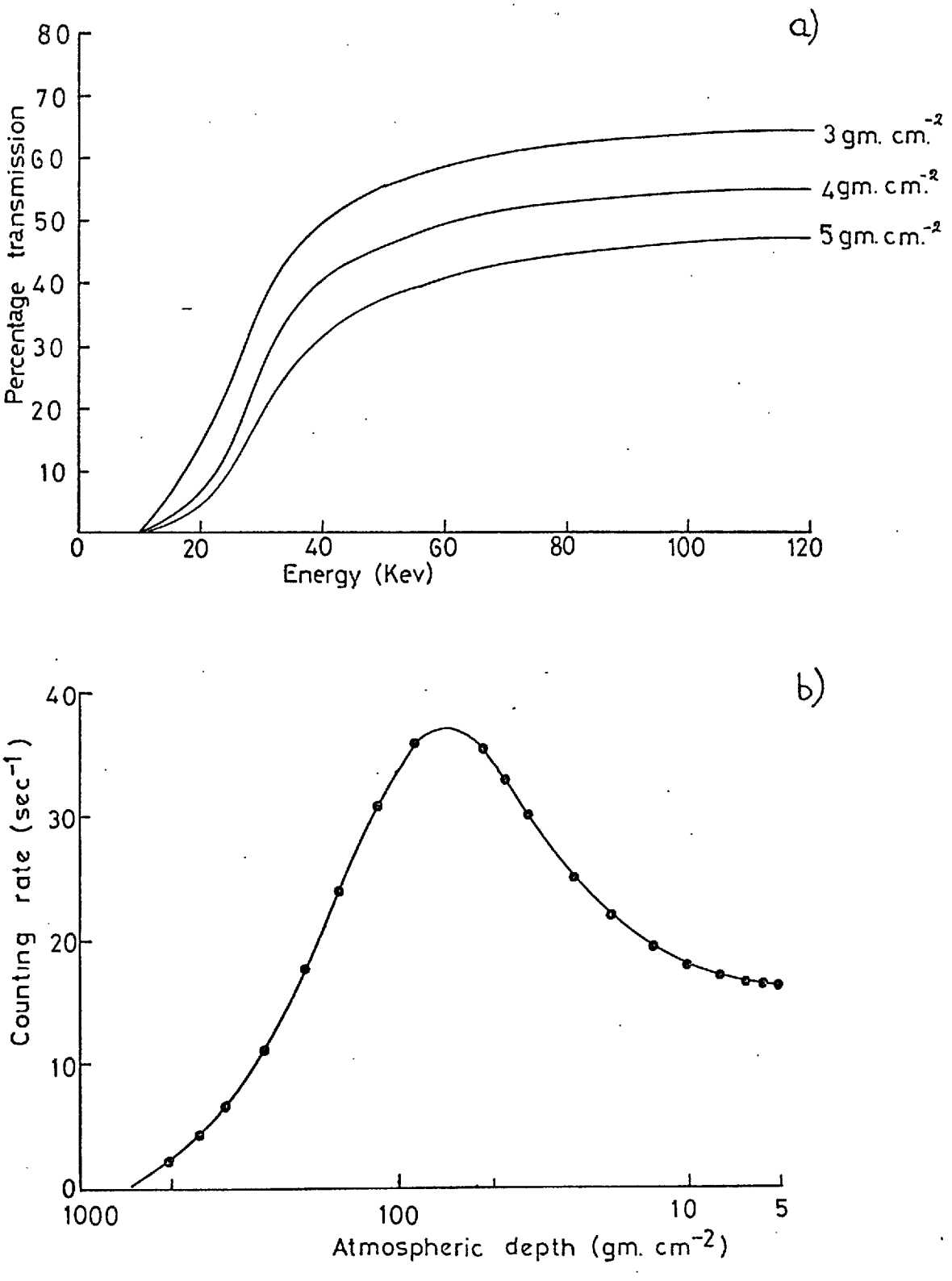

Figure 3(1) a) - The percentage transmission of a beam of X-rays penetrating to 3, 4, 5 gm.cm^{-2} of atmosphere as a function of X-ray energy. b) - A counting rate ascent curve for 25 - 75 keV X-rays given by Vette (1962). The maximum count rate at $\sim$ 70 gm.cm^{-2} is clearly evident.

range, in order to explore one aspect of pulsars and thus throw more light on their nature.

3.2 General Detector Design

The detector used in this flight comprised a single NaI scintillator crystal embedded in Nuclear Enterprises plastic scintillator NE 102A. This combination was coupled to a three inch E.M.I. photomultiplier, type 9531 R and an angle of acceptance was defined for the system by a graded metal, passive, collimator. X-ray events in NaI produce only a small light output and, hence, a correspondingly small electrical charge at the photomultiplier output. For this reason the head amplifiers were mounted directly under the photomultiplier itself.

Charged particles produce scintillations in both NaI and NE 102A but medium energy X-rays scintillate little in plastic scintillator. The encapsulating NE 102A then served the double purpose of providing partial anticoincidence against charged particles and, also, of helping to keep the hygroscopic NaI insulated from moisture. The top of the crystal was insulated with a thin cover of aluminium which allowed transmission of X-rays but not moisture.

A layout of the detector is shown in figure 3(2).

3.3 Detection of Electromagnetic Radiation

3.3.1 Electromagnetic Interactions

There are two main types of interaction with matter for X-rays in the energy range 30 - 120 keV. These are the photoelectric effect, which is the dominant process, and Compton scattering. Photoabsorption results in true exponential attenuation of an incident photon beam since the photon does not survive the interaction. Although the same is not true of Compton

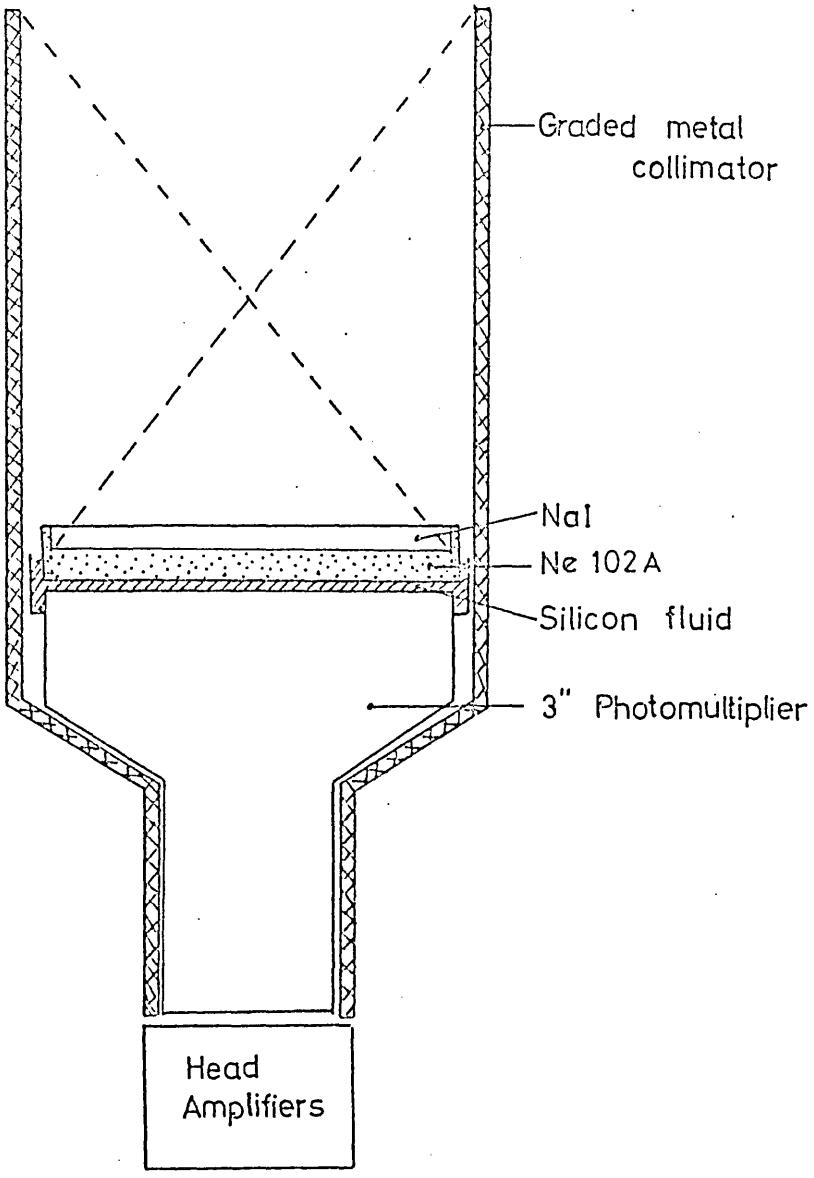

Figure 3(2). A schematic diagram of the detector.

scattering, i.e. the photon survives but with reduced energy, the attenuation can also be regarded as exponential if we consider a well collimated beam of incident X-rays within a small energy range.

The fraction f of incident photons that is removed from a collimated beam after traversing a thickness t of an absorber is

$$f = 1 - \exp(-\mu t) \qquad (3.3.i)$$

where μ, the linear attenuation coefficient, is the sum of the individual coefficients corresponding to photoabsorption and Compton scattering. Consider each of these processes now in detail.

a) Photoelectric Effect

In the event of the photoelectric effect, the photon interacts with the atom as a whole. The result is the ejection of an atomic electron that carries away most of the energy of the photon, whilst momentum is conserved by recoil of the atom. The ejected electron usually originates from the inner K or L shells of the atom and the resulting gap is subsequently filled by electrons from the outer shells dropping into lower energy states; the energy change being dissipated in a line spectrum. If the absorber is of large dimensions the energy of the resulting electron will be totally dissipated in it by ionisation and radiation losses. The line spectrum photons will also be absorbed by subsequent, similar photoelectric interactions. Thus the total energy of the incident photon will be dissipated within the absorbing material.

The attenuation coefficient $\mu_{P.E.}$ for the photoelectric effect is a complex function of incident photon energy, E, and atomic number, Z, of the absorber. The coefficient can be represented very approximately by the formula

$$\mu_{P.E.}(E) \propto \frac{Z^4}{(h\upsilon)^3} \qquad (3.3.ii)$$

(Evans, 1955, p.698)

b) Compton Scattering

The Compton effect involves the elastic collision between a high energy photon and a free electron. Even though an electron is bound to an atom it may be considered free provided its binding energy is much less than the energy of the incident photon. After the collision, both the electron and photon rebound, conserving energy and momentum within the two-body system. The photon energy before the collision, $h\upsilon$, will be reduced to a value $h\upsilon'$ after it, where the two are related by

$$h\upsilon' = h\upsilon \left(1 + \frac{h\upsilon}{m_e c^2} (1 - \cos\theta)\right)^{-1} \qquad (3.3.iii)$$

where $m_e c^2$ is the rest mass energy of the ~~photon~~ electron and θ the angle between its initial and final directions.

The greatest possible energy change in a single collision occurs when $\theta = 180^o$. This energy change is a fraction $(2\alpha/(1 + 2\alpha))$ of the initial photon energy; where $\alpha = h\upsilon/m_e c^2$. This fraction is known as the Compton edge. It is thus impossible to cause complete absorption of the photon energy in a single collision, and a Compton attenuation coefficient cannot be spoken of in the same way that the photoabsorption coefficient can be. Instead, two coefficients are needed; an attenuation coefficient that characterises the removal of photons of a particular energy from the beam, and an absorption coefficient that characterises the removal of energy from the beam. Clearly, the attenuation coefficient must always exceed the absorption coefficient.

It is the absorption coefficient that dictates the amount of energy deposited in a scintillation crystal by a photon and, hence, governs the light production. On the other hand it is the attenuation coefficient that predicts the number of photons of a particular energy, incident at

the top of the atmosphere, that penetrate to the atmospheric depth being considered. Consideration must also be given to photons which initially have energies greater than any defined energy range, but which are scattered into it by Compton collisions in the atmosphere or detector material.

The mass attenuation coefficient for Compton scattering μ_c is given by

$$\mu_c = K \frac{Z}{A} \qquad (3.3.iv)$$

(Birks, 1964, p.27)

where K is approximately a constant for photons of a particular energy. From this it can be seen that μ_c is almost independent of the material since $Z/A \sim \frac{1}{2}$ for all substances apart from hydrogen.

Of the other possible interactions of photons with matter, e.g. Rayleigh scattering, pair production, none are important in the energy range of this experiment when considering activation of scintillators.

3.3.2 The Crystal Scintillator

Alkali halides are of high density (NaI = 3.76 $gm.cm^{-3}$) and contain elements of high atomic number (Na = 11, I = 53). These have correspondingly high photoabsorption coefficients and are therefore particularly good for X-ray detection. The halide is made a more efficient scintillator by activating it with an impurity, e.g. thallium, which acts as a luminescence centre. The scintillation emission is then mainly characteristic of this luminescence centre and the host crystal is required to be transparent to the impurity emission; as is the case with sodium iodide. Thallium activated sodium iodide is the most efficient crystal scintillator at room temperatures and was chosen for use in this experiment. The crystal used was 2 mm thick and approximately 75 mm in diameter. This thickness absorbs

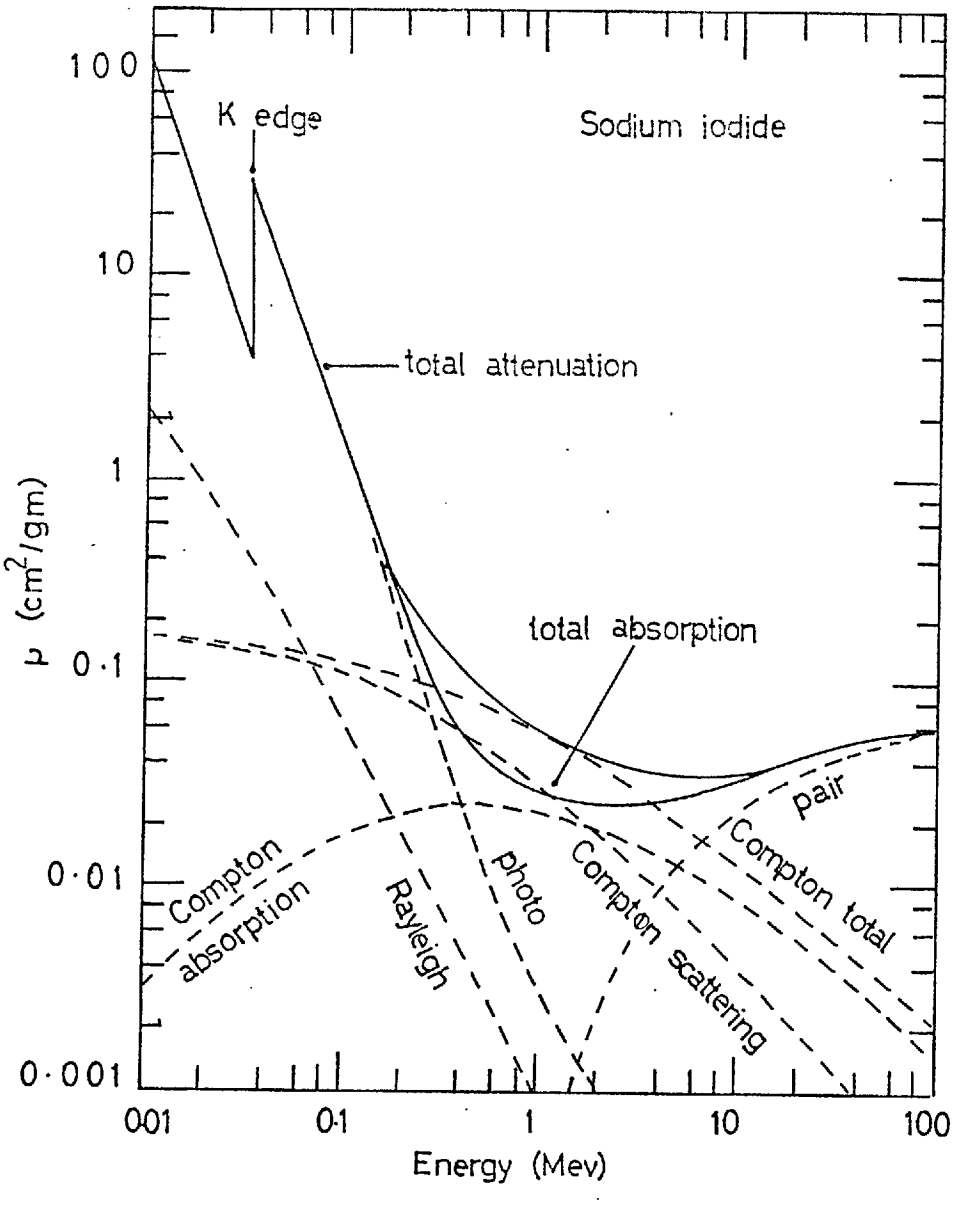

Figure 3(3). The X-ray attenuation and absorption coefficients for various electromagnetic interactions in NaI. After Evans (1955).

50% of a 120 keV X-ray beam and gives a light output of $\gtrsim$ 9 photons of visible light per keV of incident energy (see Appendix A). The absorption coefficients for the interaction processes discussed, are shown in fig. 3(3).

Scintillation in sodium iodide has a characteristic decay time of approximately 250 nanoseconds and the light output peaks at a wavelength of 4150 Angstroms. The light output per keV is fairly constant in our energy range (Birks, 1964, p.432), this fact being important when calibrating

the apparatus. The temperature coefficient is negligibly small in the range $+30^{\circ}$ C to -20° C (Cameron, 1962).

It has been pointed out (e.g. Stein and Lewin, 1960) that a correction may be necessary for the detection, in sodium iodide, of X-rays of energy greater than 32.2 keV, the K-electron binding energy. For the complete absorption of the energy of an X-ray undergoing the photoelectric effect, both the resulting electron and the X-ray products must be subsequently absorbed. However, a number of iodine K X-rays escape the crystal and these are the cause of a secondary peak - the iodine escape peak.

The probability p(E) that an incident photon will undergo photoelectric absorption with the subsequent escape of the iodine K X-ray has been calculated by Mott and Sutton (1958). For thick crystals it can be written

$$p(E) = \tfrac{1}{2} w_K \delta_K \frac{\tau}{\mu} \left[1 - \frac{\mu_K}{\mu} \ln \left(1 + \frac{\mu}{\mu_K} \right) \right] \qquad (3.3.v)$$

where μ = the linear absorption coefficient for the incident photon

μ_K = the linear absorption coefficient of iodine K X-rays

τ = the photoelectric absorption coefficient

δ_K = the fraction of photoelectric events occurring in K shell

w_K = the K-fluorescence yield of iodine.

Thick in the above sense refers to the dimensions of the crystal in relation to the absorption length of iodine escape X-rays.

The escape probability is largest for low energies since photo-absorption occurs closer to the surface. The probability of escape at 30 keV is $\sim$ 30% for photons incident on a crystal several absorption lengths from the sides and drops to 15% at 60 keV. The photoabsorption length at 29 keV is $\sim$ 0.5 mm and hence the crystal used in this experiment satisfied the thick crystal condition at points more than 1 mm from its edges.

3.3.3 Anticoincidence Encapsulation

The sodium iodide crystal was encapsulated in plastic scintillator NE102A. This scintillator has a high photon output for charged particles passing through it. The emission also has a fast rise time compared to that of sodium iodide and this comparison formed the basis of the charged particle anticoincidence in the detector.

When a relativistic charged particle of rest mass M, charge Ze and energy E is travelling in a medium containing N atoms/cm^3, each of atomic number z, it loses an amount of energy dE in travelling a distance d ℓ which is given by (Birks 1964, p.17),

$$\frac{dE}{d\ell} = \frac{4\pi e^2 Z^2}{m_o \beta^2 c^2} \cdot Nz \cdot \left[\ln\left(\frac{2m_o \beta^2 c^2}{I} \right) - \ln(1 - \beta^2) - \beta^2 \right] \quad (3.3.vi)$$

where I is an empirical constant for the medium corresponding to the mean excitation and ionisation potential, and m_o is the electronic rest mass. The particle deposits this energy in the material by excitation and ionisation of its molecules and, for a scintillator, it is partly re-emitted as photons in the visible part of the spectrum. The energy loss for a unit charge, minimum ionising particle in NE102A is $\sim$1.8 MeV $cm^2 gm^{-1}$ (Crispin and Haymen, 1964). The encapsulation was $\sim$0.5 cm thick, thus with one photon released for every 140 eV of energy deposited (Barnaby and Barton, 1961), the total photon yield for the NE102A was $\sim$6500 photons, peaking at 4250 Å. The sides and top of the encapsulation and the NaI crystal were coated, by the manufacturer, with a diffuse reflecting paint.

The coupling of the lower face of the encapsulated crystal to the photomultiplier was accomplished using the silicon fluid MS 200. This fluid is chemically and physically stable over the required temperature and pressure range and combines excellent transmission properties with a high viscosity, 500,000 cs. A bath of this fluid was constructed around the

interface (see fig. 3(2)) to ensure that no air could leak into it during vacuum cycling.

3.4 Collimator Design

Active or Passive Collimator

At balloon altitudes there is an approximately isotropic background of X-rays due to a primary, diffuse galactic component and a secondary, atmosphere produced component. A collimator is required both to limit this background and to define a field of view. Broadly, the two types of collimation that can be used are grouped active and passive. Active collimators detect all radiations, charged particle as well as X and γ -rays, impinging the telescope and then discriminate against them. Passive collimators simply attenuate any radiation passing through the telescope material. The former are the more efficient, being able to eliminate effects of X-radiation produced within the collimator itself but they have the disadvantage that active collimators of solid scintillator are very expensive and very susceptible to thermal andmechanical shock, whilst liquid scintillators, though less expensive, require suitable containing systems which necessarily make the experiment heavy. For these reasons it was decided to use the less effective passive collimator.

Geometry of the Collimator

It can be shown (Heristchi, 1967) that for a cylindrical collimator of end area A and length L, the amount of flux, N, reaching the viewing area, due to an incident isotropic flux I, is given by

$$N = I \cdot \frac{A^2}{L^2} = I \cdot A \cdot \frac{A}{L^2}$$

A^2/L^2 is the geometrical factor and has units of area-steradian. Clearly,

the larger is the geometrical factor, the larger will be the background counting rate.

The photomultiplier used in this experiment had a radius $\sim$ 4.0 cm and, hence, if it were collimated by a cylinder of length L it would have a geometrical factor of $2530/L^2$ cm^2ster. The viewing half-angle, θ , would then be given by $\tan^{-1}$ 8/L. Fig. 3(4) shows these two quantities plotted as a function of L.

The longer we made L, the heavier the collimator would be but making L shorter would increase the geometrical factor. A compromise was found in the values $\theta = 20$, L = 22 cm and hence the geometrical factor was 5.2 cm^2ster.

CP0328 is a point source. The fraction of the detection area visible to a point source at any time depended on the angle ϕ that the source made with the telescope axis at that time. If we designate this area $S(\phi)$, it can be shown that for a cylindrical telescope

$$S(\phi) = 2R^2 (\beta - \tfrac{1}{2} \sin 2\beta)$$

where $\cos\beta = \frac{L \tan\phi}{2R}$ (Courtier, 1964)

$S(\phi)$ is shown plotted for the opening angle of this experiment in fig. 3(5). The full width at half maximum is seen to be 16°.

A further effect which affected the X-ray flux from the pulsar was the extent to which photons of different energies would be absorbed in the residual atmosphere above the detector. By incorporating this into the function $S(\phi)$, the curves $S(\phi, E, 4)$ could be plotted as in fig. 3(5), representing the relative response of the detector at 4 gm atmosphere compared to that outside the atmosphere for different X-ray energies, E.

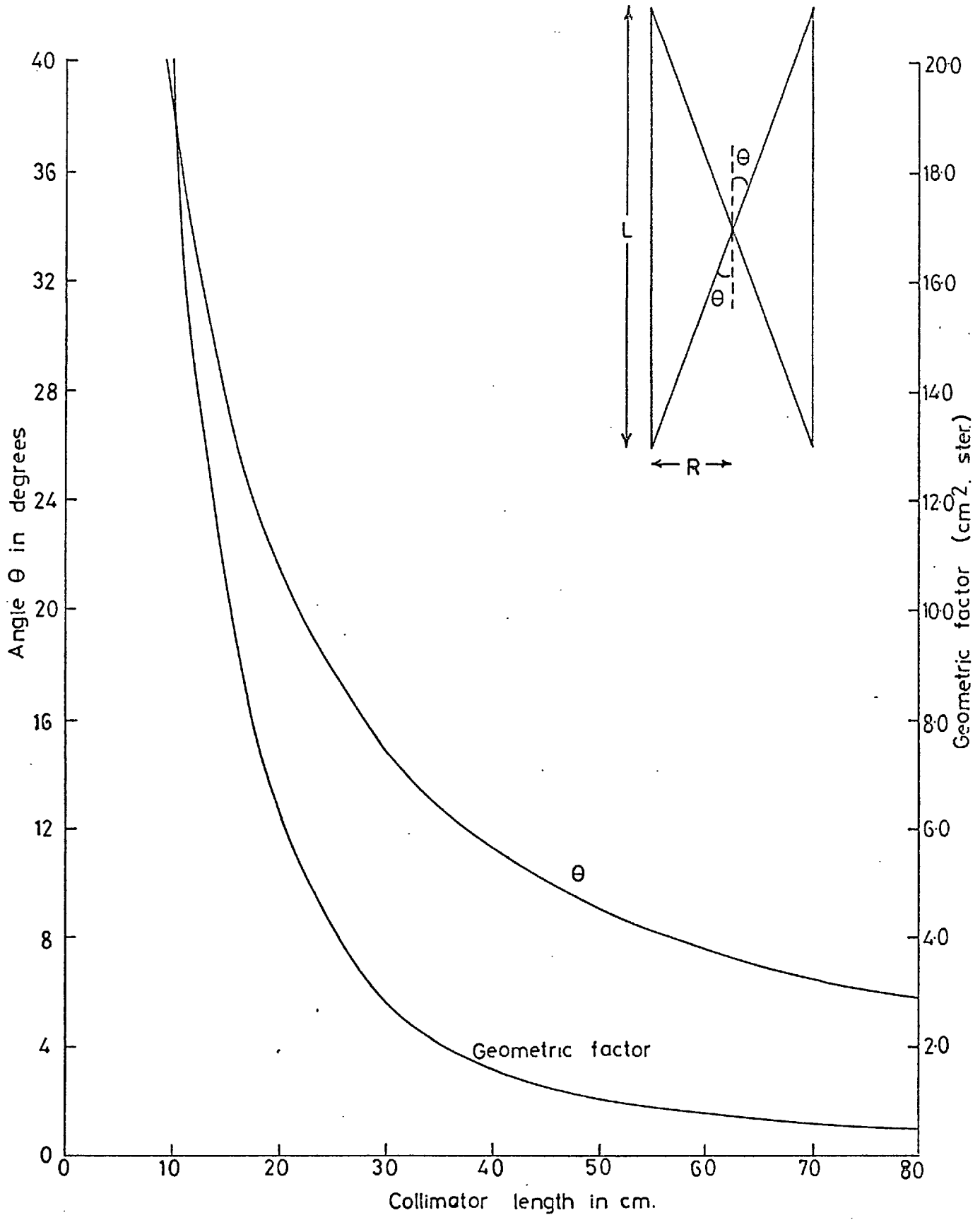

Figure 3(4). The Geometric Factor and collimator half angle as a function of collimator length.

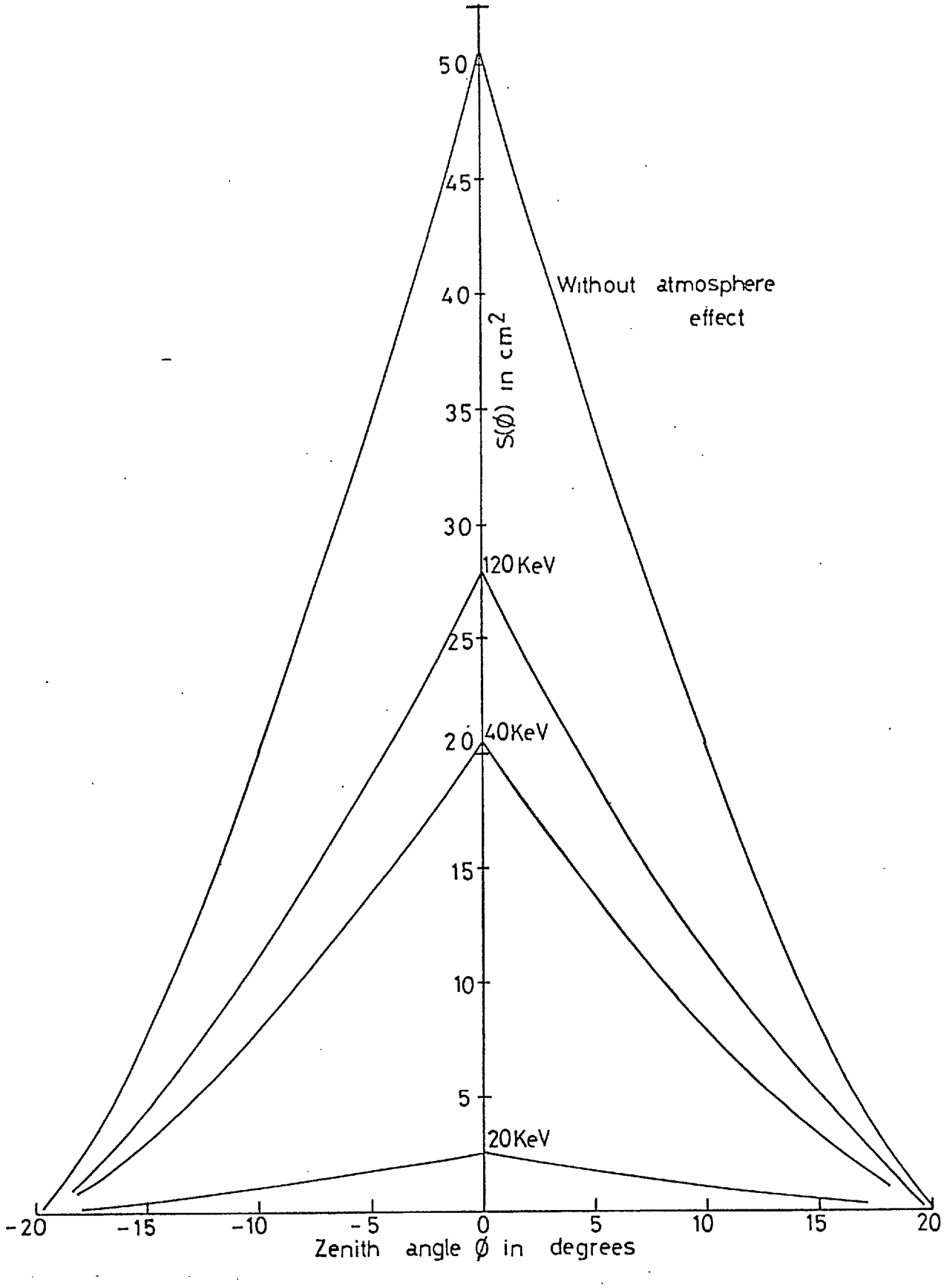

Figure 3(5). Curves of available surface area $S(\phi)$ as a function of the angle between the line of sight of an object and the telescope axis. The effects of atmospheric absorption are included at 20, 40 and 120 keV in the lower curves.

Material of the Collimator

The choice of material for the collimator depended on three factors; its efficiency as an X-ray absorber, the amount of secondary X-rays produced from it and its general utility, i.e. machinability, density and availability.

The most efficient common absorbers are lead, tin, boron and copper (including copper alloys e.g. brass). Boron can be neglected since its utility factor is low. Lead is the most efficient absorber below 33 keV and above 88 keV, but it is a copious producer of secondary products and it has a K-edge for X-rays at 88 keV, where its mass attenuation coefficient falls to 1. Tin is a lesser producer of secondary products and has a K-edge at 33 keV, whilst the copper K-edge is out of the region of interest at 8 keV.

The main contributions to the secondary products come from bremsstrahlung produced by charged particles in the material, Compton scattered γ-rays and fluorescent X-rays from the K-edge. The production of Compton scattered photons is proportional to the number of electrons encountered by the incident γ-ray flux, i.e. proportional to the atomic number, and the differential cross section for the production of bremsstrahlung is proportional to the square of the atomic number. Lead is the worst offender in the production of each of these. Fluorescent X-rays are produced by lead at 88 keV and by tin at 33 keV whilst copper produces very few contaminating X-rays. A suitable telescope design uses a graded collimator of several metals, with materials of highest atomic number on the outside.

An optimum choice of materials was found to be 1 m.m. lead, 2 m.m. tin and 0.5 m.m. copper (in that order from the outside inwards). With these metals at least 99% of all X-rays incident upon the collimator were absorbed.

An estimate of all secondary products from the collimator is made in Appendix B.

3.5 Detector Electronics

Because of difficulties in storing large quantities of information in a balloon payload and retrieving it after the flight, all the data had to be transmitted back to a ground station. Much of the data processing, however, had to be done on board the detector. The electronic components used in these facilities, in the transmitter and in the peripherals had to be stable against temperature and pressure changes. They also had to have a low power consumption to minimise the size of batteries required.

A block diagram of the electronics is shown in fig. 3(6).

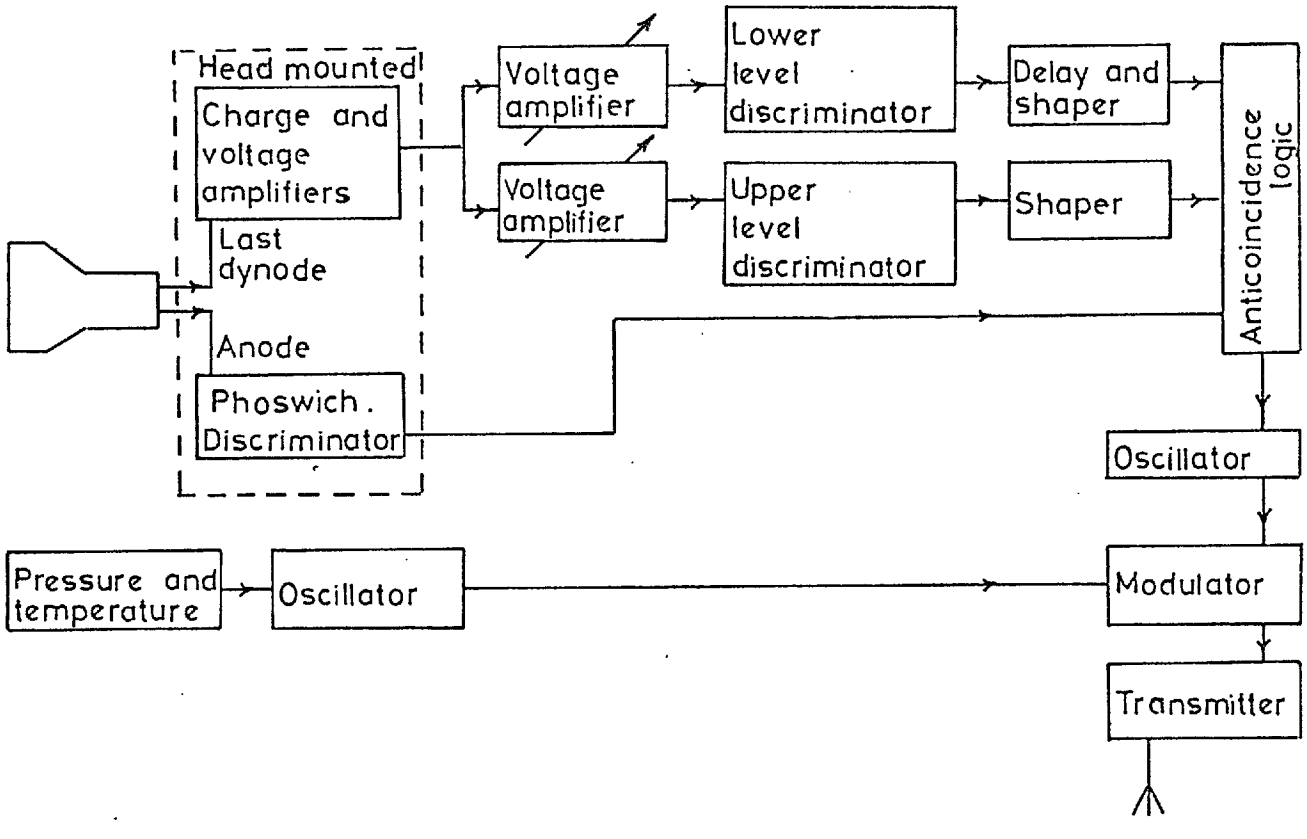

Figure 3(6). A block diagram of the detector electronics.

X-ray Event Analysis

For each scintillator event two signals were taken from the photomultiplier, a positive pulse from the last dynode of the dynode chain and a larger, negative pulse from the anode. The positive pulse was fed into a charge amplifier which produced a voltage pulse proportional to the electric charge in the photomultiplier output. Since this photomultiplier output contained charge proportional to the energy of the incident X-ray (see Appendix A), the pulse from this amplifier had a peak voltage proportional to the photon energy.

The resulting charge amplifier pulse was $\lesssim$ 100 mV and was voltage amplified before being led to the discriminator system. Here, the pulse was fed into two voltage amplifiers with variable gains. The outputs of these were each fed into discriminators, the outputs of which were put in anticoincidence. By varying the individual amplifier gains the desired energy range of detection was achieved.

The negative, anode pulse was connected direct to a phoswich discriminator. This electronic device produces an output pulse only for input pulses with fast rise times.

The rise time of scintillations in plastic scintillator is much faster than in sodium iodide. Since only charged particles scintillate appreciably in NE102A then only these produce an output pulse from the phoswich. Such pulses were used to provide anticoincidence against charged particles depositing small amounts of energy in the sodium iodide crystal.

An output pulse from the logic system was only produced from the incidence of an X-ray in the range 30-120 keV. This 10 ms standard length pulse was used to gate a 14.5 KHz oscillator whose output was fed to the telemetry.

Detector Calibration and Resolution

Only one channel was required for this detector. The 30 and 60 keV X-ray emission lines from an Am^{241} source were used to calibrate a pulse generator against the detector. Since the light output from sodium iodide varies almost linearly with energy in the range 30-120 keV, the pulse generator could be used to interpolate the points and, hence, establish the correct energy range in the detector.

The energy resolution of the system for the two Am^{241} lines was measured by feeding the prediscriminated output into a 128 channel pulse height analyser. The resolution of the peaks thus formed is defined as the ratio of the full width at half maximum of the peaks, to the peak position. These were measured to be 50% and 30% for the 30 and 60 keV lines respectively.

Electronic Peripherals

During the flight it was essential to have a continuous record of the balloon temperature and pressure. This was provided by an Olland cycle, a commercial device which, by using aneroid capsules and a bimetallic strip, is sensitive to the pressure range 0-1000 mb and to temperatures between $-60^{o}C$ and $+50^{o}C$. A fine pressure scale 0-20 mb enabled the balloon's height to be estimated to $\pm$ 0.5 mb. The device produced its information as a morse coded electrical output which was used to gate a subcarrier oscillator. Two Olland cycles were carried on the detector each of which was recalibrated shortly before the flight.

The Olland cycle and data information were mixed and fed into the transmitter. The percentage modulation was 10% each for the Ollands and 80% for the data channel. The transmitter was a 160 mW transistorised F.M.-device operating at 136.5 MHz. The signals were radiated from an aerial combining the properties of a turnstile and inverted ground plane.

The electronics needed to be powered by a supply, stable against temperature, pressure and battery voltage changes. To achieve this a L.T. converter was built to generate +6V and -15V lines, stable to ± 1% against battery changes between 8 and 15 volts. The photomultiplier required a 1300V supply which was provided by a separate E.H.T. converter. All leads and components carrying E.H.T. were potted in silastomer to prevent corona discharge at low pressures.

The power to the converters was supplied by a 12V, 2000 ma/hr rechargeable nickel-cadmium battery. The Olland cycles were powered by their own separate batteries. The power working life expectancy of the whole payload was in excess of 10 hours.

Detector Electronics Stability and Response

The entire electronics system was developed with stability against temperature changes in mind. The overall temperature coefficient in the range +40 to -20°C was determined to be 0.15% per °C. Although this represented a change of ∿ 6% from room temperature to -20°C and expanded the range to 32-138 keV, it could not invalidate any inferences made from the data but would only modify the range, provided the working temperature was known. The phoswich circuit was tested to ensure that, working at its minimum sensitivity, (i.e. at -20°C), it functioned as a discriminator. Since the device relied on pulse shape, which is virtually temperature independent, and not pulse height for its discriminating action it was easily made effective over the entire range of temperature.

The transmitter was not crystal controlled and suffered a temperature dependent frequency drift of 0.02 MHz per °C. The output power increased by some 5% when the temperature was decreased from +20 to -20°C.

The complete, functioning detector package was pressure cycled from

atmospheric pressure down to 3 mb to test for possible corona discharge or faulty electrolytic capacitors.

It was important to protect the detection electronics from electrical pick-up, e.g. from the Olland cycle motors. This was effected by appropriate decoupling of the circuits and by screening them in aluminium boxes. Leads, where necessary, were kept short, as for the charge amplifier and phoswich which were mounted onto the photomultiplier.

The noise level in the photomultiplier tube increased with temperature. The noise pulses were fast rising, however, and extra large pulses, which could be detected in the energy interval, (frequency $\sim$ 10 pulses/min at 30^{o}C) were discriminated against by the phoswich circuit.

The dead time of the detection electronics is negligible compared with that of the transmission system. The transmission dead time per event was 1.2 m.s. and with a count rate of 20/sec the chance coincidence rate is $< 0.1\%$. An upper limit to the transmission time of a pulse through the electronics was less than 1 m.s. The variation in this due to temperature changes was very small.

CHAPTER IV - GROUND EQUIPMENT AND ANALYSIS PROCEDURE

4.1 Aerial and Receiver

During the balloon flight the signals were received by a twin, 7-element Yagi aerial. The aerial could be rotated in azimuth and elevation to maintain optimum tracking. A low noise aerial amplifier was used to feed the signals to an Eddystone V.H.F. receiver. In this way it was possible to achieve a range of 300 miles.

The signals from the receiver output were fed, unfiltered, into a high-speed, field effect transistor (F.E.T.) switch and then into a recording channel of one of two Tandberg stereo tape recorders. The same receiver output was also passed through a 14.5 KHz filter and, after shaping, was used to control a paper tape punch.

4.2 Recording the Data

The essence of the experiment lay in the accuracy with which the arrival time of an event could be recorded relative to an arbitrary but constant starting time. If we were looking for a pulse with half width at half maximum of t secs, then t gave some measure of the drift in time that could be allowed and the pulse not completely lose synchronisation.

The estimated time for which the pulsar CP0328 would be in view was $\sim 1\frac{1}{2}$ hours. Assuming its period to be 0.7 secs and the pulsed component to occupy 5% of this, then dividing the period into 50 bins it can be seen that the maximum allowable time drift was $\sim$10 ms during the 90 minutes. This represents an accuracy of 2 parts in 10^6.

Two methods were used to record the data.

(i) Use was made of the dual input facility of a stereo tape recorder to

record two separate sets of data simultaneously on one tape. On one track the arrival of the individual X-ray events was recorded, along with the temperature and pressure information. On the other, a continuous 10 KHz timing signal was recorded. In this way tape stretch after recording did not alter the relative positions of events and timing pulses.

(ii) A system was developed to record the data direct onto paper computer tape. A binary scalar that could accumulate a number of up to 2^{28} ($\sim 2.5 \times 10^8$) was connected via a shift register to a Facit 4070 paper tape punch. Upon command from an external signal, the number residing in the store at any time could be punched onto 8 hole paper tape, at the same time clearing the store, if desired. The scalar was made to accumulate the 10 KHz timing signal and the punch command was given by the occurrence of an X-ray event, which also caused the store to be cleared and allowed the scalar to begin counting again from zero. A record on computer tape was thus made of the times between the occurrence of X-ray events.

A diagram of how these two systems were operated in parallel is shown in figure 4(1).

4.3 Timing the Experiment

The timer used for both recording methods was an Advance T.C.9 scalar/timer, whose quartz crystal oscillator control provided an accuracy of one part in 10^6. The output was a 3V square wave of width 20 μs and frequency 10 KHz. Whilst such a pulse could easily be shortened and fed directly into the scalar, the insufficient frequency response of the Tandbergs caused it to be badly distorted when it was recorded direct onto magnetic tape. For this reason the timing pulses were filtered to a 10 KHz sine wave and then amplified using an operational amplifier with a twin-T filter network.

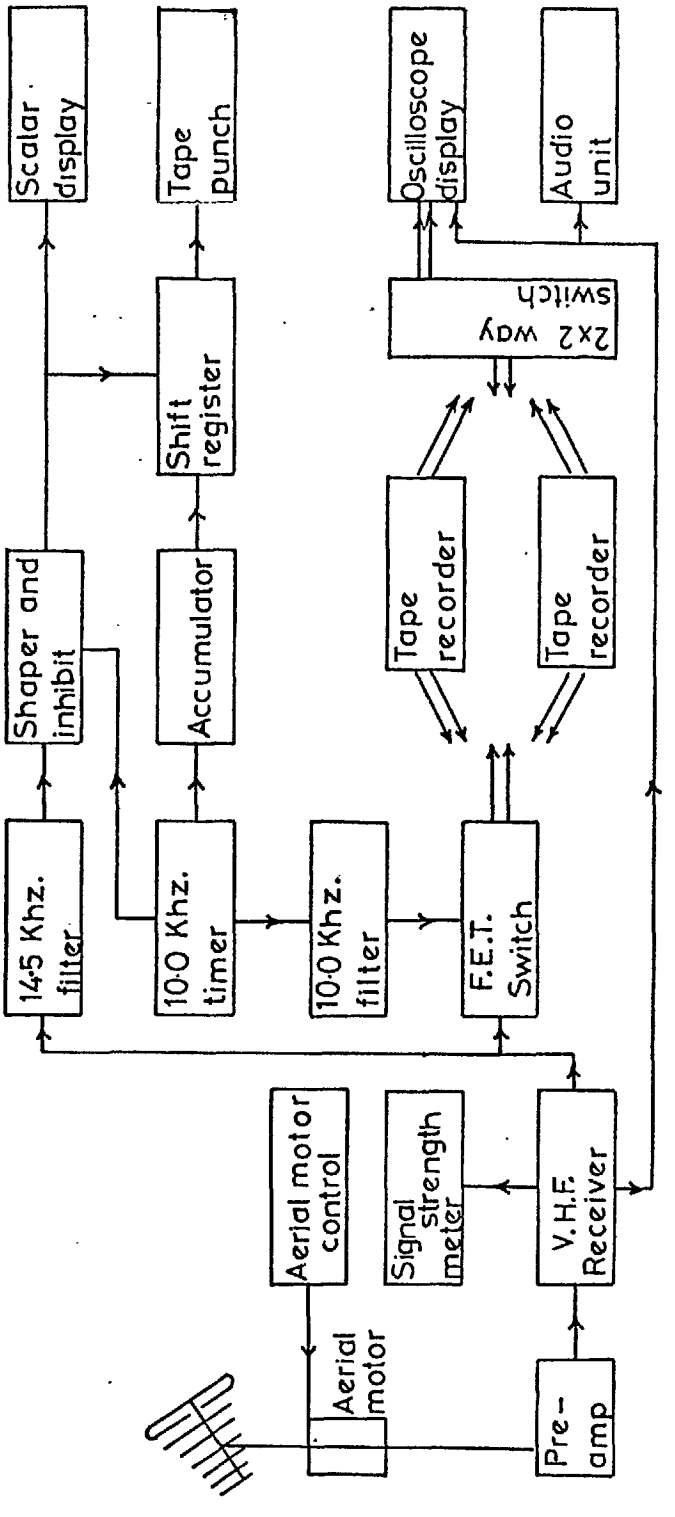

Figure 4(1) Layout of the receiving station showing the two recording systems working in parallel and the facilities for in-flight monitoring, i.e. the signal strength meter, the audio unit, the oscilloscope and scalar displays.

This sine wave was recorded without distortion and it was an easy matter to reconvert it to a square wave during playback.

For reasons which will be discussed later in the chapter the tape recorders had to be run at their maximum speed of $7\frac{1}{2}$ inches per second. This allowed approximately 40 minutes of recording on each tape. Since the pulsar passage took nearly 90 minutes three tapes were needed for recording its entire traversal. Accurate synchronisation had to be maintained throughout the passage and this was achieved by building a tape marker into the F.E.T. switch. When the switch was thrown it initially had no effect but to gate on a 14.5 KHz oscillator. This oscillation was mixed into the incoming data. After 10 m.s. the data and timing signals were switched from one tape recorder to the other, leaving the oscillator running for a further 10 m.s. before switching off. The uncontaminated data continued to be received on the second tape recorder. In this way there was, at the end of one tape and the beginning of the next, a 10 m.s. burst of 14.5 KHz oscillation that was distinguishable from any other data pulse only by its position on the tape. By suitably associating these two pulses, synchronisation could be maintained to 100 μs in one tape change. A diagram of the switch is shown in figure 4(2).

No similarly convenient method could be arranged to obtain continuity of the paper tapes. Their longer running time, however, made this a less crucial matter.

4.4 Data Reduction from magnetic Tapes

A diagram of the reduction system is shown in figure 4(3). The estimated X-ray count rate (Appendix B) at altitude was < 20/sec. The punch used had a maximum work rate of 70 character lines per second. It was required to transfer from magnetic to punched paper tape the time of occurrence of each X-ray event, from an arbitrary starting point. Using a 100 μs time unit, four eight-hole lines were required to represent the

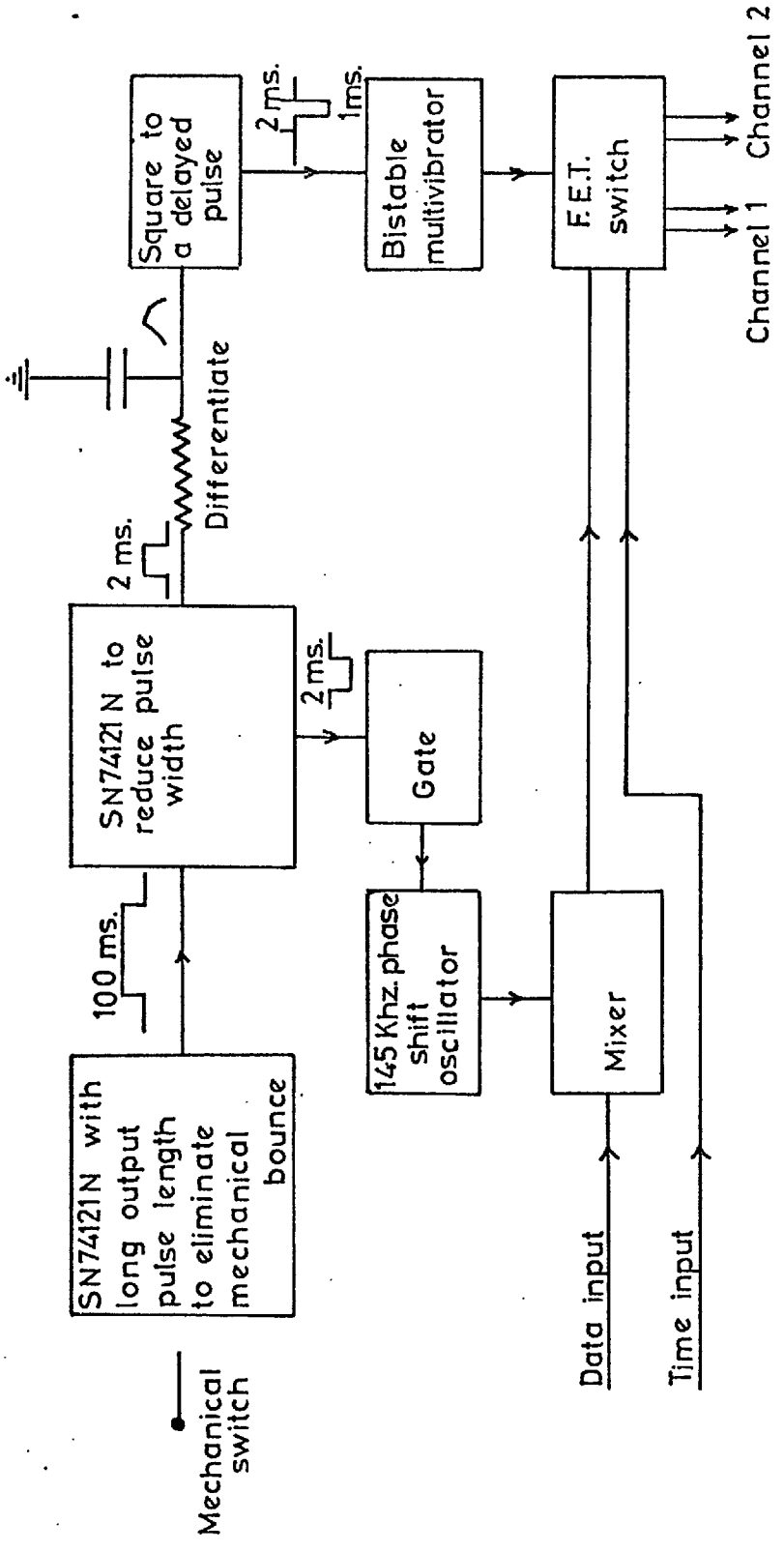

Figure 4(2) Block diagram of the high speed switch. The SN74121N is a monolithic T.T.L. monostable with d.c. triggering from positive or gated negative going inputs and with inhibit facility.

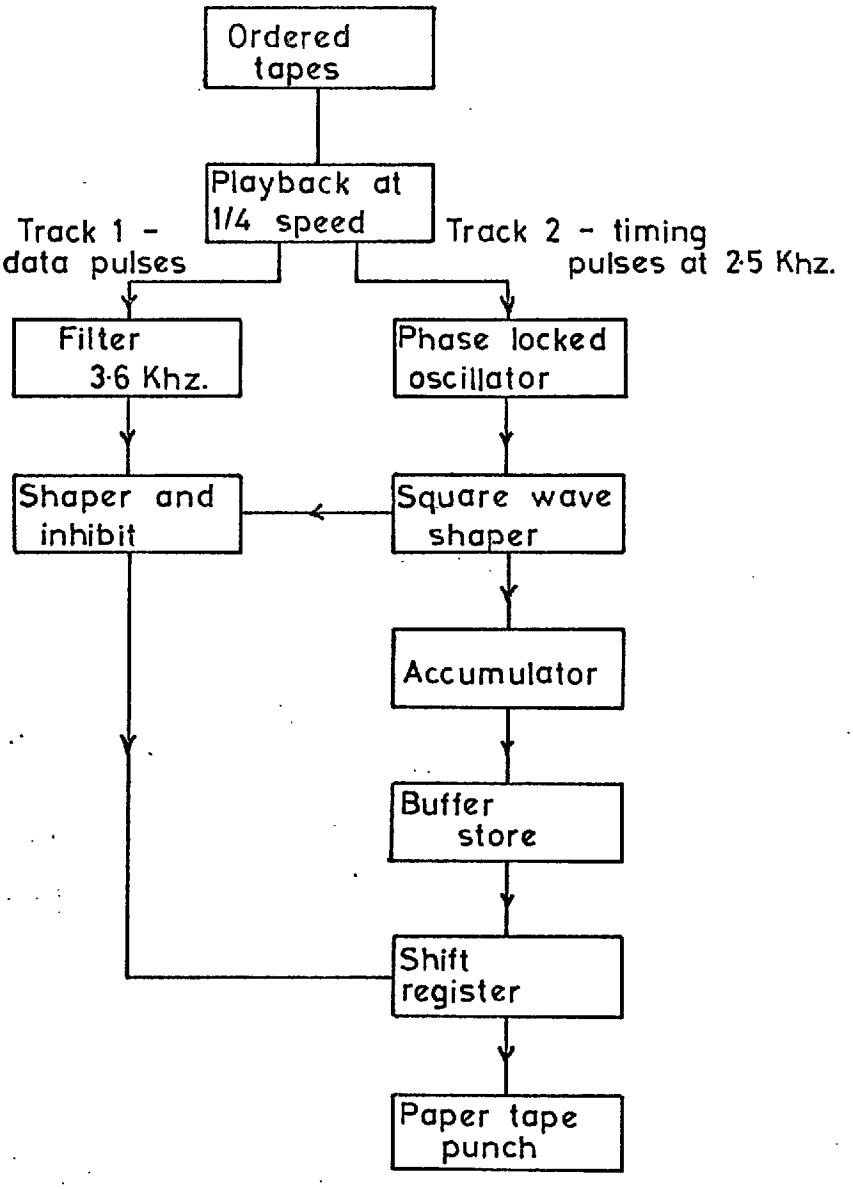

Figure 4(3) Layout of the data reduction system from magnetic tape to punched paper tape.

time of each event. For 20 counts/sec this demanded the production of an average of 80 output lines a second, which was beyond the capability of the punch. By recording the tapes at their maximum speed of $7\frac{1}{2}$ inches per second and playing them back at $1\frac{7}{8}$ inches per second, the laboratory count rate could be reduced to 5 per sec and the number of lines required to 20 per sec.

The punch dead time associated with each line of output was $\sim$ 15 m.s. and for each 4-line word was 60 m.s. The mean time between X-ray events at $\frac{1}{4}$ speed was $\sim$ 200 m.s. which represented a count rate of 0.3 per 60 m.s. interval. These were rare events and Poissonian statistics could be used.

The probability P of a number X of events occurring in a time interval with mean count rate λ is given by

$$P(X) = \frac{\lambda^X e^{-\lambda}}{X!}$$

For this experiment P(2) was $\sim$ 3.5%, a rather high figure. A buffer store was included in series with the shift register such that one number could be stored whilst another was being punched. Then a count would have been lost only if three events occurred in one dead time interval. This probability P(3) was 0.3%.

As in the direct recording case the accumulator had a number storage capacity of 2^{28} which, with a 100 μs time unit, represented an accumulation period of 8 hours before recycling would occur.

When attempting to store a time in the form of a 10 KHz sine wave on magnetic tape the problem of tape drop out was found to produce a considerable error. A loss of timing pulses in this way caused a "slowing down" of time. The problem was overcome by incorporating an oscillator in

series with the sine wave, timing pulse and locked in phase to it. When the relaxation time was correctly chosen, small regions of missing signal could be replaced by the oscillator, the system taking into account local changes of timing frequency due to tape stretch.

It is shown (Technical Interface, 1969) that if a periodic signal waveform $V_s = E_s \sin(w_s t + \phi)$, where ϕ is an arbitrary phase angle, is compared with a reference signal $V_r = E_r \sin w_r t$, then a d.c. output results only if $w_r = w_s$ and this voltage output is given by

$$V_{d.c.} = \frac{E_s E_r}{2} \cos \phi$$

When the signals are in quadrature $\phi = \pi/2$, $V_{d.c.} = 0$. A phase sensitive detector was used to compare the phase of the input signal with a reference signal from the quadrature output of a voltage programmable oscillator (P.F.O.), whose "in-phase" component eventually represented the drop-out corrected version of the incoming signal. A low pass filter smoothed the resulting a.c. component. The d.c. component was used to program the P.F.O. and hence pull it into phase with the incoming signal, whence the d.c. component fell to zero. The signals then remained locked. Richman (1954) shows that if w_s differs slightly from w_r, then the asymmetry of the resulting beat note produces a d.c. component that allows pull-in to occur prior to lock. The modular system used was supplied by AIM electronics, Cambridge.

A square wave shaper was used to interface the oscillator output and the accumulator. This pulse shape was also used to inhibit the transfer command to the shift register in the event of a command occurring whilst accumulation was taking place.

The system was tested using a dual input Lintronix scalar, and by taking advantage of the monitoring facility of the Tanberg tape recorder.

A short time after the 10 KHz sine wave signal had been recorded onto the tape it was reproduced by the monitoring heads and, after amplification, was used as the input to the phase lock system. The output from the P.F.O. was fed into one scalar channel and the direct signal from the timer into the other. The two counting channels were activated simultaneously and allowed to accumulate for the same length of time. In this way a direct comparison of input and reproduced signals was made which indicated a correspondence of better than one part in 10^6.

4.5 Direct Data Recording

It has been seen that the limiting factor for reducing the data in real time was the speed of the punch. By recording the interpulse time, the length of the punched word was reduced, as was the punch dead time. Two character lines could store a number 1.6×10^4 ($= 2^{14}$) which, with a 100 μs time unit represented 1.6 seconds. Two lines produced a 30 m.s. dead time which, for a counting rate of 20 per sec produced a 2% loss of data (including the advantage of the buffer store).

It was required to synthesise the flight time by summing the interpulse times and it was, therefore, vitally important that the accumulator did not recycle at any time during the recording. With a counting rate of 20/sec this probability was negligibly small, but to provide for a lower count rate, < 10/sec, when recycling might become a possibility, a facility was built into the punch control that enabled the output to be switched from 2 to 3 lines/character. At 10 counts/sec the loss of data due to dead time was <1% and the recycling time of the accumulator was > 200 secs.

The punch command was also used to generate a "clearing" pulse that reduced the scalar store to zero. Protection was built into the system to prevent the acceptance of a punch or clear command whilst accumulation

was in progress. The punch command was also used to increment a visual scalar to enable an in-flight observation of the X-ray counting rate to be made.

4.6 Data Analysis Programs

It was required to transfer the data from the several paper tapes onto a single computer compatible magnetic tape. This facility is provided by a standard library program but in the particular case the program was modified so that separate tapes could be time-linked by associating the markers placed at the beginning and end of each tape by the F.E.T. switch. The data on the magnetic tape was blocked into records, each containing 50 event times in coded number form. Any record could thereafter be located and accessed by subsequent analysis programs using the tape.

The analysis program required the computer to function in a multiscalar mode, scanning through the data with a period T, which value could be varied. The effect of the program was to fragment the continuous data into sections each exactly T seconds in length and to superimpose them. By so doing any structure in the data with this period, but with amplitude well below the accompanying noise level during one period, would become apparent above the noise if the number of periods superimposed was large enough.

Consider a pulsar to have been observed with period T_p secs. Fragment the period into n bins of width T_p/n secs. If an X-ray arrived at a time T_a after a fixed starting time then the pulsar would have executed T_a/T_p revolutions in this time where

$$\frac{T_a}{T_p} = r \cdot x$$

r represents the number of complete revolutions performed since the starting time, while x represents the phase of the present period at which this X-ray has arrived. The X-ray is allocated to a bin chosen by the

whole number part of the product of the phase fraction 0.x and n, the number of bins in the multiscalar.

The superimposed data were displayed as a histogram of total number of counts per bin as a function of bin number. Any periodicity at T_p secs would manifest itself as an excess of counting rate in one or more bins with its phase being represented by the position along the bin number axis. The rounding up procedure in the bin number selection produced anomalous counts in the first and last bins. Any scan made with period T was repeated twice at different phases to ensure that the periodic signal had not been lost at either extremity during the first scan.

The computer used was a CDC 6600 machine.

4.7 Complete Test of the Detection System

In the event of not detecting an X-ray signal from the pulsar, it was essential to have complete faith in the detection and analysis systems before a confident upper flux limit could be established. Thorough testing of the entire system was essential.

A synthetic pulsar was injected into the electronics of the working detector such that it was indistinguishable from any other X-ray produced pulses. Resulting signals were transmitted across the laboratory where they were received and recorded. The recorded signals were analysed to recover the injected pulsar.

The output of an Advance TC1A timer (accuracy 1 part in 10^6) was used to feed an electronic divide system that could produce a pulse of any desired frequency. The pulse was shaped and injected into the detector electronics at the output stage of the lower level discriminator. By having the photo-multiplier switched either on or off and an X-ray source nearby, the injected

pulsar could be investigated with or without accompanying background pulses.

By recording the fabricated pulsar without any background over extended periods that involved at least one tape change, an estimate of the coherence of the recorded and reproduced signals could be made. By recording the fabricated pulsar in the presence of X-ray background, the performance of the analysis programs could be estimated. The results were as follows.

a) Without any background a pulse of frequency 1.0 sec was injected into the detector. In one such test, data were recorded for 10 minutes during which time one tape change was made. The data were analysed using a search period of 10 m.s. divided into 50 bins each 0.2 m.s. wide. The result is shown in figure 4(4). The effect of the tape change is clearly represented by the count gap in channels 34 to 38 inclusive. This time discrepancy was always the same and, having measured it in this test, a correction factor could be added to the analysis programs. The counting rate per bin drift is $\sim$ 100 and since the pulses are of frequency 1/sec this represents a drift of 0.2 m.s. per 100 secs or 2 parts in 10^6. Since the timers used in this experiment were each accurate to only 1 part in 10^6 it is safe to assume that the recovery system is efficient to this same order.

b) In the presence of a background $\sim$14 counts/sec, the same 1.0 second pulsar was injected. 20 minutes of such data are shown analysed with a 10 sec search period in figure 4(5).

With this recording and recovery system, an overall accuracy of order two parts in 10^6 has been shown to be easily obtainable. In $1\frac{1}{2}$ hours this is $\sim \pm$ 10 m.s. which is the required figure quoted at the beginning of the chapter.

After the balloon flight had been made the TC9 timer used in the experiment was again compared with the TC1A. They were found to correspond to one part in 10^6.

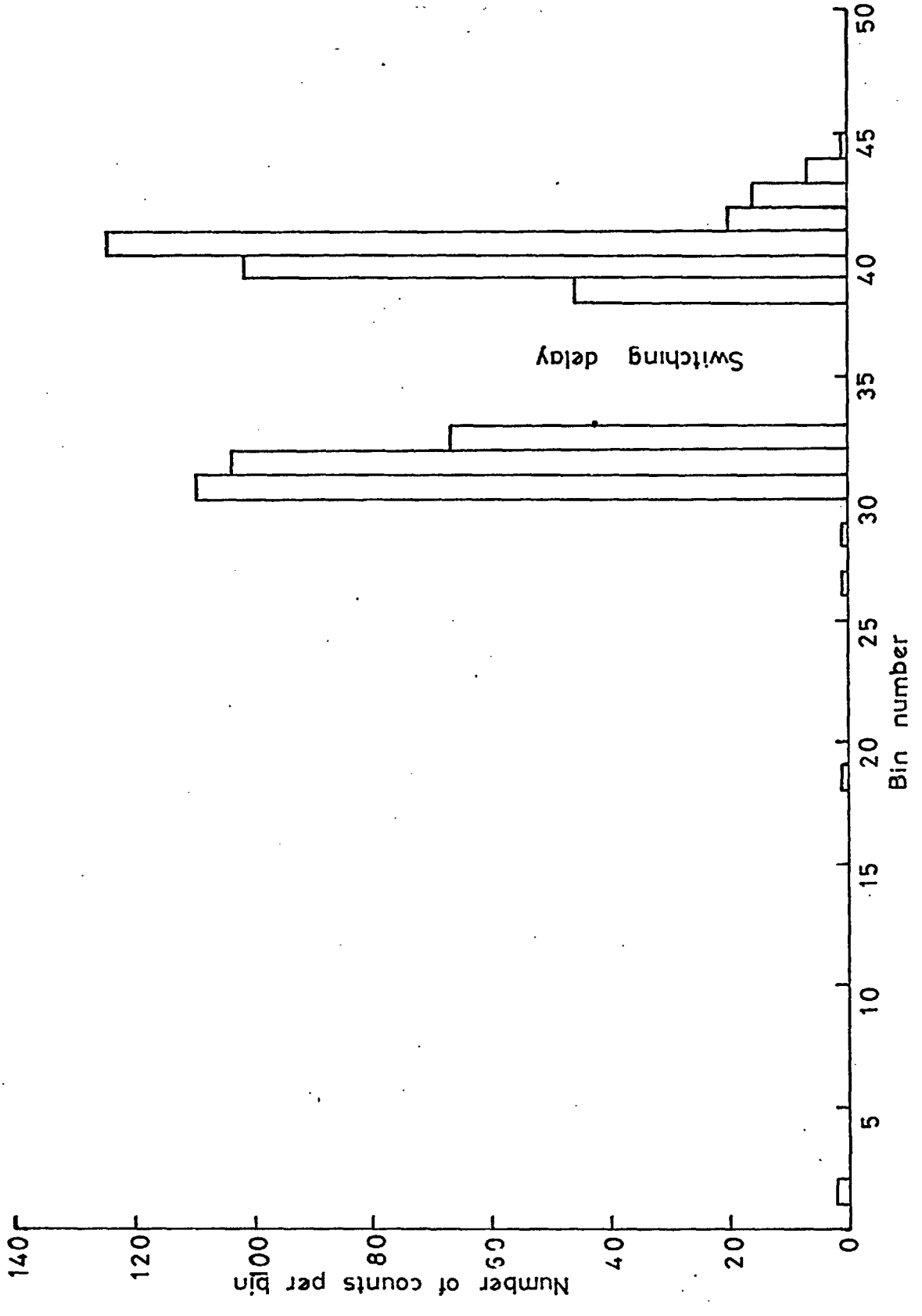

Figure 4(4) Results of the analysis of 10 minutes of test data involving only a 1.0 sec period injected pulsar subsequently scanned at 10 m.s. with 50 bins per scan. The data included one tape change.

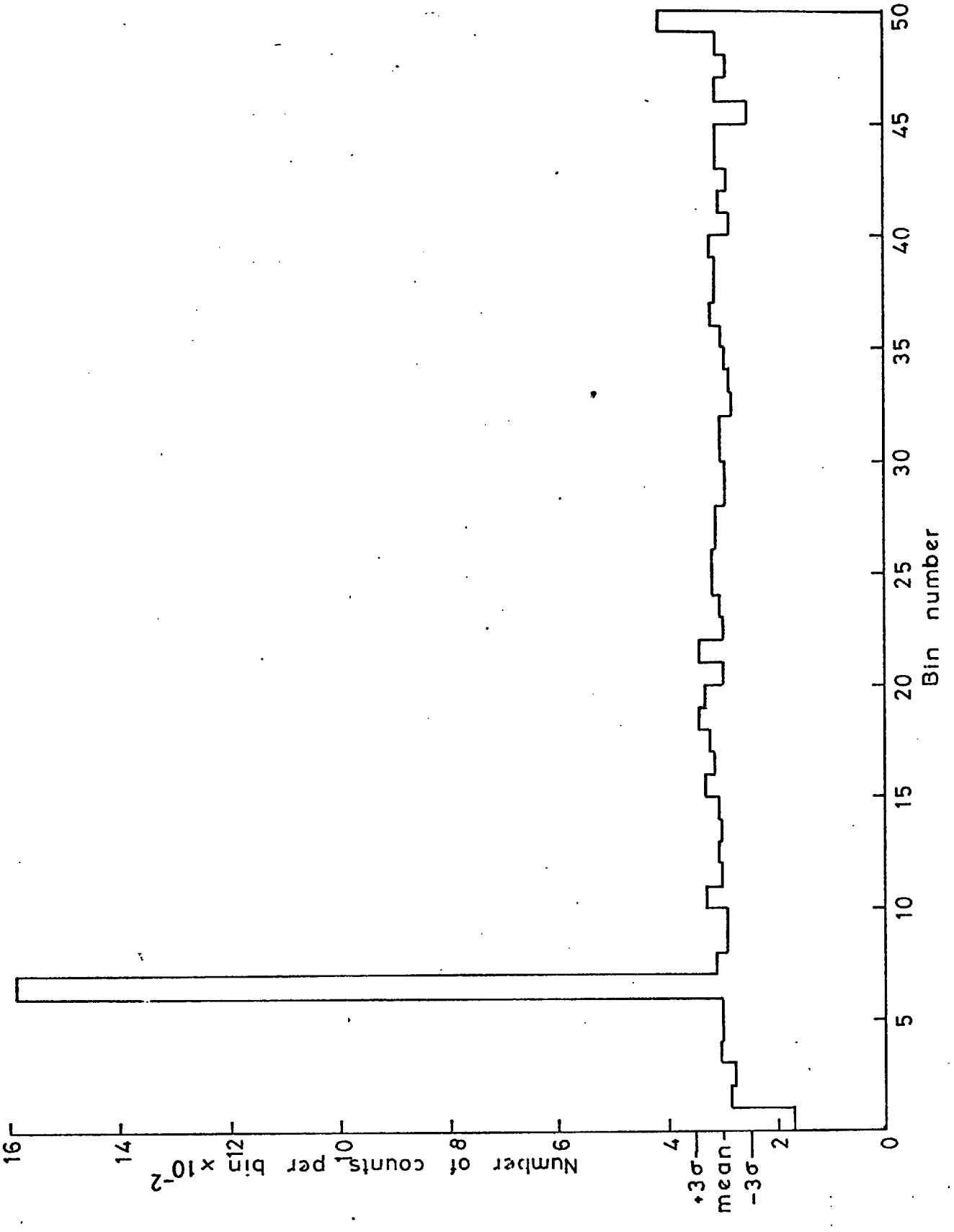

Figure 4(5) Results of the analysis of 20 minutes of test data in which a 1.0 sec period pulsar was injected against a background count rate ∿14/sec. The data was scanned at 1.0 sec with 50 bins per scan.

CHAPTER V - THE BALLOON FLIGHT AND ASCENT CURVE

5.1 The Balloon Launch

The balloon was launched from the air base, R.A.F. Cardington in Bedfordshire at 0500 hours on the 20th June, 1970. Radio signals were received and checked at the receiving station established at Imperial College, London within seconds of the launch. A 360,000 cu.ft. hydrogen inflated balloon, made by Raven industries of America was used and was expected to carry the 40.5 lb payload to a floating altitude of 4-4.5 mb. The detector was enclosed in a closely fitting box constructed from $1\frac{1}{2}$ inch thick, expanded polystyrene. The box was 50% blackened on the outside to maintain an inside temperature of $\sim$ 20°C. A clock operated cut down device was incorporated to separate the balloon and payload after ten hours flight, the descent being made by parachute. A radar reflector was also sent up with the balloon.

5.2 The Balloon Flight

The balloon reached a floating altitude of 4.1 mb two hours after launch, ascending in the manner shown in figure 5(1). A calculation based on wind velocities supplied by the meteorological office, predicted the flight path shown in figure 5(2). The wind velocity at altitude was 32 knots at 100° (i.e. blowing towards 280°). The detector blew out of radio range at 1430 hours and was timed to cut down at 1500 hours.

The counting rate as a function of altitude is shown plotted in figure 5(3). The ground level counting rate of 2/sec increased slowly until nearly 500 mb when a sharp increase took place. This increase peaked near 80 mb where the counting rate was $\sim$ 40/sec. There followed a sharp

decline in counting rate to floating altitude, where an average of $\sim$ 18 events/sec were recorded (c.f. Appendix B).

In figure 5(4) the number of pulses recorded during a 25 minute period at altitude are arranged as a function of the interpulse interval. The first channel is corrected for dead time effects in the punch. The solid curve is the predicted distribution for the random occurrence of a large number of events fitted to the observed distribution. It is a normal distribution with $\sigma = 6.72$. A χ^2 test for goodness of fit can be applied to the two distributions where

$$\chi^2 = \sum_i \frac{\left[(\text{observed value})i - (\text{expected value})i\right]^2}{(\text{expected value})i}$$

In the copious event region (interpulse time $\lesssim$ 100 ms) the probability of subsequent χ^2 exceeding the observed value is 80% and the fit is thus believed to be good. For interpulse times $\gtrsim$ 100 ms the events become progressively rarer and the shape departs from the normal distribution and tends towards the Poissonian or interval distribution. The results from this curve justify, a posteriori, the dead time analysis in Chapter 4 that was based on Poissonian statistics.

The region of the sky scanned by the detector is shown in figure 5(5).

The temperature during ascent and at altitude is shown in figure 5(6). The initial phase (prior to 0900 hours) was typical for a balloon ascent, with a slow temperature drop during the ascent through the cold tropopause and a gradual recovery after altitude had been attained, due to absorption of radiation through the blackened parts of the detector insulation. After 0900 hours there followed a dramatic rise in temperature with a time constant that was much shorter than is typical for this kind of detector insulation. That this was a genuine increase, rather than an instrumentation fault, is indisputable since it was recorded by both of the Olland cycles

and the transmitter showed a drop in transmitting power with a corresponding drift in transmission frequency consistent with such a rise. The frequency drift ($\sim$ 0.7 Mhz) was used to infer a maximum temperature of 50°C after the Olland cycle scale had been exceeded. At 1230 hours the temperature dropped once more and remained below 30°C for the remainder of the flight.

The heating effect must have had a cause external to the detector. If the total energy stored in the batteries had been dissipated in the form of heat it could not have produced such a rise in temperature and, certainly, could never have sustained it. Any damage to the insulation could only have produced a drop in temperature. The heating mechanism must have been very strong because of the sharpness of the increase, in spite of the thick thermal shield. Solar radiation from above is a very predictable quantity and the relative amount of blackening on the shield was calculated in the light of experiences of previous balloon flights which maintained a 20°C flight temperature (approx.). It is suggested that the cause of the increase was albedo radiation from below the detector. Albedo is a much less predictable quantity and in an experiment using a British Mk. 2B radiosonde temperature unit, increases in package temperature of up to 35°C were recorded due to a change in albedo from 0.1 to 0.4 (Private Communication with Meteorological Office) . Albedo is less over the sea than over land and the temperature decrease at 1230 hours is coincident with the passage of the balloon over the Irish Sea.

The effects of the increase were twofold. Firstly it modified the range of the energy channel to 28-114 keV. The second, and more serious effect, was to reduce the power of the transmitter and alter its frequency. This introduced more noise into the transmission band. As a result, great care had to be taken when filtering the data. In spite of such caution, some passages of noisy signal introduced an additional background to the

X-ray count rate (∿ 20% at maximum) and some other small, but very noisy passages had to be omitted from the analysis altogether. The noise originated from sources outside the detector and was probably due to frequency drift into the bands of other local transmitters.

5.3 The Ascent Curve

Figure 5(7) shows the counting rate ascent curve of 5(3) re-plotted on a log-linear scale. Each point is a ten second average and the time between averages is ∿ one minute.

At heights greater than 800 mb but prior to turnover the counting rate, N, is assumed to obey a law

$$N = N_o \exp(-x/L) \quad . \tag{5.3.i}$$

where x is the altitude and L the absorption length. Then

$$\log_{10} N = - \frac{\log_{10} e}{L} \cdot x + \log_{10} N_o \tag{5.3.ii}$$

which is of the form

$$y = ax + b \tag{5.3.iii}$$

If there are n corresponding values of x and y, Topping (1966) shows that a least squares fit to (5.3.iii) yields the values

$$a = \frac{n(\Sigma xy) - (\Sigma x)(\Sigma y)}{n(\Sigma x^2) - (\Sigma x)^2} \tag{5.3.iv}$$

and

$$b = \frac{(\Sigma y)(\Sigma x^2) - (\Sigma x)(\Sigma xy)}{n(\Sigma x^2) - (\Sigma x)^2} \tag{5.3.v}$$

Also if d is the deviation of a point from its least square value, then the mean square error α^2 is given by

$$\alpha^2 = \frac{\Sigma d^2}{(n-2)}$$

and the standard errors α_a, α_b in the values of a and b respectively are given by the equations

$$\frac{\alpha_a^2}{n} = \frac{\alpha_b^2}{\Sigma x^2} = \frac{\alpha^2}{n\Sigma x^2 - (\Sigma x)^2}$$

If all the points between 100 and 700 mb from figure 5(7) are fitted to (5.3.ii) in this way, a value for L of 187 mb is obtained. The largest deviations from the fitted curve are noticed at its extremities. At low altitudes this is due to large statistical fluctuations on low counting rates and at high altitudes the deviations are due to rapid approach to turnover. Following Jones (1961), a more reliable value of L is believed to be obtained by considering only points between 200-600 mb. A value of L = 173 $\pm$ 6 mb is obtained by fitting the curve between these limits.

The position of the maximum counting rate in this experiment ($\sim$80 mb) compares favourably with that observed by Jones (1961) who also notes that this position corresponds with the intensity maximum of the low-energy nucleonic component of cosmic rays.

Jones (1961) and Vette (1962), each flying detectors at 40^{o}N observed the absorption lengths for γ-ray producing radiation in air to be $\sim$163 $\pm$ 4 gm.cm^{-2}. Converting the units of the value obtained in this experiment, the absorption length derived is 176 $\pm$ 6 gm.cm^{-2}, which is $\sim$ 8% higher than the above values.

Vette (1962) demonstrates that the absorption length depends upon the type of incident radiation being observed. The present experiment was conducted at 55°N where the charged particle cut-off due to the earth's magnetic field is considerably lower than at 40°N. The charged particle spectra at the two locations are different and the respective absorption lengths should also differ slightly.

The problem of estimating the absorption length at this latitude for a calculated, incident charged particle spectrum with known X-ray production and absorption mechanisms is a very difficult one and is not attempted here. The result obtained in this experiment is compared with those of other workers in order to demonstrate that the detector was working reliably during the flight.

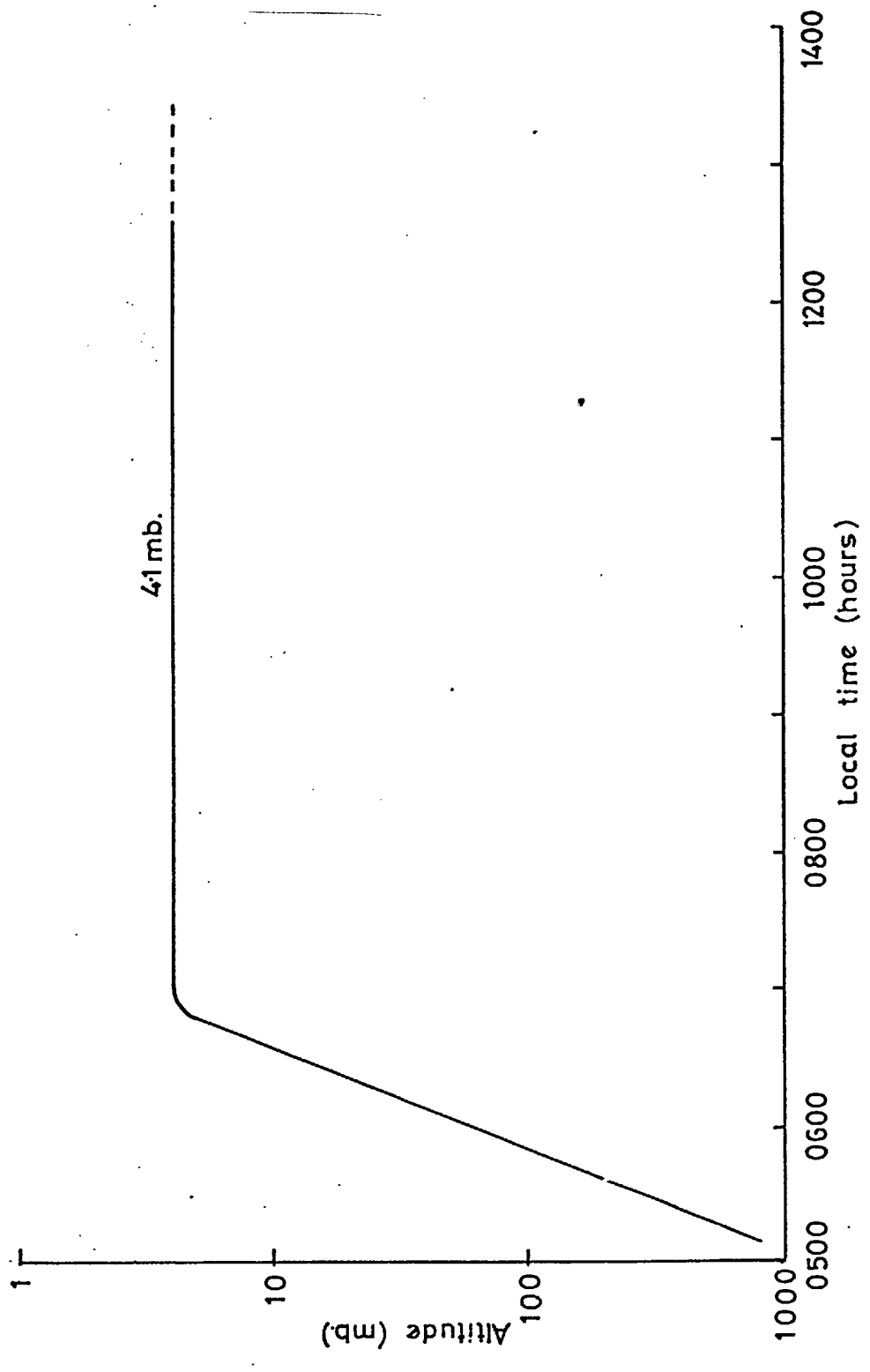

Figure 5(1): The altitude of the balloon as a function of time.

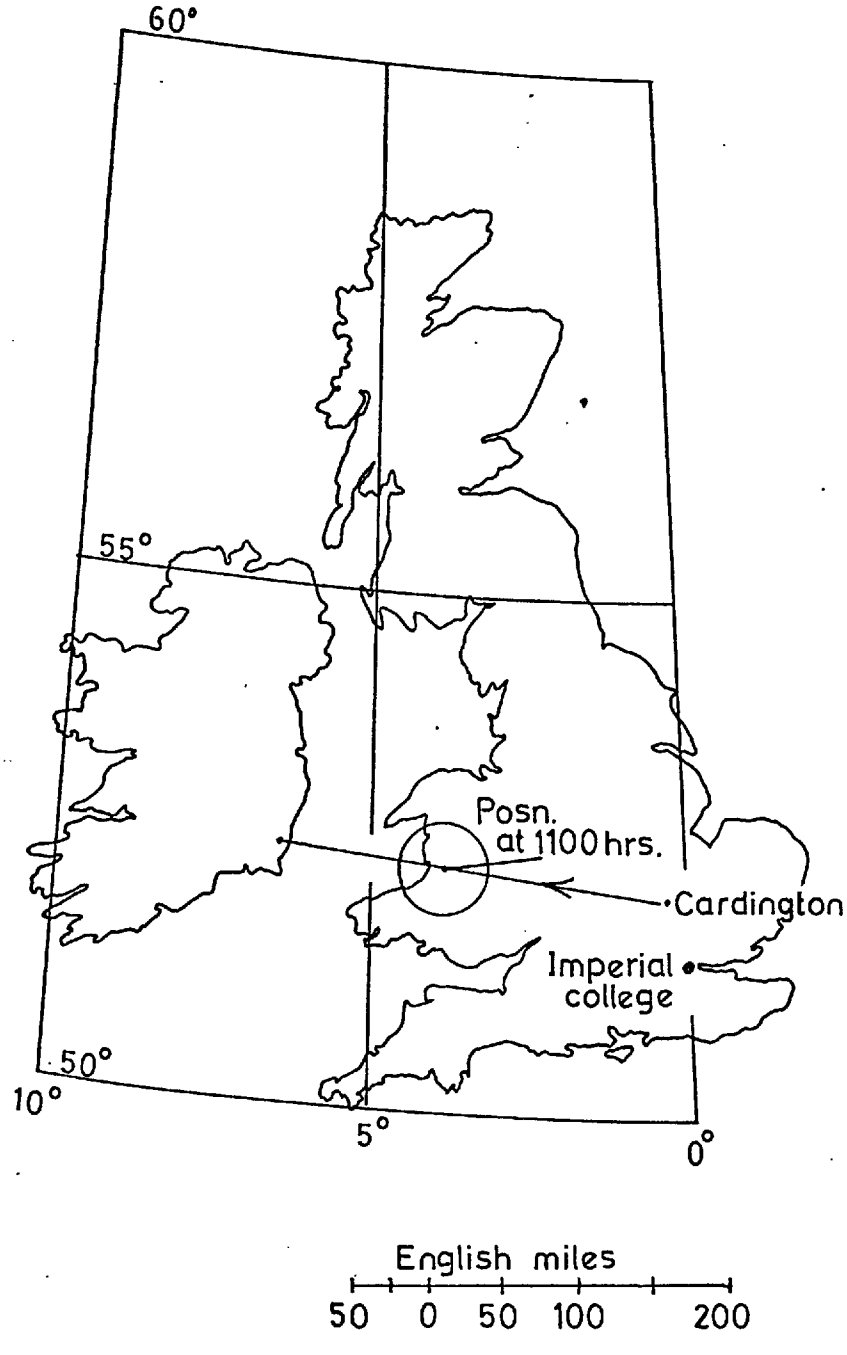

Figure 5(2): The balloon flight path showing the position at 1100 hrs, the approximate time of pulsar zenith. The circle surrounding the position is the 50% certainty circle.

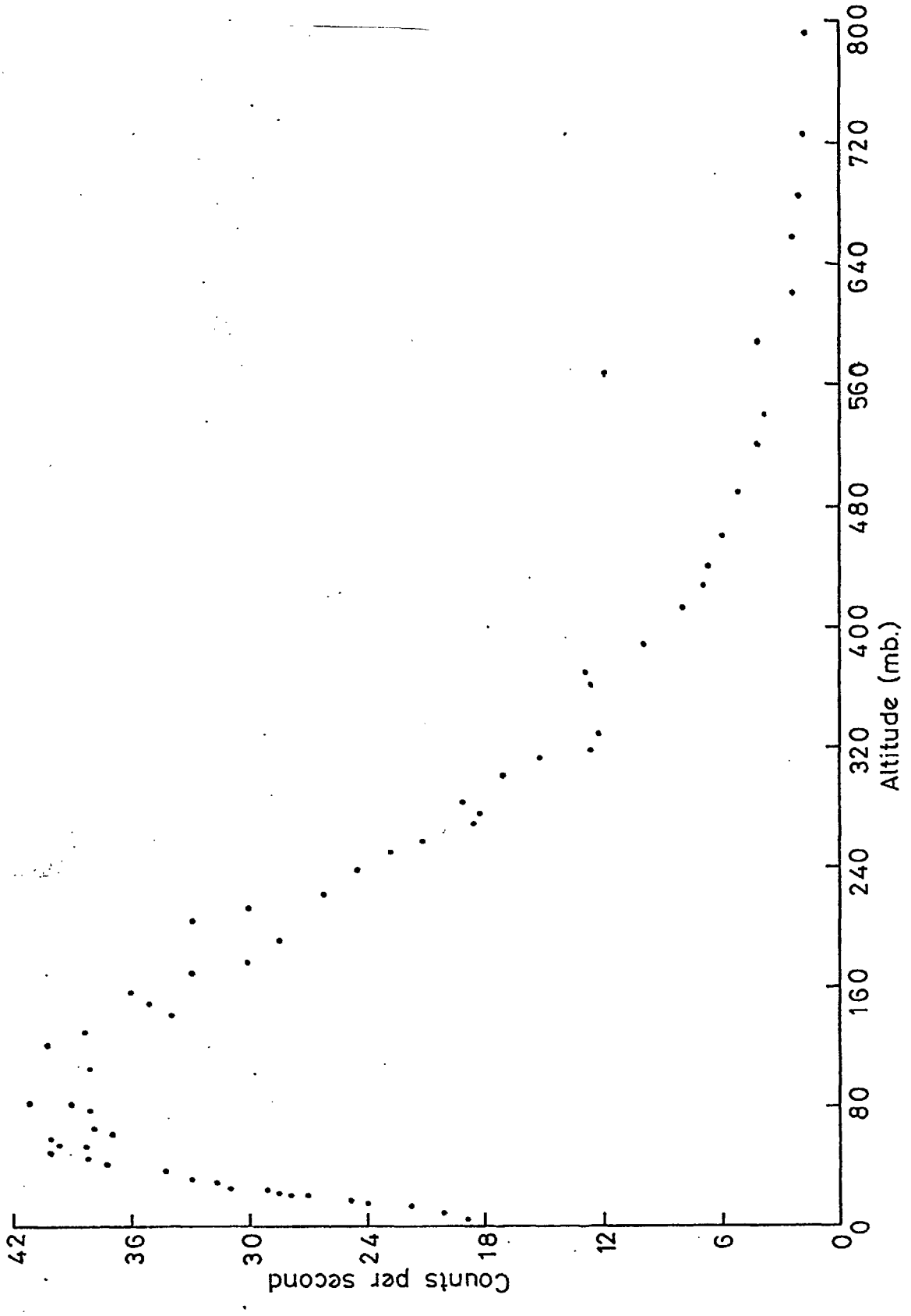

Figure 5(3): The counting rate ascent curve in counts/sec from one minute averages as a function of altitude, which is described by the pressure in mb.

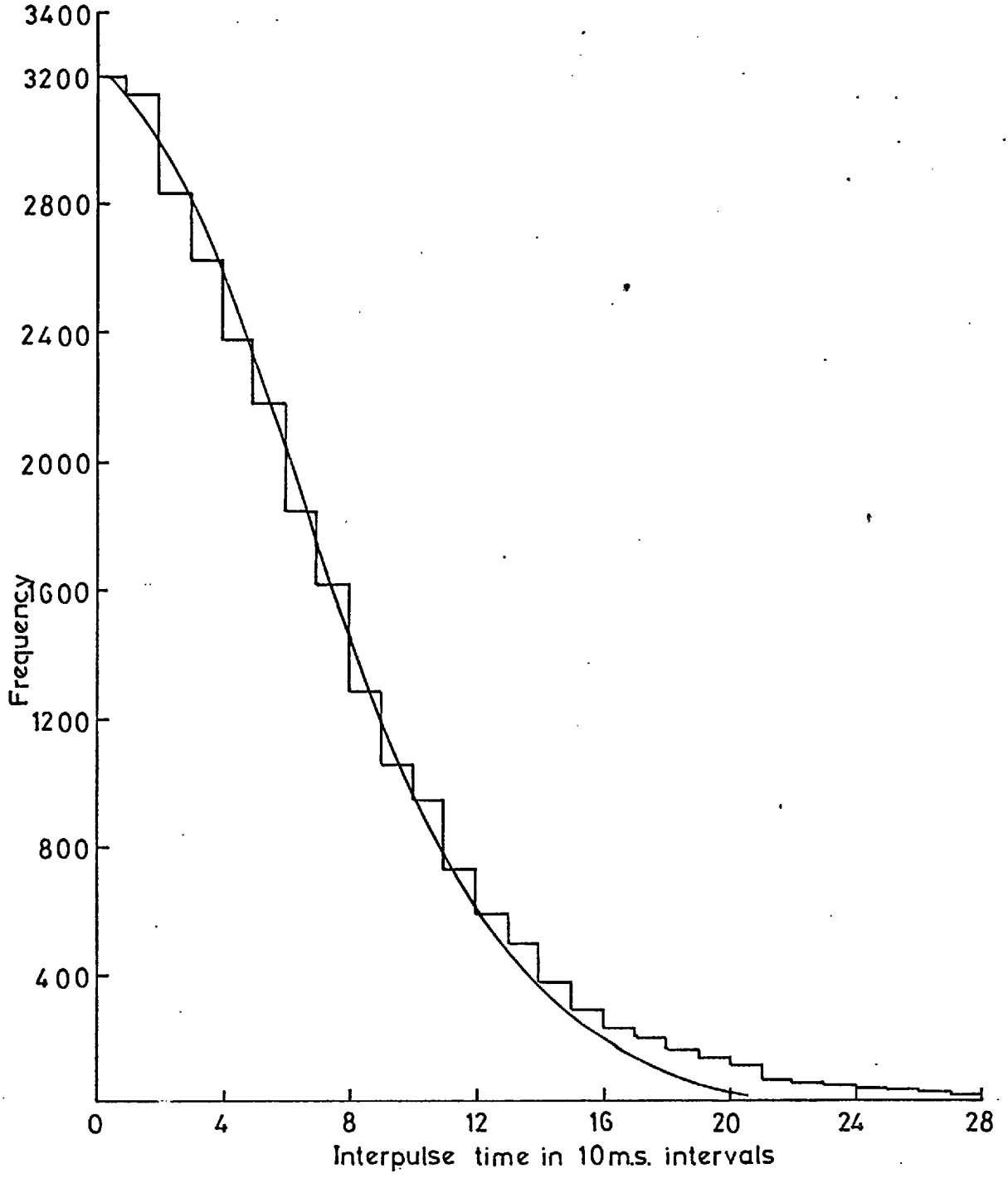

Figure 5(4): Shows a histogram of the measured frequency of occurrence of times between events during a 25 minute period at altitude.

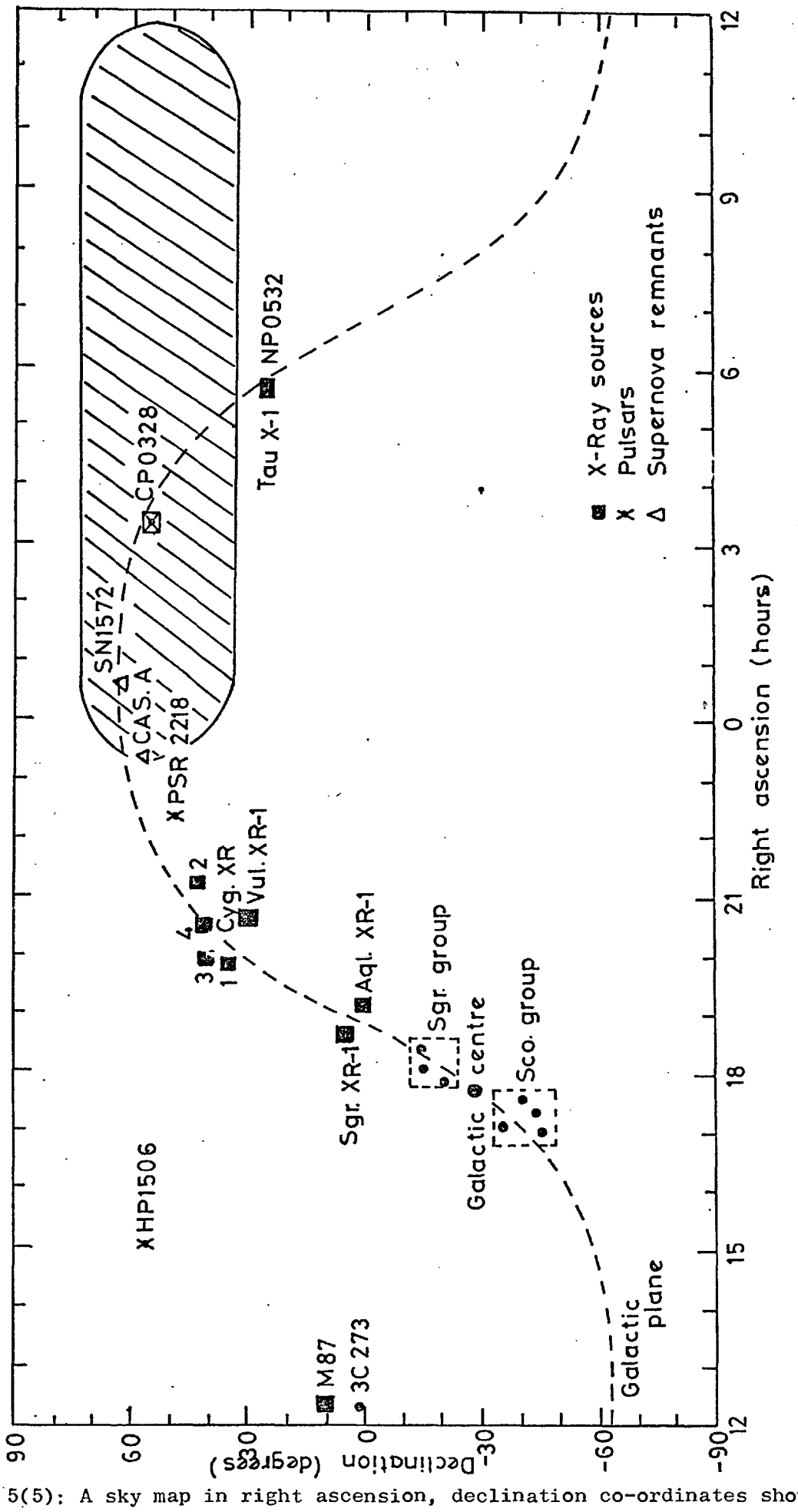

Figure 5(5): A sky map in right ascension, declination co-ordinates showing the full opening angle of the detector, $\pm 20^{\circ}$. Also plotted are the major X-ray sources, CP0328 and other pulsars near declination 55° and two X-ray emitting supernova remnants, Tychos supernova SN1572 and CAS A. The figure follows

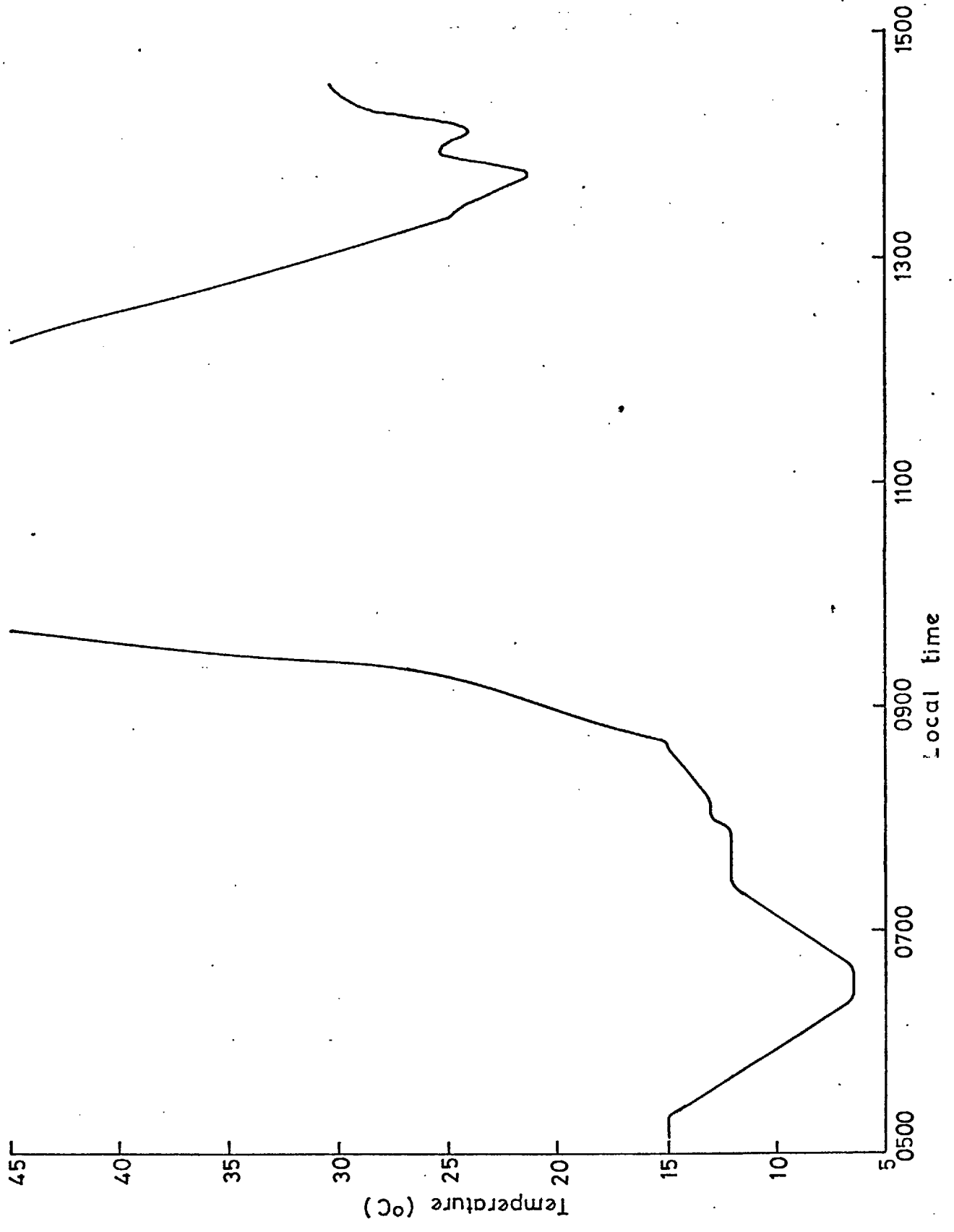

Figure 5(6): The payload temperature curve as recorded by the Olland cycles during the flight. At maximum (50°C) the cycle information was difficult to decipher and the drift in transmitter oscillator frequency was used to infer the maximum temperature.

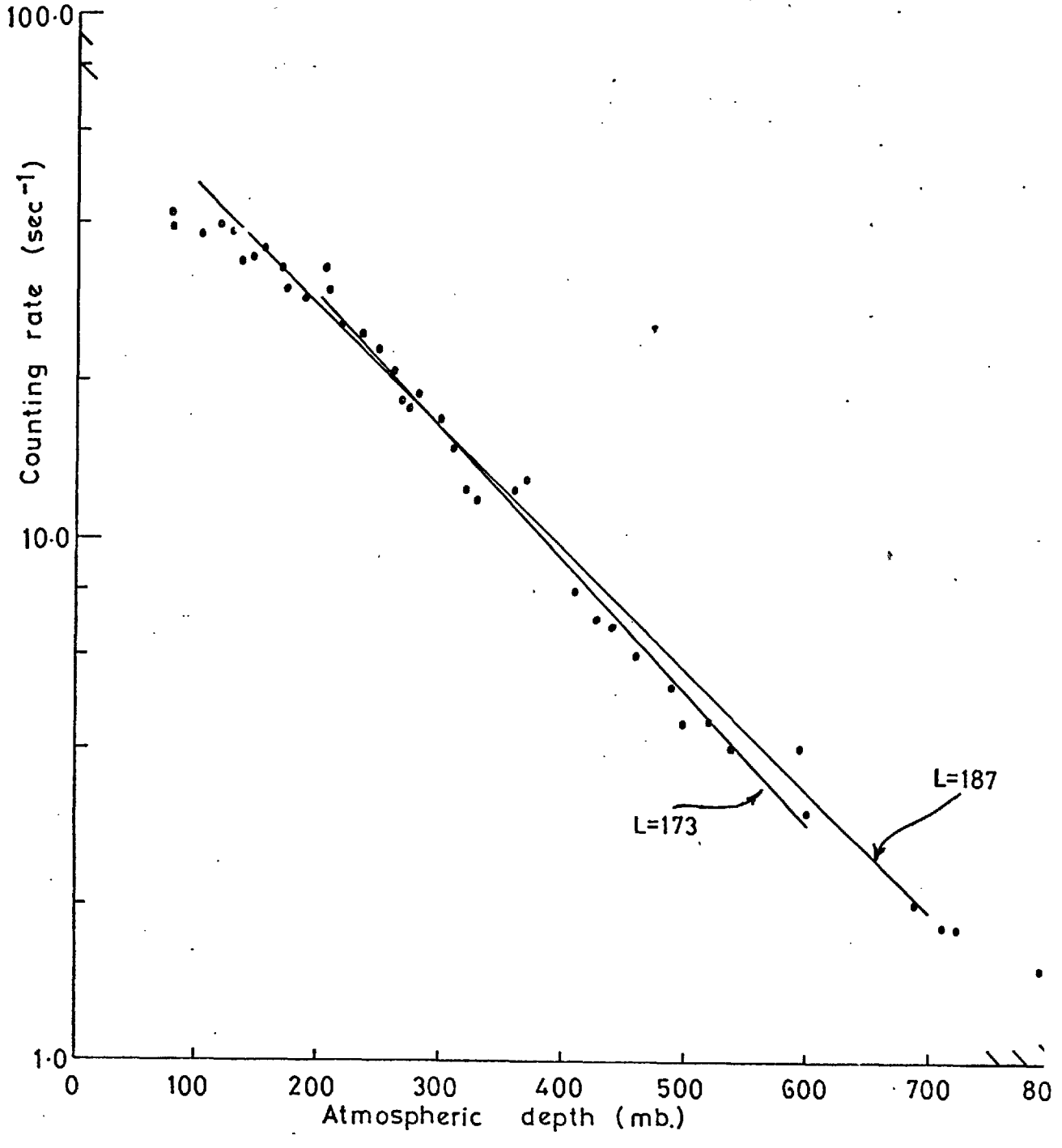

Figure 5(7): Counting rate ascent curve shown in figure 5(3) on a log linear scale.

CHAPTER 6 - AN UPPER LIMIT TO THE X-RAY FLUX FROM CP0328

6.1 Character, Position and Period for CP0328 on June 20th 1970

In order to carry out a search for CP0328 in the data, its exact period recorded at the balloon must be known and some idea of the pulse width is also required. This information must come from observations in radio astronomy

The parameters relevant to CP0328 were given by A.G. Lyne at the Herstmonceux Conference on astronomy, 1969, and by T.W. Cole (1969) as

Right ascension α	-	03h 29m 11.0s
Declination δ	-	54^{o} 24' 37.2"
Period (April 1969)	-	0.714518603s $\pm$ 15ns
Increase of period per year	-	60 $\pm$ 5ns

The period measurements are referred to the pulse arrival times at the barycentre, i.e. the centre of mass of the solar system.

CP0328 lies in the galactic plane. At the radio frequency, 408 Mhz, the half power width of its pulse is 6 ms; the total pulse width however is $\gtrsim$ 30 ms.

Due to the high time resolution of this experiment, a careful series of corrections had to be applied to the barycentric period to obtain the value at the earth on 20th June. Five effects that could have affected the period were considered.

a) There is a steady increase in pulsar period. In the 14 months from April 1969 to June 1970 the period of CP0328 increased by 70 $\pm$ 6 ns. The pulsar period at the barycentre was 0.714518673s $\pm$ 17ns on June 20th.

b) The solar system is in motion relative to the galaxy. This motion is a long term constant and the periods of pulsars referred to the barycentre will not be effected in the short term encompassed by these measurements.

c) The motion of the earth about the solar system barycentre produces a change in the observed pulsar period due to the Doppler effect. The position of the barycentre was calculated from the heliocentric positions of the planets as given in the Astronomical Ephemeris (1970). The radial distance of the earth from the barycentre on June 20th was found to be 1.014 A.U. (1.5169×10^{11} m). This distance and the earth's velocity vector relative to CP0328 are considered constant throughout June 20th. The velocity vector was calculated to be ~~29.5740~~ 29.571 ± .04 km/sec. relative to the barycentre at an angle 55.1° to the Earth-CP0328 line.

Any periodic signal suffers a Doppler change of frequency from ν to ν' in the event of a velocity, $\underline{v}$, of the observer. The frequency change obeys the equation

$$\nu' = \frac{\nu(1 - v^2)^{\frac{1}{2}}}{(1 - \underline{v}.\underline{r})}$$

where v is in velocity of light units, $\underline{r}$ is the unit vector along the line of sight.

In terms of the corresponding periods P and P'

$$P' = P \left(\frac{(1 - v_{11})}{(1 + v_{11})} \right)^{\frac{1}{2}} \cdot \frac{1}{(1 - v_{\perp}^2)^{\frac{1}{2}}}$$

where v_{11}, $v_{\perp}$ are the velocity components parallel and perpendicular to the line of sight respectively.

Substituting the relevant values for the earth's barycentric rotation, the apparent period became 0.714495197 ± 50 ns.

d) The rotation of the earth about its axis also produced a Doppler shift. At zenith the pulsar passed almost vertically overhead. At this time there could be no motion along the line of sight due to axial rotation. Only motion perpendicular to the line of sight produced a Doppler shift and this was negligible. The pulsar was not always at zenith but the line of sight correction over the ± 20° opening angle of the detector was found to be negligible.

e) The change in position of the detector during the recording affected the arrival time of pulses simply because of the change in propagation time of signals with distance. This was of the order

$$\frac{\text{(observation time x wind velocity)}}{\text{velocity of light}}$$

and, at 0.2 ms in two hours, was negligible.

The pulsar period used, in the analysis was 0.714495197s ± 50 ns.

The accuracy to which this period could be estimated, justified its sole use in the analysis since it is an order of magnitude better than the clock accuracy.

6.2 The Signal to Background Ratio

From the calculated balloon position it was estimated that the pulsar reached its zenith at 1002 hours G.M.T. With a telescope half opening angle of 20° and allowing for a westerly balloon drift of 32 kts, the pulsar fell within the field of view for approximately $2\frac{3}{4}$ hours. The continuous background, however, reduced the useful portion of these data. As the zenith angle increased, the effective detector area presented to the pulsar became smaller and the ratio of pulsar data to the background was reduced correspondingly. It is important to calculate the optimum length of data to be analysed.

Consider an experiment to detect X-rays from a pulsar and to accumulate the events into one analysis bin (viz. Chapter 4). The time average of the events yield a flux of I photons cm^{-2} sec^{-1} at the balloon floating altitude from the pulsar.

At a pulsar inclination, ϕ, to the zenith the detection rate is $IS(\phi)\cos\phi$ photons sec^{-1}, where S is the effective detector area (see Chapter 3). Since $\phi < 20^{o}$, $\cos\phi$ is small and in this calculation can be neglected. From figure 3(5) $S(\phi) = (50.5 - 2.9\phi)$ (approximately). ϕ can be expressed as a function of time:

$$\phi = (w_E + w_B)t$$

defining t = 0 when the pulsar is at zenith.

w_E is the angular velocity of the earth = $^{1}/_{240}$ degrees sec^{-1}

w_B is the angular velocity of the balloon relative to the earth, estimated to be $-^{1}/_{7,200}$ degrees sec^{-1} and hence negligible.

Then $$IS(t) = I\left(50.5 - \frac{2.9t}{240}\right)$$

During any time interval, O-T secs, the total number of counts seen is

$$\int_0^T IS(t)\,dt = I\left(50.5 - \frac{2.9T}{480}\right)T$$

provided $S(t) > 0$.

The number of background counts accumulated in this time is BT, where B is the detector background. We shall assume that the count rate from the proposed pulsar is statistically significant if its value is at least three times the standard deviation of the background rate,

i.e. if $$I\left(50.5 - \frac{2.9T}{480}\right)T > 3\,(BT)^{\frac{1}{2}}$$

since we have shown the background count to be Poissonian.

The conditions is just satisfied for

$$I = 3 B^{\frac{1}{2}} \left(50.5 T^{\frac{1}{2}} - \frac{2.9T}{480}^{3/2} \right)^{-1}$$

For any fixed B, this function represents the minimum source intensity which, according to the assumed criterion of significance, is necessary to distinguish that source above the background after viewing from zenith (t = 0) for a time T.

The function becomes infinite at T = 0 and 8359 secs. Since it is nowhere else discontinuous there must exist at least one minimum value of I between these infinite values. This value represents the most sensitive accumulation time.

Differentiating I(T) with respect to T and putting $dI/dT = 0$ gives $T \sim 46.5$ minutes. The seconderivative indicates that this is indeed a minimum point.

Thus, in order to obtain maximum sensitivity using this criterion of significance it was required to analyse data from 0916 to 1049 hours G.M.T. Unfortunately severe noise in the data channel occurred from 1040 hours and rendered subsequent observations useless until after the pulsar had passed from the field of view. 68 minutes of data were analysed. Since the data were spoiled towards the end of the viewing period this represents more than 75% of the useful data.

6.3 Estimation of detector exposure

In order to estimate the pulsar flux, the total exposure of the detector to the pulsar in cm^2 secs had to be calculated for the period of data used. Knowing the position of the balloon, the detector area exposed to the pulsar at any time could be calculated from the formula:

$$S(\phi) = 2R^2(\beta - \tfrac{1}{2}\sin 2\beta).$$ (See Chapter III)

The angle ϕ included any shift due to the balloon's latitude drift. When $S(\phi)$ was plotted as a function of time, the total exposure was given by the area beneath the curve.

The quality of the received data is included on the counting rate curve, figure 6(1). It can be seen that the signal became noisy around 9 a.m. local time. At some later times the noise became so bad that the data were completely spoiled. Any such regions occurring during the analysis period were rejected, thus reducing the detector exposure. The other data suffered a rise in background $\sim$ 20% due to noise infiltrating the data channel.

The $S(\phi)$ curve resulting from this experiment is shown in figure 6(2). The exposure calculated from it was 688 ± 59 cm^2 degrees which could be converted to $1.65 \pm 0.14 \times 10^5$ cm^{2}sec by using the simple relation between zenith angle and time. This represented some 75% of the total exposure that could have been expected had all the data been good. The possible error in this figure was due mainly to the lack of precision with which the detector crystal diameter could be measured. The contribution from the uncertainty in the balloon's position was small.

6.4 Analysis of the Data

Since only the Crab pulsar has been observed at other than radio wavelengths, it is difficult to say exactly what pulse shape should be looked for in the data. However, we can draw some firm conclusions on pulse shapes from radio observations of all pulsars and make some tentative but reasonable suggestions after considering the Crab's optical and X-ray pulses.

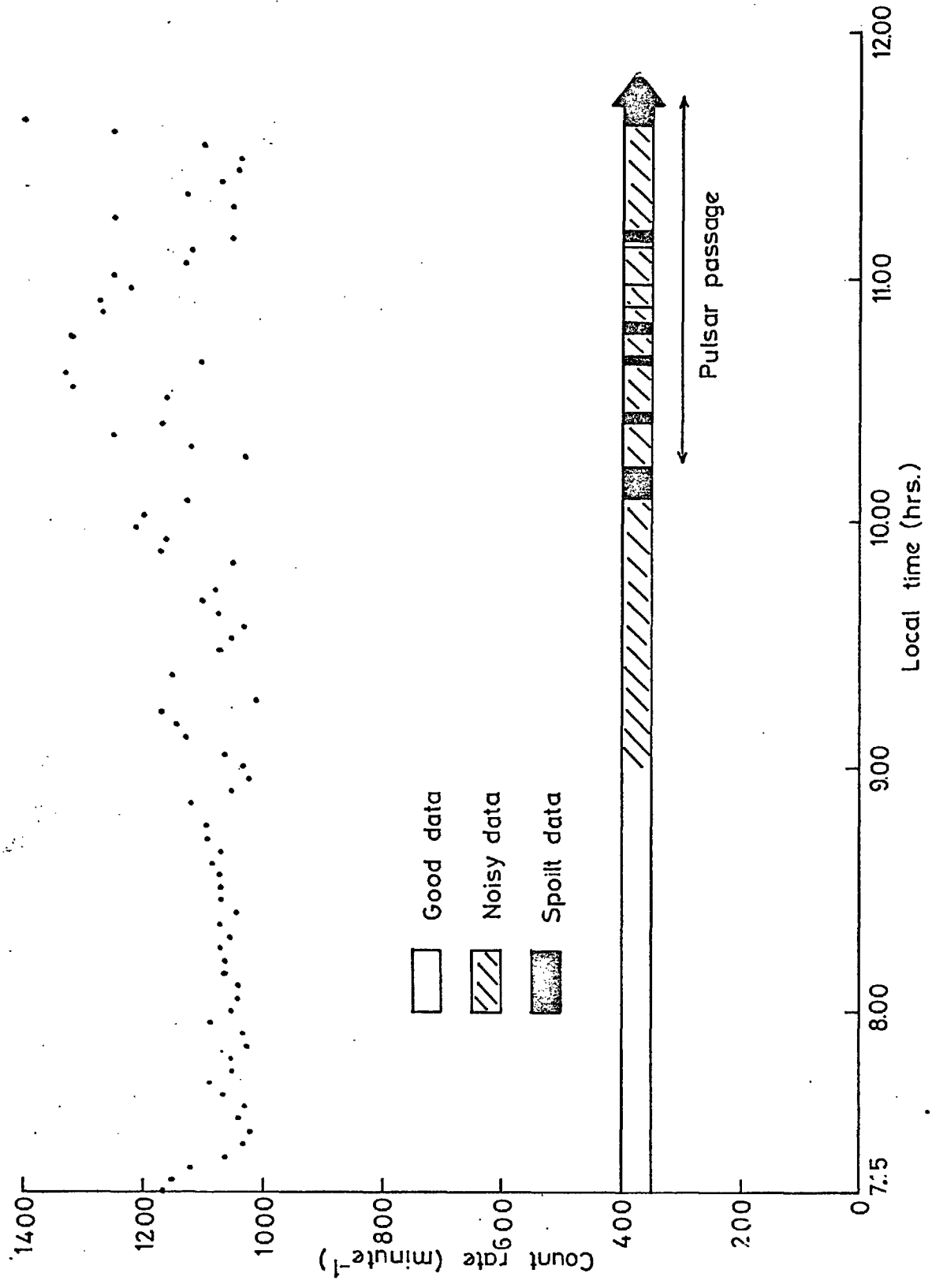

Figure 6(1): The X-ray counting rates for the first $4\frac{1}{2}$ hours of the flight, after altitude had been reached, are shown as 3 minute averages. The quality of the data is also indicated.

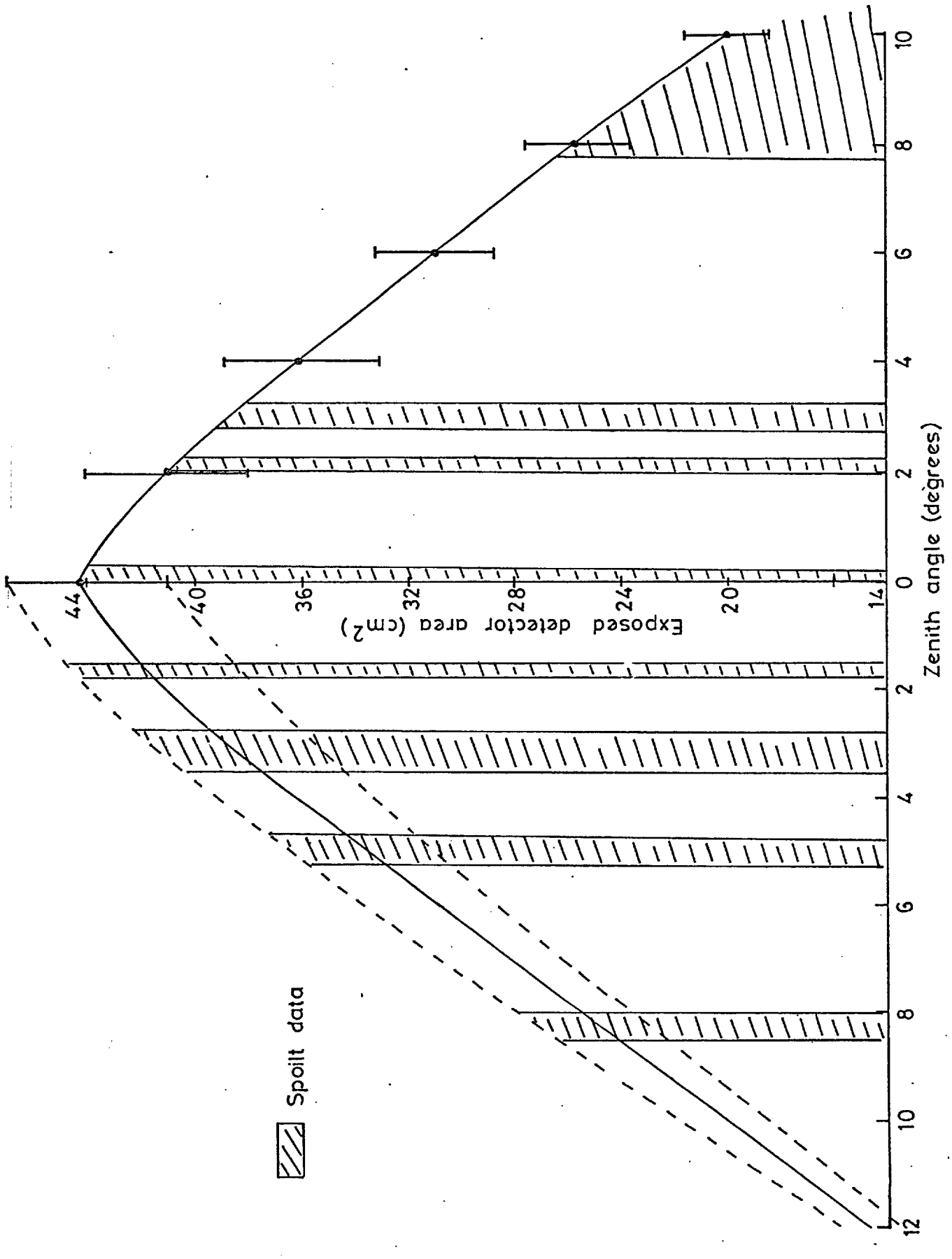

Figure 6(2): Shows the area of the detector exposed to the pulsar during its passage as a function of zenith angle. The uncertainty is introduced by inability to accurately determine the encapsulated crystal diameter.

Discounting effects of interstellar dispersion, all pulsar pulses occupy a rigidly restricted region within the period - the pulse window. Whilst the mean pulse shape at a fixed wavelength remains fairly constant, it can change considerably with varying wavelength.

For the Crab at optical and X-ray wavelengths, all fine pulse structure disappears, in particular there is no precursor in the main pulse, and the pulses assume a roughly Gaussian shape. With increasing frequency both pulses retain the same total width as the radio pulse window.

It is reasonable to conclude that the total pulse width of a pulsar does not vary with wavelength. The same is not true of the pulse shape, however, and we expect fine structure to be smoothed out and the half power width to increase at optical and X-ray energies.

The pulse window for CP0328 is $\sim$ 30 ms but the pulse width at $\frac{3}{4}$ maximum power is only 12 ms. In 80 minutes the timing drift in the experiment could be $\sim$ 10 ms and we must search for a feature whose total width is $\sim$ 40 ms but with most of its energy concentrated in a 22 ms region.

The interesting period of data was converted from magnetic tape to paper tape and analysed in the fashion described in Chapter 4 . The pulsar period was divided into 50 bins, each of width $\sim$ 14 ms. Because of the form of the analysis the first and last bins were underpopulated and overpopulated respectively. For this reason the analysis was repeated with a starting value that differed by half a period, to eliminate the possibility of a feature corresponding with one of these channels.

Two pulse widths were investigated, one at 22 ms, the other at 40 ms. In the first case the total pulse could possibly fit into two bins but was probably distributed between three. Adjacent bins were summed, beginning with bin numbers 1 and 2, to form a new set of 25 enlarged bins. This

was repeated but beginning with bins 2 and 3. If a feature of length 22 ms were present then at least 80% of its length must have fallen into one of these bins. Assuming that any X-ray feature present would have been smoothed into a roughly Gaussian shape (c.f. NP0532) then 80% of its length must represent nearly the power content of the pulse.

The search at the second pulse width was conducted in a similar way, summing individual bins into groups of three. By advancing the first bin of the count by one each time both data scans were made to produce three independent 43 ms-bin distributions.

The ten distributions are shown in tables 6(1) - 6(4).

The distributions were examined for evidence of a feature at or above the 3σ (standard deviation) level of the background count. No such deviation was found.

A decision had to be made as to which pulse width was to be used in setting the upper limit.

The most consistent quantities relevant to pulsars are their periods and total pulse widths. With the reasonable assumption that the pulse shape becomes roughly Gaussian at X-ray energies, we can say that $>$ 90% of the pulsed power must lie in one of the 43 ms bins. To make a similar statement for a 22 ms bin would necessitate making a much more detailed assumption regarding the pulse shape. It was decided to establish the upper flux limit from the 43 ms bin scan.

6.5 An Upper Limit to the Pulsed X-ray Flux from CP0328

Using Poissonian statistics, the standard deviation, σ, of a unit time sample of a random counting rate is simply the square root of the mean counting rate. A deviation from the mean by 2σ has a $4\frac{1}{2}$% probability of occurrence and 3σ a 0.3% probability. Since we have $\sim$ 100 samples,

Bin number Accumulated Counts	1 2524	2 3502	3 3449	4 3435	5 3316	6 3486	7 3357	8 3331	9 3483
	10 3405	11 3441	12 3363	13 3391	14 3424	15 3478	16 3430	17 3545	18 3343
	19 3414	20 3329	21 3389	22 3423	23 3410	24 3371	25 4326		

Bin number Accumulated Counts	1 3425	2 3489	3 3425	4 3396	5 3424	6 3385	7 3384	8 3387	9 3454
	10 3347	11 3489	12 3391	13 3417	14 3390	15 3471	16 3473	17 3391	18 3449
	19 3362	20 3351	21 3369	22 3482	23 3409	24 3373	25 3432		

TABLE 6(1): Two distributions of 25 bins each 28 ms wide from first scan.

Bin number Accumulated Counts	1 2529	2 3476	3 3422	4 3456	5 3508	6 3342	7 3361	8 3465	9 3442
	10 3375	11 3360	12 3368	13 3433	14 3367	15 3455	16 3361	17 3365	18 3443
	19 3313	20 3477	21 3418	22 3509	23 3441	24 3383	25 4294		

Bin number Accumulated Counts	1 3418	2 3423	3 3385	4 3501	5 3498	6 3389	7 3449	8 3331	9 3504
	10 3415	11 3318	12 3331	13 3465	14 3376	15 3403	16 3424	17 3300	18 3458
	19 3364	20 3396	21 3460	22 3433	23 3549	24 3358	25 3415		

TABLE 6(2): Two distributions of 25 bins each 28 ms wide from second scan.

Bin number	1	2	3	4	5	6	7	8
Accumulated Counts	4271	5156	5228	5097	5098	5023	5130	5050
	9	10	11	12	13	14	15	16
	5234	5018	5016	5145	5099	5141	5284	5049

Bin number	1	2	3	4	5	6	7	8
Accumulated Counts	5157	5152	5234	5001	5168	5050	5082	5091
	9	10	11	12	13	14	15	16
	5177	5060	5043	5129	5126	5153	5215	5102

Bin number	1	2	3	4	5	6	7	8
Accumulated Counts	5127	5227	5209	5025	5047	5136	5102	5066
	9	10	11	12	13	14	15	16
	5184	4993	5121	5047	5175	5207	5133	5985

TABLE 6(3): Three distributions of 16 bins each ∿ 43 ms wide, from the first scan.

Bin Number	1	2	3	4	5	6	7	8
Accumulated Counts	4261	5254	5096	5141	5052	5119	5069	5140
	9	10	11	12	13	14	15	16
	5157	5136	5198	5120	5082	5050	5152	5052

Bin Number	1	2	3	4	5	6	7	8
Accumulated Counts	5190	5149	5051	5154	5020	5205	5124	5103
	9	10	11	12	13	14	15	16
	5075	5203	5250	5063	5023	5059	5163	5101

Bin Number	1	2	3	4	5	6	7	8
Accumulated Counts	5226	5160	5085	5074	5082	5137	5153	5042
	9	10	11	12	13	14	15	16
	5156	5176	5159	5143	5019	5122	5138	5969

TABLE 6(4): Three distributions of 16 bins each ∿ 43 ms wide, from the second scan.

several 2σ deviations are expected but a 3σ variation, though not of very low probability, would merit further investigation. The mean counting rate was 5121 counts per 43 ms bin, with $\sigma = 71$ counts. The highest count rate is 5284, representing a 2.3σ deviation, which could not be considered significant.

For a source to have been distinguished in one channel it would have been required to contribute $\sim$ 214 counts (or 3σ) to that channel. Since this was not seen, then 3σ can be taken as an upper limit to the possible flux from the source received from the detector.

To convert the number of counts in the total viewing time to counts cm^{-2} per pulse, a multiplying factor $\frac{P}{(At)}$ is needed, where

$(At) = \int A(t)\,dt$, evaluated from figure 5(8) to be $1.65 \pm 0.14 \times 10^{5}$ cm^{2} sec

P = pulsar period = 0.715 secs.

Thus the upper limit to flux is $9.3 \pm 0.8 \times 10^{-4}$ photons cm^{-2} $period^{-1}$ as measured at the detector.

Corrections to the Upper Limit

Four corrections must be considered in evaluating the obtained upper limit. These are:

1. a correction for atmospheric absorption,
2. a correction to compensate for detector inefficiency,
3. a correction for "iodine-escape" effects (discussed in Chapter 3),
4. a correction for transmission and punch unit dead time effects.

Corrections 1, 2 and 3 are energy dependent. This creates a difficulty when working in a single, wide-energy channel of 30-120 keV with no knowledge of the source spectrum.

If the differential energy spectrum incident at the top of the atmosphere were known to be of the form $I(E)$ and the effects of 1, 2 and 3 could be represented by $f_1(E)$, $f_2(E)$, $f_3(E)$ then the observed flux resulting from the modified spectrum, $I'(E)$, would be given by,

$$\text{Flux} = \int_{28}^{114} I'(E)dE = \int_{28}^{114} I(E)f_1(E)f_2(E)f_3(E)dE$$

$f_1(E) = \exp(-\mu_{air}(E)t)$ (see Chapter 3)

$f_2(E) = 1 - \exp(-\mu_{NaI}(E)t)$ (see Appendix A)

$f_3(E)$ can be evaluated from Stein and Lewin (1966).

Since only the Crab produces a measurable pulsed X-ray energy spectrum (exponent $\sim E^{-0.9}$) it has come to be a standard in work of this kind. The result obtained in this chapter will subsequently be compared to the Crab and it does not seem unreasonable to assume a similar spectrum in estimating the corrections. This same spectrum is used in converting the photon upper limit into an energy upper limit.

When the first two corrections are applied to the spectrum it can be shown that 41% of the energy incident at the top of the atmosphere would ultimately be detected. The figure drops to 40% if a flat energy spectrum is assumed.

Application of the "iodine escape" correction reduces the detection efficiency to 36% but, as was discussed in chapter 4, dead time effects are negligible in reducing it further.

The resulting upper limits are then:

$2.58 \pm 0.23 \times 10^{-3}$ photons cm^{-2} $pulse^{-1}$

or $1.49 \pm 0.13 \times 10^{-1}$ keV cm^{-2} $pulse^{-1}$

or $2.39 \pm 0.22 \times 10^{-17}$ Joules cm^{-2} $pulse^{-1}$

or $2.39 \pm 0.22 \times 10^{-13}$ Joules m^{-2} $pulse^{-1}$.

Finally, this figure can be expressed as a function of frequency. The frequency interval from 28 - 114 keV is 2.10×10^{19} Hz. Then the upper limit to the pulsed X-ray flux from CP0328 in the range 28 to 114 keV is

$$11.3 \pm 0.95 \times 10^{-33} \text{ Joules } m^{-2} \text{ pulse}^{-1} \text{ Hz}^{-1}$$

6.6 Discussion of Result

This upper limit is converted to a time-averaged spectral power by dividing by the period. The value obtained is

$$1.6 \times 10^{-32} \text{ W m}^{-2} \text{ Hz}^{-1}$$

and is shown plotted in figure 6(3) as a function of frequency. Also shown is the upper limit at optical frequencies which is calculated from the result of Cocke and Disney (1970) who ascribe an apparent visual magnitude upper limit V = 25.5 to the pulsed emission from CP0328. The optical magnitude is converted to spectral emission using the results of a similar calculation by Gruber et.al. (1970) for CP1919. A 4000 Å band width was assumed for the optical emission.

The radio spectra of CP0328 and CP1919 are also included in figure 6(3) together with the radio, optical and X-ray spectra of NP0532 which are taken from Hewish (1970).

Whilst the time averaged spectral power gives a measure of the energy received from the pulsar, an idea of the energy radiated by the pulsar is given by the average power during the pulse. The radio pulse width for CP0328 is taken to be 40 ms. Comparing the result obtained with CP1919 and NP0532 gives the mean pulsed X-ray emission during the pulse is

for NP0532 = 1.3×10^{-30} W. m^{-2} Hz^{-1} (30 - 120 keV)

for CP0328 < 2.9×10^{-31} W. m^{-2} Hz^{-1} (28 - 114 keV)

for CP1919 < 1.0×10^{-31} W. m^{-2} Hz^{-1} (30 - 100 keV)

(Gruber et.al., 1970).

The value for NP0532 is calculated using the spectrum 0.8 $E^{-0.9}$ keV cm^{-2} s^{-1} keV^{-1} obtained from Hillier (1970).

The distance to the Crab Nebula is generally thought to be $\sim$ 1.3Kpc, although Trimble (1968) suggests that it could be as distant as 2.2 Kpc. The distance from the earth to CP0328 is reported by Davies (1969) to

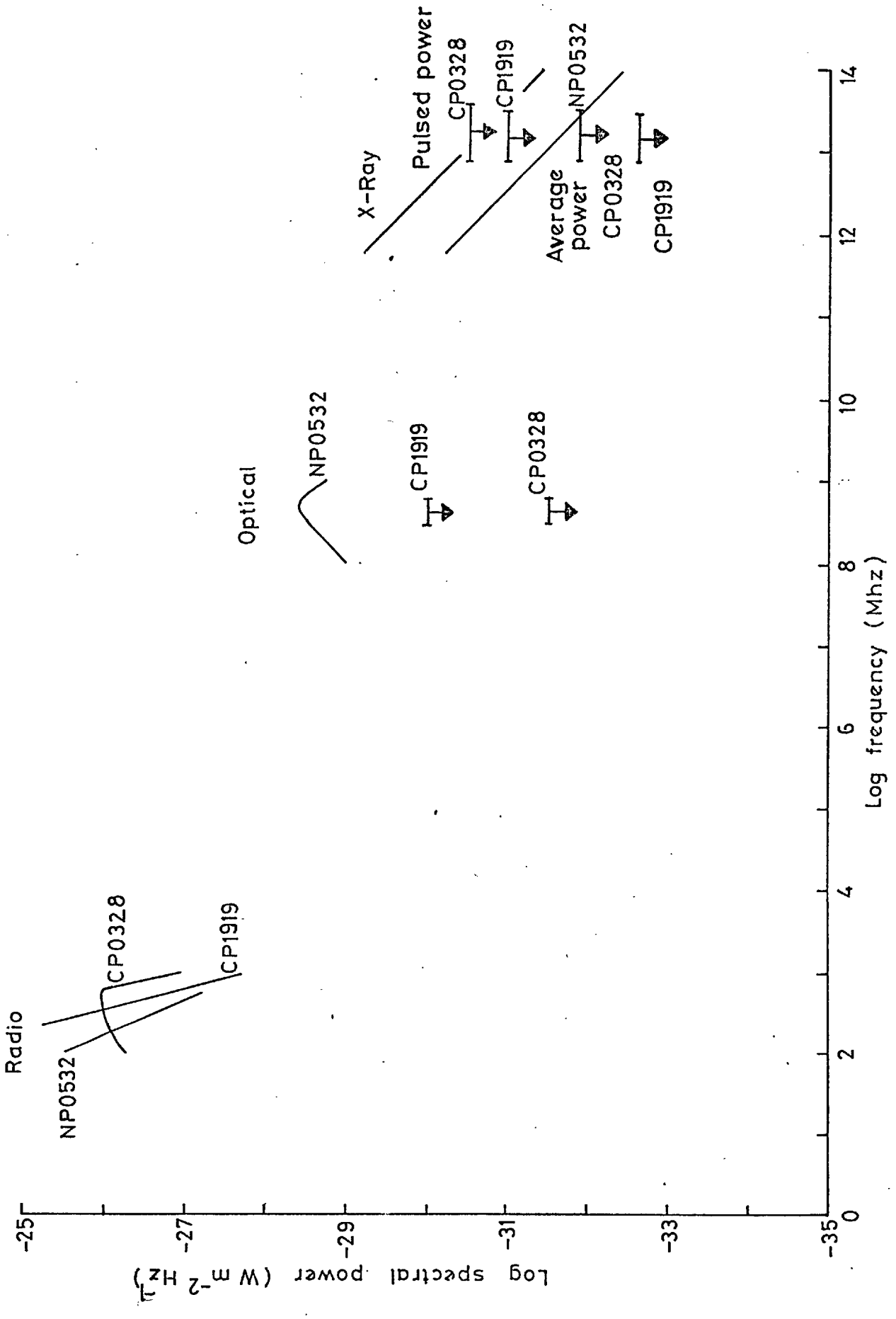

Figure 6(3): The spectral power for the pulsed emission from CP0328, CP1919 and NP0532 as a function of frequency. Only upper limits exist for CP0328 and CP1919 at other than radio wavelengths.

be 700 pc. The ratio of these distances is approximately equal to the ratio of the dispersion measures for radiation from the pulsars (i.e. 0.47) and is indicative of the validity of the estimates.

As was discussed in Chapter 2, it is probable that pulsars radiate into a cone. The intensity distribution of radiation within the cone varies in a fashion peculiar to each pulsar and can be known, at the earth, only in one line across the conic section. In view of our insufficient knowledge, it is necessary, in order to make comparisons, to assume that the average intensity in a pulsar's pulse profile, as seen from the earth, is equal to the average of any other profile for that pulsar and, hence, is representative of the average intensity throughout the whole pulse. If effects of interstellar dispersion are discounted, the decay of pulse intensity can be thought to be due only to increasing distance and hence the intensity will decrease as the inverse square of that distance. Some measure of the pulsar's intrinsic brightness relative to that of NP0532 is given by

$$\frac{\text{Measured brightness of the pulsar}}{\text{Measured brightness of NP0532}} \times \left(\frac{\text{Distance of pulsar}}{\text{Distance of NP0532}}\right)^2$$

Obtained in this way, the upper limit to the relative brightness of the pulse of CP0328 in the range 30 - 120 keV is 8×10^{-2}.

Because of the relatively long period of CP0328 and its large distance, this upper limit is not as low, relative to NP0532, as some limits placed on other nearer and faster pulsars (e.g. Gruber et.al., 1970). Since all experiments to observe X-rays from pulsars (except NP0532) have produced negative results it is more pertinent to place the result obtained here in context with values for other pulsars and to discuss the results as a whole. Also since the pulsed optical and X-radiation are believed to have a common origin it is not unreasonable to include optical results in the discussion.

In comparing to one observation of an object, results consisting only of upper limits to the observation of other objects in the same class, the problem arises of what degree of similarity can be assumed between the different objects in order to estimate the significance of the results. Too great a similarity causes unreasonably complicated models whilst too little similarity inhibits classification and hence negates comparison. It is policy to assume a high degree of similarity at the outset which can be relaxed as models become unwieldy.

It is believed that pulsars are the products of one class of star undergoing supernova explosions (e.g. Gold, 1969). The parent stars then have many similar properties e.g. mass, spin and magnetic field. The similarity in these properties is likely to be carried through the supernova explosion to reappear in the pulsars. It is not unreasonable to assume that all pulsars are intrinsically similar objects that differ only in their particular evolutionary states.

It is generally accepted that in an oblique rotator pulsar model such as that of Goldreich and Julian, 1969, the predicted total electromagnetic luminosity varies as the fourth power of the frequency. Bahcall et.al. (1970) suggest that the optical and X-ray fractions scale in the same way. If this is so and a comparison is made with NP0532 then

$$K_1 = \left(\begin{array}{c}\text{Absolute intensity of a pulsar} \\ \text{relative to NP0532}\end{array}\right) \times \left(\frac{\text{Period of pulsar}}{\text{Period of NP0532}}\right)^4 = 1$$

Thus, if upper limits can be found that show $K_1 < 1$ then this hypothesis will be brought into certain doubt.

Although no X-ray results, sufficiently sensitive to test this hypothesis, have been produced, some suitable optical results are available. CP0950 is a pulsar that is very close to the earth ($\sim$40 pc; Davies, 1969)

and also has a short period, 253 ms. It was observed by Cocke and Disney (1970) to have an absolute visual magnitude of 21.5 which implies an absolute intensity relative to NP0532 of 1.6×10^{-6}. Then $K_1 = 0.0056$, a result which seriously conflicts with the initial suggestion of a fourth power law.

It is interesting to assume that the radiative luminosity does scale in a way proportional to the $(\text{period})^{-n}$ and then to investigate the minimum value that can be ascribed to n. Assuming a direct comparison can be made with NP0532, then

$$\left(\begin{array}{c}\text{Absolute intensity of a pulsar} \\ \text{relative to NP0532}\end{array}\right) \propto \left(\frac{\text{Period of pulsar}}{\text{Period of NP0532}}\right)^{-n}$$

The results of Kristian (1970) show that $n > 8.4$ for PSR0833. This is a value far in excess of any scaling factor suggested in pulsar models.

It has also been suggested (e.g. Gold, 1969) that the total radiative energy is derived from the loss of rotational energy during the pulsar slowdown. According to the earlier assumption, all pulsars are intrinsically similar, in particular they have the same radius and hence the same moment of inertia. Then for a pulsar period P it is easy to show that the rate of loss of energy

$$\frac{dE}{dt} \propto \frac{dP}{dt} \cdot \frac{1}{P^3}$$

Again assuming that a direct comparison can be made with NP0532, then

$$K_2 = \left(\begin{array}{c}\text{Absolute intensity of the pulsar} \\ \text{relative to NP0532}\end{array}\right) \cdot \left(\frac{dP}{dt} \times \frac{1}{P^3}\right)_{\text{Crab}} \cdot \left(\frac{dP}{dt} \times \frac{1}{P^3}\right)^{-1}_{\text{Pulsar}} = 1$$

Using the values for $^{dP}/dt$ given by Hunt (1969), it can be shown that for PSR0833, $K_2 < 0.04$.

If the comparison with the Crab pulsar is to be maintained, then these examples show that either the amount of optical and X-radiation must decrease extremely rapidly with increasing period or there must be a complete cut-off at these wavelengths in older pulsars. In either case, if the radiation is assumed to be produced near the stellar surface then the magnetic field there must decay extremely rapidly in the early stages after the pulsar's production, since even such a young pulsar as PSR0833 is seen not to produce optical or X-ray emission. That strong, coherent radio emission is seen from old pulsars indicates that the decay cannot continue at the same rate. It is difficult to propose a mechanism whereby a magnetic field would decay in such a fashion.

Since pulses are seen to arrive simultaneously at radio, optical and X-ray wavelengths they must have been produced in the same region of the star. It has been shown above, however, that it is difficult to reconcile a theory which predicts production of X-rays near the surface of the star with observations. Hence all theories which are based on radio emission from near the stellar surface must also be brought into doubt.

If the radiation is assumed to come from a region near the velocity of light cylinder, the same difficulties do not arise. As a pulsar slows down the velocity of light cylinder increases in radius and the field at this distance automatically decreases rapidly, while the surface field can still decay only slowly. Particles radiating at this distance, as in the model of Paccini and Rees (1969), will no longer be able to produce high energy synchrotron radiation in the weakened field and will radiate mainly in the radio band. Optical and X-ray results clearly favour models of this kind. As was discussed in Chapter 2, however, it is difficult to establish a convincing configuration for such a model.

Since neither model seems very satisfactory, the initial assumption that all pulsars are intrinsically similar must be reconsidered. For example if NP0532 were created from a parent star that had an unusually strong magnetic field associated with it then, on contraction, the resulting pulsar field would be correspondingly strong. A situation can be imagined where the optical andX-ray production is an exceptional feature for NP0532, or at least an exceptionally strong feature, resulting from the exceptional field. This being true, the relative amounts of X-ray emission from other pulsars would be expected to be low and it is possible to revert once again to the more satisfactory "near surface" model. It is to be expected that eventually some optical and X-ray emission will be found from other pulsars.

The line of argument outlined here is not unreasonable statistically since there are few very young pulsars, i.e. with periods $\lesssim$ 250 ms, and NP0532 could easily be exceptional amongst them. Magnetic field decay at the stellar surface could still explain the lack of hard radiations from older pulsars and their eventual "turn-off" at periods $\sim$ 2 secs.

In order to test this suggestion it is necessary to locate more very young pulsars and investigate their levels of optical and X-ray emission. This may be possible for pulsars created in supernova explosions in other galaxies (Bahcall et.al., 1970). Even lower limits to the hard radiations from all pulsars are also needed, as are polarisation measurements for the X-ray emission from NP0532 to confirm its common origin with the optical emission.

APPENDIX A

Derivation of the Photon Conversion efficiency of the detector

The scintillator used for the detection of X-rays was a disc of sodium iodide, diameter 7.5 cm and thickness 0.2 cm. It was coated with a white, diffuse reflector such that light produced within it might only find exit via the front face..

Photon Production within the Scintillator

As mentioned in the text, the fraction f of X-radiation incident upon a material, that is absorbed in a thickness t to produce ionising particles is

$$f = 1 - \exp(-\mu t)$$

Consider a photon at the highest energy we wish to observe, i.e. 120 keV. The value of μ at this energy is 3.65 cm^{-1} and in 0.2 cm of sodium iodide 50% of the incident photon energy will be absorbed. Clearly this percentage increases for lower energies.

Since the conversion efficiency of sodium iodide is $\sim$ 8.4%, the amount of absorbed energy converted into visible light of wavelength 4100 Å is 5 keV.

The energy of a 4100 Å photon is 3 eV, which means that 1,700 such photons are produced by the passage of a 120 keV X-ray through 0.2 cm of sodium iodide.

Transit to the Photocathode

There are two main factors which affect the amount of light reaching the photocathode. These are the transparency of the sodium iodide to its own radiation, which can be considered 100% for the small thickness of our crystal, and a geometrical factor. The scintillator light is emitted

isotropically, producing a sphere of radiation. Which regions of this sphere eventually gain access to the photocathode is decided by the critical angle, α, between the sodium iodide and the photomultiplier.

Consider only the light that strikes the front and back faces of the crystal and assume the paint to be a plane reflector. The light will ultimately be transmitted through the front face only if it lies within a cone generated by the line passing through the point of propagation and lying at the critical angle α to the normal at the two faces. This is true, for a plane reflector, irrespective of the number of reflections it undergoes. See Figure A(1).

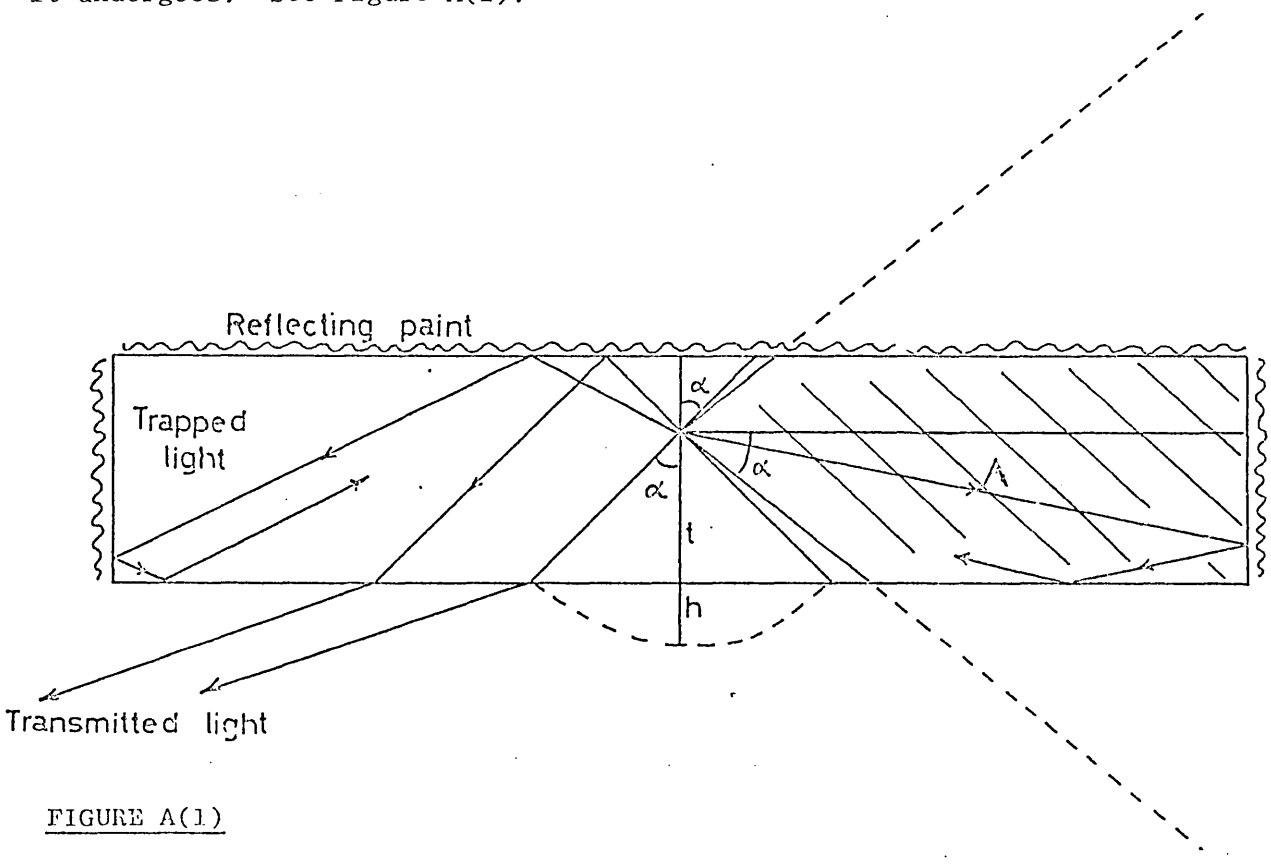

FIGURE A(1)

The spherical surface S enclosing one half of this cone of height t-h and radius r = t ... is

$$S = 2\pi t h - 2\pi r(r - r\cos\alpha)$$

and the conical solid angle $S/r^2 = 2\pi(1 - \cos\alpha)$. The total angle of escape is $4\pi(1 - \cos\alpha)$.

Now consider light impinging the sides of the crystal. As with the preceding argument we can consider a cone, half angle α generated about a normal to the sides from O. In this case, however, light propagated from within the cone will never be admitted to the photomultiplier. Because the crystal sides are small compared to the diameter, this cone is likely to enclose the whole side face, e.g. region A, fig. A(1) and, hence, all the light generated in these directions will be permanently trapped.

If we consider this always to be exactly true then the fraction of light admitted to the photomultiplier is

$$\frac{4\pi(1 - \cos\alpha)}{4\pi} = (1 - \cos\alpha)$$

(The above argument is, of course, dependent on the position of O, but will be valid in the majority of cases.)

In our case $\alpha = 60^{o}$

$$\cos\alpha = 0.5$$

and approximately 50% of the emitted light, $\sim$850 photons, will be transmitted to the photocathode.

In the experiment the paint used was a diffuse reflector and the fraction of light eventually being admitted to the photomultiplier was correspondingly increased. There is a limit, however, to the number of reflections that can occur before absorption becomes important.

Conversion into Photoelectrons

The quantum efficiency of an E.M.I. 9531 R photomultiplier for 4100 Å radiation is 24%. The number of photoelectrons produced by the arrival of 850 visible photons at the photocathode is 204.

Or, since we began with a 120 keV X-ray, we can say that a minimum of 1.7 photoelectrons are produced per keV of incident photon energy.

for X-rays in the range 30 - 120 keV.

APPENDIX B

Estimate of the background counting rate for the detector at 4 gm cm^{-2} altitude.

Seven possible contributions to the background flux are listed below with estimates of the relative magnitudes of their effects.

B1. Diffuse primary and atmospheric secondary background

The primary background can be calculated from the number spectrum given by Bleeker et.al. (1968)

$$\frac{dN}{dE} = 135\ E^{-2.4\pm0.2}\ cm^{-2}\ sec^{-1}\ sr^{-1}\ keV^{-1}$$

which, when corrected to 4 gm cm^{-2} yields a flux of 3 photons/sec. for the detector geometry.

It is also evident from Bleeker et.al. (1968) that the contribution from the atmospheric component $\lesssim$ the primary contribution at this depth. Thus, the total flux is $\sim$ 6 photons per sec.

B2. Low energy particles coming to rest in the crystal and in doing so depositing 30 - 120 keV there.

The sodium iodide was covered with a thin (0.02 mm) aluminium sheet which electrons $<$ 60 keV could not penetrate.

Sood (1969) using a $\frac{1}{8}$ inch plastic scintillator disc with an energy threshold of $\sim$ 70 keV measured the counting rate of charged particles at 4 gm cm^{-2} to be 0.07 $cm^{-2} sec^{-1} sr^{-1}$ at equatorial latitudes. If 10% of the particles are assumed to lie within the range 70 - 200 keV then the number of these striking the crystal is $\sim$ 0.04 sec^{-1}.

The geomagnetic cut-off at the equator is much lower than at 55°N. Since low energy particles rely on the interaction of high energy primaries for their production, the number of such particles is likely to be increased at these latitudes by a factor > 10 but certainly < 100 (R.K. Sood, private communication). A count rate of $\lesssim 2$ per sec does not seem unreasonable for this process.

B3. Bremsstrahlung produced by charged particles incident on the collimator

Only electrons will produce copious bremsstrahlung in the collimator. Beedle and Webber (1968) report the fluxes of electrons measured at various atmospheric depths at Ft. Churchill (lat. 58°N). From the measured values and reasonable extrapolations therefrom it is possible to estimate the flux of electrons in the range 1 - 250 MeV at 4 gm cm^{-2}.

The problem of calculating accurately the bremsstrahlung production of a wide energy range, isotropic electron beam incident on a system of different, thick absorbers is a very complicated one. We need only a rough estimate however and we make the following, simplifying assumptions.

(i) The electron range is divided into smaller, elemental ranges such that the mean energy describes the whole range.

(ii) We are dealing with high energy particles and it is assumed that the bremsstrahlung are emitted only in the electron's forward direction. Below 1 MeV electrons will not penetrate 1 mm of lead.

(iii) The electron has the same production characteristic along its total path length, i.e. it loses no appreciable amount of energy in traversing the collimator.

Then, if the production intensity per unit length for photons of energy E is $\mathcal{J}(E)$ and the linear absorption coefficient is $\lambda(E)$, then in traversing a thickness 1 the observed photon intensity is

$$I = \frac{\mathcal{I}}{\lambda}(1 - e^{-\lambda l})$$

(iv) The electrons are deflected many times in traversing the metal and the path lengths can be increased by a factor 1.5 - 4.0, depending on their energy (Evans, 1955). Assume the path length to be doubled. The electrons strike the collimator isotropically and for simplicity assume the mean free path length in the material to be $l\sqrt{2}$. Then applying the scattering factor the mean distance travelled is $2\sqrt{21}$.

(v) The incident beam of electrons is isotropic and it is safe to assume that it remains so within the collimator material. Then, according to assumption (ii) the emergent electron beam and X-ray beam will also be isotropic.

(vi) Most of the photons produced will be from the high energy end of the range because of absorption. If two photons from the same event are incident upon the NaI crystal it is likely that their sum will appear as a photon of >120 keV. Discrimination will also occur if the electron impinges the crystal.

(vii) The total radiative cross-section, σ_{rad}, for 1 cm of material, number density N, atomic number Z, for the production of a photon of energy $h\nu$ to $(h\nu + d\nu)$ by an incident electron of energy $(T + m_o c^2)$ is given as follows (Evans, 1955):

a) $m_o c^2 << T << 137\, m_o c^2\, Z^{-1/3}$ (relativistic case)

$$\sigma_{rad} = 4\left[\ln\left(\frac{2(T + m_o c^2)}{m_o c^2}\right) - \frac{1}{3}\right]\sigma_o Z^2 \quad cm^2/\text{nucleus}$$

where $\sigma = \frac{1}{137}\left(\frac{c^2}{m_o c^2}\right) = 0.58$ millibarns/nucleus $= 0.58 \times 10^{-27}$ cm^2/nucleus.

b) $T >> 137\, m_o c^2\, Z^{-1/3}$ (ultra relativistic case)

$$\sigma_{rad} = 4\left[\ln (183\, Z^{-1/3}) + 1/18\right] \sigma_o Z^2$$

The amount of energy radiated per unit path length is

$$\left(\frac{dT}{ds}\right) = N(T + m_o c^2)\, \sigma_{rad} \text{ ergs cm}^{-1}.$$

(viii) The energy intensity emitted per frequency interval is independent of the frequency and cuts off sharply at $h\nu_{max} = T$. Hence the number of photons emitted per unit length in the range $h\nu_1$ to $h\nu_2$ if the mean photon energy is ν is

$$n = \left(\frac{dT}{ds}\right) \frac{(\nu_2 - \nu_1)}{T\ \bar{\nu}}$$

and from (iii)

$$I = N(T + m_o c^2)\, 4\left[\ln\left(\frac{2(T + m_o c^2)}{m_o c^2}\right) - \frac{1}{3}\right]\sigma_o Z^2 \frac{(\nu_2 - \nu_1)}{T\ \bar{\nu}} \frac{(1 - e^{-\lambda l})}{\lambda}$$

photons per electron

in the relativistic case.

Evaluating this for 1 mm thick lead where $h\nu_1 = 30$ keV, $h\nu_2 = 120$ keV, $\bar{\nu} = 60$ keV yields $I = 0.4$ photons per 1.5 MeV electron.

(ix) Assume that if an electron produces a photon of energy > 30 keV that impinges the NaI, it produces only one such photon.

(x) Only photons of energy $\gtrsim$ 70 keV produced in the lead will penetrate the tin whereas the whole range 30 - 120 keV must be considered for production in the tin.

(xi) Since the photons are produced isotropically a simple geometric factor will decide the probability of their subsequent arrival at the NaI depending on the electron's position of incidence.

Performing a calculation on the lines of this argument it appears that between 2-3 photons sec^{-1} should be incident at the crystal due to bremsstrahlung.

B4. Compton scattering of high energy photons in the collimator material

Using the number spectrum from B1 it can be shown that more than 10^3 photons of energy >120 keV strike the collimator per second. These could be Compton scattered into the energy range of the detector and, if they emerge from the collimator in the right direction, impinge the crystal.

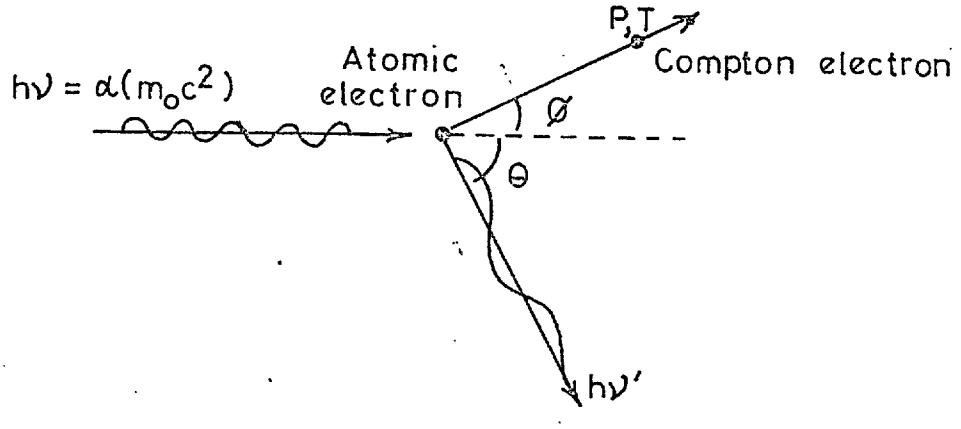

It is given (Evans, 1955) that the differential cross section $d({}_e\sigma)$ per electron energy interval dT is

$$\frac{d({}_e\sigma)}{dT} = \frac{d({}_e\sigma)}{d\Omega} \frac{2\pi}{\alpha^2 m_o c^2} \left[\frac{(1+\alpha)^2 - \alpha^2 \cos^2\phi}{(1+\alpha)^2 - \alpha(2+\alpha)\cos^2\phi} \right]^2$$

where $$\frac{d({}_e\sigma)}{d\Omega} = \frac{r_o^2}{2} \left(\frac{\nu'}{\nu_o}\right) \left(\frac{\nu_o}{\nu'} + \frac{\nu'}{\nu_o} - \sin^2\theta\right)$$

r_o is the classical radius of the electron = 2.8×10^{-13} cm.

This can easily be converted to the number-energy spectrum for scattered photons using $h\nu' = h\nu_o - T$.

By using the above formulae in conjunction with a set of simplifying assumptions comparable to those in section 3, it is possible to show that the contribution of X-rays from the Compton process is $\lesssim$ 3 photons per sec.

B5 X-rays resulting from cosmic ray induced radioactivity in the collimator and NaI crystal

During both its ascent and its flight at altitude the payload is irradiated by cosmic ray protons and neutrons. The formation of compound nuclei could result, the subsequent decay of which might release X-rays, γ-rays and charged particles.

The cross-section, σ, for the formation of a compound nucleus is < 1 barn for protons of energy 25 MeV in Cu, Sn and Pb. The number of nuclei per cm^3 is $\sim 3 \times 10^{22}$ and hence the total interaction areas for the collimator materials are: Pb = 3×10^{-3}, Sn = 6×10^{-3}, Cu = 1.5×10^{-3}. If the number of protons of this energy incident upon the collimator is ~ 1 per cm^2 then the total number of compound nuclei formed is ~ 100 per sec. A similar calculation for low energy neutrons yields $\sim$ 500 compound nuclei per second formed.

We must look for interactions oi an element E of the type

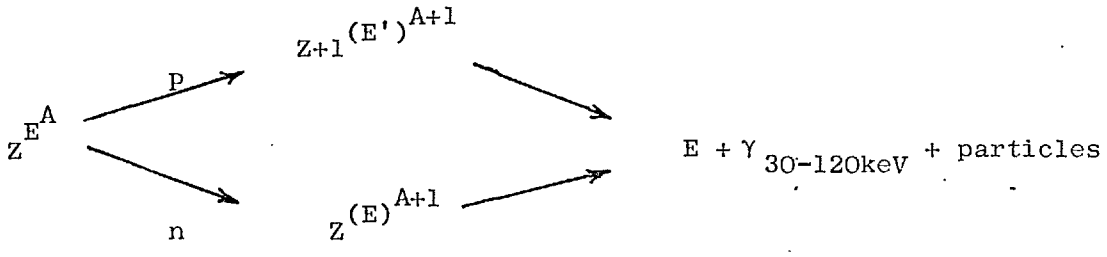

Tables of isotopes, decay schemes and products are given in Hollander et.al. (1953).

To penetrate the tin shielding and be counted any X-rays produced in the lead must lie in the range 70 - 120 keV. No such disintegrations exist for Pb or Bi isotopes.
Tin has a disintegration

$$_{50}Sn^{119} \rightarrow {}_{50}Sn^{118} + n + \gamma = 65 \text{ keV}$$

but the half life for the reaction is 250 days which is too long to be of interest.

Another decay scheme is

$$_{50}Sn^{121} + p^{+} \rightarrow {}_{51}Sn^{122} \rightarrow {}_{50}Sn^{121} + n + \gamma = 59,\ 68,\ 74 \text{ keV}$$

The relative abundance of $_{50}Sn^{121}$ is very small however and the process is not important.

The total interaction area for 0.05 cm Cu is negligibly small. It is clear that very few X-rays of energy between 30 - 120 keV are produced directly as a result of the decay of compound nuclei.

We have seen thatapproximately 600 compound nuclei are formed every second. If we assume that the same number also decay and each decay produces one photon and one electron then the numbers of photons and electrons produced in this way would be $\lesssim$ half the respective numbers considered in the production of Compton photons and bremsstrahlung (sections B3 and B4). Comparing theresults obtained in those sections

it is difficult to imagine how irradiation of the collimator could be responsible for more than 1 or 2 detected photons per second.

Peterson (1965) discovered a contribution to his X-ray counting rate at altitude from the decay of I_{128}, subsequent to its formation by irradiation of I_{127} by atmospheric neutrons. By making a suitable comparison between his experiment and the present one it is possible to demonstrate that the contribution expected from I_{128} decay is $\lesssim 0.5$ per sec.

B6 Fluorescence X-rays from Pb and Sn

There could be a large flux of these K-edge X-rays but the collimator design (Chapter 3) is such as to reduce their effects to virtually zero.

B7 Particles scintillating in the glass face

For particles to scintillate in the glass but not in the scintillator they must either pass nearly horizontally through the glass or, moving upwards, be brought to rest in the glass. The probability of either of these processes is negligible.

The sum of these contributions predicts a counting rate $\sim$ 16 per sec but in view of the enormous simplifications made, the rate could reasonably lie anywhere between 10 and 20 counts sec^{-1}.

PART II

INVESTIGATION OF THE ACCESS OF SOLAR FLARE PROTONS TO LOW ALTITUDES OVER THE POLAR CAPS.

".....The old order changeth, yielding place to new,
Lest one good 'parameter' should corrupt the world....."

Morte d'Arthur
Alfred Lord Tennyson.

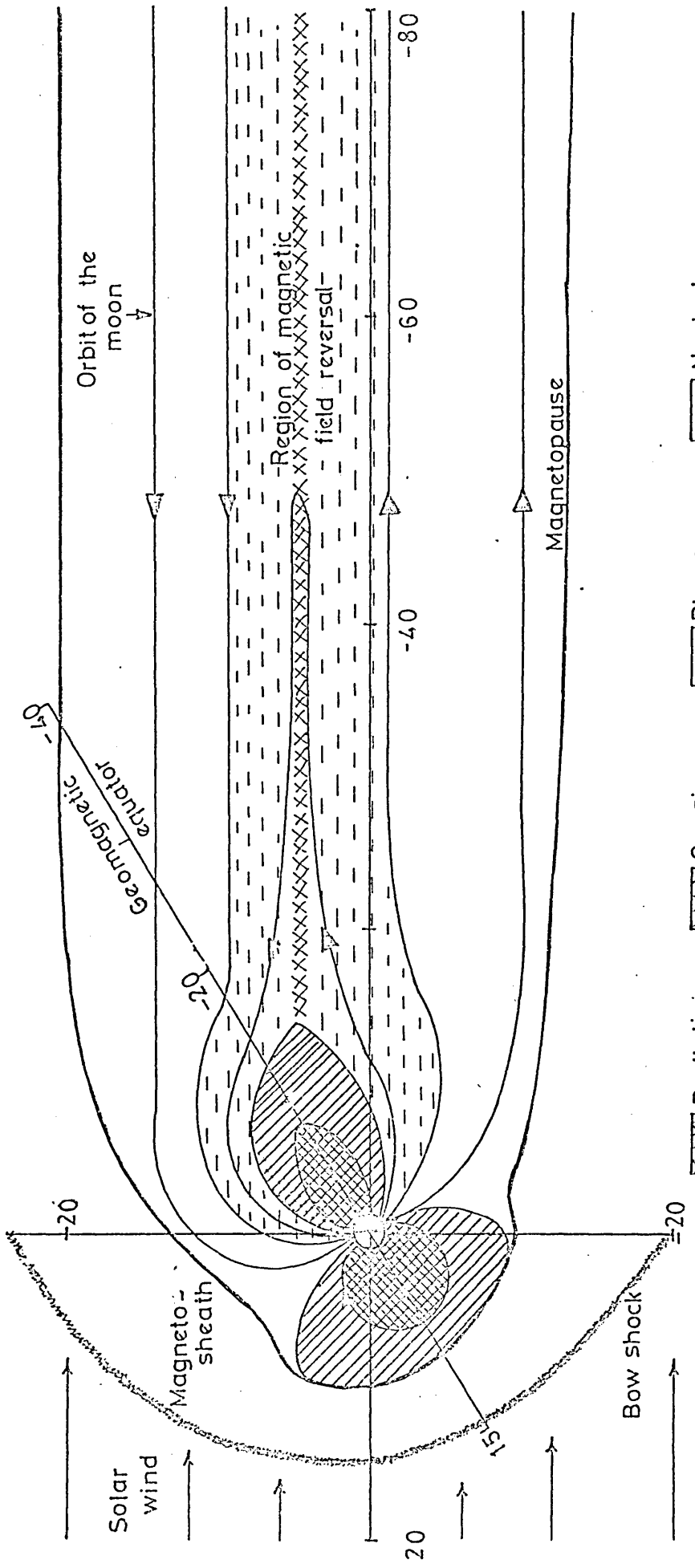

Figure 7(1). The configuration of the magnetosphere and geomagnetic tail as deduced from spacecraft measurements and reported by Ness (1969).

CHAPTER 7 - THE GEOMAGNETIC FIELD AND PARTICLE MOTIONS

The shape and formation of the magnetosphere resulting from the interaction of the solar wind with the terrestrial dipole are reviewed and the use of solar flare protons as probes for the investigation of the distant magnetotail is suggested. The inadequacy of existing magnetosphere parameters in the description of the pattern of arrival of energetic solar protons over the polar caps and auroral zones is demonstrated and a suitable alternative is suggested and developed.

7.1. Introduction to the Magnetosphere

7.1.1. The Solar Wind

Because of its high surface temperature the sun is the source of an electrically neutral plasma which is streaming radially outward at a speed typically $\sim$ 350 - 450 km.sec^{-1} at the orbit of the earth, although this speed can increase to 850 km.sec^{-1} at times. This phenomenon is the solar wind and its main constituents are protons and electrons which have average spatial densities of $\sim$ 5 cm^{-3} at the earth orbit (Negebauer, 1960). The particle density can, however, vary between 1 and 80 cm^{-3}. α-Particles are present in the solar wind in numbers that average $\sim$ 5% of the proton content. The proton temperature in the wind usually lies between 10^4 - 10^5 ^oK.

The sun is also the origin of an interplanetary magnetic field which was first detected experimentally more than ten years ago, e.g. Coleman et.al., 1960. Because it has an energy density which is much

less than the solar wind kinetic energy density ($\sim$1%), the field is 'frozen into' and carried radially outward by the solar wind. The rotation of the sun then causes the field lines to form an Archimedian spiral, much as predicted by Parker (1958). The interplanetary magnetic field strength near the earth averages at $\sim$5 γ and its mean direction points either towards or away from the sun, this direction being determined by the 'solar magnetic sector' in which the earth is lying. There are normally 2 or 4 solar magnetic sectors which, since the solar rotation period is $\sim$ 28 days, imply a time scale of $\sim$ 14 or 7 days associated with each. The average angle at which the interplanetary field intersects the earth-sun line is $\sim 45^{\circ}$ and is known as the 'Parker spiral' angle.

The magnitude and direction of the interplanetary field are highly variable on a time scale much less than that associated with a solar magnetic sector. Abrupt changes in the magnetic field may be separated by hydromagnetic discontinuities, i.e. tangential, contact and rotational discontinuities. Although it has been established that such discontinuities do exist in the solar wind (e.g. Colburn and Sonett, 1966), their frequency and power content have not been conclusively determined. Magnetohydrodynamic shock waves are also believed to exist in the solar wind.

Of particular interest in this work will be tangential discontinuities which are characterised by their lack of a magnetic field component perpendicular to the discontinuity. They can be thought of as two adjacent flux tubes whose parallel surfaces form the discontinuity. There is no flux of plasma across the discontinuity and the total pressure is continuous across it. Hence if 1,2 refer to the two flux tubes then

$$\frac{B_1^2}{8\pi} + \sum_{\substack{\text{all} \\ \text{particles}}} n_1 kT_1 = \frac{B_2^2}{8\pi} + \sum_{\substack{\text{all} \\ \text{particles}}} n_2 kT_2$$

where B is the field strength and n, T the particle density and temperature. Observations of tangential discontinuities have been reported e.g. Burlaga (1968).

Solar flares on the sun can inject into the interplanetary medium charged particles of a much higher energy than solar wind particles. These energetic particles are collimated by the interplanetary magnetic field and usually arrive at the earth some time after the event is seen in electromagnetic radiation. The delay in particle arrival is dependent on their energy and the position of the flare on the sun; clearly the lower the particle energy, the greater will be the influence of the interplanetary magnetic field on it.

7.1.2. Formation of the Distant Magnetosphere

The magnetic field intrinsic to the earth is essentially a dipole of moment $8.06.10^{25}$ gauss cm^2. The impacting solar wind distorts the dipolar field configuration, compressing the field in the solar direction and stretching it out behind the earth into a long 'magnetotail'. Figure 7(1) is a recent summary of the time-averaged features of the resulting geomagnetic field as measured by satellite experiments.

Recent theoretical descriptions of the solar wind-magnetosphere interaction treat the solar wind as a hypersonic (velocity also >> the Alfven speed), collisionless fluid in which the magnetosphere is a blunt, stationary object. A consequence of this treatment is the prediction of a detached, magnetohydrodynamic, bow shock wave, which must also be collisionless since the mean free path (m.f.p.) associated with it is

$\sim$1 astronomical unit (A.U.), Axford (1962). Since the shock is collision-free the required "turbulence" is probably associated with a wave of some sort, possibly the fast magneto-acoustic wave (Spreiter et.al., 1966).

The magnetopause is the boundary separating the magnetic fields of solar and terrestrial origin. It is generally believed to take the form of a tangential discontinuity but Sonnerup and Cahill (1967, 1968), after investigating many magnetopause crossings made by Explorer 12, concluded that one-third of the boundaries observed by the magnetometer were more likely to be rotational than tangential discontinuities. The formation of the magnetopause by rotational discontinuities at certain times implies that at these times there exists a magnetic field component normal to the boundary: a feature that could be of considerable importance when particle entry mechanisms are discussed later. Also, the likely rotational discontinuities all seemed to be associated with high magnetic field values just inside the magnetopause, indicating an association with magnetic storms or large-scale inward motions of the boundary.

Between the bow shock and the magnetopause there exists a region, the magnetosheath, containing a plasma which is completely thermalized at the 'nose' of the magnetosphere but which becomes more streamlined and eventually supersonic as the distance from the nose increases. Threading the plasma is a magnetic field of solar origin, usually turbulent and typically of strength between that of the magnetospheric and interplanetary fields. The plasma flow in this region is highly complex but has been treated theoretically in an approximate way by Spreiter et.al. (1966).

A comprehensive survey of the positions of the magnetopause and shock wave were carried out on the satellite IMP-3, Ness et.al. (1966a). The

measurements show that, although there is considerable motion of the shock and magnetopause boundaries in response to varying solar wind conditions, the mean position and shape of each correlates well with theoretical predictions. On the sunlit side, the magnetopause was found to be roughly spherical in shape, of radius $\sim 13.5\ R_E$ (earth radii) and with its centre $\sim 3.5\ R_E$ behind the earth along the earth-sun line. The shock was roughly hyperbolic in shape (similar to the aerodynamic shock wave created by a supersonic missile) with a stand-off distance from the earth of $\sim 15\ R_E$.

An important feature of the IMP-3 results was the detection of an ecliptic asymmetry in the position of each boundary. Both the shock and the magnetopause were extended further from the earth on the dusk side than the corresponding attitude on the dawn side. This possibly reflects the aberration affect of the earth's motion through the interplanetary medium.

Results from Pioneer 6 (Ness et.al., 1966b) showed there to be relatively weak, rapidly fluctuating magnetic fields in the magnetosheath which terminated abruptly at the shock wave and not quite so abruptly at the magnetopause.

Boundary measurements have been extended to greater distances behind the earth. Using results from Explorer 33, Behannon (1968) has presented evidence for the existence of the shock at $\sim 75\ R_E$ from the earth and with solar ecliptic azimuth $\phi_{S.E.} \sim 135^\circ$.

In the antisolar direction, at distances $\gtrsim 30\ R_E$, the magnetospheric field has been measured to run nearly parallel (or antiparallel) to the earth-sun line and forms the magnetotail. The magnetopause becomes roughly

cylindrical with an approximately elliptical cross-section. This aspect of the geomagnetic field will be discussed more fully later.

7.1.3. The Near Magnetosphere

The essentially dipolar shape of the earth's magnetic field is compressed on the sunlit side such that the field strength from about 6 R_E from the earth out to the magnetopause is larger than would be expected from a pure dipole. Within 6 R_E, however, the presence of a diamagnetic plasma reduces the observed field to below that expected for the pure dipole, which results in an inflation of the field (Sugiura et.al., 1969).

At low latitudes on the night-side of the earth, where the solar wind compression is not so important, the field is depressed from its dipolar value everywhere within 10 R_E near the equatorial plane. At high latitudes, however, the field is enhanced, primarily because of the polar cap flux being swept back into the magnetotail.

During magnetic storms, the appearance of low energy ($\sim$ 10's of keV) protons in the inner magnetosphere causes a further weakening of the field strength in the region about 4 R_E from the earth (Frank, 1967). The inflation is asymmetric during the early stages of the main phase of a magnetic storm with the greatest inflation occurring on the dusk side of the magnetosphere. Later in the storm the inflation spreads to the dawn side and thereafter remains symmetric.

Whilst at low latitudes the magnetic field lines take a distorted dipolar form, above auroral latitudes the effect of the solar wind is to drag the field lines back into the magnetic tail - these are called 'open field lines'. On the day side a neutral cusp may exist between the last

closed field line and the first open field line. Evidence suggests that the region of weakened field around the cusp may be filled with particles of magnetosheath origin, e.g. Winningham (1971). On the night side field lines near the auroral oval become greatly distorted and can close at considerable distances from the earth, $\sim$ 20 - 30 R_E. The region of closed field lines extends to higher latitudes on the day-side than on the night-side, the difference being $\sim 10^{o}$ latitude.

Closed field lines lead to the existence of the well-documented trapped radiation belts, the particles in which drift azimuthally many times around the earth in a fairly stable fashion. Open field lines cannot, of course, support populations of trapped particles and in a longitudinally symmetric field configuration it would be expected that the boundary between the regions where the particles might drift in longitude and where they might not would be clearly defined. However, because the geomagnetic trapping boundary is lower on the night side than on the day side, a particle finding itself on a high latitude closed field line on the day side may, in drifting to the night side, find that the corresponding line there is open to the tail. The particle is then allowed to drift only a fraction of a revolution around the earth before being lost into the tail. The region in which this is possible is called the 'pseudo-trapping' or 'quasi-trapping' region after Roederer (1967a).

It is also known that energetic particles arriving at the earth at auroral latitudes (e.g. solar flare protons) penetrate below the open field lines (e.g. Bewick et.al., 1970) and the identification of 'trapping', 'pseudo-trapping' and 'open field line' regions is important for the description of their distribution.

7.1.4. The Geomagnetic Tail

Extensive mapping of the geomagnetic field at large distances ($\gtrsim$ 20 R_E) from the earth in the anti-solar direction e.g. Ness (1965), Fairfield and Ness (1967) has shown that the magnetic field there is oriented parallel to the earth-sun line and directed either towards or away from the earth depending on whether the field lies above or below a magnetically neutral surface, designated the 'neutral sheet'. The neutral sheet has been observed at distances as close to the earth as 10 R_E.

A time averaged picture of the neutral sheet shows it to be thin, $\sim$ 0.1 - 0.8 R_E. However, since the sheet is believed to be in constant motion such that its velocity and orientation cannot be measured by a single satellite, this thickness is not yet known accurately. The presence of a field reversal across the neutral sheet implies the existence of an electric current associated with the spatial gradient of the field. Following observations from the IMP 1 satellite, Speiser and Ness (1967) have computed the equivalent current magnitude and direction from the relation J = Curl H to form a physically consistent model of the field reversal assuming the sheet to be two-dimensional.

Although designated the neutral sheet, this region does support a very weak magnetic field oriented in the Z_{SM} direction. Near to the earth ($\lesssim$ 30 R_E) the field is northerly directed (Behannon, 1968) whilst at greater distances a south-pointing field has been observed (Mihalov et.al., 1968). This suggests that reconnection of terrestrial field lines occurs across the neutral sheet near to the earth while at greater distances reconnection occurs in the opposite direction. The two reconnection regions would then be separated by a neutral line.

Ness (1971) has presented neutral sheet measurements made with high time resolution that show a north-pointing field to change to a south-pointing field on a time and distance scale that is inconsistent with the theoretically predicted motion of a single neutral line. Schindler (1971) has produced a simplified, self-consistent model of the magnetotail which predicts a diverging tail comprised of unstable, distorted magnetic loops. A consequence of this model is the prediction of multiple neutral lines in the neutral sheet region. Hence on a highly resolved time scale the neutral sheet might be expected to be magnetically turbulent. A comparison of the model with satellite measurements is made in Schindler and Ness (1971).

The geomagnetic dipole axis is inclined to both the ecliptic plane and the earth's spin axis. Hence the inclination of the dipole to the ecliptic plane changes with the spin and orbital motion of the earth so that the neutral sheet is rarely parallel to the ecliptic plane. For ease of representation, Ness (1965) introduced a 'solar magnetospheric' (S.M.) co-ordinate system in which the XZ plane is determined by the earth-sun direction and the geomagnetic dipole axis. This can easily be converted to solar ecliptic (S.E.) co-ordinates by rotating the S.M. co-ordinate system through the correct angle about the X-axis. Observations show that the neutral sheet is located above the S.M. equatorial plane in the northern hemisphere summertime and below it in the winter. Both S.E. and S.M. co-ordinates are used in the analysis and results presented here.

The shape of the magnetotail itself (as defined by magnetopause traversals) is very difficult to measure since it is in constant motion and may fluctuate radially by $\sim 10\ R_E$ in response to varying solar wind

conditions. However, using the first five months data from Explorer 33, during which time many magnetopause crossings were made, Behannon (1968) obtained a time-averaged Y_{SM}, Z_{SM} cross-section of the tail at the orbit of the moon. A circle of radius $\sim 24\ R_E$ was fitted to the crossings, with its centre at Z = 0, Y = 4 R_E. There was a tendency for crossings to be seen, however, at Z $\sim$ -30 R_E and it was suggested that a more realistic fit might be made with an ellipse with major : minor axis ratio 3:2 along the Z_{SM}, Y_{SM} directions respectively. In the X, Y plane the axis of symmetry of the tail is at Y $\sim 4\ R_E$ (see Figure 9 of Behannon, 1968).

In general the greatest component of the magnetotail field is directed parallel to the X_{SM} direction and typical quiet-time field strengths are $\sim 12\gamma$ at $X_{SM} = 40\ R_E$. A gradient in field strength as a function of distance down the tail has been observed e.g. Behannon (1968) has reported

$$|B| \quad \alpha \quad |X_{S.E.}|^{-0.3\pm0.2}$$

in the region $20 < X_{SE} < 80\ R_E$. It has been suggested that the gradient is due either to an increase in the radius of the tail with distance or to a reconnection of field lines across the neutral sheet or a combination of both (Behannon, 1970, Mihalov et.al., 1968). Measurements have been produced to illustrate this suggestion but are not sufficiently precise to exclude the additional possibility of flux loss through the magnetopause due to reconnection of the earth's magnetic field with interplanetary field as a loss mechanism.

Behannon (1970) also shows that the tail field might, on average, also have a component in the Y_{SM} direction. He makes a least squares fit to his data of

$$\phi_{SM} = 178.5 - 0.44\ Y_{SM}$$

where ϕ_{SM} is the solar magnetospheric azimuth. There is also evidence of a negative Z_{SM} component to the field for a value of $|Z_{SM}| \gtrsim 6\ R_E$. This is interpreted as indicating field line divergence in the north-south direction.

Above and below the neutral sheet there is a region of plasma. This 'plasma sheet' is some 4-6 R_E thick in the centre of the tail increasing to $\sim 10\ R_E$ thick at its edges. Behannon (1970) has shown that the magnetic fields in this region are weaker by a few gammas than the fields elsewhere in the tail.

Although the tail is well documented out to distances $\sim 80\ R_E$ the question of how much further a well-ordered, coherent tail extends is still unanswered. The spacecraft Pioneers 7 and 8 each spent several days in the expected tail region at 1000 and 500 R_E downstream from the earth. In each case unambiguous, earth-related effects were seen (Ness et.al., 1967b , Wolfe et.al., 1967) but they differed from cislunar measurements in that they occurred intermittently with durations typically $\lesssim 1$ hr. The measurements took the form of solar-antisolar alignment of the field coupled with an increase in field strength up to $\sim 7\ \gamma$.

These measurements can be interpreted either as a well-collimated tail that is 'flapping' in the solar wind and hence changing its position in space or as representing a tail that has degenerated into separate filaments. Resolution of the ambiguity cannot be made with measurements from a single satellite magnetometer.

7.1.5. Magnetospheric Substorms

Substorms are phenomena which involve the storage and subsequent

release of solar wind energy by the magnetospheric field. Substorms normally occur during periods when the interplanetary magnetic field is pointing southward (Ness 1971). There are usually two clear phases.

During the growth phase, in which the solar wind energy is stored in the magnetosphere, the dayside magnetopause moves inwards in response to a change in the direction of the interplanetary field from northward to southward. This is interpreted as an 'erosion' of the dayside magnetosphere causing the deposit of more flux into the tail (Aubry et.al., 1970). The magnetosphere becomes less dipolar as more field lines are dragged back into the tail.

Eventually the highly distorted configuration becomes unstable and the magnetosphere rapidly relaxes back to a more dipolar shape: this is the onset of the expansion phase. Although the 'trigger' for the onset is unknown the phase is interpreted (e.g. Axford 1969) as being due to the reconnection of field lines across the neutral sheet and their subsequent inwards motion towards the earth. Plasma in the plasma sheet is accelerated by this motion of the field lines and is the cause of particle precipitation events associated with substorms. Hot plasma can be seen to appear near the inner edge of the plasma sheet during all substorms (McIlwain 1971).

The expansion phase is succeeded by the recovery phase, but the physical processes involved here are probably the same as for the growth phase. The recovery phase is usually accompanied by very quiet magnetic conditions in the magnetosphere and very weak tail field strengths. Subsequent to the recovery phase the substorm cycle begins again provided that the interplanetary field remains southward directed.

7.1.6. Theoretical Models of the Geomagnetic Tail

The distortion of the terrestrial dipole by the solar wind implies a transfer of energy from the wind to the magnetosphere. Magnetohydrodynamic models have not, as yet, been very successful in describing this energy transfer, nor the resulting distortion. Several large-scale, simplified models have been produced, however, and it is in terms of these, or their derivatives, that the results presented later will be interpreted.

From recent measurements of the topology of the magnetotail using satellite instruments, it is generally believed that the tail has an 'open' configuration, i.e. the terrestrial field lines do not merge at large distances from the earth. Dessler (1964) suggested that the tail was kept open by an hydromagnetic wave radiation pressure sufficient to maintain a coherent tail of length $\sim$ 20 - 50 A.U., at which distance the solar wind terminates.

Dungey (1961, 1963) suggested that the transfer of energy from the solar wind to the magnetosphere was effected by the motion of terrestrial field lines reconnected to interplanetary field lines. As a third possible mechanism, Axford and Hines (1961) have suggested that momentum is transferred from the wind by a 'viscous-like' interaction with waves on the magnetospheric boundary. Both the Dungey and later Axford models (Axford et.al., 1965) suggest that flux can be lost from the magnetotail through the magnetopause boundary. The Dessler model does not permit such a loss. Thus in the former models charged particles can enter the magnetotail directly by following interconnected magnetic field lines whilst in the latter model, access is possibly only by diffusion. In a later model, however, Michel and Dessler (1970) suggest that the break-up of the tail into filaments could increase the rate of diffusion into the tail.

7.2. Solar Flare Protons as Probes of the Distant Magnetotail.

7.2.1. The Use of Protons as Probes

The difficulty in making direct magnetic measurements in regions of weak, moving tail field at large distances from the earth has been mentioned previously. Until clusters of satellites using highly sensitive magnetometers are employed for such measurements it is necessary to look for an alternative means of investigating this region of the magnetosphere. Energetic protons from solar flare events could prove to be a useful probe for this purpose.

It has been known for some time that the appearance of energetic protons at and above auroral latitudes can be correlated with the occurrence of a solar flare (e.g. Williams and Bostrom 1967, Bostrom 1969). Observations of these protons over the polar caps by low altitude, polar orbiting satellites show that highly structured counting rate profiles normally result. The cut-off latitude for these protons often occurs well below the limit of stable trapping for energetic particles (e.g. Bewick et.al., 1970) and, indeed, it can be shown that much of the structure below the last closed field line can be attributed to effects other than the entry mechanism of the particles into the tail (Flindt, 1970; Haskell and Hynds, 1971). Above the last closed field line, however, there often remains much structure that can only be the direct result of the entry of particles into the tail or of modification of the particle distribution during its travel to the earth. (It will be shown later that the latter effect is likely to be small.)

Solar protons can gain access to the tail either by following field lines or by diffusion. In either event it is important to know whether the structure in the open field line counting rates is predominantly caused by structure in the interplanetary proton population (e.g. pitch angle anisotropies, rapid flux gradients) or by modification of the

population by the tail itself (e.g. preferential access regions). The correlation of structure in the counting rate profiles over the polar cap with flux conditions known to exist in interplanetary space could provide an understanding of access mechanisms to the tail and hence lead to an improved model of the structure of magnetotail itself.

Archetypes of the two most probable modes of access are now discussed in more detail.

7.2.2. Entry along field lines reconnected through the magnetopause

A reconnection model of the magnetosphere has been proposed by Dungey (1961, 1963) and Axford et.al. (1965). The principle implication of the reconnection model is that lines of force from inside the auroral oval, go through the tail and are eventually indistinguishable from the lines of force of the interplanetary field.

Reconnection is believed to take place on the day side of the earth during periods when the interplanetary field is directed southward. The interplanetary field is convecting with the solar wind and, in dragging the magnetospheric line back into the tail, increases the flux there. The terrestrial end of the line then moves over the pole to the night side and the line becomes detached from the interplanetary field again at a geomagnetic latitude $\sim 68^{o}$. From this it can be inferred that the length of the tail is $\sim 10^{3}\ R_{E}$ (Dungey, 1965).

On the basis of this model, protons gain access to the magnetosphere by following the interplanetary field lines across the magnetopause to arrive on field lines that connect directly to the polar caps. Since different regions of the polar caps connect out at different distances down the tail, then structure in the proton flux in interplanetary space could result in corresponding structure over the polar caps. If scattering

across the field lines in the tail is small then even very sharp structure, as might be expected to result from discontinuities in the solar wind, would be preserved.

At low energies ($\sim$ 2 MeV) proton pitch angle anisotropies existing in interplanetary space are smoothed out at the surface of the magnetopause as has been observed by Montgomery and Singer (1969). Nevertheless, a prevailing anisotropy in interplanetary space could still have a profound effect on the resulting structure over the polar caps simply because more particles impinge the surface facing the anisotropy direction. Results which have been interpreted in terms of a model of this type have been reported e.g. Van-Allen et.al., 1971 (See Figure 7(2)).

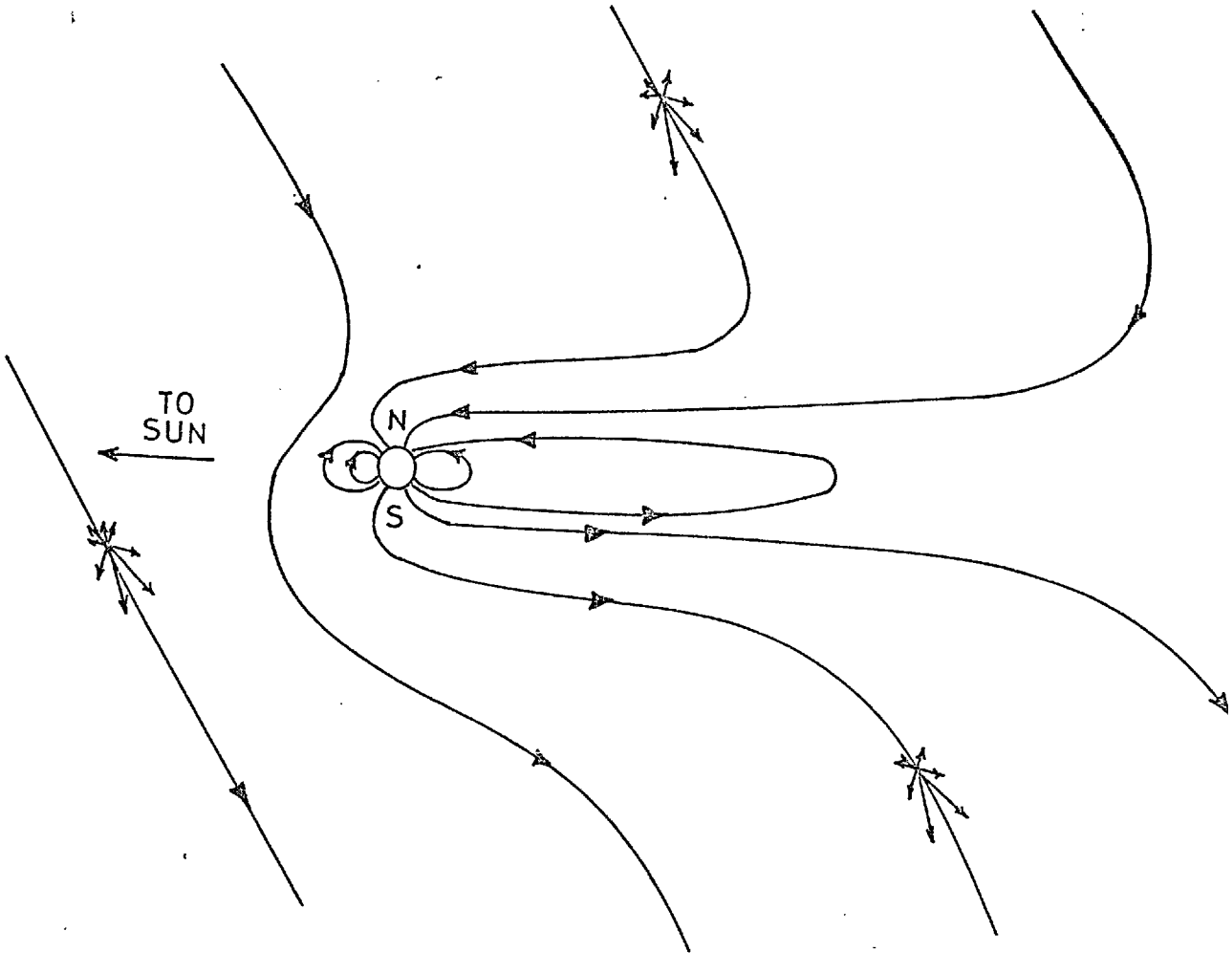

Figure 7(2): A schematic diagram proposed by Van Allen et.al. (1971) for the magnetic topology of the magnetotail in the noon-midnight meridian. Solar protons are shown to arrive at the polar caps following interconnected interplanetary and terrestrial field lines. The model was proposed to explain a north-south asymmetry in counting rate.

Evidence for the validity of the reconnection model has been reported by Gurnett (1971) who measured the persistent occurrence of reversals in the north-south component of the convection electric field in the auroral zone. Simultaneous charged particle observations showed that the reversal corresponded to the boundary between open and closed magnetic field lines. These electric field measurements could then be a direct observation of the passage of magnetic field lines across the pole and their subsequent return through the auroral regions.

7.2.3. Diffusive Entry

Michel and Dessler (1970) assume there is no flux loss across the magnetopause. They interpret magnetotail measurements such as those of Ness et.al. (1967) as indicating a coherent tail at distances $\sim 10^3$ R_E, which is moving in the solar wind.

Michel and Dessler (1970) suggest that the tail remains cylindrical within 300 R_E and can be regarded as a bundle of distinct magnetic flux tubes with slightly differing field strengths (see Figure 7(3)). Low energy particles then essentially gradient drift along the boundaries between the flux tubes with a velocity

$$V_g = \frac{1}{2} V_p \frac{\delta B}{B} \qquad \text{provided } \delta B \ll B$$

where δB is the variation of the field across the cell boundary. Closely neighbouring drift paths, which conserve the magnetic moment, μ, disect the tail. This reduces the transverse diffusion required to uniformly fill the tail and, hence, the corresponding diffusion time is also reduced.

Higher energy particles, velocity V_p, whose gyroradii ρ are large

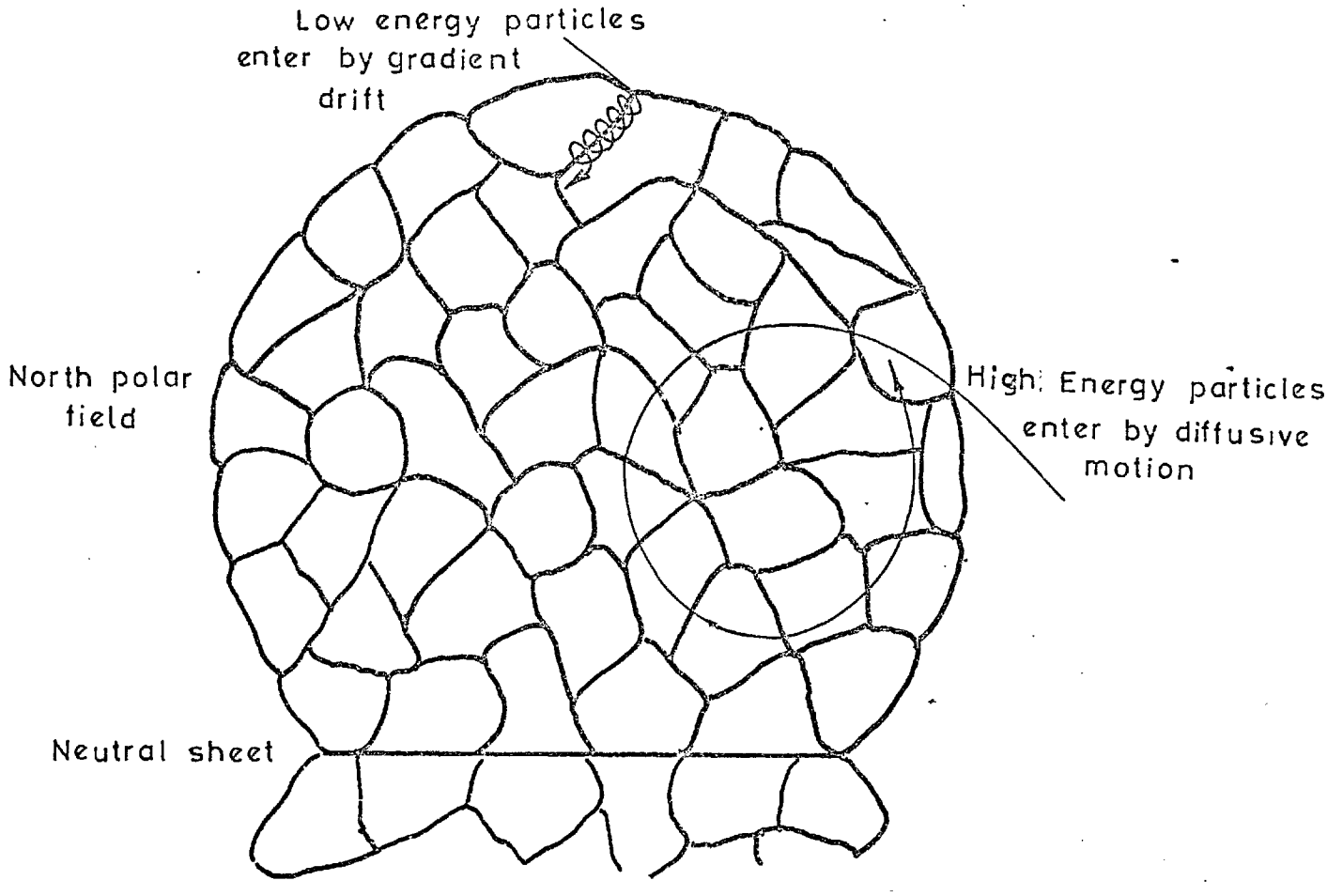

Figure 7(3): A cross section through the geomagnetic tail showing the proposed filamentary structure of Michel and Dessler (1970). The modes of particle entry are indicated.

compared with the radii of the flux tubes, r, diffuse in as their guiding centres are changed due to the changes in field strength experienced as the particle moves across flux tubes. The diffusion time t_d across the tail of radius R is

$$t_d = \frac{R^2}{2rV_p(\delta B)^2}$$

Applying these formulae to 40 keV electrons and 5 MeV protons and assuming suitable values for the parameters, Michel and Dessler (1970) found that,

$$t_{ge} = 7.10^5 \text{ sec}, \quad t_{gp} = 4x10^4 \text{ sec}, \quad t_{dp} = 4x10^5 \text{ sec}.$$

Clearly t_{ge} is too long to explain electron entry as observed by Lin and Anderson (1966) but it was claimed that some observations of 5-10 hour delays in low energy proton entry (e.g. Williams and Bostrom 1969) could be explained by gradient drift in this way.

To explain the access times observed for electrons it was necessary to look to the tail break-up region ($\sim 10^4 R_E$) where access to the separated filaments (radius $\sim 0.3 R_E$) by 40 keV electrons ($\rho \sim .0.02 R_E$) by normal diffusion could be very rapid.

7.2.4. Perpendicular drift within the magnetotail

Once solar protons are inside the tail and are travelling towards the earth it is possible that they will scatter off inhomogeneities in the field and hence any existing structure in the tail counting rates might be modified. It is important to investigate the possible magnitude of this effect.

Diffusion in the well-formed tail regions (i.e. regions not broken into filaments such as may occur in the far tail regions) is assumed to be caused by gyro-resonance particle interaction with small amplitude magnetohydrodynamic waves propagating with the Alfven speed, V_A where

$$V_A = \frac{B}{\sqrt{4\pi\rho}} \qquad \rho = \text{plasma density} = nm_p.$$

The associated electric field intensities will be $\sim \frac{\underline{V}_A \times \underline{B}}{c}$ and hence if a particle has a velocity $v >> V_A$, effects due to temporal changes in the magnetic field are relatively unimportant. To the particle

the scattering field appears stationary.

Gyro-resonance pitch angle scattering occurs at a field frequency

$$f = \frac{\sqrt{3}V_A B}{2\pi R}$$

where R is the magnetic rigidity = $\frac{\text{momentum x c}}{Ze}$ and the scattering mean free path for motion along the field lines for this process is

$$\lambda = \frac{R^2}{P_\perp V_A}$$

where $P_\perp$ is the power in the transverse fluctuations spectrum at the frequency f (Jokipii, 1966).

Using the results for $P_\perp$ of 200 γ^2/Hz at 3.10^{-3} Hz and 5 γ^2/Hz at 4.10^{-2} Hz obtained from Mariani et.al. (1969), Morfill and Quenby (1971) show that for reasonably quiet conditions (Kp $\sim$ 3.3), diffusion transverse to the field direction and pitch angle scattering are both unimportant for solar protons propagating down the field lines in the geomagnetic tail.

This result implies that particles which arrive on open field lines near the earth will have preserved certain information relating to their mode of entry. It now remains to display this information in such a way as to throw some light on the structure of the magnetotail.

7.3. A co-ordinate system for the description of polar cap measurements

7.3.1. The inadequacy of the L-parameter

Until the present time most particle measurements have been interpreted in terms of the McIlwain'L-parameter'or its derivatives (McIlwain, 1961). Whilst this is suitable for small values of L it becomes inadequate for the description of energetic particles at high L values where the parameter ceases to be related to the physical conditions in that region. The derivation of the L-parameter and its breakdown at high values are

examined below and the need for a new co-ordinate system for the description of the arrival of solar protons over the polar caps is discussed.

The motion of charged particles in a trapping field can be described by 3 adiabatic invariants:

$$\text{the magnetic moment} \quad M = \frac{p_\perp^2}{2m_o B} \quad ,$$

$$\text{the second invariant} \quad J = \int p_{ll} ds \quad ,$$

$$\text{and the flux invariant} \quad \Phi = \int \underline{A} \cdot d\underline{x} \quad ,$$

where $p_\perp$, p_{ll} are the components of the momentum perpendicular and parallel to the magnetic field $\underline{B}$ and m_o is the particle rest mass. J represents integration over the arc of a field line during a complete bounce. $\underline{A}$ is the magnetic vector potential and Φ is the integral over a closed path around the particle shell and lying in it.

It is convenient to define

$$I = \frac{J}{2p} = \frac{1}{2p} \int p \left(1 - \frac{p_\perp^2}{p^2}\right)^{\frac{1}{2}} ds = \int_A^{A'} \left(1 - \frac{B_\ell}{B}\right)^{\frac{1}{2}} ds$$

where the integral is taken over half a bounce (A, A' are the mirror points) and B_ℓ is the magnitude of the field at an arbitrary point. $B_{A,A'}$ is the field at the mirror points.

In a perfect dipolar field these quantities are genuine invariants in the motion and the "near" region of the geomagnetic field approximates so closely to dipolar that the invariants here can be considered as being conserved. Then $j_\perp$, the directional intensity of the particles perpendicular to $\underline{B}$ will be the same for all positions having the same B and I values.

From this standpoint McIlwain (1961) defines a parameter from the equation

$$L^3 \frac{B}{M} = F(I^3 \frac{B}{M})$$

which, in a good approximation to a dipolar field, varies along real lines of force very little. L is known as the magnetic shell parameter and has units of R_E.

A useful quantity derived from this parameter is invariant latitude Λ, which is defined by

$$\cos^2 \Lambda = \frac{1.0}{L}$$

Λ is much used in data presentation and is extended to high latitudes by supposing a perfect dipolar field to surround the earth.

At distances $\gtrsim 4\ R_E$ distortion of the geomagnetic field prevents L from being constant along a real line of force and hence it offers no conceptual advantage over the second invariant.

Roederer (1967a) demonstrates that at distances $\gtrsim 4\ R_E$, particles with different pitch angles but mirroring on the same field line on the noon side of the earth will move to different field lines after drifting to the midnight side. The same is true for drift from midnight to noon. This effectively 'splits' the drift shell. Roederer (1967a) also shows that an important result of shell splitting is the creation of additional loss cones.

In trapped particle motion a loss cone, centred around the field line always occurs for particles whose pitch angles are so small that they enter the earth's atmosphere before mirroring. The effect of shell splitting is to create other loss cones. In drifting from noon to midnight, particles mirroring at low latitudes are transferred to field lines nearer the earth, those mirroring at higher latitudes are not.

Thus a particle bouncing at high latitudes and initially on a closed field line, in drifting azimuthally may find itself on an open line and will 'escape' into the tail. This causes a loss cone co-axial with the atmospheric loss cone but with a larger vertical angle. On the other hand, particles on the midnight side, initially bouncing at low latitudes, leave the magnetosphere through the boundary 30-40^{o} before reaching the noon meridian, resulting in a loss cone perpendicular to the field line. The regions where particles can drift only a fraction of a revolution around the earth before being lost are known as pseudo-trapping regions. They are illustrated in figure 7(1). Regions that can support particles for many revolutions are stable trapping regions. Evidence of these suggestions is given by Roederer (1967b).

At high latitudes, above the last closed field line, the 'L-parameter', and hence invariant latitude Λ, no longer in any way represent the measured magnetic field. In this region all field lines are open and particles detected on them arrive after having travelled down the tail. Although Λ, defined from an undistorted dipole, will still, in one sense, 'order' particle data at these high latitudes it will not do so in a way that bears any relation to the physical processes that determined the arrival of the particles to those regions. It is clearly necessary to interpret the counting rate profiles of energetic particles over the polar caps in terms of a co-ordinate system that is related to the physical processes that have governed the motion of those particles, i.e. in terms of a co-ordinate system that is derived from and hence related to the magnetic structure of the earth's tail field.

In order to produce such a co-ordinate system a good model of the magnetosphere and tail is needed. Since the magnetosphere configuration

changes continually in response to solar wind conditions the model must also have the capacity to accomodate such variations, i.e. the co-ordinate system must be dynamic in the sense that the set of co-ordinates used will vary according to the prevailing solar wind and magnetosphere conditions known to exist at the time that is to be represented.

The model and its use in defining such a co-ordinate system are described in the next section.

7.3.2. A Suitable Magnetosphere Model

The configuration of the magnetosphere varies according to the prevailing solar wind conditions and a dynamic model whose defining parameters can be suitably adjusted to take this into account is needed in order to establish a co-ordinate system.

Mead (1964) suggested a model based on a 3-dimensional solution to the Chapman-Ferraro problem of a solar plasma wind incident on a perpendicular dipole. A surface was formed separating the magnetic cavity from the solar wind and in which currents were flowing. The magnetic effect of these currents, B_s, was included with the earth's dipole field, B_i, to define a total geomagnetic potential, V_T. Both components of V_T were expressed as expansions of spherical harmonics whose coefficients were determined from a least squares fit to the distorted field as calculated at a number of points inside the magnetosphere.

Williams and Mead (1965) added to this model a tail field contribution $B_{c.s.}$ which was caused by a truncated, semi-infinite current sheet (the neutral sheet) that began some distance back from the earth. Current flow was in the direction of the earth's orbital velocity vector and the resulting field was towards the earth in the northern hemisphere and away

from it in the southern.

This model predicted an 'open' night-side magnetosphere and was able to explain the behaviour of energetic trapped electrons. Such as were observed by Frank et.al., 1964.

4 parameters specify this model:

(i) R_s, the stand-off distance to the subsolar point which for a solar wind pressure of $2nmv^2$ is given by

$$R_s = 1.068 \left(\frac{M^2}{4\pi nmv^2} \right)^{1/6}$$

where M is the magnetic dipole moment,

(ii) R_n, R_f the near and far distances to the current sheet, and

(iii) B_T, the tail field strength.

Roederer (1969) has compared the field predicted at the synchronous orbit (6.6 R_E) from the Mead-Williams (M-W) model with actual measurements made there by the ATS satellite. It was found that for any quiet, or even moderately disturbed time, the local-time dependence of the magnetic field could be predicted with great accuracy provided suitable parameters were used in the model.

Using $R_n = 10.0 - 0.06\ (B_T - 10.0)\ R_E$ and $R_f = 200\ R_E$, Roederer (1969) calculated the values of the field at noon and midnight for various combinations of R_S and B_T. The results are shown plotted in Figure 7(4). It was suggested that such plots used in conjunction with magnetometer measurements on a synchronous satellite would be a convenient instrument for predicting the configuration of the magnetosphere at any time.

The field used in this work is calculated from

$$\underline{B} = \underline{B}_i + \underline{B}_s + \underline{B}_{c.s.}$$

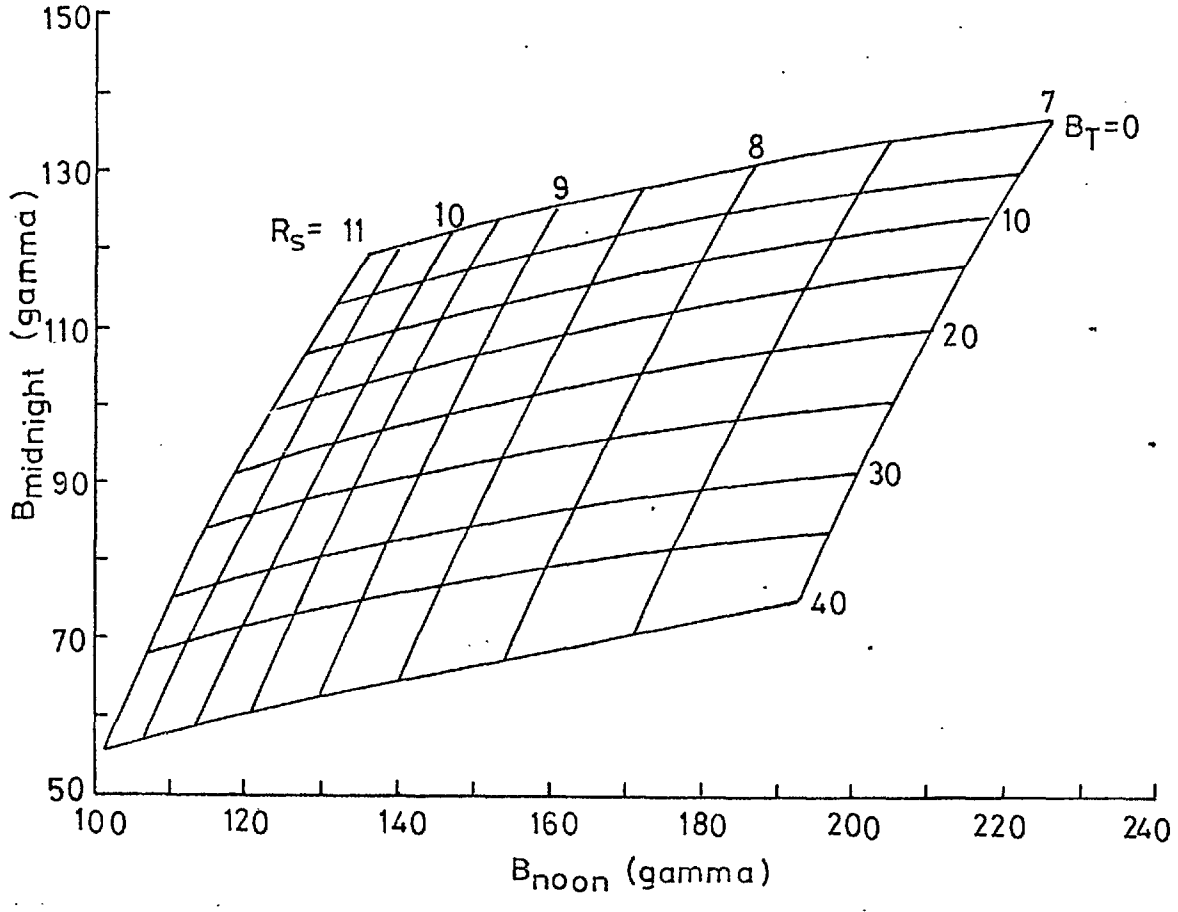

Figure 7(4): Noon and midnight B values at the synchronous orbit (6.6 R_E) as predicted by the Mead-Williams model for different values of the stand-off distance R_s and the tail field intensity B_T. (After Roederer, 1969).

The details of the calculation are given in Morfill and Quenby (1971).

$\underline{B}_s$ is calculated using the 6-term expansion fitted by Mead (1964). Although Olson (1969) points out that the dipole tilt causes an inaccuracy in this contribution, the correction only becomes of importance near the neutral points and provided care is exercised in interpretation it will not affect the results obtained here.

7.3.3. Mapping the Tail Field

Geomagnetic field lines from the same invariant latitude but different longitudes are swept back to different regions of the magnetosphere and tail. Lines emanating from high invariant latitudes are all confined within the tail, figure 7(5.A), whereas those

from lower invariant latitudes may continue down the tail, or close on themselves depending on their longitudes (Figure 7(5.B)).

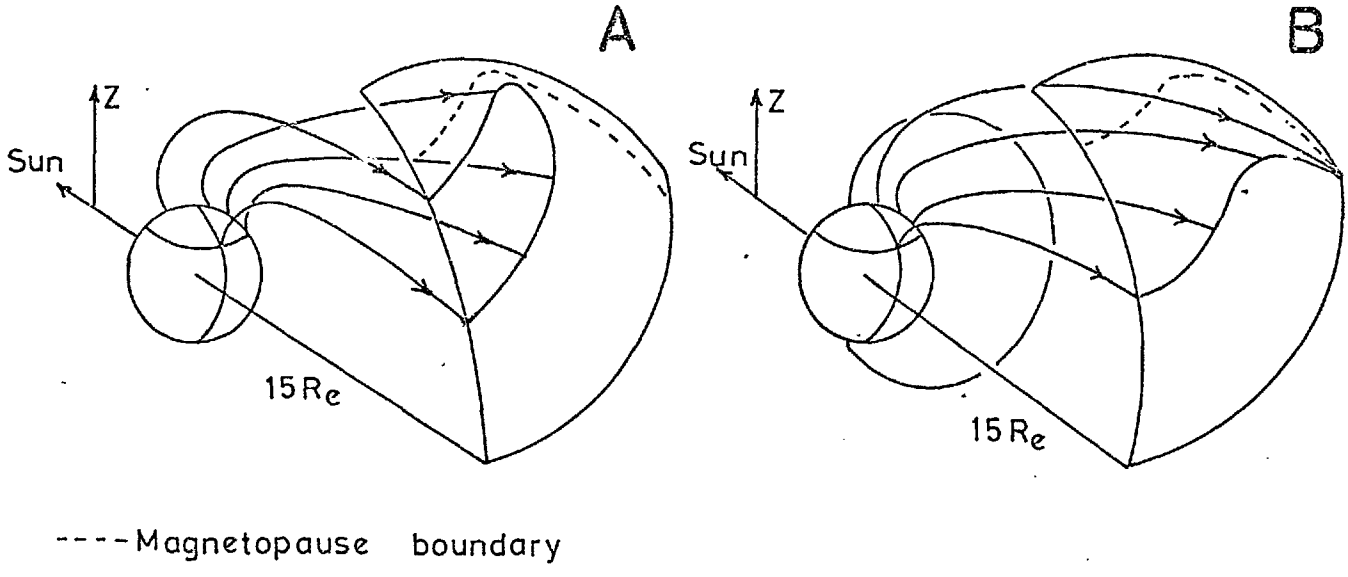

Figure 7(5): Field lines from different longitudes along a constant invariant latitude impinging a spherical surface, centre at the centre of the earth and radius 15 R_E.
A. - High invariant latitude, e.g. $\sim 80^{\circ}$.
B. - Low invariant latitude, e.g. $\sim 60^{\circ}$.

If a spherical surface is placed at $R_s = 15\ R_E$ from the earth, the positions at which field lines impinge the surface can be plotted two dimensionally using $R_s.\cos\theta$, $R.\phi$ co-ordinates. Using the M-W model described earlier the configuration produced in one half of the tail for a typical tail field strength 12.5 γ is shown in figure 7(6). (The area contained in one of these plots is equal to the area of the sphere from which the plot was projected.)

The plots are seen to comprise two distinct sets of lines; those that are open for all longitudes and those that are not. The former produce a closed pattern about the 'single line' from the pole. Open lines from the same longitudes but different latitudes on the noon side are seen to be closely bunched towards the magnetopause - the position

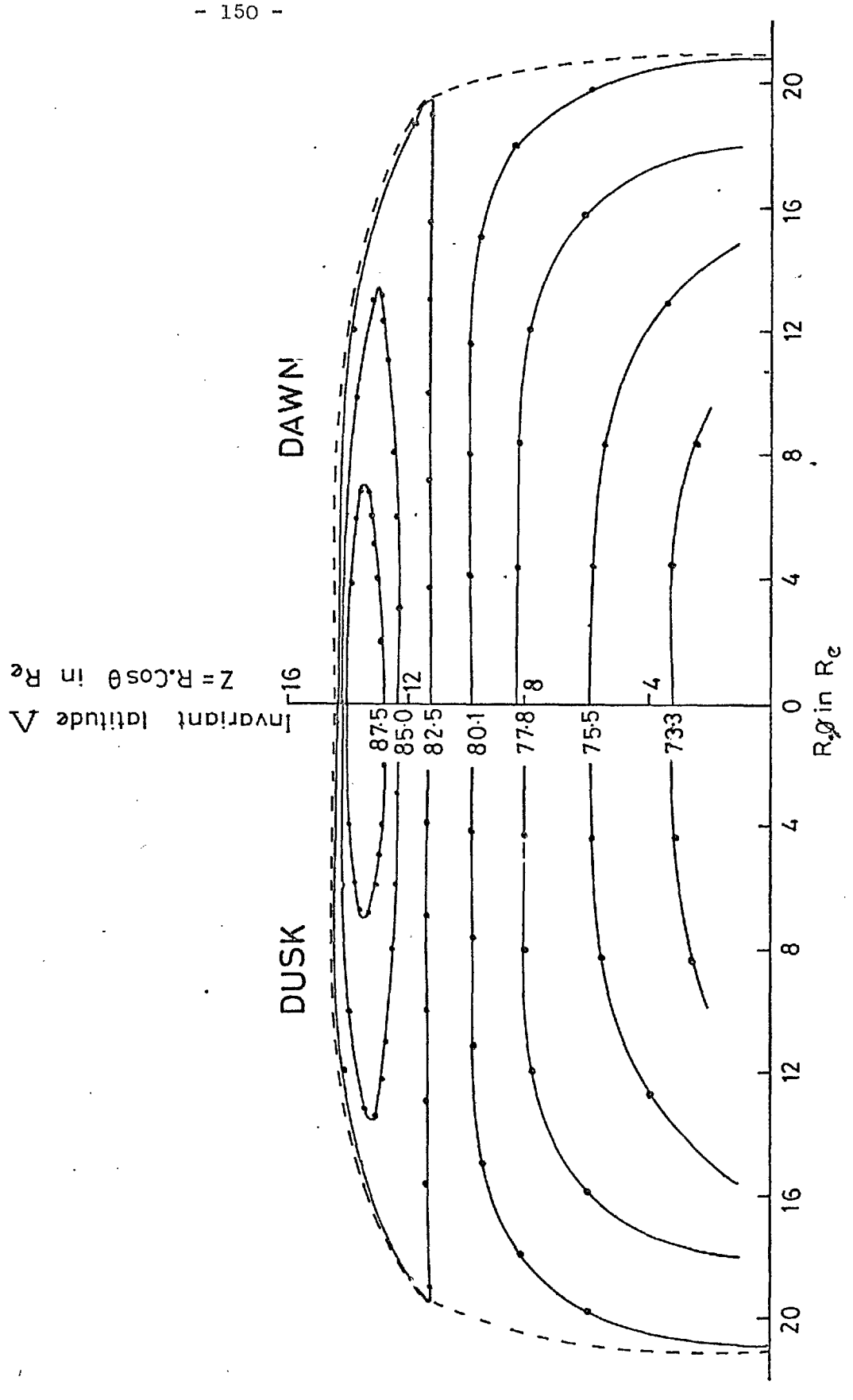

Figure 7(6): Points at which field lines from different invariant latitudes impinge a sphere of radius R(=15 R_E) centre the earth. Each point on the same Λ line is incremented 20^o in M.L.T.
The co-ordinates used are $R\cos\theta$, $R\phi$ where θ, ϕ are co-latitude and azimuth angles respectively.
An increment in area in this co-ordinate system is $dA = d(R\cos\theta)d(R\phi) = -R^2\sin\theta\, d\theta\, d\phi$
and $A = R^2 \iint \sin\theta\, d\theta\, d\phi$ = spherical surface area.
Hence these are equal area co-ordinates.

of which is calculated using the shape given by Mead and Beard (1964). The other set of lines tend to lie in planes, parallel to the neutral sheet, for the night-side field lines, and with equal spacings for equal incriments in longitude. As the longitude increases towards the day-side the lines dip sharply towards the neutral sheet and thereafter are closed.

The θ and ϕ co-ordinates used in this work are solar magnetospheric colatitude and azimuth respectively. Midnight has azimuth 180^{o}, noon 0^{o} and dawn 270^{o} such that the definitions are similar to those for solar ecliptic co-ordinates.

7.3.4. Particle trajectories in a model magnetosphere

A low energy particle with a small pitch angle, travelling along a field line at R_s will arrive at a low altitude on nearly the same field line. Because of the convergence of the magnetic field, all particle pitch angles will tend to increase and only particles with very small initial pitch angles will arrive at low altitudes. If the particle intensity at R_s were completely uniform in space and time then Liouville's theorem would ensure that, outside of any loss cone, the same intensity would be seen at low altitudes.

If the spatial distribution at R_s in the tail is structured then similar structuring of the low altitude distribution will also be expected. The intensity at a low altitude point still reflects the intensity at the point in the tail connected to it by the same field line. Thus, by projecting the loss-cone corrected counting rates, observed by a polar orbiting satellite, onto the surface at R_s, the structure of the proton intensity distribution in the geomagnetic tail is revealed. Also, since the drift perpendicular to the field lines is negligible whilst the particles

are travelling down the tail, this structure must also represent, in some way, the pattern of proton entry.

Such a method of investigating particles in the tail has the advantage that a scan of half the tail can be made in the time taken for one polar crossing by satellite, $\sim$ 20 minutes.

The particles studied in this work are protons of energy 2-17 MeV and $>$ 30 MeV. They are too energetic to follow the field lines exactly and their arrival position in the tail at 15 R_E should be calculated by integrating the particle trajectories in a model magnetosphere, back from their known positions of arrival at low altitudes. This was done for 3.4 MeV protons propagating in a M-W model magnetosphere. The trajectories were computed using a modified McCracken program by numerically integrating the equation of motion

$$\ddot{\underline{r}} = \frac{q}{m} \dot{\underline{r}} \times \underline{B}$$

The procedure is described in Morfill and Quenby (1971) and Morfill (1971).

The results are shown in Figure 7(7). As can be seen, at this low energy the arrival points do not differ very much from the field line approximation of Figure 7(6). One significant difference is that there exist regions where particles arrive having gained entry via the magnetopause boundary near the earth.

A similar integration was performed for 44 MeV and 120 MeV particles. The results are shown in Figures 7(8), 7(9). It should be noted that the co-ordinates used in Figures 7(5,6,7) are solar magnetospheric longitude and latitude and not equal-area co-ordinates.

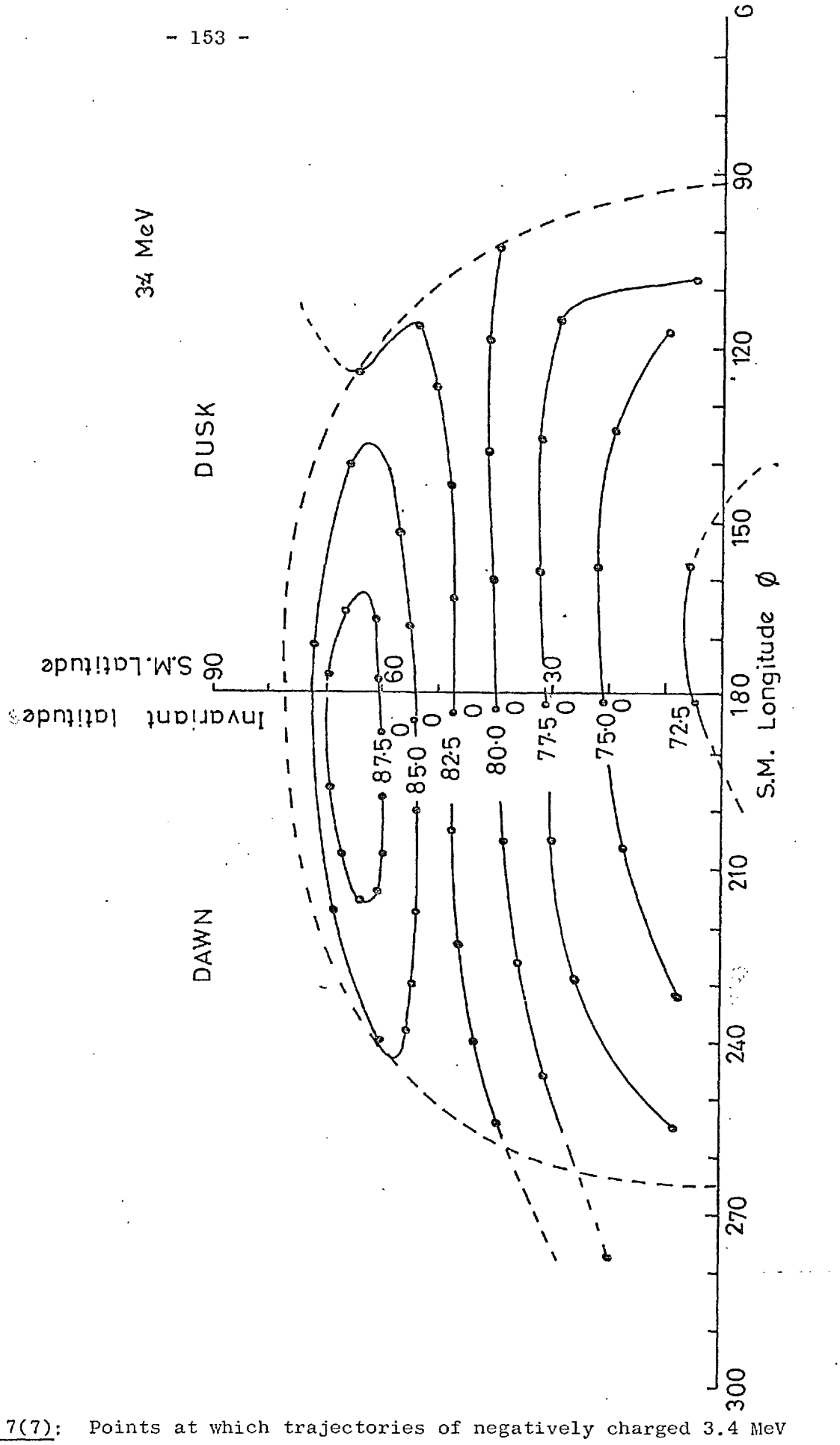

Figure 7(7): Points at which trajectories of negatively charged 3.4 MeV particles propagating in a M-W model magnetosphere with a 12.5γ tail field impinge a sphere of radius R_s(=15 R_E) centre the earth. Each line represents trajectories from the same invariant latitude and each point on the line represents a 30° increment in magnetic longitude. The co-ordinates used are solar magnetospheric colatitude and longitude.

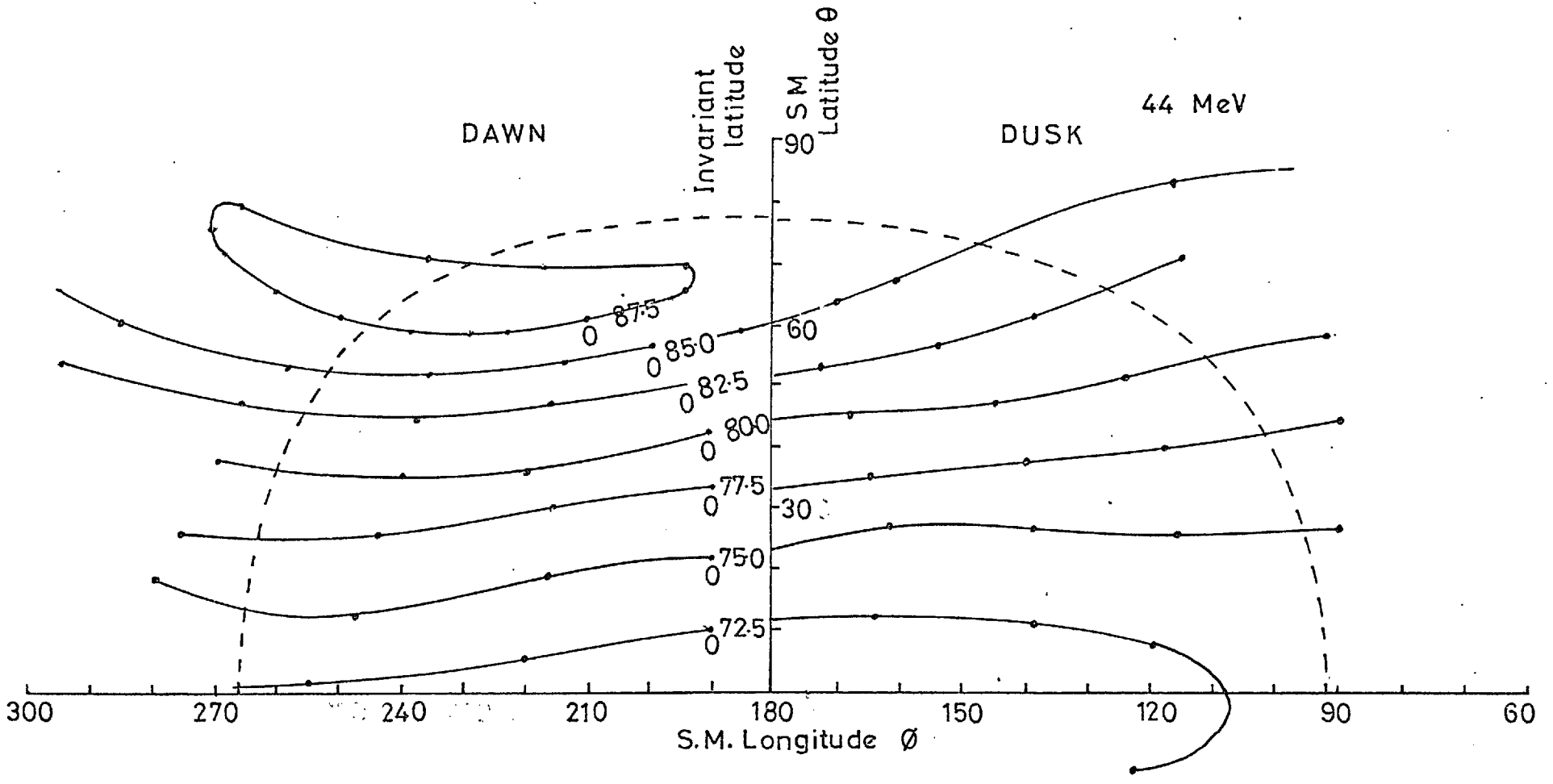

Figure 7(8): A similar projection as Figure 7(7) for 44 MeV protons.

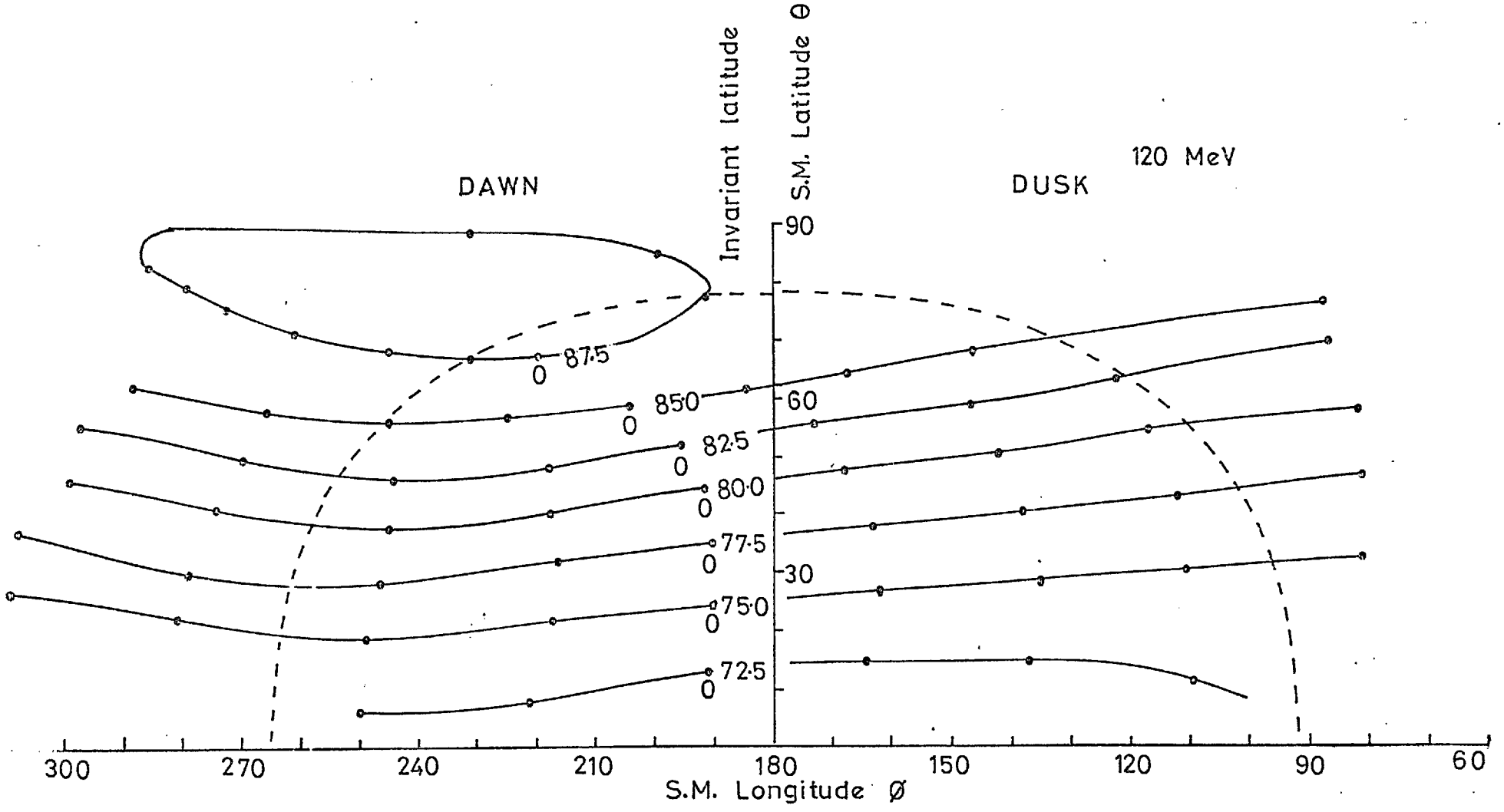

Figure 7(9): A similar projection as Figure 7(7) for 120 MeV protons.

From the figures it can be seen that for increasing energy, particles originating just on the dawn side of the noon-midnight meridian in the tail at 15 R_E penetrate correspondingly further into the dusk side of the polar cap on arrival at the earth. This is due to the increasing azimuthal gradient drift of the particles with increasing energy.

Examination of the figures also shows that, for increasing energy, progressively smaller regions of longitude, at the same invariant latitude, are connected directly to the tail. The particle gyro-radius increases with energy and some points lying within the magnetopause at 15 R_E might penetrate the boundary if the integration could be taken further, perhaps to 25 R_E. The extent of this effect can be estimated by investigating the pitch angles and gyroradii for the points near the surface. The net result is that the region of the polar cap which is directly connected to the tail shrinks with increasing energy. In particular the pole itself ($\Lambda = 90^{\circ}$) loses all significance relative to the tail configuration at energies $\gtrsim$ 100 MeV since trajectory integrations show that particles arriving there entered the magnetosphere through the magnetopause on the dawn side near the earth.

The choice of proton energies 3.4, 44 and 120 MeV for the integrations was decided upon since these were the mean energies of detected protons for the experiments designated S-27, S-25 and S-28 which were flown in the ESRO II satellite. The results from these experiments are used in the analysis of the November 18th solar flare event. These results will be discussed in Chapter 8 where the experiments will also be described.

7.3.5. Polar Plots

Whilst tail field plots can tell us much about particle distributions on open field lines they tell us nothing of the distribution on the closed field lines. Such information can be displayed on a polar plot of Λ against eccentric dipole magnetic local time, figure 7(10). Magnetic field boundaries can be calculated using the M-W field model for a particular tail field strength and projected onto the plots together with satellite trajectories. Counting rates along the trajectories can be examined for correspondence with magnetic features, such as the last closed drift shell and last closed field line.

Trajectory calculations can be used to map areas in the tail from which particles arriving at certain (Λ, M.L.T.) positions must have emanated. These areas, projected back onto the polar diagram, will produce a more realistic polar plot. Such a mapping procedure can be extended into the pseudo-trapping region by following the trajectory as it bounces around closed field lines, figure 7(11). The corresponding diagram for 44 MeV protons is shown in figure 7(12) which illustrates how the region of the polar cap populated directly by particles from the far tail shrinks with increasing energy whilst those regions populated by particles which enter through the near earth magnetopause enlarge. The pseudo-trapping region is also seen to shrink.

The longitude parameter used in the polar plots was derived from the eccentric dipole magnetic local time. Midnight is taken to be 0^{o}, noon 180^{o} and dawn 90^{o}. This parameter removes from the magnetic co-ordinate system the effects of the spin of the earth and the non-alignment of the spin and magnetic axes.

The two most important features of these plots are the last closed field line and last closed drift shell, it is therefore instructive to look at some measurements of these regions.

7.3.6. Identification of the last closed field line and stable trapping boundary.

Bewick et.al. (1970) consider the high latitude boundary of outer zone electrons of energy > 1.2 MeV to define the limit of stable trapping. It is shown that even during periods of considerable magnetic activity this boundary does not fluctuate much until the occurrence of a sudden commencement. They suggest that measured changes in the trapping boundary thus defined, do not agree with the predicted changes of Williams and Ness (1966).

McDiarmid and Burrows (1968) propose that the 35 keV trapped electron boundary (defined to be the latitude Λ_b at which the 35 keV electron count drops to a plateau 'background' level) demarcates the last closed field line at all local times. It appears that this boundary should be coincident with the limit of stable trapping of 1.2 MeV electrons at local midnight where the last closed field line and last closed drift shell are defined by the same line. The 1.2 MeV boundary is seen to be considerably lower, however. By plotting the 35 keV boundary as a function of local time a dawn-dusk asymmetry is revealed which is interpreted as an asymmetry in the magnetic field itself. Field lines are closed up to 3-4^{o} higher on the dawn side than on the dusk. In a later paper McDiarmid et.al. (1969) show that the 35 keV boundary is at considerably lower latitudes at times of small geomagnetic axis tilt than for large tilts.

Whilst the 1.2 MeV electron boundary of Bewick et.al. (1970) must represent the limit of stable trapping at that energy, and probably at higher energies, it is unlikely that it does so for lower energies. This presents no problem if the field lines on the night-side of the earth become severely distorted before they actually open. Then energetic (1.2 MeV) electrons will be lost in the cusp region where great line curvature is encountered whereas low energy electrons, whose gyroradii are considerably smaller, will still be able to follow these lines.

7.4. Summary - A note of Caution

From the Mead-Williams model of the magnetosphere it has been possible to produce two diagrams, directly related to the geomagnetic field, on which solar proton counting rates at and above the auroral regions can be represented. Although the diagrams are a great improvement on the invariant latitude parameter used hitherto, a word of caution must however be given as to their use. The new representation systems are, as yet, still at a low level of sophistication; they are defined by a dynamical, model magnetosphere and are themselves, therefore, subject to fluctuation on all time scales in response to varying magnetic conditions. In their present form it is advisable that they be used only during times of magnetospheric quiet ($Kp \lesssim 4$) and even then with great heed to other indices that may indicate magnetospheric disturbance (e.g. A.E. index).

Used sensibly, however, the co-ordinate systems can provide a far greater ordering of the solar proton data with respect to the 'real' magnetosphere than has hitherto been possible and hence offer a greater insight into magnetospheric processes.

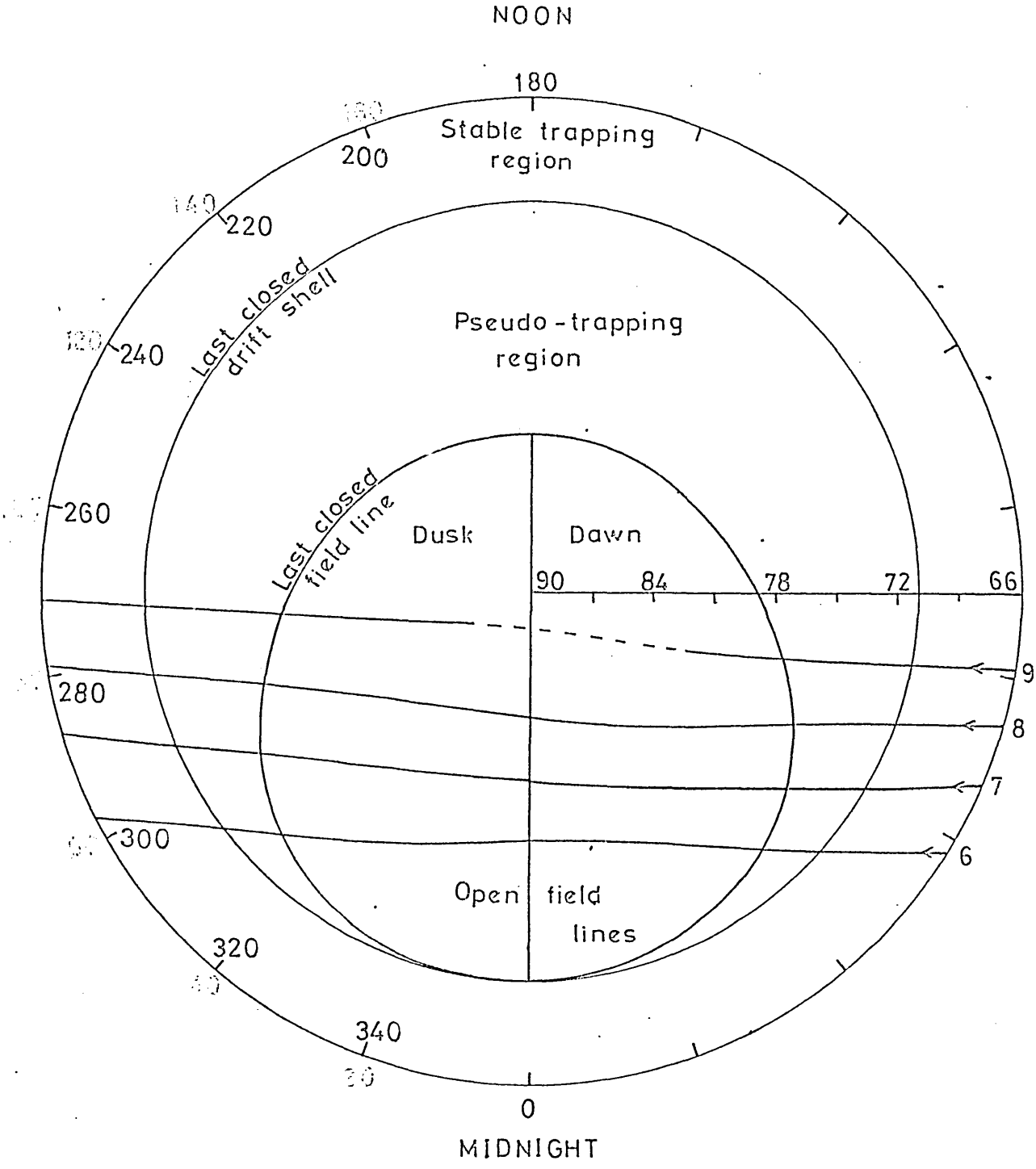

Figure 7(10): A polar plot of successive trajectories (6, 7, 8, 9) of the ESRO II spacecraft over the northern polar cap during the solar proton event of June 9th 1968. The radial axis is marked in degrees of invariant latitude Λ, the circular axis is in degrees corresponding to magnetic local time (24 hrs = 360^{o}). The gradual precession of the spacecraft across the polar cap for successive orbits is clearly demonstrated. Superimposed are the projected last closed field line and last closed drift shell boundaries calculated for a M-W magnetosphere with a 10 γ tail field.

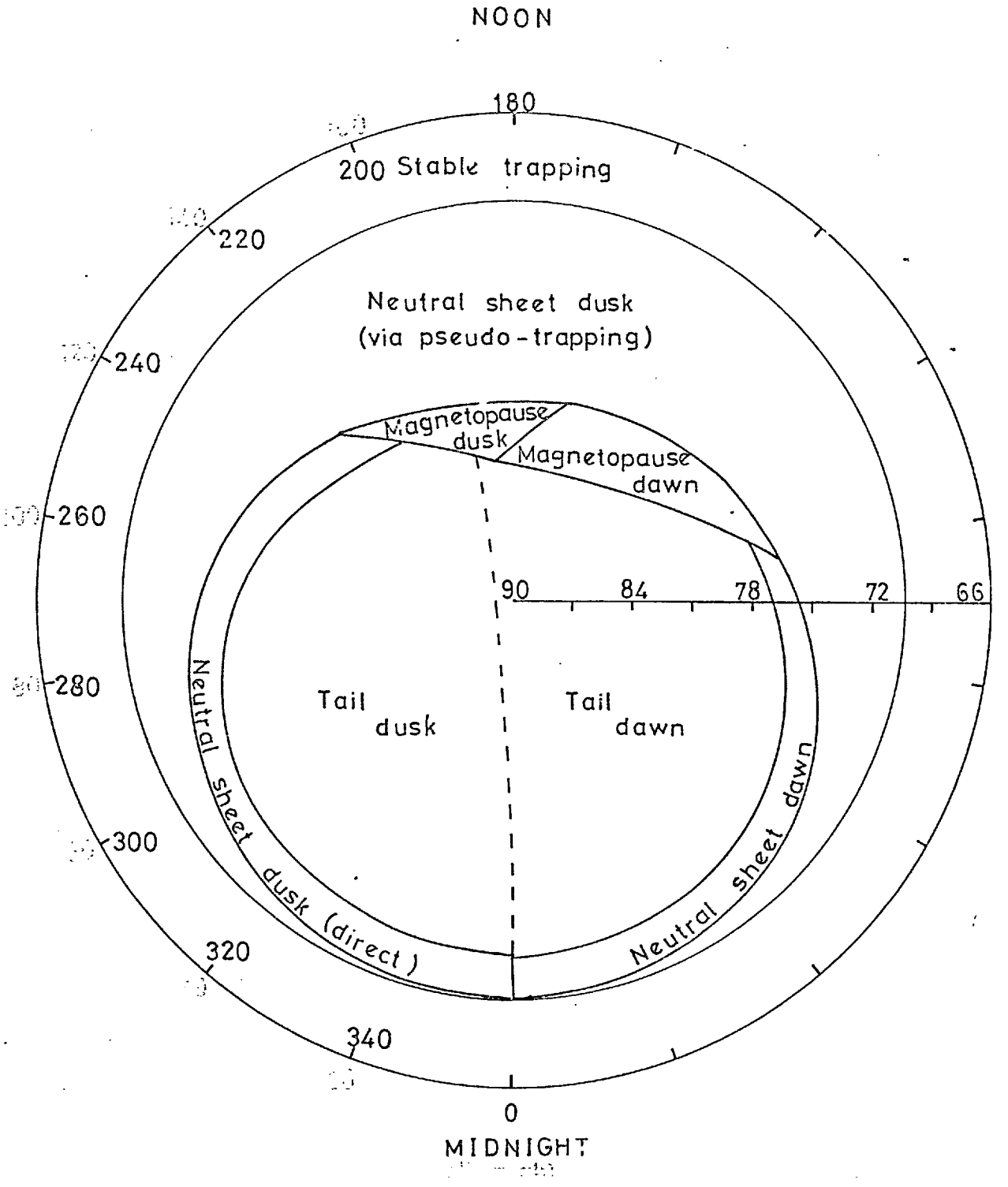

Figure 7(11): A polar plot showing the projected regions of the magnetosphere from which a particle of 3.4 MeV must have originated to arrive at low altitude over the pole in the given (Λ , M.L.T.) position. The regions were estimated using trajectory calculations in a M-W magnetosphere model with tail field strength 12.5γ . All parts of the pseudo-trapping region eventually connect to the dusk side of the neutral sheet.

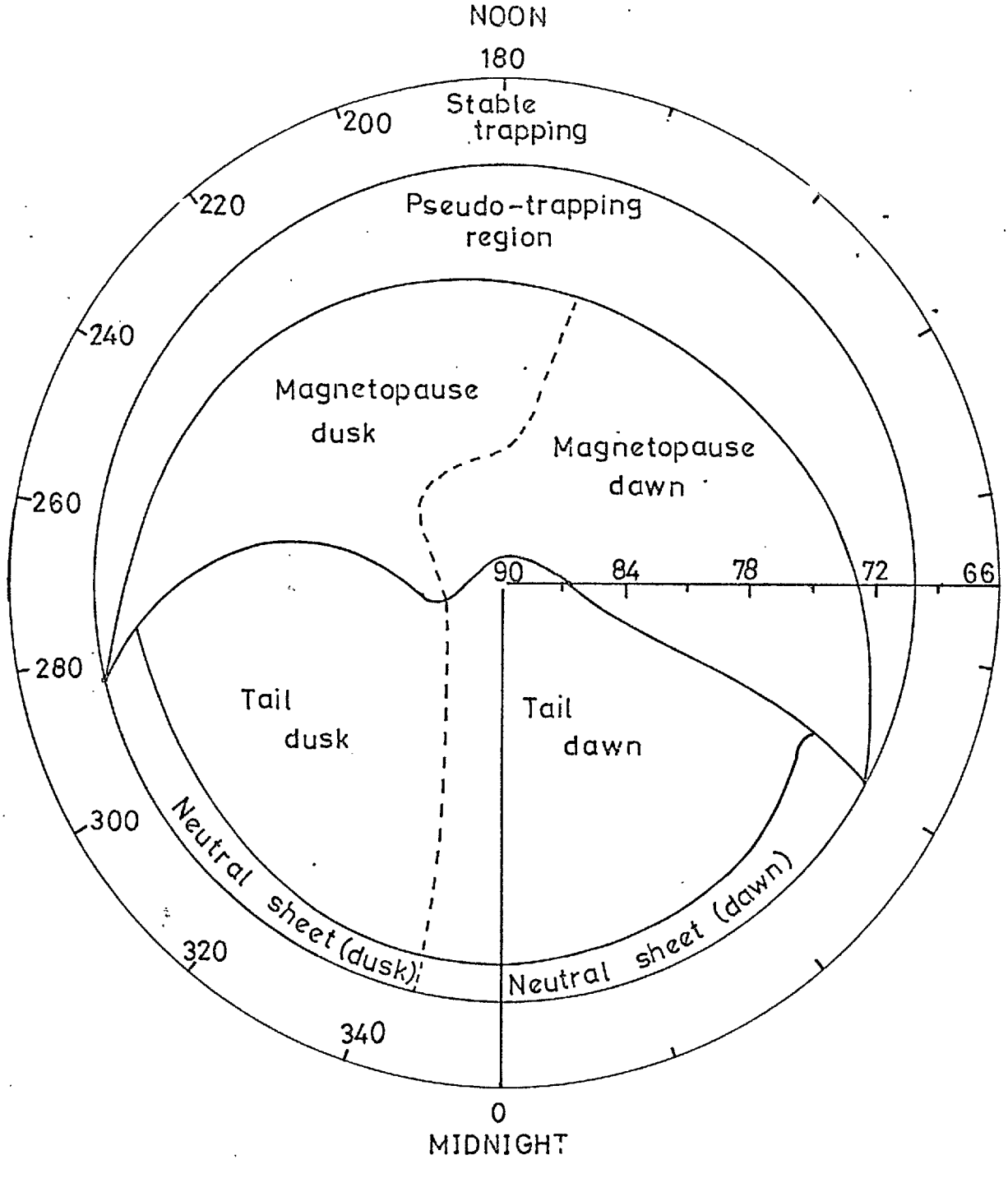

Figure 7(12): A polar plot as in figure 7(11) for 44 MeV protons.

CHAPTER 8 - THE SOLAR PROTON EVENT OF NOVEMBER 18th 1968

In this chapter the methods of data presentation developed in Chapter 7 are applied to the proton fluxes observed over the polar caps subsequent to the solar flare event of November 18th 1968. The data were obtained from the proton telescopes carried on two, low-altitude polar-orbiting satellites, ESRO I and ESRO II. Interplanetary particle and magnetic data were available from the NASA spacecraft Explorer 34 and 35. Comparison of interplanetary and magnetospheric data was possible and the consequences are discussed in terms of current magnetosphere and magnetotail models.

8.1. The Detectors

In this work data from two detectors, flown on the ESRO II spacecraft by the Imperial College group, are discussed. These are a proton telescope, designated experiment number S-27 and a general charged particle detector, experiment number S-25. The satellite was launched by NASA on 16th May 1968 from the Vandenberg A-F.B., California into a low altitude, elliptical, polar orbit.

The orbit was sun-synchronous with an inclination 98°, period $\sim$ 100 minutes, apogee $\sim$ 1100 km and perigee $\sim$ 340 km. The satellite was spin stabilized, the spin axis being maintained perpendicular to the earth-sun line, and contained a tape recorder which provided a data recovery rate > 90% until it failed 6 months after launch. Direct transmission was also possible whenever the satellite was in line of sight of a tracking station.

8.1.1. Experiment S-27

The experiment S-27 was designed to detect protons in the energy range 2 to 100 MeV. The detector was a range-energy telescope comprising 4 fully depleted, surface barrier silicon diodes, each 400 μ's thick and physically arranged in series. Four energy channels were defined from the threshold levels set for each detector. Absorbers were placed between the last 3 diodes to expand the range to include 2 to 100 MeV protons. The geometries of channels 2, 3 and 4 were defined by coincidence requirements between the individual detectors. Channel 1 recorded protons in the range 2-17 MeV and had its geometry defined by the absorber surrounding the front end of the detector which had a minimum cut-off for 80 MeV protons. In this work only data from channel 1 are considered.

Channel 1 had a geometrical factor of 2.7×10^{-2} $cm^2 sr$ and an opening half-angle of 10^{o}. It was protected from direct sunlight by thin aluminised mylar which covered the front detector. A 'broom' magnet shielded the entranc of the detector from electrons of energy < 350 keV. If sufficient numbers of these electrons were incident on the detector within the resolution time of the electronics the resulting 'pile-up' effect might cause channel 1 to trigger. The combination of this magnet with a relatively high triggering level ensured a negligible response to electrons. This could be confirmed by comparison with experiment S-25 during the passage of the spacecraft through the outer Van Allen Belt.

The telescope was arranged to look radially outwards from the satellite spin axis. The satellite was spinning at $\sim$ 40 r.p.m. Data from S-27 were sampled once every 15.875 seconds and were hence averaged over $\sim$ 11 spin periods. The telescope sampled over 360^{o} of azimuth relative to the satellite spin axis and in that sense can be considered omnidirectional.

Because the inclination of the satellite spin axis relative to the local magnetic field was continuously changing, the viewing cone of the telescope occasionally scanned through part of the atmospheric loss cone for particles at that field position. A correction for the loss of counts was made by calculating the extent of the loss cone and assuming an isotropic pitch angle distribution outside of it. The correction was never > 20% during this event.

8.1.2. Experiment S-25

Experiment S-25 comprised two Geiger tube detectors, an Anton 112 and an Anton 302. Each was operated independently and particle selection depended purely on the penetration of the shielding around the tubes. The thresholds for the shielded detectors were:

Anton 112	-	proton threshold	22 MeV
		electron threshold	1.2 MeV*
Anton 302	-	proton threshold	32 MeV
		electron threshold	2.3 MeV*

The tubes were mounted equatorially on the spacecraft and scanned through 360° of azimuth due to the satellite spin. This was similar to S-27. The opening angle was ∿ 120° at the threshold energies, giving a response which, for most purposes, could be considered omnidirectional.

8.2. A General Description of the Event

The solar flare event of November 18th was observed at optical and X-ray

---

* These were the penetration thresholds, defined to be the 'knee' of the ~~penetration~~ absorption curves for particles in lead.

wavelengths to onset at 10.26 U.T. The flare was classified to be of importance 1b and its solar position was N 19°, W 90°. It occurred during the recovery phase of a Forbush decrease in cosmic ray intensity at the earth which had begun with a sudden commencement at 0900 hrs on November 16th. Neutron monitors (e.g. Calgary) recorded an increase in count rate ∿ 12% due to the arrival at the earth of high energy solar particles at about 10.50 U.T. on November 18th. Low energy protons were first seen to arrive at the satellites Explorers 34 and 35 at ∿ 11.20 U.T. (Lanzerotti 1970, Venkaterangen et.al. 1969). The counting rate profiles for the arrival at Explorer 34 of solar protons in various energy ranges between 2-17 MeV throughout the 5-day particle event are shown in Figure 8(1A).

Figure 8(2) shows the magnetic conditions, both terrestrial and interplanetary, during Nov. 18th. A magnetic bay was seen in the H-component magnetic record of the high latitude station, College, at about 0930 U.T. This indicated the end of the magnetic storm that had begun on Nov. 16th. There was then a very quiet period that lasted until the end of Nov. 18th. This quiet period was also evident in the H-component records of low latitude stations, e.g. Tangarang. The S.I. that appeared at ∿ 16.30 could be correlated with a change in the direction of the interplanetary field. The interplanetary field components from 10.00 to 23.00 U.T. are shown in Figure 8(2) and were measured by the magnetometer on board Explorer 35.

A very strong field-aligned anisotropy from the Parker spiral direction (solar ecliptic azimuth ∿ 315°) was observed in the low energy proton fluxes immediately they were detected at Explorer 35 at ∿ 12.30 U.T. The anisotropy persisted until about 1630 U.T. and occasionally had an amplitude ∿ 100%, where amplitude is defined by the parameter, C from equation 8.1.(i) (below) and expressed as a percentage. At 16.30 U.T. there was an

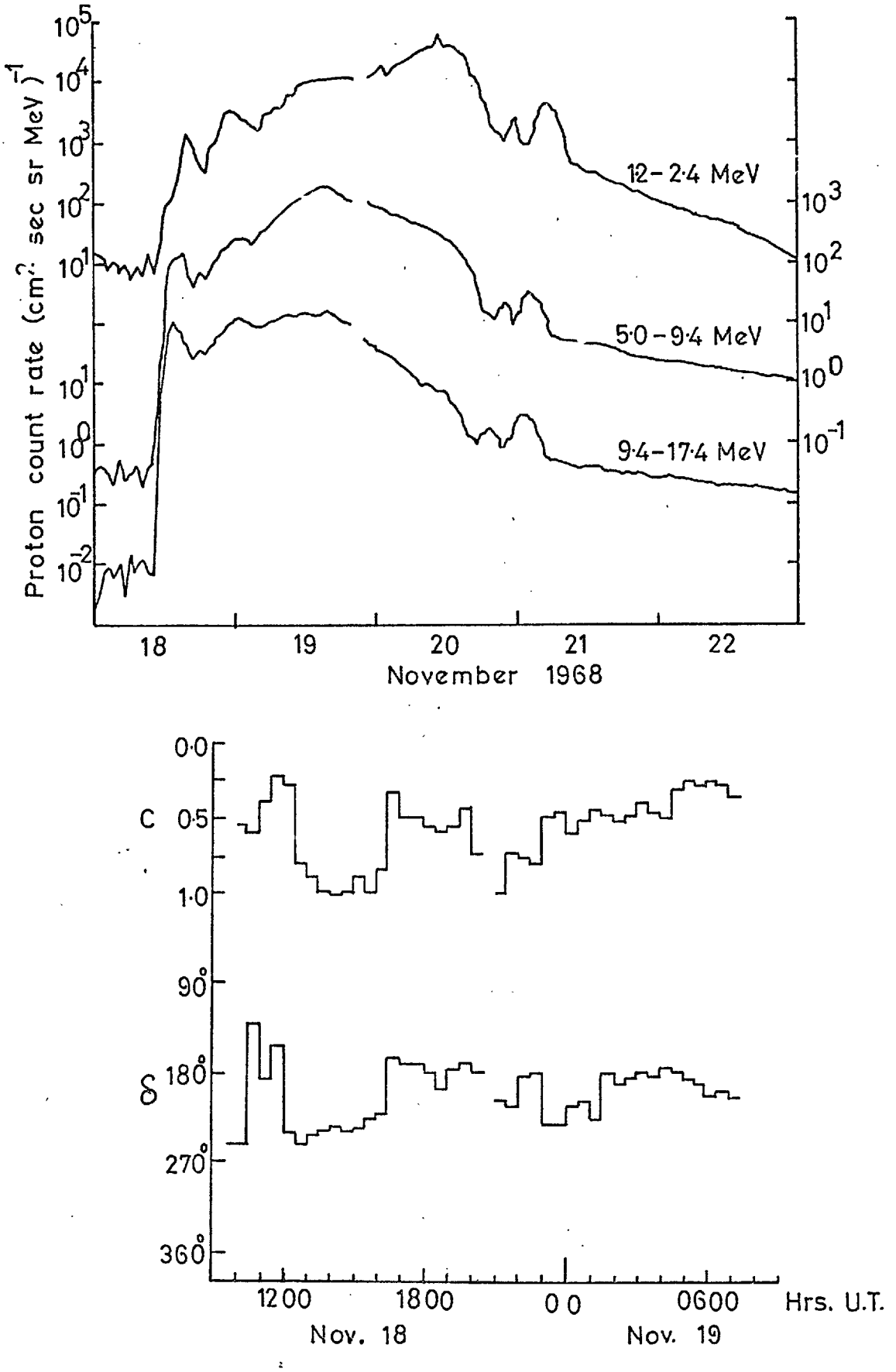

Figure 8(1): A. Counting rate profiles of solar protons of various energies for the 5 days following the November 18th event (after Lanzerotti 1970).
B. The parameters C and δ from the formula $N = A\left[1 + C\cos(\phi - \delta)\right]$ which was fitted by Venkatarangan et.al. (1969) to the anisotropy data in interplanetary space for 0.3 to 6.3 MeV protons during the event of November 18th.

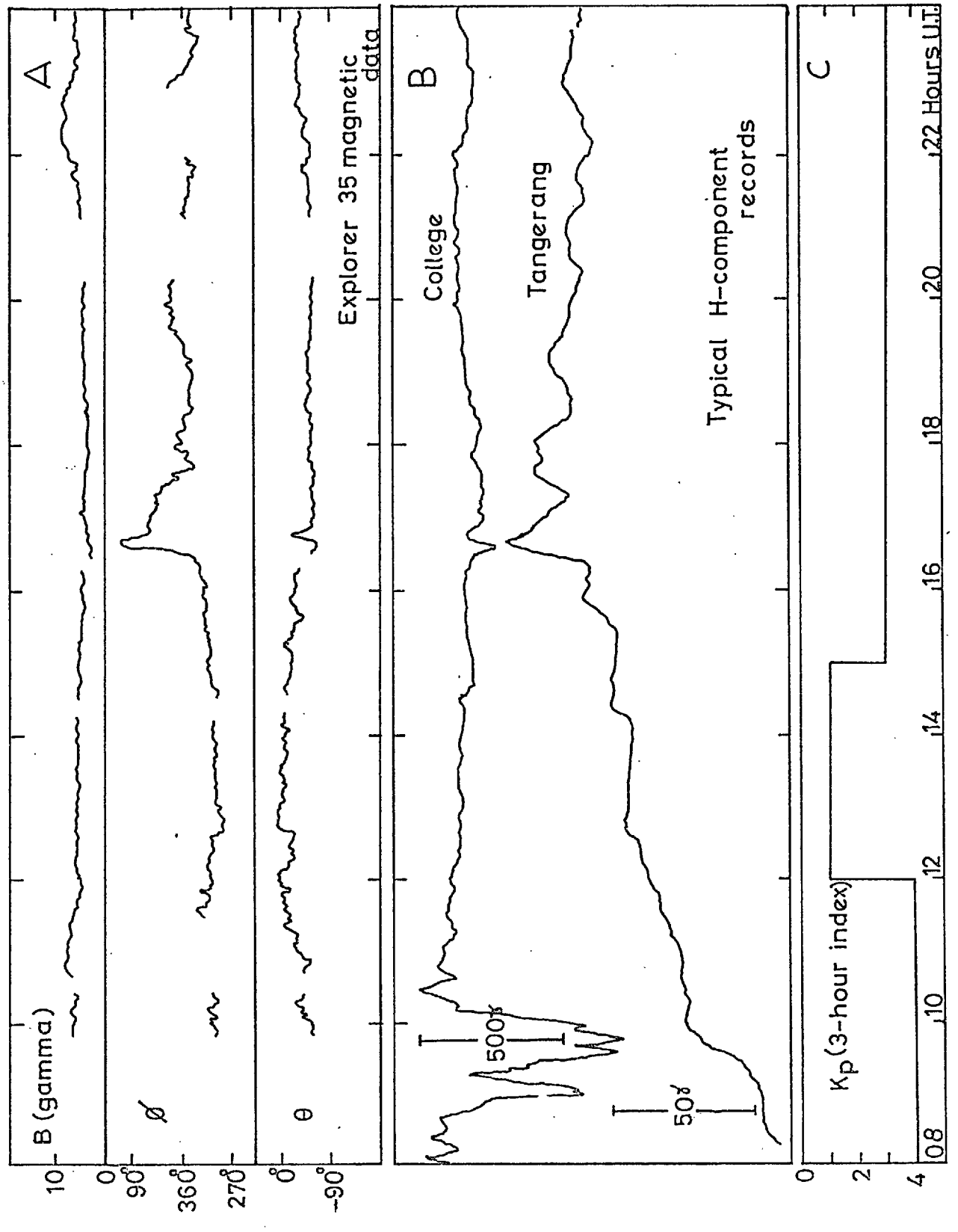

Figure 8(2): Magnetic conditions during November 18th 1968.

A. The Interplanetary magnetic field as measured by Explorer 35 and displayed in solar ecliptic co-ordinates.
B. Typical H-component records for the high latitude station, College and the low latitude station Tangarang.
C. The 3-hour index, Kp.

80° change in the direction of the anisotropy which also reduced in amplitude to $\sim$ 50%. This was coincident with a large change in the ϕ component of the interplanetary field and also with a sharp reduction in the proton count rate. At 2100 U.T. the count rate increased once more, the anisotropy enlarged and reverted to the Parker spiral direction. As the event proceeded the anisotropy reduced and became variable in direction.

Venkatarangan et.al. (1969) fitted an equation of the form

$$N = A \left[1 + C \cos (\phi - \delta)\right] \qquad 8.1.(i)$$

to the interplanetary data of solar protons in the range 0.3 to 6.3 MeV for a detector with four channels sampling different azimuthal regions in the ecliptic plane. ϕ is the spacecraft centred solar ecliptic azimuth such that $\phi = 180^{\circ}$ represents particles arriving from the solar direction, $\phi = 270^{\circ}$ represents those from the dawn direction. The values of C and δ measured by Venkatarangen et.al. (1969) are shown in Figure 8(1B).

8.3. Data Coverage for the Event of November 18th 1968.

During the first 12 hours of the particle event the satellite ESRO II passed over the northern polar cap from west to east on the night side along the trajectories shown in Figures 8(5-10). Data coverage from both experiments S-25 and S-27 was nearly 100% with only two small gaps during the passes beginning 12.56 and 14.29 U.T. Although southern polar cap data were available the satellite trajectories reached only low latitudes on the day side and did not move up to intersect open field lines until fairly late in the event.

Particle data from the experiment S-71E on board the satellite ESRO I

for the same period were also available. This experiment was a proton telescope consisting of two detectors, a totally depleted, silicon surface barrier detector and a caesium iodide scintillator with photomultiplier. Coincidence counts in the two detectors gave a three point differential spectrum in the energy range 6-30 MeV; counts in the solid state detector gave the intensity at 1-6 MeV and counts in the scintillator gave the integral intensity above 30 MeV. This experiment is further described in Thomas and Dalziel (1970).

The ESRO I trajectory was from midnight to noon across the northern polar cap and corresponding crossings by ESRO I and II always occurred within 15 minutes of each other. ESRO I was stabilized with respect to the geomagnetic field such that the axis of the viewing cone of S-71E was in the anti-field direction.

The experiment S-71E is described in Thomas and Dalziel (1970). The two channels of interest are the 1-30 MeV proton channel and the integral channel > 30 MeV.

In addition, interplanetary particle and magnetic data were available from the satellites Explorer 34 and 35. The former had a highly elliptical orbit and was near apogee at $\sim$ 30 R_E whilst the latter was lunar anchored. Both were well outside the magnetosphere on November 18th.

8.4. Presentation of the Data

8.4.1. Philosophy of the data presentation

The magnetic conditions within the magnetosphere during the first 10 hours of the Nov. 18th event were quiet, as is typical for post substorm times. The Kp index was $\leq$ 3 at all times. Under such conditions the Mead-Williams model field is believed tc represent the magnetosphere accurately,

as was discussed in Chapter 7. In the analysis performed here, the validity of the particle trajectory calculations presented in Chapter 7 is assumed and those trajectories are used as a basis for the interpretation of the solar proton data.

The data are presented in two ways. Firstly, a comparison is made of time averaged counting rates in different regions of the magnetosphere and in interplanetary space. This is to investigate the temporal response of these regions to the prevailing interplanetary conditions and also to obtain a time perspective of the event. Then a detailed presentation of the data is given to investigate the significance of some aspects of the polar cap proton counting-rate profiles.

8.4.2. Average Proton Counting Rates

Because of the good data coverage during the first 12 hours of the event, it is instructive to compare the proton counting rates over the poles with those in interplanetary space at different energies. This is done in Figures 8(3) and 8(4) for protons of energy < 17.5 MeV and > 30 MeV resp. Because of the coarse time scale of the observations these plots are indicative rather than definitive. Only data from the ESRO II satellite are used.

The interplanetary data were plotted as hourly averages. The auroral peak counting rates shown were the highest counting rates measured within the dawn and dusk auroral zone regions during each satellite pass. This gives some measure of the peak efficiency with which protons were admitted to and possibly retained in these regions.

The polar cap region was divided into the dawn and dusk sides by the point of intersection of the noon-midnight meridian with the satellite

trajectory which had been plotted onto the tail field projection of particle trajectories for the respective particle energy, see Figures 7(7) and 7(8). The counting rates in each half of the polar cap were then averaged over all data points irrespective of any structure that might be present.

Low energy plots - The interplanetary rate shows a trough around 1600 hrs which had completely recovered by 2100 hrs. A more careful examination of all the available data suggests that the time scale of the onset of the trough was probably a good deal faster than could be resolved by these hourly averages. This will be discussed more fully later but, bearing it in mind, it appears that the auroral peaks track the interplanetary rate with a delay which, as far as this scale can determine, is $\lesssim$ 1 hour.

The mean of the polar cap counting rates tracks the interplanetary rate in a less precise manner than do the auroral peaks and with a greater delay, $\sim$ 2 hours. It is interesting to note that in the first polar cap measurement subsequent to the change in interplanetary anisotropy direction ($\sim$ 1630 U.T.) the greater counting rate over the polar cap had changed from the dawn side to the dusk side.

It is dangerous to attach too much significance to the dawn : dusk ratios derived from these data before $\sim$ 1800 hrs since the data coverage on the dawn side was not good. The plot does, however, indicate a response, in the polar cap regions, which can be correlated with the prevailing interplanetary anisotropy.

> 30 MeV plots - The interplanetary flux at these energies reached a maximum earlier than the low energy proton flux and did not recover from the decrease to about $^1/_3$ the maximum rate which occurred at $\sim$ 1600 U.T. The auroral

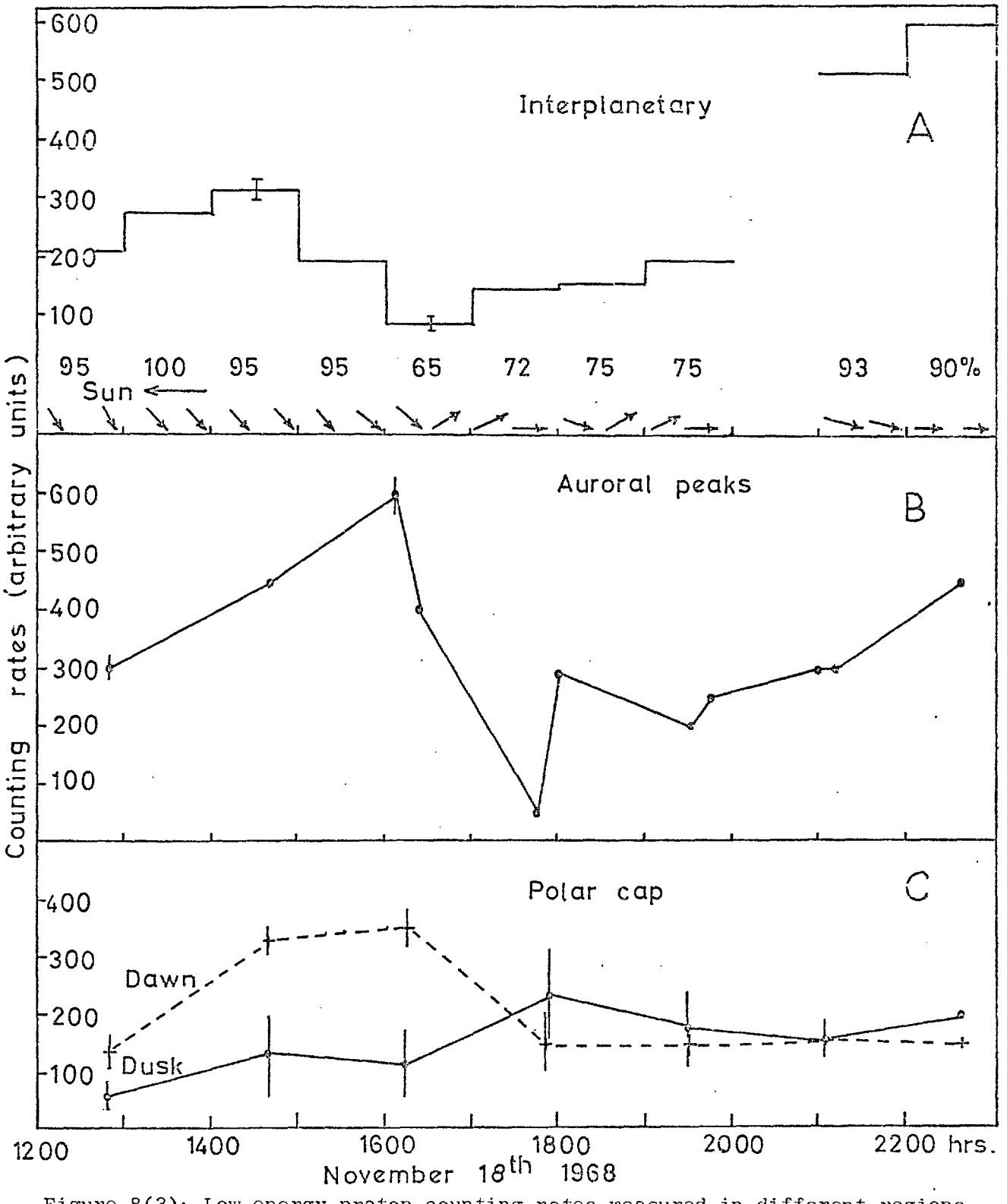

Figure 8(3): Low energy proton counting rates measured in different regions of space during November 18th, 1969.

A. Interplanetary counting rates measured by Explorer 34 and shown as hourly averages. The arrows indicate the direction of the anisotropy and the numbers indicate its magnitude in that direction as defined by C from formula 8.1(i), p.169 expressed as a percentage.

B. The peak counting rate occurring in the auroral zone regions of the magnetosphere measured by experiment S-27.

C. The mean counting rates measured by experiment S-27 over the dawn and the dusk sides of the 'open field line' regions of the polar cap. The regions were determined from the M-W model for a 12.5γ tail field.

All the counting rates are shown in arbitrary units.

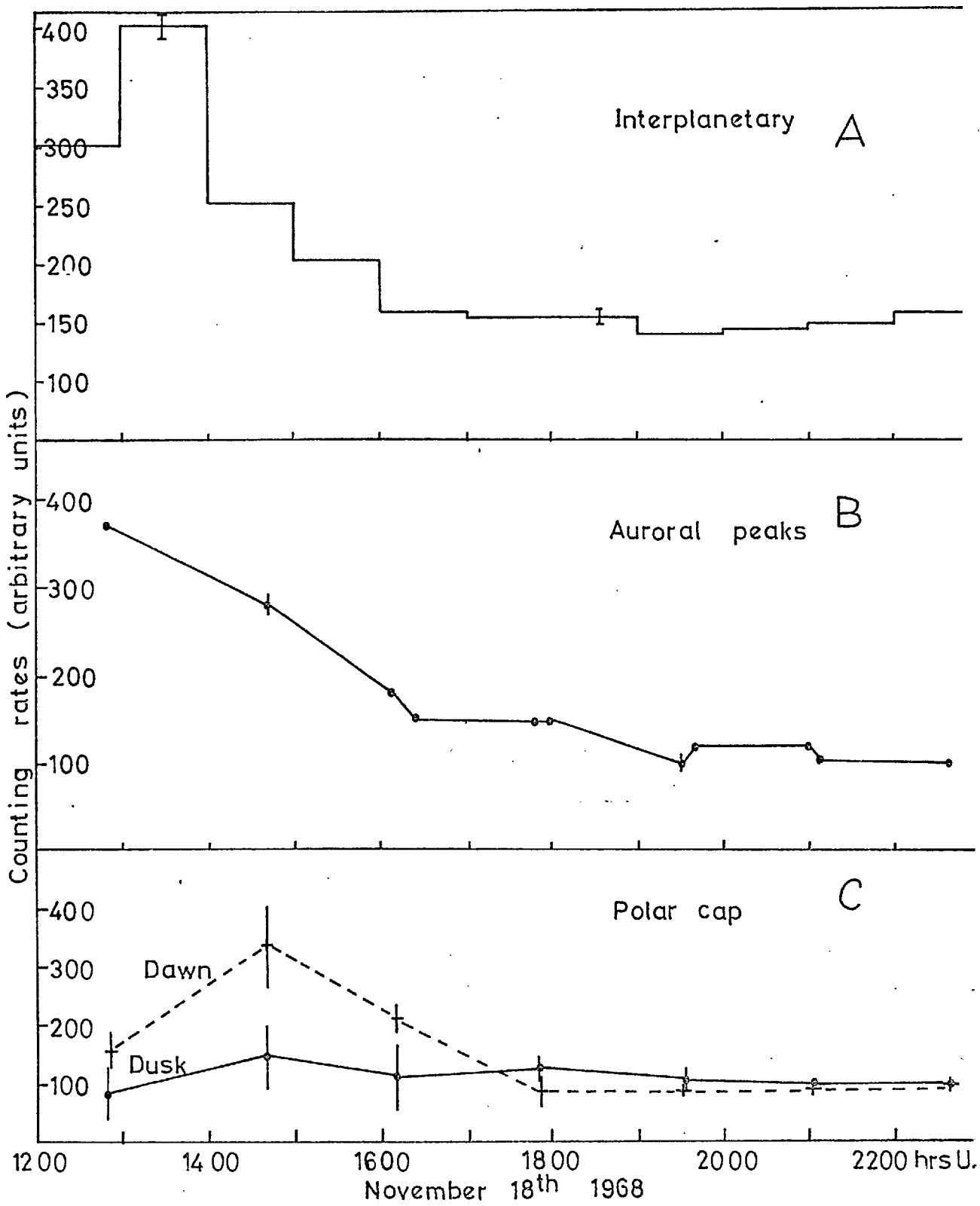

Figure 8(4): Counting rates for solar protons of energy > 30 MeV in different regions of space during November 18th, 1968.
A. Interplanetary counting rate measured by Explorer 34.
B. The peak counting rate occurring in the auroral zone regions of the magnetosphere measured by experiment S-25 302.
C. The mean counting rates of the dawn and dusk sides of the open field line regions of the polar cap, measured by experiment S-25 302.

The errors indicated in both 8(3) and 8(4) are one standard deviation for diagrams A and B and C.

peaks tracked the interplanetary flux accurately and with little discernible delay.

The polar cap counting rates indicate a delay of $\lesssim$ 1 hour and also demonstrate the change from dawn to dusk excess at 1800 U.T.

8.4.3. Preliminary Discussion of the Data

For a solar proton event suitably situated on the sun, the first particles to arrive at the earth do so by travelling along the Parker spiral directed field. Particle pitch angle distributions in interplanetary space are expected to be strongly field aligned at these times. As the event proceeds, low energy ($\lesssim$ 30 MeV) particles arrive at the earth having been convected out from the sun in the solar wind and the anisotropy becomes radial (McCracken et.al., 1971). A field aligned anisotropy was observed in the solar ecliptic plane for low energy particles during the early stages of the Nov. 18th event by Explorer 35 and since we are investigating only the first ten hours of the event it is assumed that the anisotropy maximum in the solar ecliptic θ-direction also followed the field lines. At higher energies ($\gtrsim$ 30 MeV), the field aligned anisotropy was assumed to exist only for the first six hours.

The discontinuous change in the direction of the azimuthal component of the interplanetary magnetic field $\sim 180^{\circ}$, that was observed by Explorer 35 at $\sim$1630 U.T. is taken as evidence that a discontinuity of some kind might have existed there. This could possibly have taken the form of a rotational or tangential discontinuity. Such discontinuities are believed to convect with the solar wind, i.e. at a velocity $\sim 220\ R_E$/hr. (This is substantially true even for the rotational discontinuity since the Alfven velocity, with which it is believed to propagate, is $<<$ the solar wind speed.)

Quenby and Sear (1971) have suggested that tangential discontinuities inhibit particle motions in a direction perpendicular to the discontinuity surface. Motion across the discontinuity is energy dependent with higher energy particles crossing it more easily than lower energy particles. This aspect of discontinuities could explain the existence of large particle gradients over small distances in interplanetary space.

Also at $\sim$ 1630 U.T. a factor 4 change in counting rate occurred in the low energy ($\sim$ 1 MeV) proton fluxes in interplanetary space within 15 minutes and at a time coincident with both the 180° change in interplanetary magnetic field azimuth and the S.I. observed at the earth (L.J. Lanzerotti, private communication). This correlation suggests that the magnetic field structure might have played some part in producing the particle gradient and, further, the observations may represent the passage of a tangential discontinuity.

Irrespective of their mode of entry, particles are believed to arrive at high latitudes over the polar caps after having entered the magnetotail at some distance from the earth (e.g. Michel and Dessler, 1970; Van Allen et.al., 1971). If in interplanetary space there exists a discontinuity, across which there is a change of flux of low energy particles, then this change in particle flux will reach the far regions of the magnetotail at the same time as the discontinuity. Since such discontinuities are believed to convect with the solar wind speed, their existence in interplanetary space could produce delays in the appearance of changes in particle populations over the polar caps after their observation in near-earth interplanetary space. High energy particles are not confined so efficiently by discontinuities and need not show pronounced delays of this type. The separation of two populations of low energy particles by the discontinuity, believed to

have been seen by Explorer 35 at 1630 U.T., and its subsequent drift down the tail could have been responsible for the time delay in the tracking of the interplanetary flux by the polar cap fluxes at these energies. This is in contrast to the better tracking at higher energies where the discontinuity would not have effected such an efficient separation, see figures 8(3C), 8(4C). It is interesting to note that, although the absolute counting rate tracks better for the higher energy particles, the change from dawn to dusk excess over the polar cap occurs at the same time as for the lower energy particles.

From investigation of particles trajectories (as in Chapter 7) it is to be expected that particles reaching the auroral zone regions do so primarily after having entered the magnetosphere from the dawn side of the neutral sheet. This being the case, then, the tracking of the interplanetary flux as measured close to the earth, by the auroral peaks should be rapid and counting rates in the peak will be greatest, for the same interplanetary flux, when the anisotropy is from the Parker spiral direction. Figures 8(3A and B) show that this pattern of behaviour was observed during the Nov. 18th event.

8.4.4. Detailed Presentation of the Proton Data

The comprehensive interplanetary data coverage during the Nov. 18th event makes it expedient in the analysis of the polar passes, to pay particular attention to the open field line regions, the counting rates on which only become meaningful in the light of such information. The low energy (< 30 MeV) proton data relevant to the first ten hours of the event are shown in Figures 8(5-10). Each figure consists of four diagrams, A-D, which are described below.

'A' shows the trajectories of ESRO I and ESRO II across the northern polar cap. The trajectories are presented on a polar cap 'regional diagram' as described in section 7.3.4 and illustrated in Figure 7(II). In the absence of magnetic tail field data a field strength of 12.5γ was assumed throughout. This is a typical field strength during such quiet-time conditions as prevailed during the second half of November 18th. The direction of the pass is indicated and the universal times at the beginning and end of the crossing are also given.

'B' and 'C' show the counting rates along the ESRO II and ESRO I trajectories respectively. The position (Λ , M.L.T.), to which any counting rate on the curve relates, is found by joining that point to the trajectory with a line parallel to the counting rate axis. The counting rate units for B and C are arbitrary, but consistent for the set of B diagrams and C diagrams. Those counting rates relating to 'permanently trapping' regions, 'pseudo-trapping' regions and 'open field line' regions are indicated by T, P and O respectively.

Diagrams 'D' show the tail field projection described in section 7.6. and shown in Figure 7(5). The projections are used here to show the satellite trajectories, which have been projected back into the tail, and the counting rates which were found there. The trajectories naturally correspond to those sections of diagrams B and C marked with an 'O'. The counting rates are represented by the lengths of the lines which point perpendicularly from the smooth, continuous satellite trajectories. The units are again arbitrary but, apart from Figure 8(5), are consistent for all diagrams D. Some attempt at normalisation of the counting rates from S-27 and S-71E has been made by comparing the rates in the auroral zones and at points of trajectory intersection. In view of the different energy ranges of the experiments, however,

and the different times at which the polar crossings took place, this comparison is not very meaningful and must only be used as a guide.

It is important to notice that the dawn side changes from the right to the left hand side of the page between diagrams A and D. In A the observer is looking onto the polar cap facing the sun (12% or 180° M.L.T.), whilst in D he is looking downstream into the tail in the anti-solar direction (180° solar magnetospheric azimuth).

Figures 8(11-13) demonstrate the corresponding data at a higher energy (> 30 MeV). The polar cap diagram and tail field projection are those for 44 MeV particles. Only 3 passes are shown at this energy because passes after ∿ 1800 U.T. recorded relatively low and steady fluxes with little polar cap structure. In flare events isotropy often occurs much earlier for particles of higher energies and such constant, isotropic fluxes, independent of the interplanetary field direction cannot yield much insight into magnetosphere entry mechanisms.

The pass beginning at 12.56 U.T. has also been omitted. At this time the proton spectrum was hard and since the S-25 experiment recorded all protons of energy > 30 MeV, a large contribution was to be expected from particles of energy > 100 MeV. This would increase the mean energy response of the channel to considerably greater than the 44 MeV and hence render particle trajectories, calculated at that energy, useless in this context.

Inspection of the S-25 data relative to the high energy (> 100 MeV) proto detector S-28, also on board ESRO II, showed this to be the case. Some contamination of experiment S-27 also occurred during this pass but it was slight and could not affect any conclusions drawn from this analysis.

The prevailing interplanetary magnetic field conditions (field strength and direction in solar magnetospheric latitude and longitude) are given at the bottom of each of Figures 8(5-13) at the time the pass was taking place and one hour beforehand.

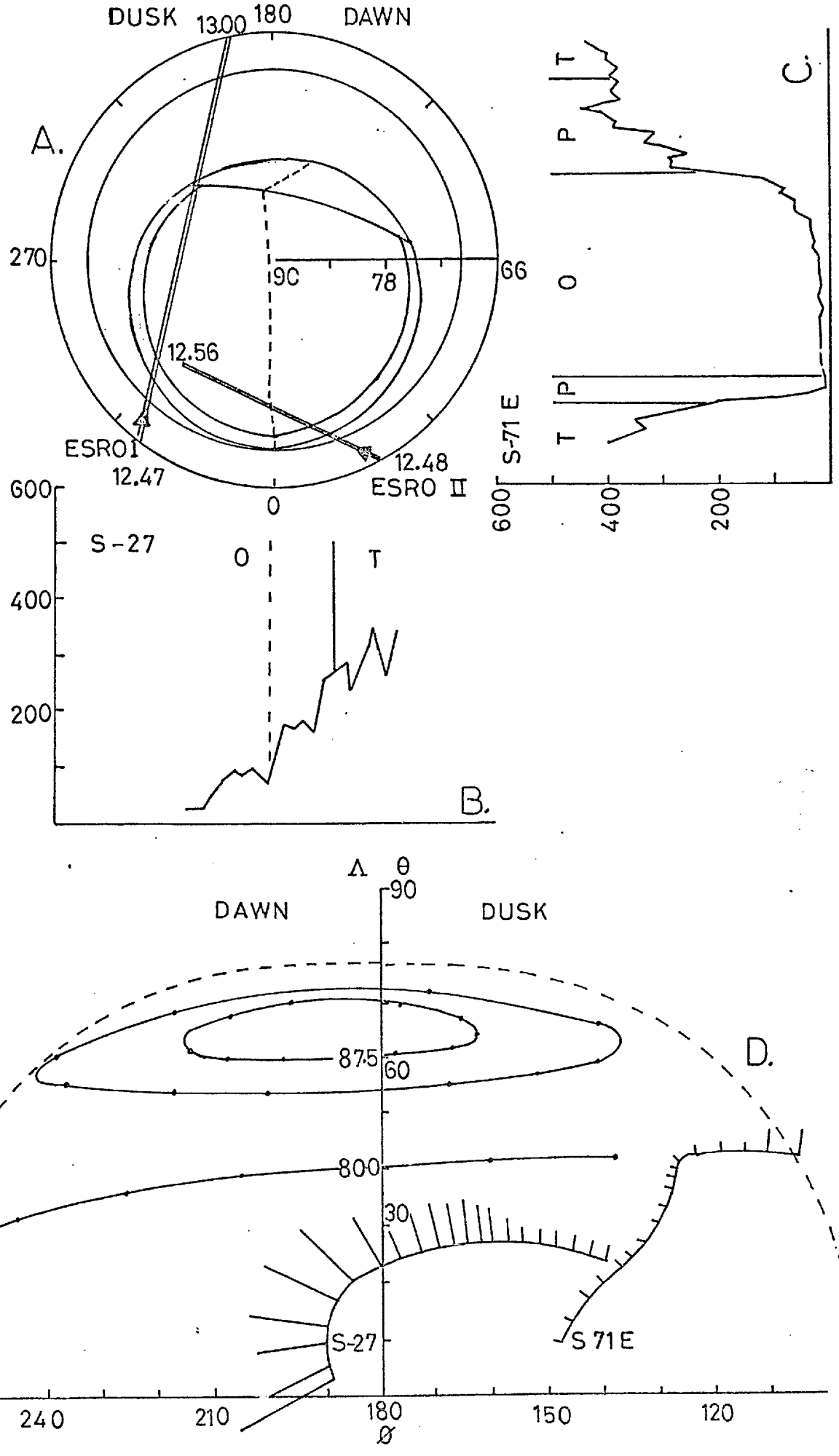

Figure 8(5): Pass 1 for low energy (< 30 MeV) detectors

B_{1200}, θ, ϕ = 6γ , + 24°, 310°

B_{1300}, θ, ϕ = 5γ , + 27°, 300°

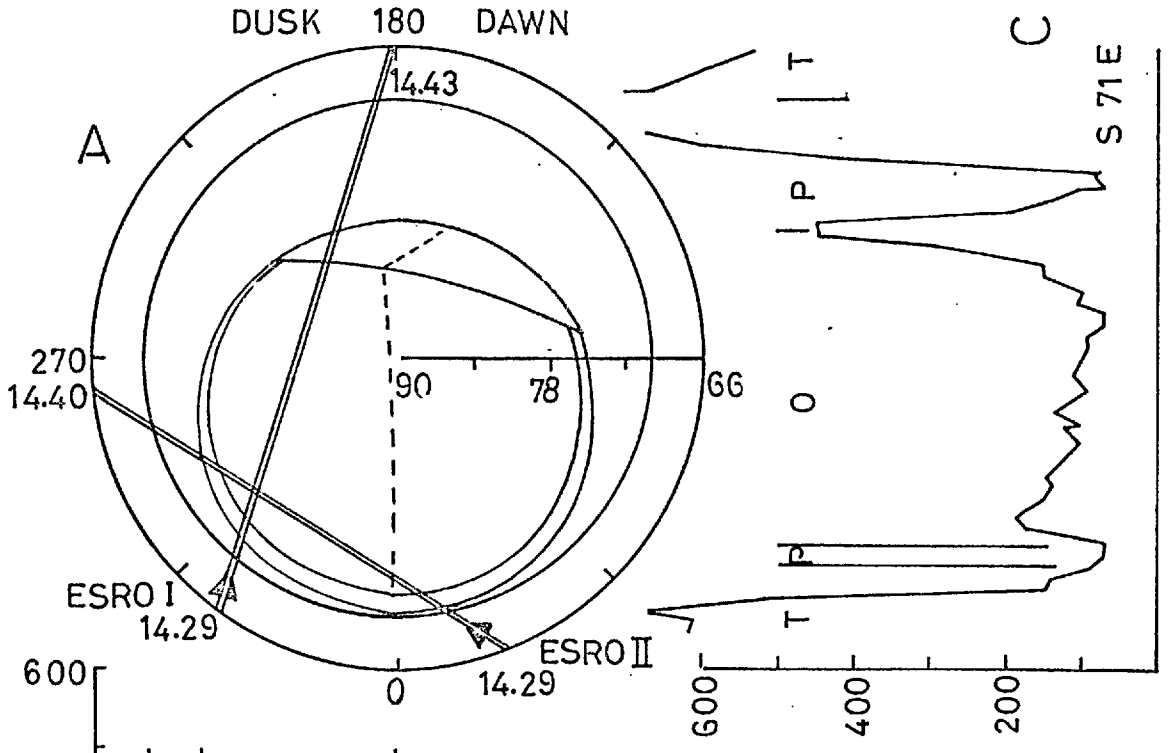

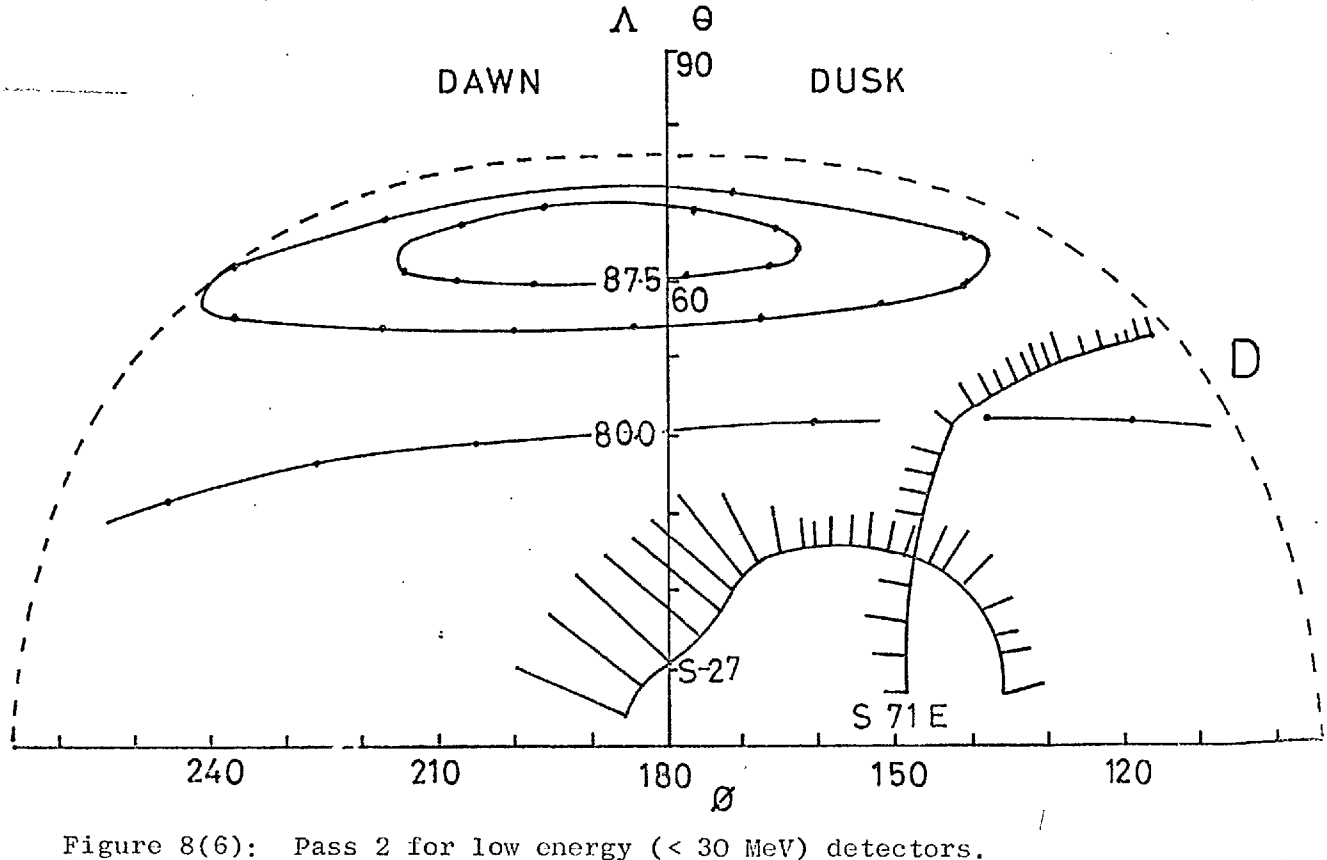

Figure 8(6): Pass 2 for low energy (< 30 MeV) detectors.
$B_{1340'}$, θ, φ = 5γ , +12°, 303°
$B_{1440'}$, θ, φ = 5γ , +13°, 302°

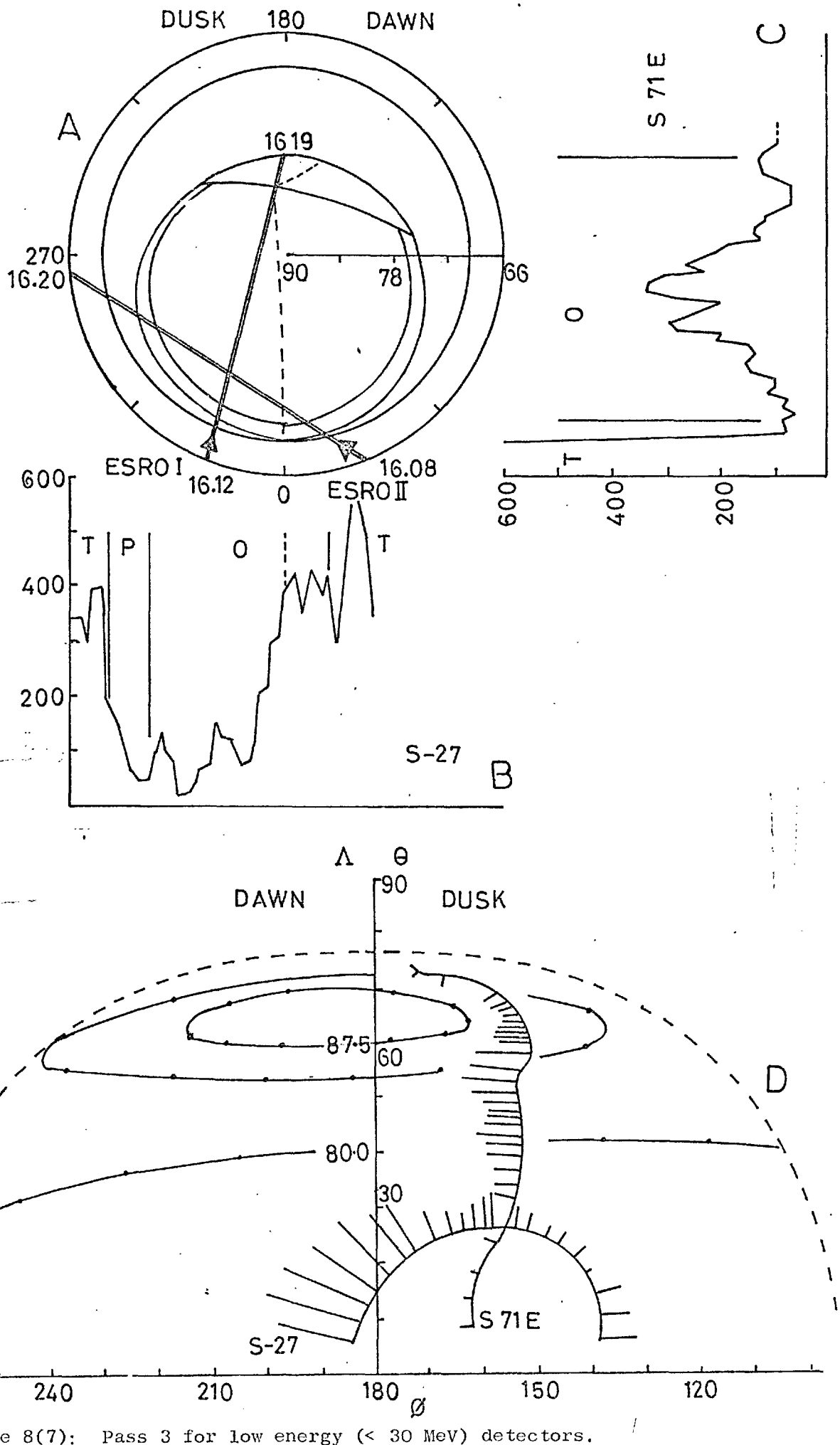

Figure 8(7): Pass 3 for low energy (< 30 MeV) detectors.
B_{1515}, θ, φ = 5 γ, +11°, 315°
B_{1616}, θ, φ = 4 γ, -13°, 325°

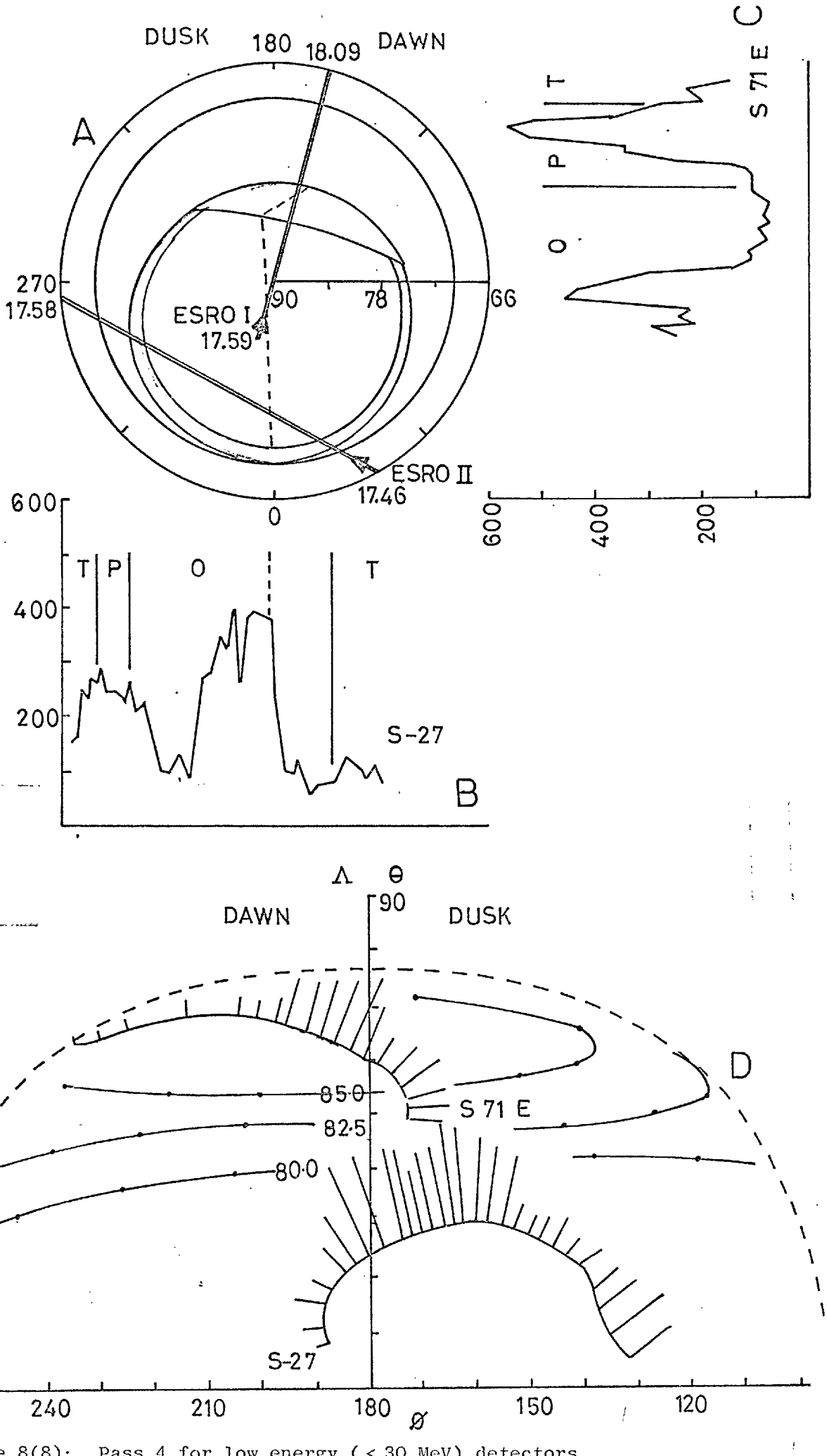

Figure 8(8): Pass 4 for low energy (< 30 MeV) detectors
$B_{1650'}$ θ, φ = 4γ , -62°, 65°
$B_{1750'}$ θ, φ = 3γ , -50°, 0°

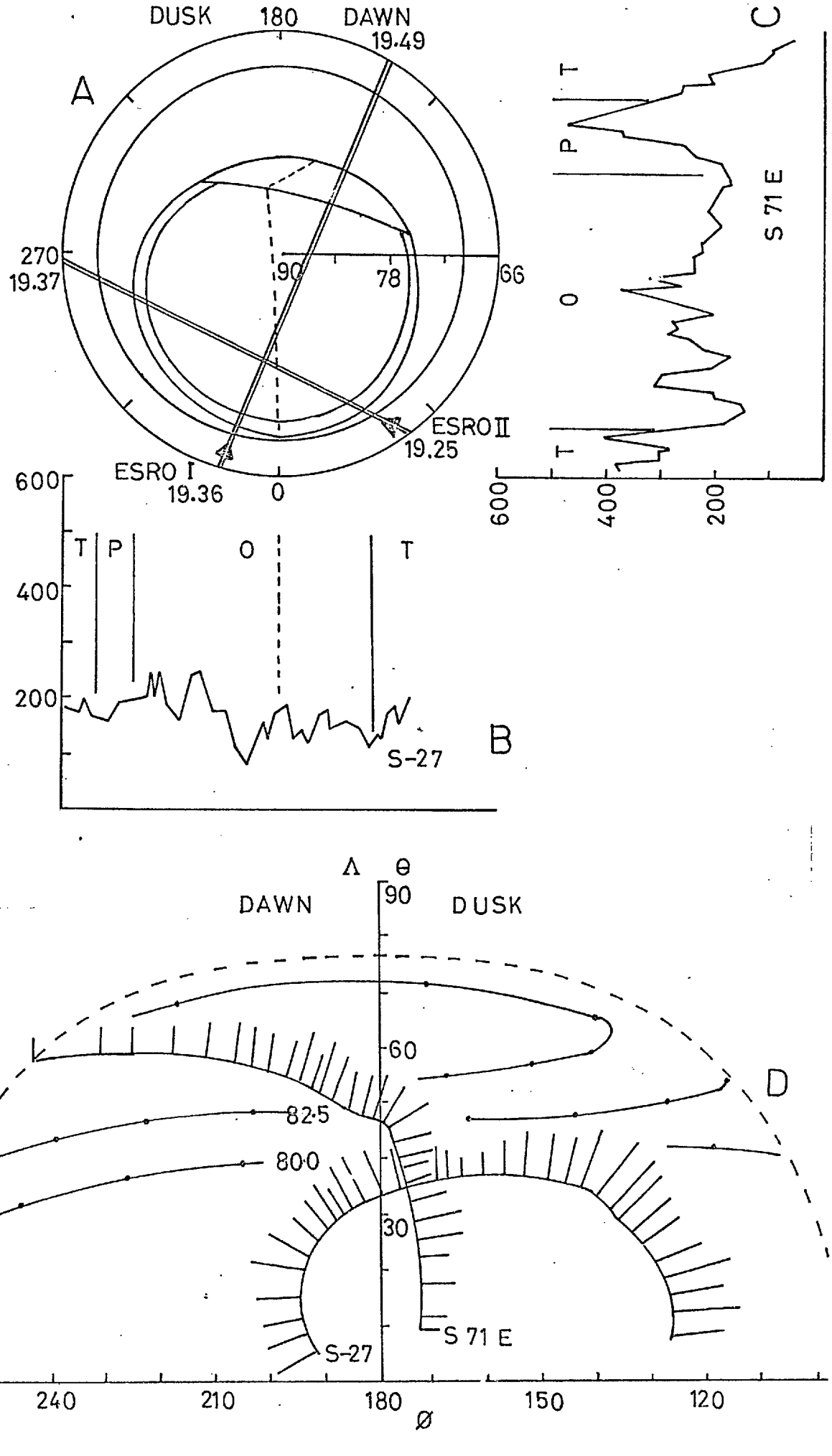

Figure 8(9): Pass 5 for low energy (< 30 MeV) detectors.
$B_{1830'}$, θ, φ = 4γ , -43 , 345
$B_{1930'}$, θ, φ = 4γ , -51 , 20

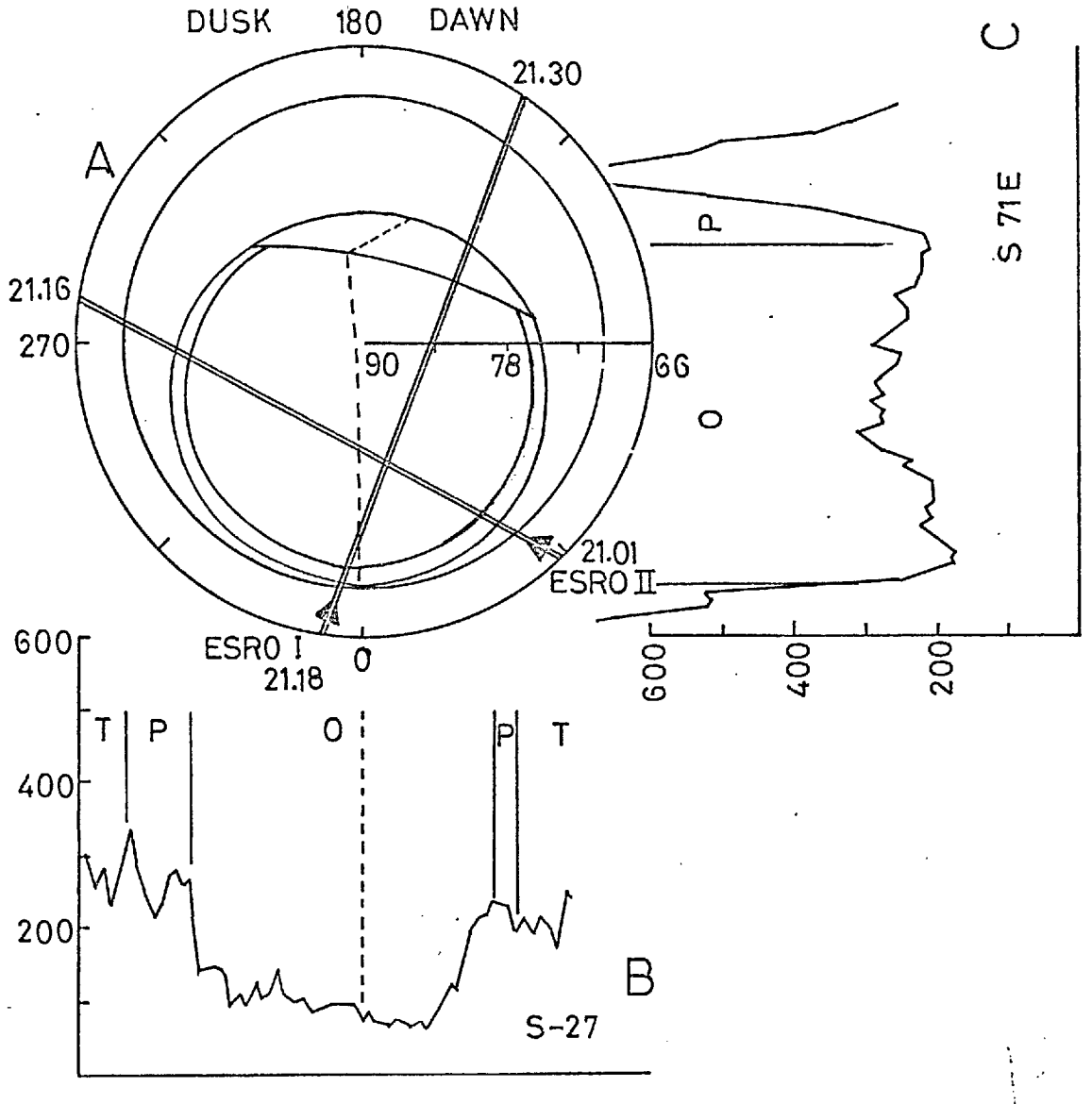

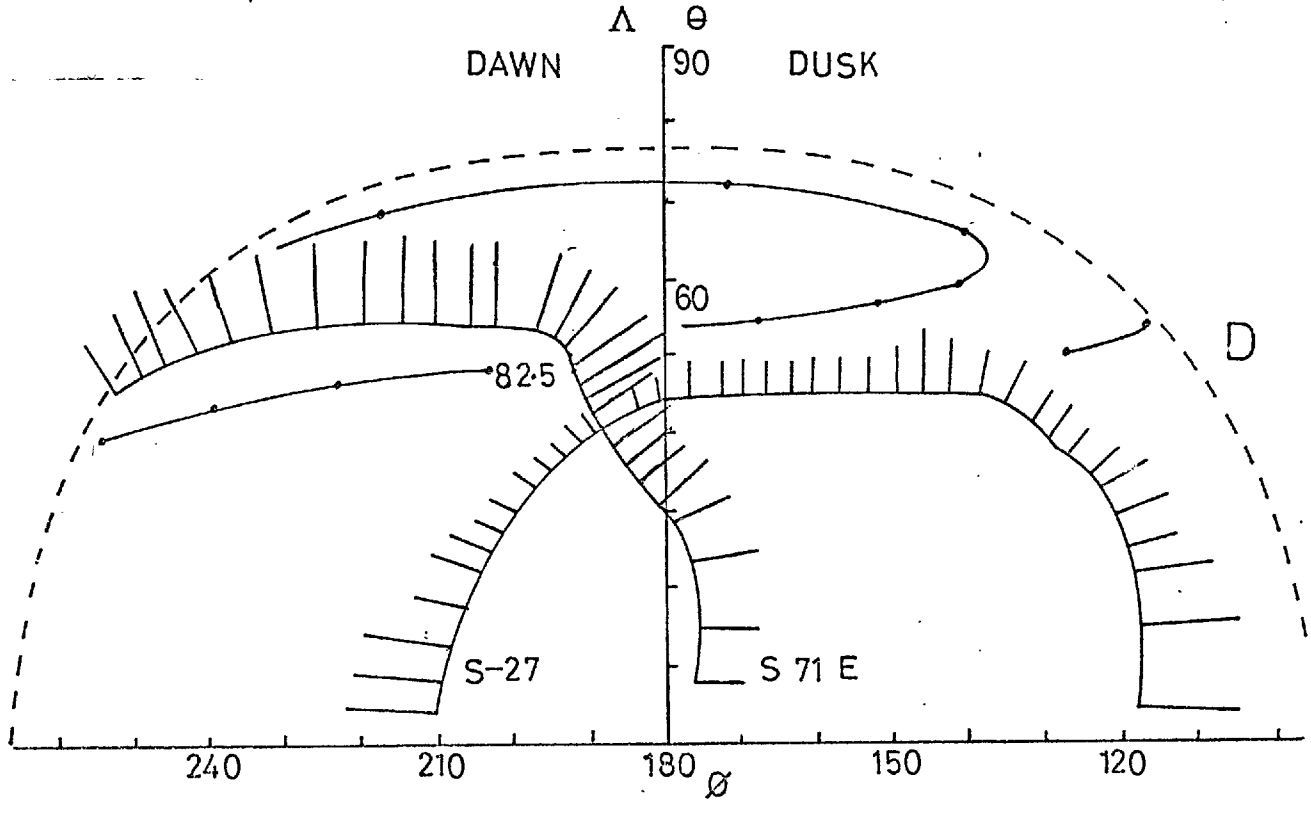

Figure 8(10): Pass 6 for low energy (< 30 MeV) detectors
B_{2018}, θ, ϕ = 4 Y, -45, 25°
B_{2118}, θ, ϕ = 4 Y, -45, 0°

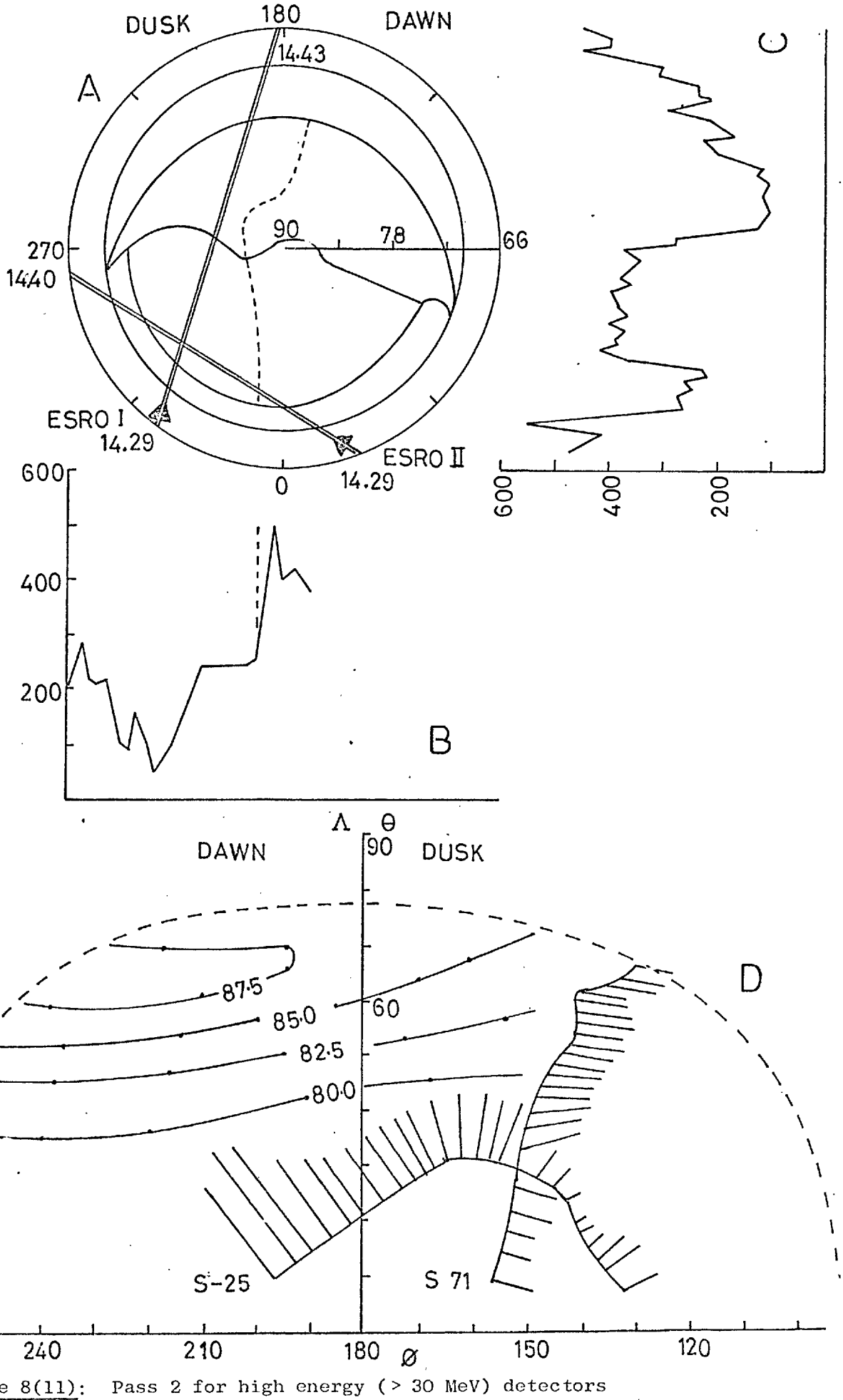

Figure 8(11): Pass 2 for high energy (> 30 MeV) detectors
B_{1340}, θ , φ = 5γ , +12°, 303°
B_{1440}, θ , φ = 5γ , +13°, 302°

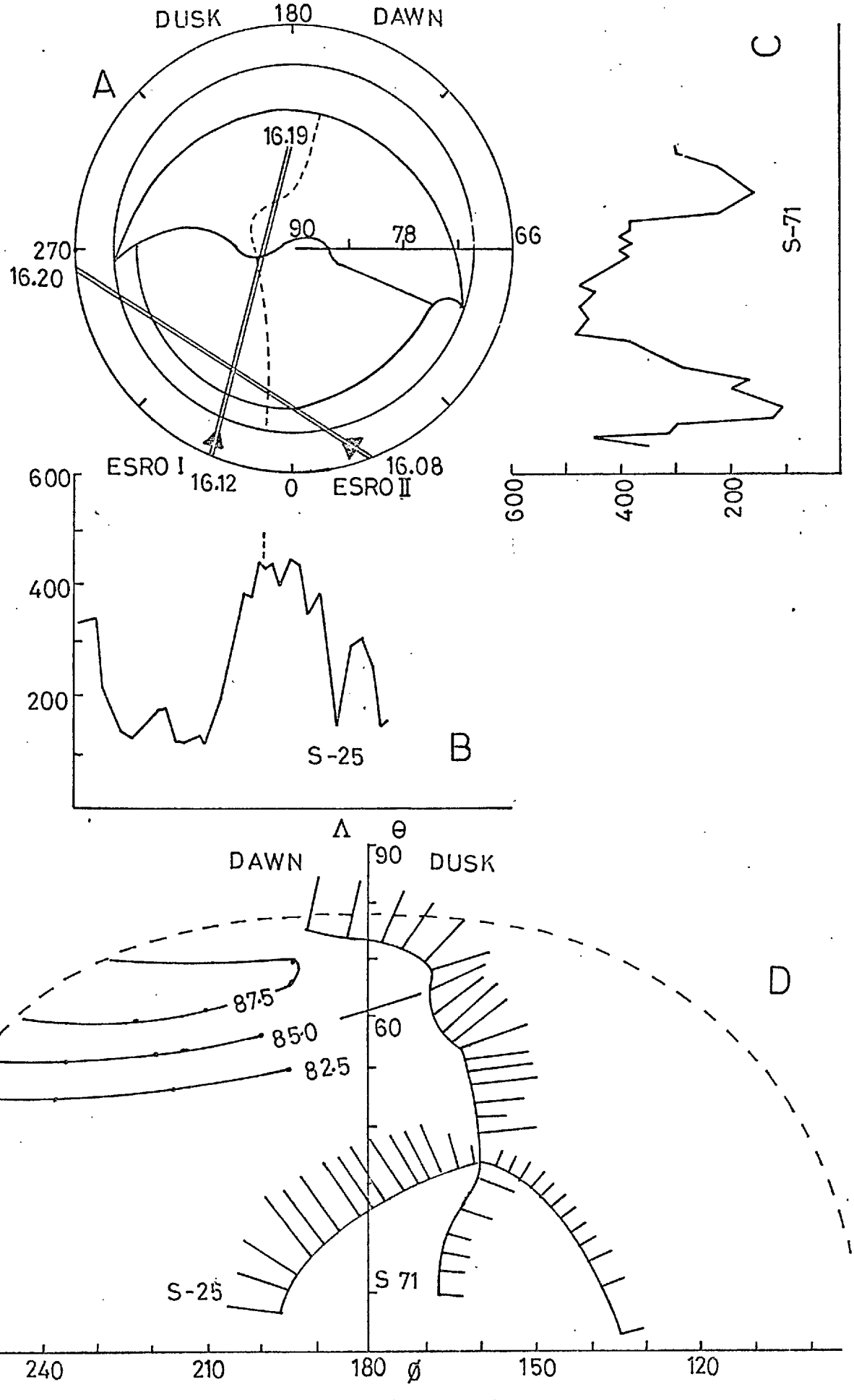

Figure 8(12): Pass 3 for high energy (> 30 MeV) detectors
B_{1515}, θ, ϕ = 5 γ, +11°, 315°
B_{1616}, θ, ϕ = 4 γ, -13°, 325°

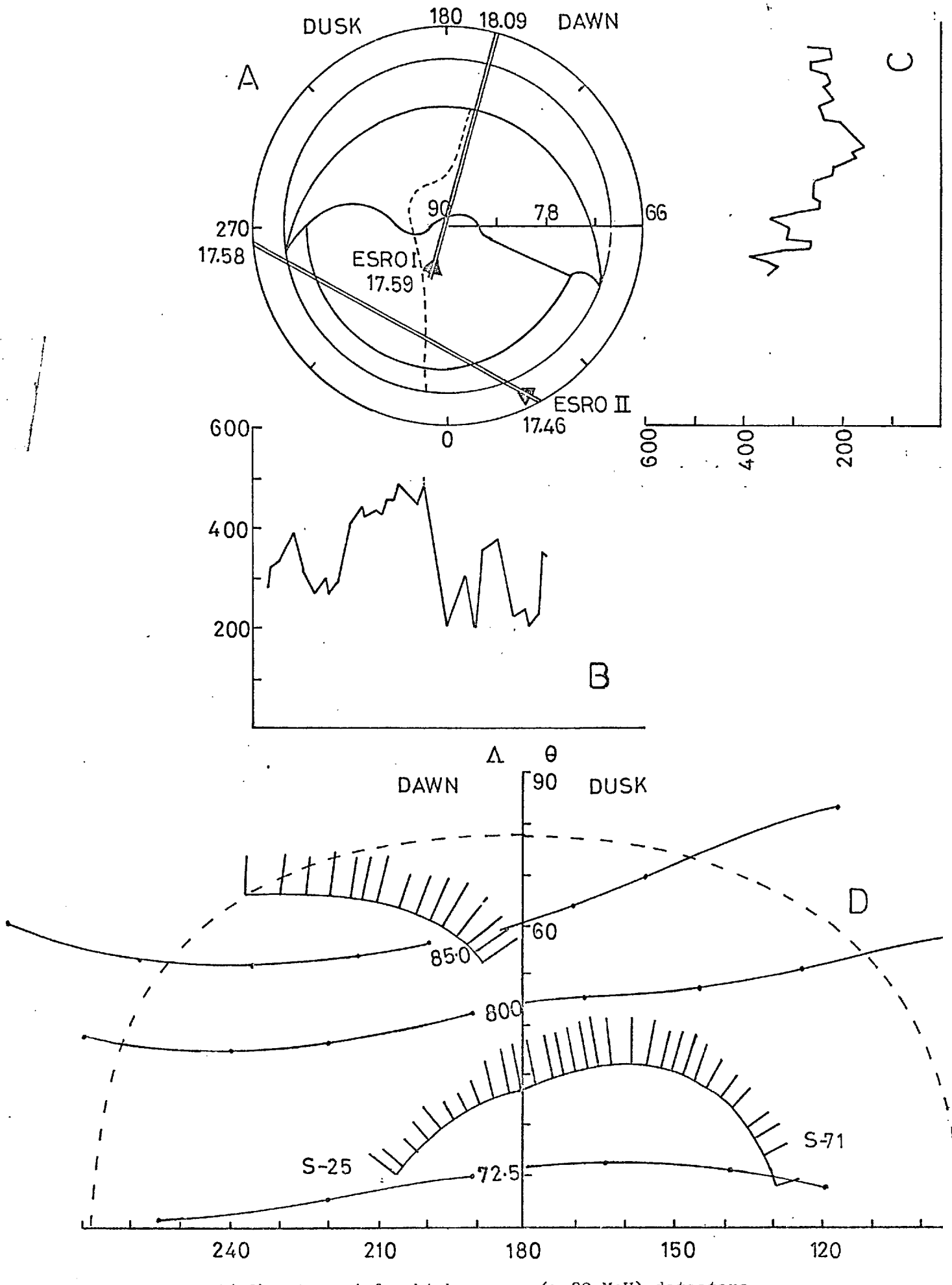

Figure 8(13): Pass 4 for high energy (> 30 MeV) detectors.
$B_{1650'}$ θ, φ = 4γ , -62°, 65°
$B_{1750'}$ θ, φ = 3γ , -50°, 0°

8.4.5. Description of the Results

Low energies (<30 MeV; Figures 8(5-10)) The trajectories of passes 1, 2, 3 for ESRO II were very similar, entering the open field line region on the dawn side close to local midnight and leaving at $\sim$ 1900 hrs M.L.T. on the dusk side. Diagrams 'D' for passes, 1, 2, 3 show that the counting rate profiles for S-27 were also very similar. All show high counting rates at all latitudes on the dawn side with some penetration of these high counting rates into the dusk region. This is especially noticeable during pass 2. Apart from this penetration region, the dusk sides of the diagrams exhibit much lower counting rates than do the dawn (typically $\sim$ $^1/_6$).

By comparison with high energy data, also obtained from an experiment on board ESRO II, it was seen that the small peak in the S-27 data at 2300 hrs M.L.T. during pass 1 was due to contamination by large fluxes from a high energy, proton impact zone. It is the only example of contamination that can be discerned in the whole period of data under consideration.

From pass to pass, the trajectory of ESRO I moved steadily across the polar cap from dusk towards dawn. In passes 1 and 2, S-71E observed a region of very low proton counting rate across the whole of the open field line dusk side with little structure except for a small, negative gradient away from the neutral sheet (pass 2, diag. D). In pass 3, however, there was a broad peak in the centre of the tail region with low counting rates near the neutral sheet and near the magnetopause.

A small peak was observed by S-27 in pass 3 at the intersection of the ESRO I and II trajectories. It appears that S-27 just clipped the region of enhanced proton counting rate, a cross section of which was 'seen' by S-71E.

It is interesting to note, in pass 2, a large peak in the region that

connected to the near-earth, dusk magnetopause. Also in pass 3 there is a 4:1 flux ratio between those regions connecting directly to the neutral sheet on the dawn and dusk sides, Figure 8(7B).

The prevailing interplanetary magnetic field during this time was directed along the Parker spiral ($\phi_{S.M.} \sim 315^{o}$). The magnetic conditions within the magnetosphere were generally very quiet throughout, ($1 \lesssim kp \lesssim 2$). Interplanetary particle data show that the dawn side of the magnetosphere faced the anisotropy maximum during the first 3 passes. The interplanetary flux reached a maximum at $\sim$ 1500 U.T. but shortly after 1600 U.T. there was a large decrease (see Figure 8(2)).

In pass 4, S-27 showed a dramatic departure from the pattern of the previous 3 passes. The high latitude central portion of the tail had a high counting rate which was almost identical to the rates hitherto recorded on the dawn side at lower latitudes. Also, the rates measured at lower latitudes in the tail showed a slight dusk excess over dawn. The S-71E detector showed that during this pass there was very little flux close to the magnetopause on the dawn side. Deeper in the tail the rates become much higher but, unfortunately, data loss at the beginning of the pass prevented comparison at the point of trajectory intersection. It does, however, appear that the whole of the central region of the tail was filled with particles while the edges remained depleted.

The particle discontinuity measured by Explorer 35 reached the earth sometime between passes 3 and 4 and, assuming the discontinuity to convect with the solar wind with a speed $\sim$220 R_E/hr, should have been $\sim$ 330 R_E downstream by 1800 U.T.

As in pass 3, there is a large flux difference in pass 4 between the dawn and dusk neutral sheet regions. This time however the dusk shows an

excess over the dawn. This is particularly interesting in view of the change in the interplanetary particle anisotropy direction between these two times.

Between 1700 and 1900 U.T. the interplanetary flux was low and showed a reduced anisotropy whose direction varied within the half-hour time scale on which it was measured, Figure 8(3). On average, however, the anisotropy maximum was directed from the east and impinged the dusk side of the magnetopause.

In pass 5 both S-27 and S-71E detected large amounts of small-scale structure. S-27 showed a small, but consistent excess in the dusk counting rate compared with the dawn and S-71E determined that the rates were still higher near the centre of the tail field than at its edges. The excess, however, was not as large as in the preceding pass.

Measurements in pass 6 failed to show the small-scale structure observed in the preceding pass and flux conditions appeared to have 'settled down' once again. At low latitudes, near the neutral sheet, there were considerably higher counting rates than at points deeper in the tail (S-27, diag. D). Also the dusk-dawn excess was represented by a smooth gradient across the tail.

ESRO I crossed the cap $\sim$ 15 minutes later than ESRO II and showed the tail to be filling up with particles once again.

High energies It is clear from the S-25 and S-71E measurements of protons $>$30 MeV shown in Figures 8(11D), 8(12D) that regions of high proton counting rate penetrated deeper into the dusk region of the tail field than did lower energy protons at that time in the event, Figures 8(6D), 8(7D). However at low latitudes in the tail, S-25 measured a region of much reduced flux

intensity on the dusk side, as was noticed at low energies, but the trough was less extensive than that measured by S-27.

There was a large difference in counting rates between those regions connecting directly to the neutral sheet dawn and dusk sides (S-25, Figure 8(11A,B)). Diag. C in Figure 8(11) shows that the number of particles which had direct access from the dusk magnetopause was small. This is contrary to the low energy situation.

An interesting feature is illustrated in Figure 8(12) where the ESRO I trajectory intersected the region whose particles enter from the near-earth magnetopause first on the dawn side and then on the dusk. On the dawn side there was a plateau of high counting rate but on the dusk side there was a trough. At that time the prevailing interplanetary anisotropy was from the dawn direction.

Figure 8(13) is similar to 8(8) in that it shows the maximum count rate to come from the central tail regions and also exhibits a dusk-dawn excess.

8.4.6. Summary of results

1. During the first 3 passes there existed in interplanetary space a large particle anisotropy directed along the Parker spiral field lines. The tail field projections demonstrate that during this time the dawn quadrant (facing the anisotropy) showed an enhanced counting rate over the dusk quadrant for proton energies up to or even greater than 30 MeV.

2. When a particle discontinuity existed some 300-400 R_E downstream the tail exhibited a high flux in its central region and low fluxes near the edges. A dusk enhancement in count rate over the dawn was seen in those regions where the count rates were low.

The high energy data exhibited similar features.

3. During passes 5 and 6 the prevailing particle anisotropy was from the east, although the direction varied considerably prior to pass 5. In response the tail showed a dusk excess count rate over the dawn and in pass 5 there was abundant small scale structure.

4. The dawn and dusk neutral sheet regions (which include the pseudo-trapping region since computed trajectories show this to be ultimately connected to the dusk side neutral sheet) show a great variety of structure. In particular the dawn and dusk sides seem to be able to support highly different counting rates at certain times.

8.5. Discussion

It has been seen from the data that the proton population within the geomagnetic tail responds directly to the prevailing interplanetary anisotropy. The tail also seems to be able to support very large flux gradients, pass 4 is a particularly good example of this. A major feature of the data is the speed at which changes in the interplanetary proton flux conditions are apparently reflected in changes in the proton distribution in the tail. The results obtained are now compared with the entry mechanisms discussed in chapter 7.

8.5.1. Comparison of Results with the Diffusion Model

- Passes 1, 2 and 3 demonstrate persistent, highly asymmetric dawn-dusk counting rates. Later in the event, passes 5 and 6, the asymmetry is seen to be present in the reverse sense. Michel and Dessler (1970) suggest that diffusion occurs into two separate regions but it is difficult to see how either alternative could be responsible for such gradients. In the 'well-formed' tail region they suggest that there is strong draping of interplanetary field lines around the magneto-

pause, which also implies good coupling of low energy particles around the boundary. In addition Montgomery and Singer (1969) nave shown that pitch-angle distributions of low energy ($\sim$ 1 MeV) particles become isotropised at the magnetopause and these circumstances predict a uniform particle flux around the boundary. Hence, unless the diffusion coefficient varies in some anomalous way across the tail, dawn-dusk gradients do not seem a reasonable result of this diffusion process. In the 'break-up' region each separate filament should see the same incident flux (nearly) and once again flux gradients do not seem reasonable.

In passes 1, 2 and 3 the high and low counting rate regions are separated by very sharp, edge like boundaries, e.g. in pass 2 the counting rate falls by a factor ~ 4 in a tail region ($\phi < 10^{o}$, $\theta < 5^{o}$). If diffusion were responsible for bringing particles into the tail it would be expected that any resulting gradients would be smooth rather than precipitous as is seen here. Such a criticism could break down if the filaments in the coherent part of the tail changed their position within the tail cross section with their distance down the tail, such that filaments at the centre of the tail near the earth might reach the surface at greater distances.

In response to the sharp reduction in the interplanetary proton flux, probably associated with the magnetic discontinuity which was evident between passes 3 and 4, the tail is seen, in pass 4, to support a central region of high counting rate surrounded by an area of low counting rate. Once again the edges between the regions are very sharp and, on a diffusion model, can only be explained by diffusion into different tail regions at different distances. Since the lower interplanetary counting rate results from a later particle population, the implication is that the area of lower counting rate in the tail represents regions where particles have diffused in nearer the earth whilst the high count areas represent regions of access further

from the earth. The time scale for diffusion into the 'well-formed' near region of the tail is required by Michel and Dessler (1970) to be $\sim$ 5-20 hours, whereas the time observed here for the change from high to low count rate is $\lesssim$ 90 minutes (i.e. one satellite pass). There is serious conflict here.

Michel and Dessler (1970) expect rapid access of protons in the break-up, filamentary region of their tail model. Assuming that access is immediate for this process and assuming also that the interplanetary magnetic discontinuity does indeed separate regions of high and low proton population whilst being convected in the solar wind, an upper limit to the length of the coherent tail required by their model can be estimated. By the end of pass 5 the whole tail had responded to the decrease in interplanetary flux, i.e. the low flux region had reached a distance at which the tail had broken into filaments. Assuming that the discontinuity had reached the earth at the end of pass 3 then it must have convected some 10^3 R_E downstream by the end of pass 5 (assuming a solar wind speed $\sim$ 500 km/sec). Hence the upper limit to the length of a coherent tail is $\lesssim$ 10^3 R_E, a result that does not agree very well with the 2.10^3 to 10^4 R_E suggested by Michel and Dessler (1970).

8.5.2. Comparison of the Data with the Reconnection Model

It does then appear that a diffusion process is incapable of explaining the observed features of the proton profiles and attention must now be turned to a reconnection type of model.

Van Allen et.al. (1971) used the early reconnection model of Dungey (1961, 1963) to explain a large excess of low energy protons that was observed over the northern polar cap, as compared with the southern polar cap, on January 24th, 1969. At this time an interplanetary proton flux was ob-

served to be anisotropic with a strong southward component (see Figure 7(2)) and particles could follow the reconnected field lines (provided

$$\frac{\rho \cdot \nabla B}{|B|} \lesssim 0.1$$ where ρ is the particle gyroradius in the magnetosheath field B.)

As pointed out by Morfill and Quenby (1971) and Durney et.al. (1972) this model can also apply at higher proton energies provided the radius of curvature of the reconnected field lines is large ($\sim$ several hundreds of R_E) and, indeed, appears to do so during the proton event of Feb. 25th when the interplanetary flux had an anisotropy maximum directed southward and a proton excess was again seen over the northern polar cap. On Nov. 18th, however, there was a northward maximum to the interplanetary flux but the proton excess was again seen over the northern cap whilst the model would predict a southern polar cap excess. It was clear that the model did not offer a complete explanation of the observed phenomena.

One aspect of this early Dungey model is that reconnection of the terrestrial and interplanetary fields occurs along smoothly connected lines of force that change their orientation through bends of radii large compared with the gyroradii of low energy protons. Thus, low energy particles in interplanetary space that are following field lines, will continue to do so around such bends and will find access to the polar caps. Hence, if the interplanetary proton flux and pitch angle distribution are constant along the length of the tail then, irrespective of that pitch angle distribution, the whole of the polar cap should be uniformly distributed with particles. In the case of the Nov. 18th event, although the pitch angle distribution remained constant the interplanetary flux between 1230 and 1630 U.T. varied and a tail flux gradient could be predicted from this model along the Z_{SM} direction. This cannot, however, explain the dawn-dusk asymmetry that was

observed to persist during this phase of the event and again this model seems to be inadequate.

8.5.3. Proposed Model to Explain the Data

Instead of Dungey reconnection, Morfill and Quenby (1971) have suggested a model of the magnetopause based on the earlier magnetotail model of Axford (1965). The magnetopause is represented by a rotational discontinuity during times of reconnection: experimental evidence of this was presented by Sonnerup and Cahill (1967, 1968). Using a magnetometer on board Explorer 12 they concluded that of the magnetopause boundaries observed, one third were more likely to be rotational than tangential discontinuities. Flux, on average, is lost uniformly around the region where the discontinuity is rotational, and reconnected field lines are often sharply kinked there. Such flux loss implies a diverging tail field, evidence for which was given by Behannon (1970).

After examining high energy proton data during two solar flare events, Morfill and Quenby produced their idealized model, shown in Figure 8(14).

The model requires that field lines from different regions of the polar cap reconnect across the magnetopause at different distances down the tail; field lines emanating from points deeper in the polar cap extend further down the tail. Since particles travelling along field lines in the tail follow them accurately, then the positions at which these particles arrive over the polar caps are determined by the points where the field lines, to which they were tied, reached the surface of the magnetopause. If magnetic flux is assumed to be lost uniformly through the magnetopause, it should be possible to map 'equal flux contours', the magnetic field lines in which connect out at the same distance down the tail and the particles lying in which originated from the same population.

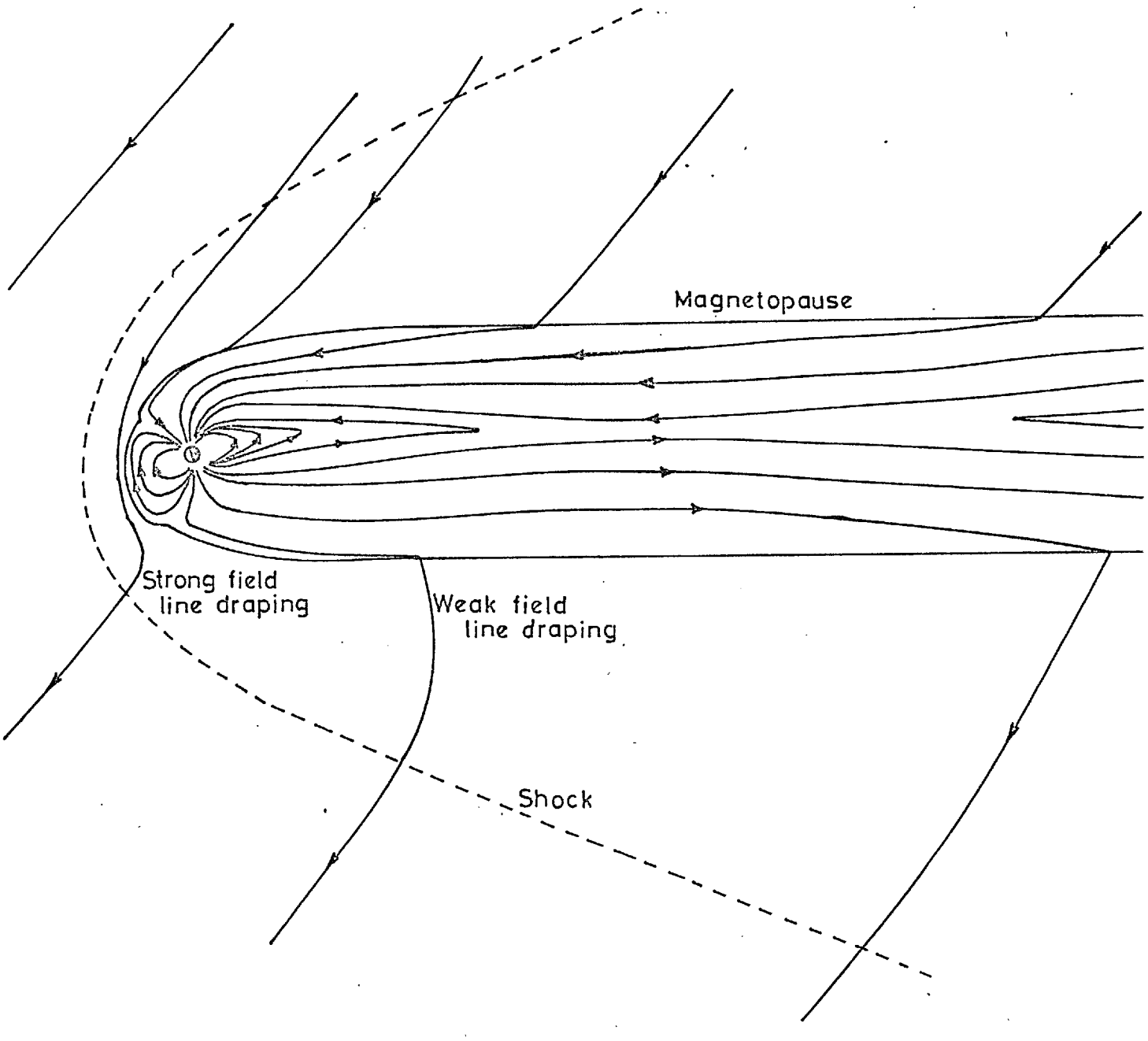

Figure 8(14): A model of the magnetosphere and local interplanetary field based on the reconnection theory of Axford (1965) and proposed by Morfill and Quenby (1971).

The results of Behannon and Fairfield (1969) suggest that at fairly large distances down the tail ($\gtrsim$ 40 R_E), where the shock is weak, the magnetosheath field is very similar to the interplanetary field even close to

the magnetopause. It is suggested that there is much weak draping of the interplanetary magnetic field over the magnetopause in these regions in addition to some reconnection. These features are illustrated in Figure 8(15). The maximum gyroradius of a 5 MeV proton in a 5γ interplanetary field is $\sim$ 12 R_E, thus any such particles which are 'tied' to field lines that are $>$ 12 R_E away from the magnetopause cannot possibly interact with the boundary.

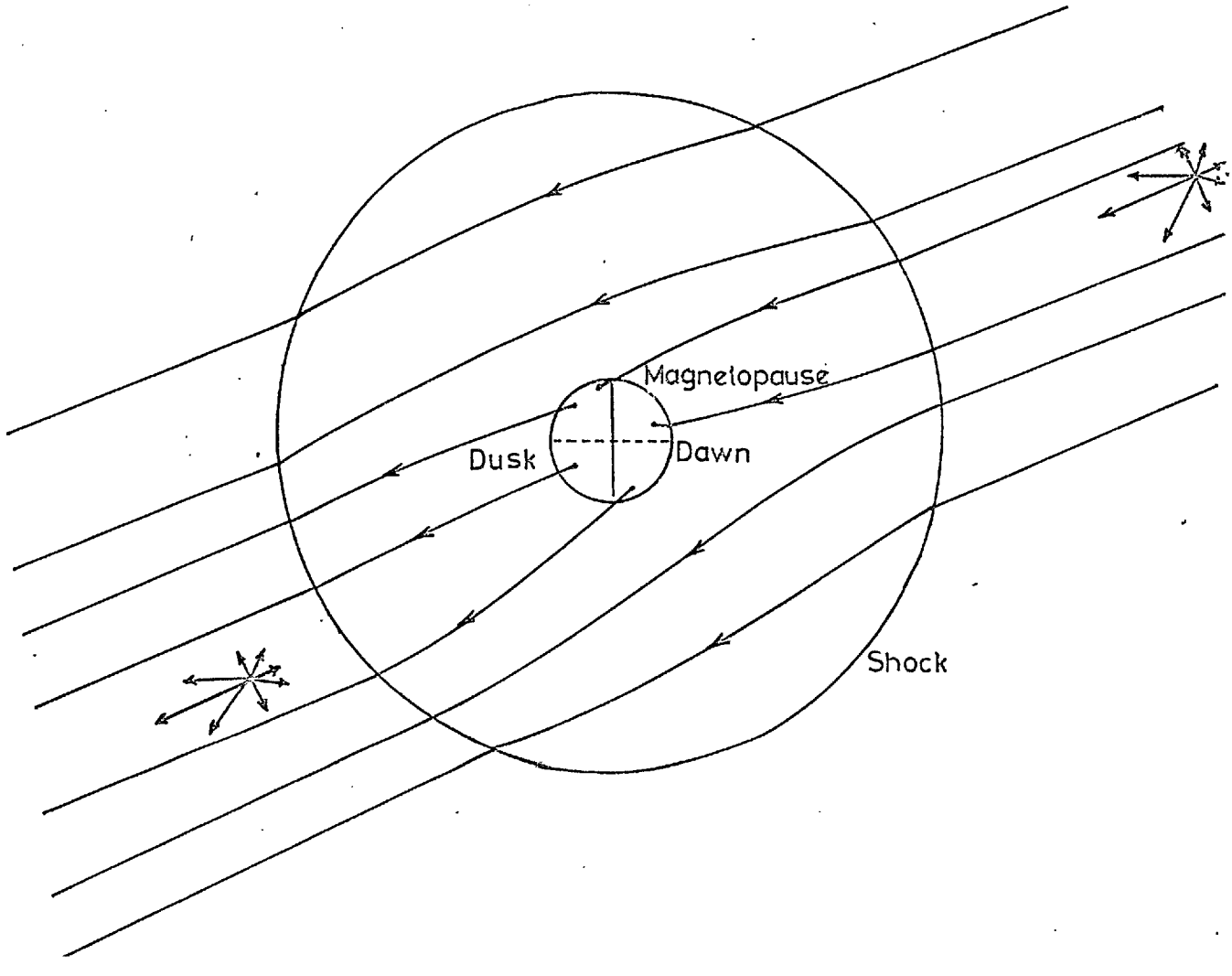

Figure 8(15): A cross-section of the magneto tail and shock showing reconnectin and draped field lines. This illustrates how isotropisation of low energy particle fluxes at the magnetopause will not prevent a response to the interplanetary anisotropy within the tail.

It has been mentioned that low energy particles impinging the magnetopause will tend to lose any pitch angle anisotropy distribution due, probably, to their interaction with irregularities on the magnetopause surface, e.g. Kelvin-Helmholtz instabilities (Southwood, 1968). Such an effect was observed by Montgomery and Singer (1969). Even so, it can be seen in Figure 8(15) that the side of the magnetopause facing an interplanetary particle anisotropy maximum will have a greater number of particles impacting it than the side facing the anisotropy minimum. Thus all points on the magnetopause surface sample isotropic proton distributions, the densities of which differ according to the direction in which each part of the magnetopause is looking with respect to the interplanetary anisotropy and magnetic field. This situation will be maintained provided there is no particle coupling around the magnetopause within $\sim 10\ R_E$ of the surface (e.g. by strong field line draping or penetration via the neutral sheet).

In summary, then, it is proposed that between the interplanetary and magnetotail field regimes there exists, at times, a rotational discontinuity type of magnetopause boundary. Such boundaries are characterized by a perpendicular magnetic field component across them. Thus if an isotropised particle distribution exists on one side of the boundary, penetration across it can be achieved by particles following the field lines reconnected across the discontinuity. Also, if the isotropised flux varies around the boundary then polar cap structure can result.

With these assumptions the model can be applied to the interpretation of the results presented in Figures 8(5-13).

8.5.4. Comparison of the Model and Results

An explanation of the difference in the dawn-dusk proton counting

rates across the tail follows directly from the fact that field lines reconnecting across different sides of the magnetopause sample different parts of the pitch-angle distribution prevailing in interplanetary space. Neither does the existence of sharp 'edges' between regions of high and low counting rate present a problem, since this simply results from particles following field lines emanating from points which are close together in longitude at the surface of the earth, ultimately reconnecting out across different sides of the magnetopause. In this entry mechanism there is almost immediate access across the magnetopause and hence the rapid change in the direction of the tail gradient in response to the change in the interplanetary anisotropy direction between passes 3 and 5 is also a natural consequence of this mechanism.

Field lines from different regions of the polar cap connect across the magnetopause at different distances down the tail and the existence somewhere along the tail, in interplanetary space, of a magnetic discontinuity which separates different populations of low energy particles could explain many of the features of pass 4. For both the S-27 and S-71E data the counting rates decrease towards the magnetopause (see diag. 8(8D)) where field lines reconnect close to the earth and would see the later, lower flux. They are, however, high towards the centre where field lines reconnect across the magnetopause a long way down in the tail and, if this occurred further from the earth than the distance the discontinuity had reached, would see the higher, earlier population. The edges separating the counting rate regions are sharp, as would be expected if the discontinuity were a thin feature. Examination of the interplanetary magnetic data, Figure 8(2) and high resolution particle data (L.J. Lanzerotti, private communication) showed both the magnetic and associated particle discontinuities to be thin.

Also, provided this interpretation is correct and the discontinuity convects with the solar wind speed, a lower limit of $\sim$ 400 R_E can be deduced from Figure 8(8) for the length of the coherent tail. Since there is no indication of the high proton population during pass 5 it is not unreasonable to suppose that the discontinuity had by this time swept past the coherent tail altogether and, assuming a solar wind speed of $\lesssim$ 500 km/sec, an upper limit to the length of the tail is $\sim 10^3$ R_E.

The large amount of fine structure in pass 5 could be interpreted as a result of the rapidly changing anisotropy direction at that time in interplanetary space; as is evident from Figure 8(3).

Isotropisation of the higher energy ($\gtrsim$ 30 MeV) particles at the magnetopause is unlikely to occur to any great extent (Montgomery and Singer, 1969). This is believed to be due to the fact that isotropisation at lower energies is due to a'resonance-type' interaction with irregularities on the magnetopause surface: a process that breaks down as the particle gyroradius increases. Hence anisotropies in the high energy fluxes should play an even greater part in determining the structure of the polar cap profiles and impact-zones could result (see Engelmann et.al., 1971; Morfill and Quenby, 1971).

Quenby and Sear (1971) point out that at higher particle energies magnetic discontinuities are less efficient in reflecting the particles incident upon them and hence are less likely to maintain such significant separation of particle populations. Comparing Figures 8(8) and 8(13), i.e. the same pass at different energies, it can be seen that whilst the profiles show the same trends, the separation of regions of different counting rates over the polar cap are not so well defined at the higher energy. This could be interpreted in terms of the declining efficiency of the magnetic

discontinuity for separation of particle populations of increasing energy.

Displayed and interpreted in this way these data also require that there are areas on the polar caps, the particles from which originate in the neutral sheet dawn and dusk sides and which, in one satellite pass, can support counting rates that differ by a large amount, e.g. Figures 8(7, 8, 11). In the case of Figure 8(8) the effect could possibly have been temporal but in Figures 8(7 and 11) it is extremely unlikely that such large decreases could occur in so short a space of time. If the effect is indeed a spatial one then the implication is that the 'neutral sheet' can support large particle gradients. This would hardly be feasible if the sheet were genuinely thin, quiet and magnetically neutral, since particles within it would have great freedom of movement across the sheet. If, however, the structure of the sheet corresponded rather more closely to the model of Schindler (1971), Schindler and Ness (1971) who predict a series of neutral lines within the neutral sheet resulting from a magnetic 'loop-type' structure of the tail then it might not be unreasonable to expect quite large gradients to exist since the 'neutral sheet' would appear magnetically turbulent. This kind of neutral sheet would also help keep the two sides of the magnetopause uncoupled.

The conditions closer to the earth are different from those far down the tail and it is interesting to see if the model also applies in this region. The model requires that considerable field line draping can exist around the front of the magnetopause. This being so, then for low energy particles good coupling will also occur around the magnetopause and, because of particle isotropisation at the boundary a fairly uniform particle intensity should exist around it. Hence, it is to be expected that the regions shown on the polar plots for low energy particles, that connect out to both

the dawn and dusk magnetopause boundaries near the earth will show very similar counting rates. Also, these rates should be quite high unless there exists a very low interplanetary flux near the earth. An indication of the validity of these conclusions is given in the low energy data where the 'magnetopause-connected' regions in passes 1, 2 show high counting rates, those in 3, 4 do not whilst in 5, 6 the counting rates increase again. Comparison with the interplanetary fluxes shown in Figure 8(3) indicates that the data are consistent with the model. This aspect of the comparison is weakened, however, by the poor time resolution of the interplanetary data.

At 30 MeV, existing anisotropies are not destroyed on contact with this region of the magnetopause. 'Impact zone' effects result and are well demonstrated in Figures 8(11, 12). In Figure 8(11), S-71 'sees' only the dusk magnetopause zone, which exhibits a low counting rate (c.f. 8(6)). In Figure 8(12) the ESRO I trajectory is seen to intersect both the dawn and dusk magnetopause zones. In the dawn zone there is a high counting rate which reduces to a low rate as the satellite crosses into the dusk zone. This is consistent with the prevailing interplanetary anisotropy and indicates the accuracy of the predicted boundaries.

The model appears to be consistent with most aspects of the data, it now remains to apply it to some more general aspects of particle access to the polar caps.

Delayed access to the polar caps. - Delays in the arrival of protons corresponding to features observed in the flux in interplanetary space have been observed on a number of occasions (e.g. Kane et.al., 1968; Evans and Stone, 1969). The observed delays vary from $\sim \frac{1}{2}$ hr to $\sim$ 20 hrs and have often been interpreted in terms of diffusion delays. With the kind of model suggested here, the tail itself can produce no delay since access across the magnetopause is very swift; rather, it is suggested that all such 'delays'

can be interpreted in terms of conditions in interplanetary space.

A genuine delay can be produced if flux gradients exist in interplanetary space and convect with the solar wind. Such gradients could be caused by magnetic (e.g. tangential) discontinuities which, as has been shown, can produce access delays $\underline{\sim}$ 1 - 3 hours. Secondly an 'apparent' delay can be caused when satellite detectors sample proton polar profiles which are not representative of the overall polar structure. As an example of this latter effect it can be imagined that only the ESRO I spacecraft data were available for passes 1, 2 and 3 of the Nov. 18th event. Then the results of S-71E would have been consistent with a delayed access of particles to the northern polar cap of $\sim 3\frac{1}{2}$ hours. Since, however, S-27 data were also available this was seen not to be the case. It is an excellent example of how inadequate data coverage would perhaps have led to an incorrect interpretation. Such examples underline the need for clusters of satellites in order to obtain unambiguous results.

Van Allen et.al. (1971) have pointed out that a response to interplanetary anisotropies might also be the cause of observed north-south counting rate differences. Whilst the present model does, in principle, agree with such an interpretation, it would suggest that the reconnection were of an 'Axford' type rather than the early Dungey type as suggested by Van Allen et.al. (1971).

Access of High Energy Protons. - The trajectories of high energy ($\lesssim$ 360 MeV) protons in model magnetospheres and magnetotails have been studied by Morfill (1971), Engelmann et.al. (1971) and the results applied to satellite data e.g. Engelmann et.al. (1971), Morfill and Quenby (1971). At such energies, existing anisotropies are not destroyed at the magnetopause boundary and the resulting polar structure is even more sensitive to the

anisotropy direction than at low energies. It was concluded by Morfill and Quenby (1971) that transfer of the protons from interplanetary to tail field lines takes place under conditions approaching a discontinuity model for the tail magnetopause and that much of the polar cap structure at these energies is due to 'impact-zone' effects resulting from interplanetary particle anisotropies.

Access of Electrons. - Electrons ($\gtrsim$ 40 keV) show rather less structure over the polar caps than do protons and the access time has been shown to be very short indeed (Lin and Anderson, 1967; Van Allen, 1969). These effects are probably due to the fact that there is little interplanetary structure due to the difficulty in maintaining gradients with particles that are nearly relativistic. Also the gyroradii of the particles, when crossing the magnetopause, are so small that there are no 'impact zone' effects. Hence most electron profile structure to be expected would be gradients across the tail (as with low energy protons) which result from anisotropies that might exist early in the event.

Pseudo-trapping and Permanent Trapping Regions. - Apart from the few remarks made earlier in the chapter these regions are beyond the present scope of this work. Literature that has been published to explain the structure includes Flindt (1970), Haskell and Hynds (1971) and strong scattering in the pseudo trapping region is discussed in Morfill (1972).

It is suggested, however, that the polar plots would provide a good framework within which to study these regions.

8.6. Summary and Conclusions

The ordering system developed in Chapter 7 based on particle trajectories in a high simulation model magnetosphere was used in interpreting the low

energy proton polar cap counting rate profiles obtained during the solar proton event of Nov 18th. The results were compared with interplanetary particle and magnetic data. A correlation was found between the polar cap data and interplanetary particle anisotropies and magnetic conditions. The results were found to be irreconcilable with a diffusion model of particle access and difficulties were also encountered in an attempt to interpret the data on the basis of the Dungey (1961, 1963) reconnection model.

The rotational discontinuity model of the magnetopause, suggested by Morfill and Quenby (1971) was proposed to explain the data. In this interpretation low energy particle pitch angle distributions are isotropised at the magnetopause boundary by interaction with irregularities there (e.g. Kelvin-Helmholtz instabilities). Particles then follow field lines, normal to the rotational discontinuity, that reconnect to the interplanetary field. Although isotropisation occurs at the boundary the interplanetary anisotropy still causes differences in the flux around it. As a result gradients can exist across the tail.

This same model was able to explain structure in the higher energy ($\gtrsim$ 30 MeV) profiles where 'impact-zone' effects are believed to become important. Thus, taken with the high energy ($\lesssim$ 360 MeV) results of Engelmann et.al. (1971) and Morfill and Quenby (1971) it appears that particle trajectories in a model magnetosphere, having as its boundary a magnetopause that often takes the form of a rotational discontinuity, can explain much of the observed structure in the proton polar cap profiles over the wide energy range (2 - 360 MeV).

The low energy results also suggest that the neutral sheet might be able to support particle gradients, a result which necessitates a model

that predicts magnetic turbulence in the sheet (Schindler, 1971; Schindler and Ness, 1971).

A rapid change of interplanetary particle flux was observed to be coincident with a discontinuous change in interplanetary magnetic field direction. Certain aspects of the polar cap proton profiles were interpreted in terms of the convection of this discontinuity with the solar wind. Quenby and Sear (1971) have suggested that the motion of low energy protons might be inhibited across tangential discontinuities. The coincident observations of particle and magnetic discontinuities might have been an observation of this phenomenon.

On the basis of these observations it was possible to suggest that limits to the length, L, of the coherent, geomagnetic tail are $400\ R_E < L < 10^3\ R_E$.

The co-ordinate system developed in this work is still at a low level of sophistication. An obvious improvement would involve improving the magnetosphere model used. Since any such model must be dynamic, then suitable parameters must be measured in space for use in such a model. It is suggested (following Roederer, 1969) that use of the ATS satellites could be made in providing a continuous monitoring of suitable parameters: much in the way that geomagnetic activity indices are available on a day-to-day basis.

Also, the form of the co-ordinate system can be improved. If magnetic flux is being 'lost' uniformly across the magnetopause and across the neutral sheet then it should be possible to draw 'contours of equal flux loss' on the 'tail diagrams' used in this analysis. These would bear a direct relation to the distance down the tail at which the flux was lost and hence also relate to the distance of particle entry. Such contours could be

used as the basis of an improved ordering system for particles arriving over the polar caps from distances far down in the geomagnetic tail.

REFERENCES

Allen, C.W., Astrophysical Quantities, 2nd edition, p.100. Univ. of London Athalone Press, 1963.

Astronomical Ephemeris, 1970.

Aubry, M.P., Russell, C.T., and Kivelson, M.G., J.G.R., vol.75, p.7018, 1970.

Axford, W.I., J.G.R., vol.67, p.3791, 1962.

Axford, W.I., Reviews of Geophys., vol.7, p.421, 1969.

Axford, W.I. and Hines, C.O., Can. Journal Phys., vol.39, p.1433, 1961.

Axford, W.I., Petschek, H.E. and Siscoe, G.L., J.G.R., vol.70, p.1231, 1965.

Backer, D.C., Nature, vol.228, p.42, 1970.

Bahcall, J.W., Rees, M.J. and Salpeter, E.E., Astroph. J., vol.162, p.737, 1970.

Barnaby, C.F. and Barton, J.C., Proc. Phys. Soc., vol.76, p.750, 1961.

Beedle, R.E. and Webber, W.R., Can. Journal Phys., vol.46, S1014, 1968.

Behannon, K.W., J.G.R., vol.73, p.907, 1968.

Behannon, K.W., J.G.R., vol.75, p.743, 1970.

Behannon, K.W. and Fairfield, D.H., Plan. Sp. Sci., vol.17, p.1803, 1969.

Bergamini, R., Londillo, P. and Selti, G., Il Nuovo Cimento, vol.52B, p.493, 1967.

Bertoti, B., Cavaliere, A. and Pacini, F., Nature, vol.223, p.1351, 1969.

Bewick, A., Haskell, G.P. and Hynds, R.J., J.G.R., vol.75, p.4605, 1970.

Birks, J.The Theory and Practice of Scintillation Counting, Pergamon Press, 1964.

Bleeker, J.A.M., Burger, J.J., Dereenberg, J.H., Scheepmaker, A., Swanenburg, B.N., Tananka, Y., Hayakawa, S., Makino, F. and Ogawa, H., Can. Journal Phys., vol.46, S464, 1968.

Bleeker, J.A.M., and Dareenberg, J.M., Astroph. J., vol.159, p.215, 1970.

Bostrom, C.O., ESLAB/ESRIN Symposium on Intercorrelated Satellite Observations related to Solar Events, Noordwijk, Holland, September 1969.

Bowyer, S., Byram, E.T., Chubb, T.A. and Friedman, H., Science, vol.146, p.912, 1964.

Bowyer, S., Lampton, M., Mack, J. and Mendonca, F., Astroph. J. Lett., vol.150, L1, 1970.

Brecher, K. and Morrison, P., Phys. Rev. Lett., vol.23, p.802, 1969.

Burbidge, G.R., Astroph. J., vol.159, L105, 1970.

Burlaga, L.F., Solar Physics, vol.4, p.67, 1968.

Byram, E.T., Chubb, T.A. and Friedman, H., Science, vol.158, p.257, 1967.

Byram, E.T., Chubb, T.A. and Friedman, H., Nature, vol.229, no.5286, p.544, 1971.

Cameron, J.F., Nuclear Electronics, vol.1, p.100, I.A.E.A., 1962.

Cocke, W.J., Disney, M.J. and Taylor, D.T., Nature, vol.221, p.525, 1969.

Cocke, W.J. and Disney, M.J., Astroph. J., vol.160, L139, 1970.

Colburn, D.S. and Sonett, C.P., Space Sci. Rev., vol.5, p.439, 1966.

Cole, T.W., Nature, vol.223, p.487, 1969.

Coleman, P.J., Jr., Davis, L., Jr. and Sonett, C.P., Phys. Rev. Lett., vol.5, p.43, 1960.

Coleman, P.J., Sr., Polar Ionosphere and Magnetosphere Meeting, Royal Society, Dec. 1970.

Courtier, G.M., Ph.D. Thesis, University of London, 1964.

Crispin, A. and Hayman, P.J., Proc. Phys. Soc., vol.83, p.1051, 1964.

Davies, R.D., Nature, vol.223, p.355, 1969.

Dessler, A.J., J.G.R., vol.69, p.3913, 1964.

Drake, F.D. and Craft, H.D., Nature, vol.220, p.231, 1968.

Dungey, J.W., Phys. Rev. Lett., vol.6, p.47, 1961.

Dungey, J.W., Geophyscs, The Earth's Enviornment, ed. De Witt et.al., p.503, pub. Gordon and Breach, N.Y., 1963.

Dungey, J.W., J.G.R., vol.70, p.1753, 1965.
Durney, A.C., Morfill, G.E., Quenby, J.J., To be published in J.G.R., 1971.
Ekers, R.D. and Moffet, A.T., Astroph. J., vol.158, L1, 1969.

Endean, V.G. and Allen, J.E., Nature, vol.228, p.348, 1970.

Engelmann, J., Hynds, R.J., Morfill, G., Axisa, F., Bewick, A., Durney, A.C., and Koch, L., J.G.R., vol.76, p.4245, 1971.

Evans, R.D., "The Atomic Nucleus", pub. McGraw Hill, 1955.

Evans, L.C. and Sone, E.C., J.G.R., vol.74, p.5127, 1969.

Fairfield, D.H., G.S.F.C., preprint, X-692-70-163, 1970.

Fairfield, D.H. and Ness, N.F., J.G.R., vol.72, p.2379, 1967.

Fairfield, D.H. and Ness, N.F., J.G.R., vol.75, p.7032, 1970.

Felten, J.E., IAU Symposium, No.37, Rome, May 1969.

Felten, J.E. and Morrison, P., Astroph. J., vol.146, p.686, 1966.

Felten, J.E. and Rees, M.J., Nature, vol.221, p.924, 1969.

Flindt, H.R., J.G.R., vol.75, p.39, 1970.

Frank, L.A., J.G.R., vol.72, p.3753, 1967.

Frank, L.A., Van Allen, J.A. and Craven, J.D., J.G.R., vol.69, p.3155, 1964.

Friedman, H., Proc. I.R.E., vol.47, p.278, 1959.

Fritz, G., Henny, R.C., Meekins, J.F., Chubb, T.H. and Friedman, H., Science, vol.161, p.711, 1969.

Giacconi, R., Gursky, H. and Paolini, F.R., Phys. Rev. Lett., vol.9, p.439, 1962.

Giacconi, R., Reidy, W.P., Vaiana, G.S., Van Speybroeck, L.P. and Zehnpfennig, T.F., Space Science Reviews, vol.9, p.3, 1969.

Ginzburg, V. and Syrovatskii, S., Ann. Rev. Astron. and Astroph., vol.3, p.297, 1965.

Gold, T., Nature, vol.218, p.731, 1968.

Gold, T., Nature, vol.221, p.25, 1969.

Goldreich, P., Proc. Astron. Soc. of Australia, vol.1, no.5, p.227, 1969.

Goldreich, P. and Julian, W.H., Astroph. J., vol.157, p.869, 1969.

Gruber, D., Malteson, J.L., Pelling, M.R. and Peterson, L.E., Nature, vol.226, p.532, 1970.

Gurnett, D.A., XV IUGG General Assembly, Moscow, 1971.

Gursky, H., Giacconi, R., Gorenstein, P., Waters, J.R., Oda, M., Bradt, H., Garmire, G. and Sreekantan, B.V., Astroph. J., vol.146, p.310, 1966.

Haskell, G.P. and Hynds, R.J., To be published in "The Earth's Particles and Fields", ed. Billy McCormac, 1971.

Hawson, G.L., Private Communication with the Meteorological Office.

Hayakawa, S., Proc. Int. Conf. Cosmic Rays, Calgary, part A, p.82, 1967.

Heristchi, D.J., Nuclear Instruments and Methods, vol.47, p.39, 1967.

Hewish, A., Ann. Rev. Astron. and Astroph., vol.8, p.265, 1970.

Hewish, A., Bell, S.J., Pilkington, J.D.H., Scott, P.F. and Collins, R.A., Nature, vol.217, p.709, 1968.

Hillier, R.R., Jackson, W.R., Murray, A., Redfern, R.M. and Sale, R.G., Astroph. J., vol.162, no.3, part 2, L177, 1970.

Hollander, Perlman, Seaborg, Rev. Mod. Phys., vol.25, no.3, p.490, 1953.

Holt, S.S., Boldt, E.A. and Serlemitsos, P.J., Astroph. J. Lett., vol.158, L155, 1969.

Horstman, H. and Horstman-Moretti, E., Nature Phys. Sci., vol.229, p.148, 1971.

Hunt, G.C., Nature, vol.224, p.1005, 1969.

Jokipii, J.R., Astroph. J., vol.146, p.480, 1966.

Jones, F.C., J.G.R., vol.66, p.2029, 1961.

Jones, F.C., Phys. Rev., vol.137, part B, p.1306, 1965.

Kane, S.R., Winckler, J.R. and Hoffman, D.J., Pl. Sp. Sci., vol.16, p.1381, 1968.

Kardeshev, N.S., Soviet Astronomy AJ, vol.14, no.3, p.375, 1970.

Komesareff, M.M., Nature, vol.225, p.612, 1970.

Kristian, J., Astroph. J., vol.162, p.173, 1970.

Lanzerotti, World Data Report UAG 9, p.34, 1970.

Large, M.I., Vaughn, A.E. and Mills, B.Y., Nature, vol.220, p.340, 1968.

Lin, R.P. and Anderson, K.A., J.G.R., vol.71, p.4213, 1966.

Lin, R.P. and Anderson, K.A., Solar Physics, vol.1, p.446, 1967.

Lyne, A.G., Herstmonceux Conference on Astronomy, April 1969.

McCracken, K.G., Rao, U.R., Bukata, R.P. and Keath, E.P., Solar Physics, vol.18, p.100, 1971.

McDiarmid, I.B. and Burrows, J.R., Can. Journ. Phys., vol.46, p.49, 1968.

McDiarmid, I.B., Burrows, J.R. and Nilson, M.D., Proc. IEEE, vol.57, no.6, p.1051, 1969.

McIlwain, C.E., J.G.R., vol.66, p.3681, 1961.

McIlwain, C.E., to be published in "The Earth's Particles and Fields", ed. Billy McCormac, 1971.

Manchester, R.N., Nature, vol.228, p.265, 1970.
Mariani, F. and Ness, N.F., J.G.R., vol.74, p.5633, 1969.
Mead, G.D., J.G.R., vol.69, p.1181, 1964.

Mead, G.D. and Beard, D., J.G.R., vol.69, p.1173, 1964.

Michel, F.C., Plan. Sp. Sci., vol.13, p.753, 1965.

Michel, F.C., Astroph. J., vol.159, L25, 1970.

Michel, F.C. and Dessler, J.G.R., vol.75, p.6061, 1970.

Mihalov, J.D., Colburn, D.S. and Sonett, C.P., J.G.R., vol.173, p.943, 1968.

Mills, B.Y., Nature, vol.224, p.505, 1969.

Montgomery, M.D. and Singer, S., J.G.R., vol.74, p.2869, 1969.

Morfill, G.E., to be published in Plan. Sp. Sci., 1971.
Morfill, G.E., to be published in J.G.R. 1972.
Morfill, G.E. and Quenby, J.J., To be published in Plan. Sp. Sci., 1971.

Morrison, P., Ann. Rev. Astron. Astroph., vol.5, p.325, 1967.

Mott and Sutton. "Encyclopaedia of Physics", ed. S. Flugge (Berlin: Springer Verlag), vol.45, p.86, 1958.

Ness, N.F., J.G.R., vol.70, p.2989, 1965.

Ness, N.F., Rev. of Geophys., vol.7, p.97, 1969.

Ness, N.F., To be published in "The Earth's Particles and Fields", ed. Billy McCormac, 1971.

Ness, N.F., Scearce, C.S. and Seek, J.B., Trans. American Geophys. Union, vol.47, p.162, 1966(a).

Ness, N.F., Scearce, C.S. and Cantarano, S., J.G.R., vol.71, p.3305, 1966(b).

Ness, N.F., Scearce, C.S. and Cantarano, S., J.G.R., vol.72, p.3769, 1967(a).

Ness, N.F., Behannon, K.W., Cantarano, C.S. and Scearce, C.S., J.G.R., vol.72 p.4577, 1967(b).

Neugebauer, M. and Snyder, C.W., "The Solar Wind", ed. R.J. Mackin and M. Neugebauer, p.3, Pergamon Press, New York, 1960.

Olson, W.P., J.G.R., vol.74, p.5642, 1969.

Ostriker, J.P. and Gunn, J.E., Astroph. J., vol.157, p.1395, 1969.

Paccini, F., Nature, vol.219, p.145, 1968.

Paccini, F. and Rees, M.J., Nature, vol.226, p.622, 1970.

Parker, E.W., Astroph. J., vol.128, p.664, 1958.

Peterson, L.E., J.G.R., vol.70, p.1762, 1965.

Peterson, L.E. and Jacobson, A.S., Astroph. J., vol.145, p.965, 1966.

Pounds, K.A., Nature, vol.229, p.303, 1971.

Quenby, J.J. and Sear, J.F., Plan. Sp. Sci., vol.19, p.95, 1971.

Radhakrishnan, V. Komesaroff, M.M., Cooke, D.J. and Morris, D., Nature, vol.221, p.443, 1969.

Radhakrishnan, V. and Cooke, D.J., Astroph. Lett vol 3 p. 225 1969.
Radhakrishnan, V. and Manchester, R.N., Nature, vol.222, p.228, 1969.

Rappaport, S., Bradt, H. and Mayer, W., Nature, Phys. Sci., vol.229, p.40, 1971.

Rees, M.J., Trimble, V.L. and Cohen, J.M., Nature, vol.229, p.396, 1971.
Richards, D.J. and Comella, D. Nature vol 222 p. 552 1969.
Richman, Proc. I.R.E., vol.42, p.106, 1954.

Ricket, B.J. and Lyne, A.G., Nature, vol.218, p.934, 1968.

Roederer, J.G., "Shell Splitting and Radial Diffusion of Geomagnetically trapped Particles", Lecture at the Advanced Study Institute, "Earth's Particles and Fields", Freising, Germany 1967(a).

Roederer, J.G., "Experimental Evidence on Radial Diffusion of Geomagnetically Trapped Particles", Lecture at the Advanced Study Institute "Earth's Particles and Fields", Freising, Germany, 1967(b).

Roederer, J.G., Rev. Geophys., vol.7, p.77, 1969.

Ruderman, M., Nature, vol.223, p.598, 1969.

Sandage, A.R., Giacconi, R., Gursky, H., Bradt, H., Sreekantan, B.H., Osawa, K., Osmer, P., Gorenstein, P., Water, J., Garmine, G., Oda, M., and Jugaku, J., Astroph. J., vol.146, p.316, 1966.

Schindler, K., To be published in "The Earth's Particles and Fields", ed. Billy McCormac, 1971.

Schindler, K. and Ness, N.F., preprint to be published in J.G.R., 1971.

Shlovskii, I.S., Astroph. J. Lett., vol.159, L77, 1970.

Silk, J., Astroph. J. Lett., vol.151, L19, 1968.

Sonnerup, B.U.O. and Cahill, L.J., J.G.R., vol.72, p.171, 1967.

Sonnerup, B.U.O. and Cahill, L.J., J.G.R., vol.73, p.1757, 1968.

Sood, R.K., Thesis. University of London, 1969.

Southwood, J.D., Plan. Sp. Sci., vol.16, p.587, 1968.

Speisser, T.W. and Ness, N.F., J.G.R., vol.72, p.131, 1967.

Spreiter, J.R., Summers, A.L. and Alksne, A.Y., Plan. Sp. Sci., vol.14, p.223, 1966.

Staelin, D.H. and Reifenstein, E.C., Science, vol.162, p.1481, 1968.

Stein, J.A. and Lewin, W.H.G., M.I.T. preprint 2098-243, submitted to Phys. Rev. Lett.

Sturrock, P.A., Astroph. J., vol.164, p.529, 1971.

Sugivra, M., Skillman, T.L., Ledley, B.G. and Heppner, J.P., G.S.F.C. preprint no. X-612-69-359, 1969.

Taylor, J.H., Astroph. J. Lett., vol.3, p.209, 1969.

Technical Interface vol.1, no.3, Aim Electronics, Cambridge, England.

Thomas, G.R. and Dalziel, R., Space Research Radio and Space Research Station, Slough, Bucks. preprint no. A790.

Topping, J. "Errors of Observation and Their Treatment", Chapman and Hall Limited, London, 1961.

Trimble, V., Astron. J., vol.73, p.535, 1968.

Tucker, W.H. and Gould, R.J., Astroph. J., vol.144, p.244, 1966.

Van Allen, J.A., Proc. of S. Barabara Conf., 1969.

Van Allen, J.A., Fennel, J.F. and Ness, N.F., J.G.R., vol.76, p.4262, 1971.

Venkatarangan, P., Venkatesan, D. and Van Allen, J.A., Proc. 11th Int. Conf. Budapest, 1969.

Vette, J.I., J.G.R., vol.67, p.1731, 1962.

Walker-Fillius, R., "Satellite instruments using Solid State Detectors", p.26, pre-print.

Wampler, E.J., Scargle, J.D. and Miller, J.S., Astroph. J., vol.157, p.L1, 1969.

Williams, D.J. and Mead, G.D., J.G.R., vol.70, p.3017, 1965.

Williams, D.J. and Ness, N.F., J.G.R., vol.71, p.5117, 1966.

Williams, D.J. and Bostrom, C.O., J.G.R., vol.72, p.4497, 1967.

Williams, D.J. and Bostrom, C.O., J.G.R., vol.74, p.3019, 1969.

Winnigham, J.D., To be published in "The Earth's Particles and Fields", ed. Billy McCormac, 1971.

Woolf, J.H., Silva, R.W., McKibbin, D.D. and Mason, R.H., J.G.R., vol.72, p.4577, 1967.

Zeissig, G.A. and Richards, D.W., Nature, vol.222, p.151, 1969.